



Interactions of Flow Field and Combustion Characteristics in a Swirl Stabilized Burner

vorgelegt von
Ahmed Abdelrazek Emara,
Magister -Ingenieur,
aus Ägypten

Von der Fakultät V – Verkehrs- und Maschinensysteme
der Technischen Universität Berlin
zur Erlangung des akademischen Grades

Doktor der Ingenieurwissenschaften
– Dr.-Ing. –

genehmigte Dissertation

Promotionsausschuss:

Vorsitzender: Prof. Dr. rer. nat. Valentin Popov
Gutachter: Prof. Dr.-Ing. Christian Oliver Paschereit
Gutachter: Prof. Dr. Eng. Mahmoud Shahin

Tag der wissenschaftlichen Aussprache: 28. September 2011

Berlin 2011

D 83



Interactions of Flow Field and Combustion Characteristics in a Swirl Stabilized Burner

By

M.Sc. Ahmed Abdelrazek Emara

M.Sc. Mechanical Power Engineering- Helwan University- Cairo- Egypt- 2004

A Thesis

Submitted to Faculty of Mechanical Engineering and Transport Systems-

TU Berlin

in Partial Fulfillment of the Requirement for

the Degree of Doctor of Philosophy in Mechanical Engineering

Approved Dissertation

Promotion Committee:

Chairman: Prof. Dr. rer. nat. Valentin Popov

Referee: Prof. Dr.-Ing. Christian Oliver Paschereit

Referee: Prof. Dr. Eng. Mahmoud Shahin

Day of scientific debate: 28 September 2011

Berlin 2011

D83

Dedication

This Thesis is dedicated to the memory of my late wife, Dr. Fayseer Zaid, who died in children birth on August 19, 2010 at the age of 29. I did not realize until her death how she influenced the lives of so many people. I loved her and will always love her, and am proud of what she accomplished in her short life.

Also to my daughters Aiah and Arwa,

my late father and brother,

my mother and family, and

Nermin

Acknowledgements

First and foremost, countless thanks go to the God.

I would like to express my great appreciation, deepest gratitude and sincerest thanks to my advisor and supervisor Prof. Dr. Ing. C. O. Paschereit as he pushed me in the proper directions. I also have been benefited greatly from his expertise, guidance, valuable advice, and fruitful discussions throughout all stages of my work particularly when the going was hard. My great thanks go to Prof. Dr. Eng. M. Shahin for his deep advice and scientific support. I thank him for withstanding the hard times in reviewing and modifying my dissertation.

I am deeply indebted by the assistance of Dr. C.N. Nayeri and my colleagues at the institute, especially A. Lacarelle, J. Moeck, K. Oberleithner, and C. Pfifer for their valuable advice, help, and discussions. I gratefully acknowledge their contributions. Thanks also go to Mr. R. Grüneberger in DLR- Berlin for his sincere advice during the designing and manufacturing some parts of my test facilities. I would like to extend my sincere thanks to ISTA and DLR guys, without naming everyone, especially the combustion, water, and boundary layer lab- mates and friends I have had during my work in Berlin. Thanks to Dipl. Ing. H. Stolpe for his help in electronic requirements during the work in doctorate.

Special thanks go to the secretary members; Ms. Lilli Lindemann, Ms. Kristin Halboth, and Sandy and also to Ms. A. Pätzold and Ms. Kulzer for their help during my work. I would like to thank the whole technicians and workshop members, especially Mr. Mettchen, for their help in manufacturing the required parts to my work.

Gratefully, I would like to thank the Egyptian Ministry of Higher Education and Scientific Research for financial support and the Egyptian embassy in Berlin for moral support.

I wish to give a special recognition, great thanks, and mercy to my nine years companion, my late wife Dr. Tayseer Zaid for her unconditional love and sincere standing beside me throughout all stages of my work until the end of her life some months ago. Thanks for supporting, motivating, and pushing me in pursuit of my dreams, desires and hopes. I could never have achieved any thing without you Tayseer. I love you so much and hopefully to be together on the date of the meeting in Paradise. Thanks to my small daughters Aiah and Arwa for their patience far from me to help me to concentrate in my work. I gratefully thank my mother, my mother-in-law and Dr. Nahed Wahba, the wife of my brother, for taking care and sincere support of my daughters in life and study at my homeland Egypt. Thanks also to the whole family; Nagy, Mahmoud, Kareem, Neema, and Reham. I love you all. Thanks to Nermin for her sincere support.

Finally, I would like to thank all people who helped me to finish this thesis.

Zusammenfassung

Die vorliegende Arbeit beschäftigt sich mit Verbrennungscharakteristiken, Strömungsfelduntersuchungen sowie Wechselwirkungen des Strömungsfeldes in einem drallstabilisierten Brenner. Das Hauptziel ist es, eine stabile Verbrennung bei geringen Emissionen zu gewährleisten. Um das zu erreichen, werden drei Ideen untersucht. Die erste Idee ist die Verwendung eines neuen Modells eines in den Brenner integrierten rückgekoppelten fluidischen Oszillators. Die zweite ist die Modulation einer in denselben Brenner eingelassenen Piloteinspritzdüse, die mit mehreren Löchern versehen ist. Die letzte Idee umfasst eine Änderung des Brennerauslasses und der akustischen Randbedingung.

Der fluidische Oszillator hat keine beweglichen Teile oder Ventilregelungen, nur die Fluidbewegung selbst ist verantwortlich für die Erzeugung einer pulsierenden Strömung. Die Schwingung erfolgt selbsterregt. Untersucht werden das Strömungsverhalten im inneren und äußeren Bereich des fluidischen Oszillators sowie dessen Verhalten in aktiven Kontrollregelungen. Die optimale Oszillatorkonstruktion überwindet dabei Größeneinschränkungen sowie Hochfrequenzstörungen bedingt durch Hochdruckschwingungen und wird im Brenner unter reagierenden und nichtreagierenden Bedingungen getestet. Das kohärente Strömungsfeld und die Wechselwirkung zwischen Eindüsung und Brennerströmungsfeld werden an drei coaxialen Positionen im Brenner nachgewiesen. Die Frequenzanalyse der Signale bei verschiedenen Massenströmen zeigt einen linearen Zusammenhang für das gewählte Schwingungsmodell auf. Die Druckschwankungen liegen in sicherer Distanz zu den erwarteten Verbrennungsinstabilitäten. Die Strouhalzahl ist nahezu linear im untersuchten Bereich.

Der zweite Teil hat die Zielsetzung, die Wirkung unterschiedlicher Piloteindüisungen auf die Stabilität, die Emissionen und das Strömungsfeld in einem industrienahen, drallstabilisierten Brenner bei verschiedenen akustischen Randbedingungen (kurzer und langer Brennkammerraum) zu erklären. Die Art der Eindüisung (Brennstoff mit/ohne Luft, nur Luft) sowie Form und Position (im Brenner unten, mittig, oben) der Düse werden bei konstantem globalem Äquivalenzverhältnis überprüft. Die Eindüisung von über das Hauptrohr transferierter Luft durch die Pilotlanze und einer im Brenner unten liegenden Piloteinspritzdüse zeigen die besten Resultate. Die Unterdrückung von Instabilitäten wird bei magerer Verbrennung erreicht.

Der letzte Teil dieser Arbeit beschäftigt sich mit Änderungen des Dralls in der Strömung, welcher stark durch die Auslassbedingungen der Brennkammer beeinflusst wird. Untersucht wird dies mittels eines industrienahen, drallstabilisierten Brenners unter nichtreagierenden Strömungsbedingungen. Die Brennkammerlänge und das Auslasskontraktionsverhältnis werden variiert und ergeben die größte Änderung im Strömungsfeld bei einer kurzen Brennkammer und dem kleinsten Kontraktionsverhältnis.

Die verwendeten Messtechniken sind Mikro- und Hydrofone, PIV, LIF, Hitzdrahtanemometrie, Thermoelemente, Gasanalytoren und OH* Chemilumineszenz-Photomultiplier mit Kamera.

Abstract

This work deals with combustion characteristics, flow field investigations, and flow field interaction in a swirl-stabilized burner. The main goal is to provide stable combustion at low emissions. To achieve this in the combustor, three concepts are inspected. The first one is applied by using a new model of feedback fluidic oscillator (designed, modulated, and manufactured at TU Berlin) integrated with the burner. The second concept is modulating a new multi-hole pilot injector inserted into the same swirl-stabilized burner. The last concept is by changing of the combustor outlets and acoustic boundary conditions.

The fluidic oscillator has no moving parts or valve arrangements but the fluid movement itself is responsible of generating a pulsed flow. The oscillation comes without any external excitation and is described as self-exciting. The behavior of the fluid flow inside and outside the fluidic oscillator is studied as well as the oscillator performance in active control schemes which include high-frequency flow modulation. The optimum oscillator design overcomes size restrictions and higher frequency penalties reproduced from higher pressure oscillations and it is tested inside the swirl stabilized burner at non-reacting and reacting conditions. Phase averages reconstructed on proper orthogonal decomposition (POD) as well as acoustic measurements was used to characterize the coherent structures shed from the oscillator and the burner. The coherent flow field and the interaction between injector and burner flow field are demonstrated at three proposed coaxial mounting positions inside the burner. The frequency contents of the signals at different mass flows show a linear representation for the proposed oscillator model. The pressure oscillations also lie in a safe range far from expected combustion instabilities. The Strouhal number is almost linear at a specified range which contains the combustion investigations.

Influence of this oscillator on stability and combustion control is demonstrated by implementing some transfer of the main fuel, air or both inside the fluidic oscillator, in an attempt to enhance the combustion performance at a constant overall equivalence ratio. The air transfer inside the oscillator (2.73%) is the best way to reduce the emissions at the whole coaxial mounting positions while the combustion is free of instabilities. Some small amounts of fuel transfer plus air inside the fluidics may be also useful in reduction of nitrogen oxides at low values of carbon monoxide and at stable conditions. It was determined that the optimum mounting position of the fluidics was at the underside the burner. So, the fluidics may have an advantage to work better with some new or other burner configurations and different positions inside the burner to reduce emissions and instabilities which, in turn, enhances the combustion and complies with global environmental

laws at the whole world.

The second part aims to explain the effect of different pilot injections of the new pilot injector on stability, emissions, and flow field in an industrial swirl-stabilized burner at different acoustic boundary conditions (short and long combustor). The pilot injector is moved coaxially to three mounting positions from the burner underside to the burner dump plane, the same as the fluidics. Type of injection (fuel only, air and fuel premixed, and air only) as well as shape and mounting position (burner bottom, middle, and top) of the injector are investigated at a constant overall equivalence ratio. The injection of air transferred from the main tubes through the pilot lance shows better results than the pilot fuel and premixed pilot injection. The stability as well as lower NO_x emissions is achieved by transferring less than 10% of the main air flow through the pilot. The suppression of the instabilities of those two different combustion chambers is achieved at lean combustion. At different coaxial locations, the transferred air is generally able to perform the stability while the best results are achieved when the injector is located at zero position.

PIV measurements performed downstream of the burner show that the pilot injection has a strong impact on the mean flow field at the flame stability locations. The strong pilot air momentum increases the mixing of fuel and air, helps in flame stabilization outside of the burner, and prevents flame oscillation which is one source of thermoacoustic instabilities in the present combustor. The results also show an increase in the flow velocity at the reacting conditions due to the faster motion of the hot spots than in the cold flow. Velocity magnitudes in the conical jet as well as in the recirculation zone increase as a consequence of the heat released by the flame. The corner vortices change in size depending on the pilot momentum. The cone angle in the reacting flow changes because of the buoyancy effect.

The last part is concerned with the changes of swirling flow which can be strongly influenced by the outlet conditions of the combustion chamber, especially at subcritical flow conditions. The effect of such changes on the mean flow or coherent structures is still unclear. It is investigated in the present work in an industrial swirl inducing burner in cold flow conditions with help of PIV technique. Proper orthogonal decomposition (POD) as well as acoustic measurements was used to characterize the coherent structures shed from the burner mouth.

The combustor length (8.17 D and 24.63 D) and the outlet area contraction ratio (1, 0.56, 0.27, and 0.09) are varied. Major changes in the flow field are achieved when using the short combustor and the smallest contraction ratio. For this case, a central jet with streamwise velocity is added to the typical central recirculation zone. The POD analysis of the contraction ratios 1 and 0.09 for the long combustor shows that the first helical mode as well as Kelvin Helmholtz

vortices are present with minor changes for both cases. At a contraction ratio of 0.09, some new structures at the jet location and near the combustor wall appeared. Measurements techniques used in non-reacting and reacting flow investigations are acoustic measurements with a microphone, hydrophone, PIV, LIF, Hot Wire, temperature measuring with thermocouple, gas analysis, and OH* chemiluminescence photography with camera.

List of Contents

	Page No.
Acknowledgements	VII
Zusammenfassung	IX
Abstract	XI
List of contents	XIV
List of figures	XVIII
List of tables	XXIX
Nomenclatures	XXXI
Introduction	1
<u>Part (1) Fluidic oscillator for jet streams integrated into a pilot fuel lance.</u>	7
Chapter (1): Introduction	8
Chapter (2): Experimental Test Facilities and techniques	13
Test Facilities	14
Fluidic Oscillator	14
The Burner	16
Measurements Techniques	17
Hot wire setup	17
Microphone setup	19
PIV setup	21
Hydrophone setup	23
Thermocouple and emissions probe setup	24
ICCD setup	24
Results and Discussions	25
Chapter (3) fluidics design Variations	26
Description of the fluidic Injector	27
1st Design Variation- Fx0	28
2 nd Design Variation	32
Design optimization	32
1 st Fluidic oscillator model- Fx1	32
Other Fluidic oscillator models	37
Chapter (4) Fluidics flow field (inside and outside)	43
LIF Flow visualization	44

PIV Flow visualization in the fluidic oscillator	50
Chapter (5) PIV flow field and influence of a fluidic pilot on combustion in a swirl stabilized burner with inserted fluidic oscillator inside.	65
1- The fluidics at the burner bottom ($X_f=0$)	66
A- Effect of ϕ overall at constant m° air.	70
B- Fuel transfer inside the oscillator at constant main air and constant overall equivalence ratio (0.552).	74
C- Air transfer inside the fluidics at Constant main Fuel and at overall equivalence ratio = 0.552.	75
D- D- Air transfer inside the fluidics at 14% pilot fuel ratio at overall equivalence ratio= 0.552.	76
E- Transfer of Air inside the fluidics at 28% and 42% pilot fuel ratio of the main fuel at overall equivalence ratio 0.552.	78
F- Air transfer inside the fluidics at constant main fuel and at overall equivalence ratio= 0.575.	80
2- The fluidics at the middle of the burner.	81
A- Effect of ϕ overall at constant m° air.	86
B- Air transfer inside the fluidic oscillator at constant main fuel and at constant ϕ overall (0.552).	87
C- Air transfer inside the fluidic oscillator at constant main fuel and at constant ϕ overall (0.575).	88
3- The fluidics at Top (Apex) of the burner.	90
A- Effect of ϕ overall at constant m° air.	100
B- Transfer of fuel inside the oscillator at constant main air and constant ϕ overall (0.552).	101
C- Transfer of Air inside the fluidics at Constant Fuel and at ϕ overall= 0.552.	103
D- Transfer of Air inside the fluidics at constant fuel and at ϕ overall= 0.575.	104
Chapter (6) Conclusion and Recommendations.	105
1. Conclusions.	105
2. Recommendations.	112
References.	114

<u>Part (2) Pilot injector influence on Flow Field Interaction and Combustion characteristics in a Swirl stabilized Burner.</u>	117
Chapter (1): Introduction.	118
Chapter (2): Experimental techniques and facilities.	122
2.1. The Burner.	123
2.2. The test facilities.	125
2.3. Thermocouple and emissions probe setup.	126
2.4. Microphone setup.	126
2.5. ICCD setup.	126
2.6. PIV Setup.	127
Chapter (3): Results and Discussion.	129
3. 1. Control Authority and Combustion Characteristics.	130
A. Injection of pilot fuel and premixed pilot fuel.	130
A.1 Stability by Pilot fuel at short combustion chamber.	130
A.2. premixed pilot fuel injection at short combustion chamber.	134
A.3. Stability of long combustion chamber with pilot fuel only.	136
B. Transfer of part of main air flow through the pilot injector.	137
B.1. Pilot air transfer at short combustion chamber.	137
B.2. Control authority for long combustion chamber.	139
3.2. Flow field Characteristics.	144
A. Isothermal flow.	144
At $X_p = 0.5 \cdot X_{max}$.	144
At $X_p = 0.68 \cdot X_{max}$.	146
B. Isothermal and reacting flow field comparison.	151
C. Reacting flow field.	154
At $X_p = 0.5 \cdot X_{max}$.	154
At $X_p/X_{max} = 0.68$.	155
Chapter (4) Conclusions and Recommendations.	157
1. Conclusions.	158
2. Recommendations.	159
References.	161

<u>Part (3): Planar Investigation of outlet boundary conditions effect on isothermal flow fields of a swirl- stabilized burner.</u>	164
Chapter (1) Introduction	165
Chapter (2): Experimental techniques and facilities	168
The Burner	169
The test facilities	170
PIV Setup	171
Chapter (3): Results and Discussion	173
Independency of the flow field with varying Reynolds Number	173
Coherent structure	177
Outlet boundary conditions effect at the same combustion chamber length 670 mm	178
Outlet boundary conditions effect at different combustion chamber lengths	181
Impact of outlet conditions on coherent structure	182
Chapter (4): Summary and Conclusion	186
References	188
Final Conclusion	190

List of Figures

Figure No.	Title	Page
	<u>Part (1) Fluidic oscillator for jet streams integrated into a pilot fuel lance.</u>	7
Figure 1.1:	The fluidic oscillator schematic.	14
Figure 1.2:	The electronic oscillator	15
Figure 1.3:	Sketch of the Swirl Stabilized Burner	16
Figure 1.4:	The Hot wire calibration chamber	17
Figure 1.5:	Schematic diagram of the Hot Wire calibration system.	18
Figure 1.6:	Schematic diagram of the Hot Wire measurements technique.	19
Figure 1.7:	Basic elements of a condenser microphone.	20
Figure 1.8:	Schematic diagram of the fluidics measurements.	22
Figure 1.9:	Schematic diagram of the water tunnel.	23
Figure 1.10:	Hydrophone photo in air.	24
Figure 1.11:	Hydrophone photo in air.	27
Figure 1.12:	Power Spectral Density of the microphone signals for different Re numbers.	28
Figure 1.13:	Fluidics frequency at Re numbers.	29
Figure 1.14:	Strouhal number of the dominant and 1st frequency peak at different Re numbers for Fluidics.	29
Figure 1.15:	RMS (p) at different Re.	30
Figure 1.16:	Time history of the velocity oscillation for the Fluidics exit limbs at Re of 7468 air.	31
Figure 1.17:	Cross power spectrum of hot wire signal for the Fluidics limbs at Re of 7468 air.	31
Figure 1.18:	1 st Fluidics model Fx1	32
Figure 1.19:	Power Spectral Density of HW signal for different Re of air- Fx1.	33
Figure 1.20:	Fluidics frequency at different Re of air for Fluidic oscillator Fx1.	33
Figure 1.21:	PSD comparison between HW signal and Microphone signal at Re 10923 (3kg/hr) of air- Fx1.	34
Figure 1.22:	Figure: Cross power spectrum of the hot wire signal for the Fluidics limbs at Re 10923 (3kg/hr) of air- HW- Fx1.	34

Figure 1.23: time history of the pressure oscillation for the fluidics limbs at Re 18205 (5kg/h) air for Fluidics- HW- Fx1.	35
Figure 1.24: Fluidics velocity at different air mass flows for Fluidics Fx1.	35
Figure 1.25: Figure: Fluidics St at different Re for Fluidic oscillator Fx1.	36
Figure 1.26: Fluidics RMS (p) at different Re for Fluidic oscillator Fx1.	36
Figure 1.27: Power Spectral Density of the microphone signal for different mass flows- original Fx.	37
Figure 1.28: 2 nd Fluidics model Fx2.	37
Figure 1.29: Power Spectral Density of HW signal for different mass flows- Fx2.	38
Figure 1.30: 3 rd Fluidics model Fx3.	38
Figure 1.31: Power Spectral Density of HW signal for different Re numbers- Fx3.	33
Figure 1.32: 4 th Fluidics model Fx4.	39
Figure 1.33: Fluidics frequency comparison at different Re of air flows for different fluidic oscillators.	40
Figure 1.34: RMS (p) at different Re of flows for different fluidic oscillators.	40
Figure 1.35: St number at different Re numbers- HW mounted directly at exit of different fluidic oscillator models.	41
Figure 1.36: Flow velocity U m/s measured at exit of the fluidic oscillators at different Re numbers of air flows.	42
Figure 1.37: Fluidics signal amplitude comparison at different air mass flows for different fluidic oscillators.	47
Figure 1.38: Fluidics frequency at different water mass flows for Fluidic oscillator Fx1.	47
Figure 1.39: Single-sided amplitude spectrum at different water mass flows for Fluidic oscillator Fx1.	45
Figure 1.40: Fluidics oscillating water flow field at 87 L/h- Fx1.	46
Figure 1.41: Fluidics oscillating water flow field at 184 L/h- Fx1.	47
Figure 1.42: Fluidics oscillating water flow field at 87 L/h- Fx3.	48
Figure 1.43: Fluidics oscillating water flow field at 144 L/h- Fx3.	48
Figure 1.44: Fluidics oscillating water flow field at 202 L/h- Fx3.	49
Figure 1.45: Fluidics oscillating water flow field accompanied with the suction resulted from the oscillation process at 144 L/h for- Fx4.	49

Figure 1.46: Fluidics oscillating velocity vectors field at different phase averaged and at a volume flow of 87 l/h for Fx1.	52
Figure 1.47: Contours of phase averaged vorticity (s^{-1}) at different phase angles at a volume flow of 87 l/h for Fx1.	53
Figure 1.48: Contours of phase averaged streamwise (left) and radial (right) velocity components (m/s) at different phase angles at a volume flow of 87 l/h for Fx1.	55
Figure 1.49: Contours of phase averaged streamwise velocity (m/s) components Fx1 (left) and Fx3 (right) at different phase angles and at a volume flow of 202 l/h.	56
Figure 1.50: Contours of averaged streamwise velocity (m/s) components Fx1 (left) and Fx3 (right) at a volume flow of 202 l/h at average of 500 PIV images.	57
Figure 1.51: Contours of averaged streamwise velocity (m/s) components Fx1 (left) and Fx3 (right) at a volume flow of 202 l/h at average of 500 PIV images directly outside the Fluidics.	57
Figure 1.52: Contours of phase averaged radial velocity (m/s) components Fx1 (left) and Fx3 (right) at different phase angles and at a volume flow of 202 l/h.	58
Figure 1.53: Contours of averaged radial velocity (m/s) components Fx1 (left) and Fx3 (right) at a volume flow of 202 l/h at average of 500 PIV images directly outside the Fluidics.	59
Figure 1.54: Contours of averaged vorticity (s^{-1}) components Fx1 (left) and Fx3 (right) at a volume flow of 202 l/h at average of 500 PIV images.	59
Figure 1.55: Contours of phase averaged vorticity (s^{-1}) Fx1 (left) and Fx3 (right) at different phase angles and at a volume flow of 202 l/h.	60
Figure 1.56: Contours of averaged vorticity (s^{-1}) Fx1 (left) and Fx3 (right) at a volume flow of 202 l/h at average of 500 PIV images directly outside the Fluidics.	61
Figure 1.57: Contours of averaged shear strain (s^{-1}) (left) and turbulence intensity with velocity vectors at exit of Fx1 (right) at a volume flow of 202 l/h (average of 500 PIV images) directly outside the Fluidics.	62

Figure 1.58: Contour plot of averaged turbulence intensity for Fx3 at a volume flow of 202 l/h at average of 500 PIV images.	62
Figure 1.59: Contours of averaged streamwise velocity (m/s) components Fx1 (left) and Fx4 (right) at a volume flow of 202 l/h at average of 500 PIV images directly outside the Fluidics.	63
Figure 1.60: Fluidics oscillating velocity vectors field at different phase averaged and at 202 l/h for Fx4.	63
Figure 1.61: Fluidics oscillating averaged vorticity (s^{-1}) Fx1 (left) and Fx4 (right) at 202 l/h and at average of 500 PIV images.	64
Figure 1.62: Single-sided amplitude spectrum at different fluidics water volume flows at burner exit (XF=0).	67
Figure 1.63: velocity profiles comparison between the base case and 4.5% of the main water flow as a stable case at different axial locations (XF=0).	68
Figure 1.64: Streamwise (left) and radial velocity (right) contour plots at fluidics water mass flows of 0% (up) and 4.5% (down) of the main water mass flow (XF=0).	68
Figure 1.65: Vorticity and shear strain contour plots at fluidics water mass flows of 0% (up) and 4.5% (down) of the main water mass flow (XF=0).	69
Figure 1.66: Effect of ϕ overall at constant m° air and at (XF=0).	70
Figure 1.67: Effect of ϕ overall on exhaust temperature (XF=0).	71
Figure 1.69: Power Spectral Density of microphone signal for different equivalence ratios (XF=0).	72
Figure 1.70: OH- chemiluminescence at different overall equivalence ratios (XF=0).	73
Figure 1.71: Influence of fuel transfer inside the fluidic oscillator on emissions at constant main air mass flow and at ϕ overall= 0.552 (XF=0).	74
Figure 1.72: OH- chemiluminescence at different fuel transfers inside the oscillator by constancy of the main air mass flow and at ϕ overall= 0.552 (XF=0).	75

Figure 1.73: Influence of air transfer inside the fluidic oscillator on emissions at constant main fuel mass flow and at $\phi_{\text{overall}} = 0.552$ (XF=0).	75
Figure 1.74: OH- chemiluminescence at different air transfers inside the oscillator by constancy of the main fuel mass flow and at $\phi_{\text{overall}} = 0.552$ (XF=0).	76
Figure 1.75: Effect of air transfer inside the fluidic oscillator on emissions at 14% pilot ratio of the main fuel and at $\phi_{\text{overall}} = 0.552$ (XF=0).	77
Figure 1.76: OH- chemiluminescence at different air transfers inside the fluidics plus 14% pilot ratio of the main fuel and at $\phi_{\text{overall}} = 0.552$ (XF=0)	77
Figure 1.77: Effect of air transfer inside the fluidic oscillator on emissions at 28% and 42% pilot ratios of the main fuel and at $\phi_{\text{overall}} = 0.552$ (XF=0).	78
Figure 1.78: OH- chemiluminescence at different air transfers inside the fluidics plus 28% pilot ratio of the main fuel and at $\phi_{\text{overall}} = 0.552$ (XF=0).	79
Figure 1.79: OH- chemiluminescence at different air transfers inside the fluidics plus 42% pilot ratio of the main fuel and at $\phi_{\text{overall}} = 0.552$ (XF=0).	79
Figure 1.80: Influence of air transfer inside the fluidic oscillator on emissions at constant main fuel mass flow and at $\phi_{\text{overall}} = 0.575$ (XF=0).	80
Figure 1.81: OH- chemiluminescence at different air transfers inside the oscillator by constancy of the main fuel mass flow and at $\phi_{\text{overall}} = 0.575$ (XF=0).	80
Figure 1.82: Single-sided amplitude spectrum at different fluidics water volume flows (XF=0.5).	81
Figure 1.83: Streamwise velocity (left) and radial velocity (right) profiles comparison between the base case and 4.5% of the main water flow as a stable case at different axial locations (XF=0.5).	82
Figure 1.84: Streamwise (left) and radial velocity (right) contour plots at fluidics water mass flows of 0% (up) and 4.5% (down) of the main water mass flow (XF=0.5).	83

Figure 1.85: Vorticity and shear strain contour plots at fluidics water mass flows of 0% (up) and 4.5% (down) of the main water mass flow (XF=0.5).	84
Figure 1.86: Vorticity (left) and shear strain rate (right) profiles comparison between the base case and 4.5% of the main water flow as a stable case at different axial locations (XF=0.5).	84
Figure 1.87: Effect of overall equivalence ratio at constant main air mass flow rate and at (XF=0.5).	86
Figure 1.88: OH- chemiluminescence at different overall equivalence ratios (XF=0.5).	87
Figure 1.89: Influence of air transfer inside the fluidic oscillator on emissions at constant main fuel mass flow and at $\phi_{\text{overall}} = 0.552$ (XF=0.5).	85
Figure 1.90: OH- chemiluminescence at different air transfers inside the oscillator by constancy of the main fuel mass flow and at $\phi_{\text{overall}} = 0.552$ (XF=0.5).	88
Figure 1.91: Influence of air transfer inside the fluidic oscillator on emissions at constant main fuel mass flow and at $\phi_{\text{overall}} = 0.575$ (XF=0.5).	88
Figure 1.92: OH- chemiluminescence at different air transfers inside the oscillator by constancy of the main fuel mass flow and at $\phi_{\text{overall}} = 0.575$ (XF=0.5).	89
Figure 1.93: Single-sided amplitude spectrum at different fluidics water volume flows (Xf=1).	90
Figure 1.94: Streamwise velocity (left) and radial velocity (right) profiles comparison between the base case and 4.5% of the main water flow as a stable case at different axial locations (XF=1).	92
Figure 1.95: Streamwise (left) and radial velocity (right) contour plots at fluidics water mass flows of 0% (up) and 4.5% (down) of the main water mass flow (XF=1).	92
Figure 1.96: Instantaneous velocity vectors six phase averages reconstructed on POD modes at 4.5% fluidics water transfer of the main mass flows (Xf=1).	94

Figure 1.97: Instantaneous vorticity contour plots six phase averages reconstructed on POD modes at 4.5% fluidics water transfer of the main mass flows (XF=1).	95
Figure 1.98: Vorticity (left) and shear strain rate (right) profiles comparison between the base case and 4.5% of the main water flow as a stable case at different axial locations (XF=1).	96
Figure 1.99: Vorticity and shear strain contour plots at fluidics water mass flows of 0% (up) and 4.5% (down) of the main water mass flow (XF=1).	97
Figure 1.100: velocity, vorticity, and shear strain rate contour plots horizontal slice mean of 500 images of PIV at $y=0.25D$ for 0% fluidics water transfer of the main mass flows (Panel (A)) and 4.5% fluidics water transfer of the main mass flows (Panel (B)) (XF=1).	98
Figure 1.101: Instantaneous velocity vectors at 50° phase average reconstructed on POD at 0%(left) and 4.5% (right) fluidics water transfer of the main mass flow (XF=1).	99
Figure 1.102: Effect of ϕ overall at constant m° air and at (XF=1).	101
Figure 1.103: Influence of fuel transfer inside the fluidic oscillator on emissions at constant main air mass flow and at ϕ overall= 0.552 (XF=1).	102
Figure 1.104: OH- chemiluminescence at different fuel transfers inside the oscillator by constancy of the main air mass flow and at ϕ overall= 0.552 (XF=1).	102
Figure 1.105: Influence of air transfer inside the fluidic oscillator on emissions at constant main fuel mass flow and at ϕ overall= 0.552 (XF=1).	103
Figure 1.106: Influence of air transfer inside the fluidic oscillator on emissions at constant main fuel mass flow and at ϕ overall= 0.575 (XF=1).	104
<u>Part (2) Pilot injector influence on Flow Field Interaction and Combustion characteristics in a Swirl stabilized Burner</u>	117
Figure 2.1: Sketch of the Swirl Stabilized Burner (left) and the pilot injectors (right).	124
Figure 2.2: Sketch of the Swirl Stabilized Burner flow (left) and flame zones (right).	124
Figure 2.3: Schematic of the test facility accompanied with Photo of the powder disperser.	125

Figure 2.4: P_{RMS} at different pilot locations for the short combustion chamber.	130
Figure 2.5: Pressure spectra (top) and OH^* spectra (bottom) for different X_p/X_{max} at 7% transfer of pilot fuel mass flow for the short combustion chamber.	131
Figure 2.6: NO_x (ppm) ref. to 15% O_2 at different pilot locations for the short combustion chamber.	132
Figure 2.7: CO (ppm) normalized to 15% O_2 at different pilot locations.	132
Figure 2.8: OH^- chemiluminescence at different pilot fuel mass flows and at the burner apex.	133
Figure 2.9: RMS P at different pilot locations and at 0.45% air transfer.	134
Figure 2.10: NO_x ref. to 15% O_2 at different pilot locations and at 0.45% transfer of the main air.	134
Figure 2.11: RMS P at different pilot air mass flows.	134
Figure 2.12: Pressure (top) and OH^* spectra (bottom) for the multi injection pilot, position $X_p/X_{max}=0.5$ showing the stabilizing effect of increasing air injection (green, 2.7% of the main air and red, 7.3% of the main air) at constant fuel mass flow compared to the case without pilot injection (blue).	135
Figure 2.13: RMS P at burner bottom for long and short combustion chambers and at different fuel transfer.	136
Figure 2.14: RMS P at different axial locations.	137
Figure 2.15: NO_x (ppm) ref. to 15% O_2 at different axial locations.	137
Figure 2.16: CO (ppm) ref. to 15% O_2 at different axial locations.	137
Figure 2.17: Influence of pilot air injection on OH^- chemiluminescence at short combustion chamber (8.17 D). Multi injection pilot located at burner quarter ($X_p/X_{max}=0.25$) axial location, left: no air injection, right: air injection is 6.8% of total air mass flow.	138
Figure 2.18: RMS (P) at different pilot locations, long combustion chamber 15.85 D, and $\Phi=0.552$.	139
Figure 2.19: NO_x ref. to 15% O_2 at different pilot locations, long combustion chamber 15.85 D, and $\Phi=0.552$.	139
Figure 2.20: Pressure oscillations for $X_p/X_{max}=0$ at different pilot air mass flows for the long chamber.	140

Figure 2.21: Pressure oscillations for $X_p/X_{max}=0.25$ at different pilot air mass flows for the long chamber.	140
Figure 2.22: Pressure oscillations for $X_p/X_{max}=0.5$ at different pilot air mass flows for the long combustion chamber.	141
Figure 2.23: Pressure oscillations for $X_p/X_{max}=0.68$ at different pilot air mass flows for the long combustion chamber.	141
Figure 2.24: Influence of pilot air injection on OH-chemiluminescence at multi injection pilot, $\Phi= 0.552$ and 15.85 D. The left four figures at $X_p/X_{max}=0$ and the last right one at $X_p/X_{max}=0.68$ pilot position.	142
Figure 2.25: RMS P at different pilot shapes and at $\Phi_{overall} 0.552$.	143
Figure 2.26: RMS P at different pilot shapes and at $\Phi_{overall}= 0.583$.	143
Figure 2.27: Radial profiles of the streamwise velocity at different pilot air injections while the injector is at burner middle position.	144
Figure 2.28: Streamwise velocity contours, velocity vectors, and streamtraces at pilot air mass flows 0% (right) and 8.64% pilot air (left).	145
Figure 2.29: Radial profiles of the streamwise velocity (up) and radial velocity (down) at different pilot air injections and at different axial locations.	146
Figure 2.30: Streamwise velocity contours, velocity vectors, and streamtraces at pilot air mass flows 0% (left) and 4.5% of the main air (right) at $X_p/X_{max}=0.68$.	148
Figure 2.31: Flow map of streamwise velocity contours, velocity vectors, and streamtraces at pilot air mass flows 0% (left) and 4.5% of the main air (right) at $X_p/X_{max}=0.68$.	149
Figure 2.32: Isolines of $u=0$ for different pilot air mass flows 0% and 4.5% transfer of the main air at $X_p/X_{max}=0.68$.	149
Figure 2.33: vorticity axial profiles and vorticity contour plots at pilot air mass flows 0% (left) and 4.5% (right) transferred from the main air flow.	150
Figure 2.34: Normal strain rate contour plots at pilot air mass flows 0% (left) and 4.5% (right) of the main air flow.	151
Figure 2.35: Radial profiles of the streamwise velocity and radial velocity at 8.64 % of the main air and at $X_p/X_{max}=0$ for reacting flow (blue) and isothermal conditions (red).	152

Figure 2.36: Isolines at $u=0$ for 8.64 % transfer of the main air and at $X_p/X_{max}=0$ for reacting flow and isothermal conditions.	153
Figure 2.37: Radial profiles of the streamwise velocity at 7.3 % of the main air and at $X_p/X_{max}=0.5$ for isothermal and reacting flow.	153
Figure 2.38: Radial profiles of the streamwise velocity at different pilot air mass flows (0 %, and 8.64 %) and at $X_p/X_{max}=0.5$ for reacting flow at $\Phi_{overall}= 0.552$.	154
Figure 2.39: Isolines of $u=0$ at different pilot air mass flows (0 %, and 8.64 %) and at $X_p/X_{max}=0.5$ for reacting flow at $\Phi_{overall}= 0.552$.	154
Figure 2.40: Radial profiles of the streamwise velocity at different pilot air mass flows (0 %, and 7.3 %) and at $X_p/X_{max}=0.68$ for reacting flow at $\Phi_{overall}= 0.552$.	155
Figure 2.41: Isolines of $u=0$ at different pilot air mass flows (0 %, and 7.3 %) and at $X_p/X_{max}=0.68$.	156
Figure 2.42: Streamwise velocity contour plots at pilot air injections of 0% (left) and 7.3% (right) of the main air and at $x/D= 0.68$ for reacting flow at $\Phi_{overall}= 0.552$.	156
<u>Part (3) Planar Investigation of outlet boundary conditions effect on isothermal flow fields of a swirl- stabilized burner.</u>	164
Figure 3.2: Sketch of the Swirl Stabilized Burner	169
Figure 3.2: Schematic of the test facility	170
Figure 3.3: Flow streamlines (left half) and vector flow field (right half) plot at $Re=52136$, $Cr=1$ and short combustion chamber.	174
Figure 3.4: Isolines of $u=0$ for different air mass flows (Reynolds numbers 37917, 52136, and 61616).	175
Figure 3.5: Radial profiles of the streamwise velocity u , radial velocity v , and turbulence intensity Tu at different air mass flows and at different axial locations.	176
Figure 3.6: Power Spectral Density of the microphone signal for different Reynolds numbers at short combustion chamber length (8.17 D) and $Cr=1$.	177
Figure 3.7: Strouhal number of the dominant frequency peaks depending on the Reynolds number.	178

Figure 3.8: Radial profiles of the streamwise velocity u and radial velocity at different exit contraction ratios ($Cr= 0.09, 0.27, 0.56,$ and 1.0), and at $8.17 D$ height from burner exit for air mass flow of $Re= 52136$	179
Figure 3.9: Radial profiles of the streamwise velocity u at different exit contraction ratios ($Cr=0.09$ and 1.0), and at $8.17 D$ height from burner exit for air mass flow of $Re= 52136$.	180
Figure 3.10: Vector flow field contour plots- Comparison between minimum (right $Cr= 0.09$) and maximum (left $Cr= 1$) exit contraction ratios at $Re= 52136$ of air mass flow and at height $8.17 D$ from burner mouth.	180
Figure 3.11: Isolines of $u=0$ for different exit contraction ratios ($Cr= 0.09, 0.27, 0.56,$ and 1) and at $8.17 D$ height from burner exit for $Re= 52136$.	181
Figure 3.12: Radial profiles of the streamwise velocity u at exit contraction ratio $Cr= 0.09$, and at different heights from burner exit ($8.17 D$ and $24.63 D$) for air mass flow rate at $Re= 52136$.	182
Figure 3.13: Influence of the outlet diameter on the dominant frequency recorded by the microphone mounted upstream of the burner (Combustor length $o=24.63 D$).	183
Figure 3.14: First six POD modes of the radial velocity v for $Cr= 1$ and $Cr= 0.09$ outlet conditions. The analysis was done with 600 snapshots for each case.	184
Figure 3.15: Total Turbulent Kinetic Energy of the POD eigenvalues for $Cr= 1$ and $Cr= 0.09$.	185

List of Tables

Title	Page
<u>Part (3) Planar Investigation of outlet boundary conditions effect on isothermal flow fields of a swirl- stabilized burner.</u>	
Table 3.1: Measurement cases	171

Nomenclature

Part (1)

CCD Charge Coupled Device is the silicon chip inside the digital camera that records the image.

CO Carbon monoxide

DAQ Data acquisition system.

D The swirl stabilized burner diameter

Fx Fluidic oscillator

G Gain

HW Hotwire anemometry

LIF Light induced florescence

m^oair Mass flow rate

Micro Microphone

NOx Nitrogen oxides

OH Hydrogen oxides

PIV Particle image velocimetry

POD Proper orthogonal decomposition (POD)

Rair Gas constant (287.058 J/kg.K)

Re Re calculated from the given mass flows

RMS Root mean square

RTD Resistance temperature detector

St Strouhal number

U Flow velocity (m/s)

Vin Input voltage

Vout Output voltage

XF	Fluidics position inside the burner (0-1).
α	Phase angle
η	The vorticity
ϕ	Equivalence ratio
γ	Heat capacity ratio (1.4)
γ_{xy}	The shear strain

Part (2)

CRZ	Corner or external recirculation zone (ERZ)
D	Diameter [mm]
f	focal length
IRZ	Internal recirculation zone
m_{pr}°	Premixed mass flow rate (kg/h)
m_{pilot}°	Premixed mass flow rate (kg/h)
U	Mean bulk velocity
u/U	Normalized streamwise velocity to U
v/U	Normalized radial velocity to U
x/D	Axial location downstream of the burner
X_{max}	Burner length
X_p	Pilot injector position
Φ_{over}	Overall (Total) equivalence ratio
Φ_{inj}	Injection equivalence ratio
$\frac{\partial p}{\partial r}$	Pressure gradient
τ	Pulse timing

Part (3)

A_{cc}	Combustion chamber area
A_{co}	Contraction area
Cr	Contraction ratio (A_{co} / A_{cc})

D	Burner diameter
f	Focal length
f	Excitation frequency
Re	Reynolds number = $u_0 D / \nu$
S	Swirl Number
St	Strouhal number = fD/u_0
Tu	Turbulence intensity = $((u'^2 + v'^2)/2u_0)^{0.5}$
u	Streamwise mean velocity
u_0	Mean Bulk velocity at the burner outlet
v	Radial mean velocity
u', v'	Velocity oscillation
x	Streamwise axis
τ	Pulse delay

Introduction

Introduction

The demand for gas turbine engines with reduced emission levels, stable combustion conditions and low specific fuel consumption is the goal at the past two decades to perform an efficient combustion (Rankin 2007 and Seyfried 2007). Gas turbine manufacturers have developed and continue to enhance lean premixed combustion systems to comply with emissions regulations for nitrogen oxides, carbon monoxide, and unburned hydrocarbons. For power generation, premixed gas turbine combustors need to be operated as lean as possible to secure sub-10 ppm concentrations of NO_x emission. In a combustor under fuel-lean conditions, achieving stable combustion requires overcoming several inter-related problems such as flame stabilization, flame stability and extinction, and combustion oscillations or thermoacoustic instabilities which depend on the boundary conditions of the engine. The present work inspects new designs for auxiliary parts used to achieve these goals of emissions reduction at stable combustion conditions. It is divided to three main parts. The first part focuses on the usage of the fluidic oscillator in performing the emission reduction at stable operating combustion conditions. The second part investigates the using of a new pilot injector configuration to achieve the same target. The last one investigates the changes in the flow field downstream of the burner at different combustor outlets as it used for combustor stability.

Part (1) Fluidic oscillator for jet streams integrated into a pilot fuel lance.

The fluidic oscillator is used as a new technology in different industrial applications. The usage in combustion field especially in the jet engines is new and may be the first in allover the world to be inserted in a swirl stabilized burner for emissions reduction and for stability performing. It considers a viable mean for systems implementation in industrial fields. One or more may be used together but they are synchronized with each other to perform the job better and faster than one oscillator at some applications. The fluidic oscillator possesses all the following characteristics: (1) Rapid response to changes in fluid flow rate, (2) Freedom from flow instabilities, (3) no power requirements, (4) Capability for scaling, to provide design flexibility, (5) Low cost, light weight, and ease of removal for servicing, (6) Low susceptibility to damage during installation.

Integrating the oscillator into the swirl stabilized burner similar as a pilot injector is one of the new ideas which have been clarified and investigated at the present study. The behavior of the fluid flow is investigated inside and outside the fluidic oscillator and the performance of the

oscillator in active control schemes which include high frequencies flow modulation is also studied. The influence of this oscillation on the combustion control, the flow field, and the flow field interaction without the need of complex and fast moving parts is tested. The design idea of oscillation is taken normally from the electronic oscillation circuits. The design complexities are mainly coming from the size restrictions inside the burner and the higher frequencies.

Several measuring techniques are used in the flow field measurements and the flow interaction clarification and for the combustion control. Constant-temperature hotwire anemometer is used to investigate the flow velocity and the pressure oscillations at the exit of the fluidic oscillator. A condenser microphone is used to measure the pressure oscillations of the flow downstream of the fluidics. PIV laser system was used to measure the flow field inside and outside the fluidic oscillator alone and when it is inserted inside the swirl stabilized burner. The oscillating flow field has been visualized at different volume flow rates by using LIF technique. A standard hydrophone provides uniform unidirectional sensitivities in both horizontal and vertical planes up to high frequencies and considers an excellent transducer for making absolute sound measurements and calibrations. K-type thermocouples with 1.5 mm diameter were used to measure the temperature of the preheated air upstream and the exhaust temperatures at 0.6 m downstream of the burner exit. The recordings of the OH- Chemiluminescence of the flame were obtained with an ICCD camera equipped with a bandpass filter centered at 312 ± 2 nm. The wavelength range matches OH radical emission spectrum which has a maximum at 306.7 nm.

Two design variations are carried out in order to reach the optimum design model. The first one (Fx0) overcomes the size restrictions but is not suitable for working in combustion space because of instability problems according to the higher produced frequencies. At the second design variation, four models are modulated from Fx0 and tested to find out the optimum one or more for inserting inside the swirl stabilized burner in reacting flows.

The study of the flow field in the fluidics models, using LIF and PIV, is performed at a small water aquarium and a big water tunnel. Subsequent applied Fourier transformation produced from the hydrophone signal exhibits a linear relation between the frequency and the volume flow rate. Defining the internal jet traces through the flow visualization is implemented.

The results offer a big similarity between Fx1 and Fx2 oscillators in the flow field. The modulations in the control parameters give changes in the flow field between Fx1 and both Fx3 and Fx4. This mixing characteristic highlights the usage of the fluidic oscillator Fx1 for fluid

mixing applications as well as the usage in the targeting work for emissions reduction at stable reacting flow conditions. From the previous investigations to these four models, Fx1 is selected in combustion tests as what will be explained later.

Fx1 is inserted inside the swirl stabilized burner to study the flow field interaction between the oscillator and the burner. The flowfield, at three axial locations inside the swirl stabilized burner (the burner bottom, the middle position and at the burner dump plane), is investigated by PIV.

At thermal reacting flow, a test, for integrated fluidics Fx1 inside the burner, is done trying to find the optimum mounting position inside the burner in order to perform the combustion operation with low NO_x and CO emissions at stable combustion conditions. During the combustion test, some transfers are done to the main fuel and air inside the fluidic oscillator trying to enhance the combustion performance at the same overall equivalence ratio (ϕ) overall during the study between transfer and no transfer.

The effect of the equivalence ratio is studied at first for the whole movement locations inside the burner from the bottom to the top. OH camera captured around 300 images for each measurement point in order to find the average of these pictures to show the chemiluminescence emitted from the flame besides the gas analyzer which is used for emissions measurements and k-type thermocouples for temperature measurements. After testing a wide range of overall equivalence ratio, the range of operation is selected to be far from the lean blow off and also in the safe range of stability. Fuel's Transfer inside the fluidics at a constant main air and at a constant ϕ overall of 0.552 is done to clarify the effect on the emissions and the temperature. The transfer of air inside the fluidic oscillator from the main line at a constant main fuel and at a constant overall equivalence ratio (0.552 and 0.575), is also performed to clarify the air transfer only on the performance of the designed oscillator. Mixing of air and fuel transfer inside the fluidics is also done also to investigate this effect on the oscillator performance at a constant ϕ overall of 0.552. The air pilot ratio is between 0% and 2.73% of the main air while 14% of the main fuel is injected together with transferred air. The percentage of fuel increased from 14% gradually to double and triple times this value at the increase of the air inside the fluidics. The results show that, the air transfer considers the best and the optimum way to reduce the emissions at the whole injector mounting locations. This gives merit to the fluidics under test to work better with some new or other burner configurations and at different positions inside the burner.

Part (2) Pilot injector influence on flow field interaction and combustion characteristics in a swirl stabilized burner

It is common to rely on a pilot injector to operate lean premixed gas turbines. The pilot fuel allows the reaction to continue even if the reaction, produced by the main fuel/air mixture, starts to suffer some degree of instability. The pilot injector is generally directed into a strategic location in the combustor to enrich a region that will help sustain the reaction.

This part of work investigates the changes induced by pilot injections in the main flow field at reacting and non-reacting conditions in a swirl stabilized burner. The behavior, of these injections, regarding the flow field interaction, stability, and emissions in that burner, is studied also at several acoustic boundary conditions represented in the combustion chamber length (short and long). These changes are affecting the flame stability especially in the lean premixed combustion due to large structures resulting from vortex breakdown and the swirling shear-layers.

The pilot injector is mounted on the centerline inside the burner, upstream of the internal recirculation zone. The pilot transfer from the main passages (fuel only, air and fuel premixed, and air only) as well as the shape and the axial location of the injector inside the burner is exhaustively investigated at different overall equivalence ratios.

It is expected that forcing the flame to stabilize outside the burner should be regarding NO_x emission positive because it ensures a long enough mixing path of gas and air, and would also prevent the oscillating movement of the flame which could lead to strong instabilities. Two different pilot injectors are tested for forcing the flow: a single injection pilot and a multi injection pilot. The single injection pilot contains a single hole with diameter of 5mm. The multi pilot injector has 5 holes of 1 mm orifice diameter and 4 holes of 45° around it. Three pilot locations inside the burner are tested (0, 0.5, and 0.68 of the burner height). The multi hole injector, as a new pilot injector, is designed where a high amount of air is injected through a certain number of holes to increase the premix dispersion and enhance the mixing with the main flow. The strong jet momentum has a strong impact on the flow field and should make it possible to force the flame to stabilize outside of the burner, preventing instabilities and ensuring low NO_x emissions. A detailed PIV measurements are performed downstream of the burner to reveal the pilot impact on the mean flow field and the flow field interaction between the injector and the burner. A microphone is mounted 411 mm upstream of the burner and allows for identification of the acoustic pressure oscillations corresponding to the flow downstream of the combustion chamber.

OH camera shows the chemiluminescence emitted from the flame besides the gas analyzer which is used for emissions measurements and k-type thermocouples is used for temperature measurements.

Part (3) Planar investigation of outlet boundary conditions effect on isothermal flow fields of a swirl- stabilized burner.

The swirling flow can be strongly influenced by the boundary conditions of the combustion chamber (combustor length and diameter of outlet) especially at subcritical flow conditions. The effect of such changes on the mean flow or coherent structures is still unclear using this type of burners. The flow field is investigated at this part using PIV measuring technique. A microphone is mounted 411 mm upstream of the burner and identifies the acoustic pressure oscillations corresponding to the flow downstream of the combustion chamber. Proper orthogonal decomposition (POD) as well as acoustic measurements was used to characterize the coherent structures shed from the burner mouth. The combustor length (8.17 D, and 24.63 D) and the outlet area contraction ratio (1, 0.56, 0.27, and 0.09) are varied during the investigation.

Part (1)

Fluidic Oscillator for Pilot Fuel Injection.

Chapter (1)

Introduction

Chapter (1):

Introduction

Fluidic technology has matured rapidly in the last three decades. The increase in their reliability over the mechanical-pneumatic devices has made them the rivals of electrically operated components. This technology has proved to be a viable mean for systems implementation in industrial, commercial, and military systems (Kirshner, 1976). The word "Fluidics" is derived from two words "fluid" and "logic" and is used specifically to describe the technology of the control of fluid force components (Giles, 1977). The fluidic oscillator is a device that generates an oscillating jet when supplied with a pressurized fluid (Gregory, et al 2002). Based on the operation principles, the fluidic oscillators are categorized as the feedback oscillator, the Karman vortex oscillator, and relaxation oscillator (Yang, et al. 2005). The Coanda effect has a major contribution to fluidic technology first described in the 1930's (Giles, 1977). It describes the tendency for a jet of fluid (the fluid can be a liquid or a gas) issuing from a nozzle to adhere to the surface of the wall adjacent to it (Griffin et al 1996). Although the flow oscillation in a fluidic oscillator is usually initiated by the Coanda effect, the features of oscillation could be significantly altered by the design of feedback channels and the flow control loop (Yang, et al. 2005).

The term fluidic device should rigorously be applied only to devices in which there are no moving parts except the fluid movement itself which works as a source of pulsations (Griffin et al 1996). The oscillation comes without any external excitation and as such is described as "self-exciting". Fluidics is preferred to use in comparison to the valve arrangements. However, some tools that produce a pulsed jet through mechanical interruption or mechanical excitation of the normal or steady fluid flow would cause large energy losses, as well as mechanical wear and fatigue on the indispensable moving parts and seals (Griffin et al 1996). Thereby, it is no need for maintenance requirements in the fluidics system which makes it highly appropriate for application in industrial gas turbines and has a long lifetime (Follows et al 2005).

The modulation of dynamic behavior of the fluidic oscillator is performed by interactions among flow fluctuations in the inlet area, the growth of the recirculation flow, and the flow structure near step-walls and splitters (Yang 2006). Yang also used this type of oscillators (conventional feedback fluidic oscillator) to measure the flow rate of the fluid as a flowmeter (Yang, et al.

2005). Gregory adapted a fluidic oscillator as a dynamic calibration device for pressure instrumentation such as pressure-sensitive paint (PSP) (Gregory et al 2002).

Integrating the oscillators into the burner as a pilot lance is one of the new ideas which need to be investigated. The present work demonstrates the behavior of the fluid flow inside and outside the fluidic oscillator and the performance of the oscillator in active control schemes which include high frequencies flow modulation. The influence of these oscillators on flame stability and combustion control without the need of complex and fast moving parts is the main goal. Based on the operation principles, this tested fluidic oscillator is categorized as feedback oscillator. The fluidic oscillator outer diameter is 16.8 mm (20.5% D) and has two rectangular outlets.

The design variation of certain oscillator dimensions from 102×38×22mm to 16.8Ø× 60mm was the challenge. For each exit limb, the dimensions are changed from 7×3 mm to 3.7×6 mm to keep the frequency fluctuations in the range of combustion stability depending on the operating range of fuel and air flows. The feed back effect and the inner dimensions are important in the oscillator modulation. Yang revealed that enhancing the feedback effect and lessening the inhibition of vortex evolution and residence time improve the oscillation characteristics (Yang 2006).

A microphone is placed almost 3mm upstream of the fluidics and recorded the frequencies which were tuned by varying the inlet air mass flow to the oscillator and the pressure fluctuations are induced by the coherent structure. The power spectra, recorded of the microphone signal for different Re-numbers, show a fundamental peak which scales with the Reynolds number in almost linear relation at a certain range of Re number. Hot wire (IFA- 100) is used to investigate the oscillation characteristics for fluidic oscillator. Two hot wires of 5µm diameter and 2mm length at 6.41Ω/ 23°C are used. Hot wire and microphone signals offer a consistency of power spectra.

Asymmetry of the velocity oscillation of the actuator at the two exit limbs is shown and the fluctuation is similar to an on-off valve. Frequency fluctuations are directly proportional to the mass flows up to certain number of Re. Spectra of the velocity oscillations for the two fluidics limbs at exit exhibit typical fluctuations generated by the flows.

In a certain range of Reynolds number, the Strouhal number remained almost constant, and therefore the oscillation frequency was linearly proportional to the flow rate and independent of the fluid properties. Decay of velocity oscillations axially far from the outlet is noticed from time traces and spectra of the velocity oscillations.

The flow oscillation in a fluidic oscillator is usually initiated by the Coanda effect and the features of oscillation could be significantly altered by the design of feedback channels and the flow control loop which is the key to make it suitable for the thermal flows in the next steps.

Proper orthogonal decomposition (POD) as well as acoustic measurements was used to characterize the coherent structures shed from the oscillator and from the oscillator when it is inserted in the burner.

The targeting fluidic oscillator is used in the emissions reduction for the combustion engines, mixing of gases, dispersal of liquids, and the application of cyclically repetitive momentum or pressure forces to various materials, structures of materials, and to living body tissue surfaces for therapeutic massaging and cleansing purposes. Our tests are totally interested in the using only in the emission reduction in jet engines at a stable combustion's conditions.

Chapter (2)

Experimental Test Facilities and Techniques

Chapter (2):

Experimental Test Facilities and techniques

All measurements presented in this work were carried out using the test facilities of the institute of fluid dynamics and engineering acoustics- TU Berlin.

Test Facilities

Fluidic Oscillator

As shown in Fig. 1.1, a fluidic oscillator includes an oscillator body having two attachment walls defining an oscillating chamber therebetween, an inlet duct extended to the oscillating chamber for guiding a flow of fluid entering into the oscillating chamber, two outlet ducts communicatively extended from the oscillating chamber for guiding the flow of fluid exiting from the oscillating chamber, and two feedback channels communicating with the oscillating chamber. Each attachment wall has an upstream portion and a downstream portion integrally extended therefrom as a step shouldering manner to form a modulating shoulder for modulating an oscillation of the flow within the oscillation chamber so as to stabilize the flow of the fluid to pass through the oscillator body. A flow splitter divides the exit duct after the control throat into two equal parts.

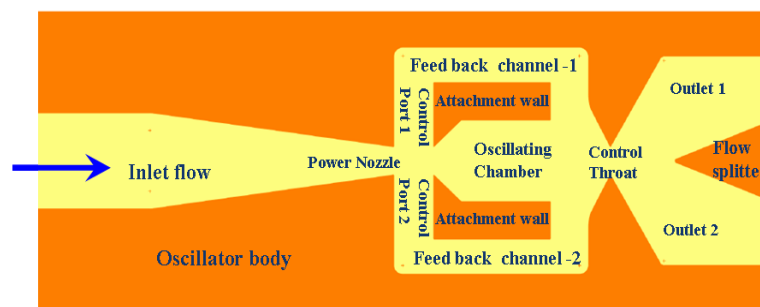


Figure 1.1: A schematic diagram of the fluidic oscillator.

To understand the idea of oscillation, normally, electronic circuits are taken in consideration. In an electronic oscillator, a tuning element is selecting a specified frequency. Subsequently, an amplifier and a feedback mechanism are taking some of the amplified signal and feeding it back to the beginning with some phase according to the schematic Fig. 1.2. Oscillation will occur if the phase is correct. Feedback can influence the input signal in one of two ways; positive or negative. In a positive in-phase feedback signal, a positive-going wave on the input leads to a positive-

going change on the output. This will amplify the input signal leading to more modification. In a negative feedback, a feedback signal which is inverted, where a positive-going change on the input leads to a negative-going change on the output, will dampen the effect of the input signal, leading to less modification.

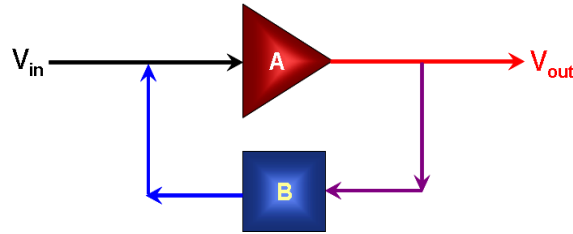


Figure 1.2: The electronic oscillator.

A represents the amplification factor of the amplifier and $\pm B$ the gain and phase of the feedback circuit. A little algebra shows the origin of the gain **G** of the amplifier/oscillator. The amplifier multiplies the total input voltage V_{in} , composed of input plus feedback, by **A** yielding the output voltage V_{out} as shown below.

$$A(V_{in} \pm BV_{out}) = V_{out} \quad (1)$$

$$G = \frac{V_{out}}{V_{in}} = \frac{A}{1 \mp AB} \quad (2)$$

Similarly, when a flow of fluid passes through the inlet port to fill up the oscillating chamber, the fluid is guided to flow towards the outlet and back to the oscillating chamber through the feedback channels, such that the fluid is started to oscillate within the oscillating chamber and then guided to split at the splitter to two outlets. It is systematically evaluated the function of flow splitter while systematically varied its location and length and this has an effect on Strouhal number. When the fluid flows into a symmetric divergent or sudden-expansion channel, it often diverts toward either side in a specific range of Reynolds number due to the Coanda effect. Then the flow develops to be either an asymmetric flow structure or a periodically oscillating flow pattern. As the oscillation frequency is linearly proportional to the volume flow rate at certain range of flow, the oscillator could be adopted as a flowmeter at this range. Moreover, these specific correlations are also widely used for atomizers, mixers, and memory and control devices (Yang, et al. 2005).

The Burner

The burner used in this investigation was a full size conical swirl burner designed by ABB with a cross-sectional area expansion ratio of 4 for flame stabilization (Fig. 1.3). It consists of two half cones shifted with respect to each other in radial direction (Guyot et al. 2007). The diameter of each cone-half at the outlet is $D = 82$ mm. This diameter is used as a reference length for all characteristic numbers. The airflow enters the cone circumferentially through two lateral inlet slots of constant width. This generates a strong azimuthal velocity component resulting in a high degree of swirl (Swirl no. = 0.7). Together with the area jump at the burner outlet, this leads to a vortex breakdown near the burner mouth followed by a recirculation zone where the flame is stabilized aerodynamically (Duwig 2007). During the combustion conditions, the mixing of swirled air and main fuel results in nearly premixed combustion (Albrecht 2006).

A natural helical flow structure corresponding to a helical instability could be observed at the burner outlet in the cold and reacting conditions (Lacarelle 2008). During combustion, the recirculation of hot combustion gases, inside the flame, leads to a second oxidation and to a reduction of carbon monoxide. The disadvantages of this type of flame stabilization are flow instabilities accompanied by complex three-dimensional coherent structures (Lacarelle 2008).

The burner is mounted just upstream of the combustion chamber ($2.44 D$). The first part of the chamber is a silica tube of $3.66 D$ height followed by a steel tube, giving a length of $8.17 D$ from the burner outlet to the combustion chamber outlet. A second longitudinal tube can be placed on the top of it to increase the length to $24.6 D$. A microphone is mounted 411 mm upstream of the burner and is used to record the pressure oscillations of the flow downstream of the combustion chamber. At this position, it is still possible to record pressure oscillations induced by the flow field in the combustion chamber.

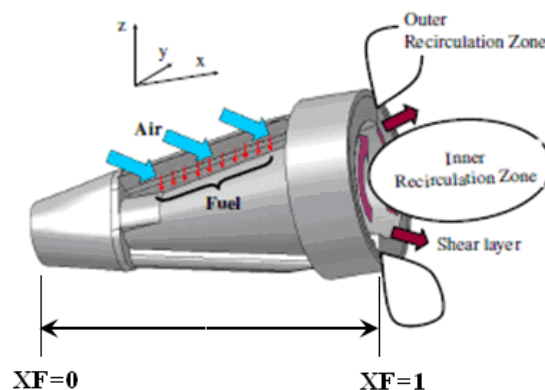


Figure 1.3: Sketch of the Swirl Stabilized Burner.

Measurements Techniques

Hot wire Setup

Constant-temperature hotwire anemometer type TSI IFA-100 is used to investigate the flow velocity and the pressure oscillations at the exit of the fluidic oscillator. The used transducer is a small resistance element that is heated and controlled at an elevated temperature. The electrical energy dissipated in the sensor is a measure of the cooling effect of the fluid flowing around the heated sensor. This cooling effect is balanced by the electrical current to the wire and the change in current, due to a change in flow velocity, shows up as a voltage at the anemometer output. When selecting a thermal anemometry probe, the choosing is based on the fluid characteristics, the velocity range, the number of velocity components, contamination in the flow, and access to the flow (TSI 1995). The sensor is a fine platinum cylindrical wire measuring $5\mu\text{m}$ in diameter. The hot wire is mounted on a probe of 3mm width and connected to the anemometer at the end of standard coaxial cable. Two hot wires are used to investigate the pressure oscillation and *velocity* at different mass flows for the two exit limbs of the fluidics with cable lengths of 5m and 20m. The operating resistance is set at $6.23\text{ohm}/22^\circ\text{C}$ and $6.27\text{ohm}/22^\circ\text{C}$ for these two wires consecutively to operate the sensor at a resistance that is high enough to achieve the required operating temperature.

As the change in flow velocity is shown up as a voltage at the anemometer output, calibration is very important for the hot wire to determine the flow velocity. As shown in Fig. 1.4, a DLR calibration chamber is used for calibration.

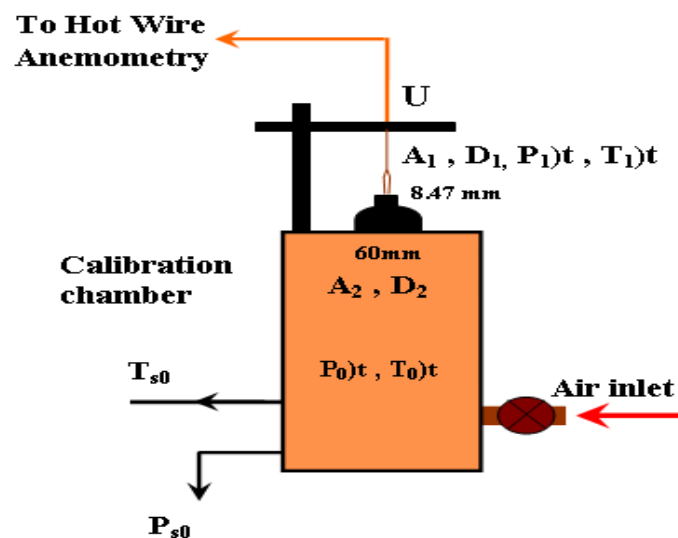


Figure 1.4: The Hot wire calibration chamber.

According to the next equation, the flow velocity U (m/s) is calculated.

$$U = \sqrt{\frac{\frac{2\gamma}{\gamma-1} \cdot R_{air} \cdot T_{s0} \cdot \left[1 - \left(\frac{P_{s1}}{P_{s0}} \right)^{\frac{\gamma-1}{\gamma}} \right]}{\left(1 - \left[\left(\frac{A_1}{A_2} \right)^2 \cdot \left(\frac{P_{s1}}{P_{s0}} \right)^{\frac{2}{\gamma}} \right] \right)}} \quad (3)$$

Where γ is the heat capacity ratio (1.4) for dry air at the room temperature, R_{air} is the gas constant (287.058 J/kg.K), and P_{s1} is the atmospheric pressure (101325 pas). A_1 and A_2 are the areas of the exit hole and the chamber and calculated from D_1 (8.47mm) and D_2 (60mm) consecutively.

By using **RTD** sensor inside the chamber, the temperature of T_{s0} is measured and presented on the multimeter (Keithley 2000) (see Fig. 1.5). The pressure of P_{s0} is detected using a baratron 10 kPascal maximum range with sensitivity of 1 kPa/v. The baratron data, which is presented in volt, is transferred to a pressure in Pascal from the baratron sensitivity value. The maximum pressure range of the baratron is calculated depending on the maximum theoretical velocity from Bernoulli's equation.

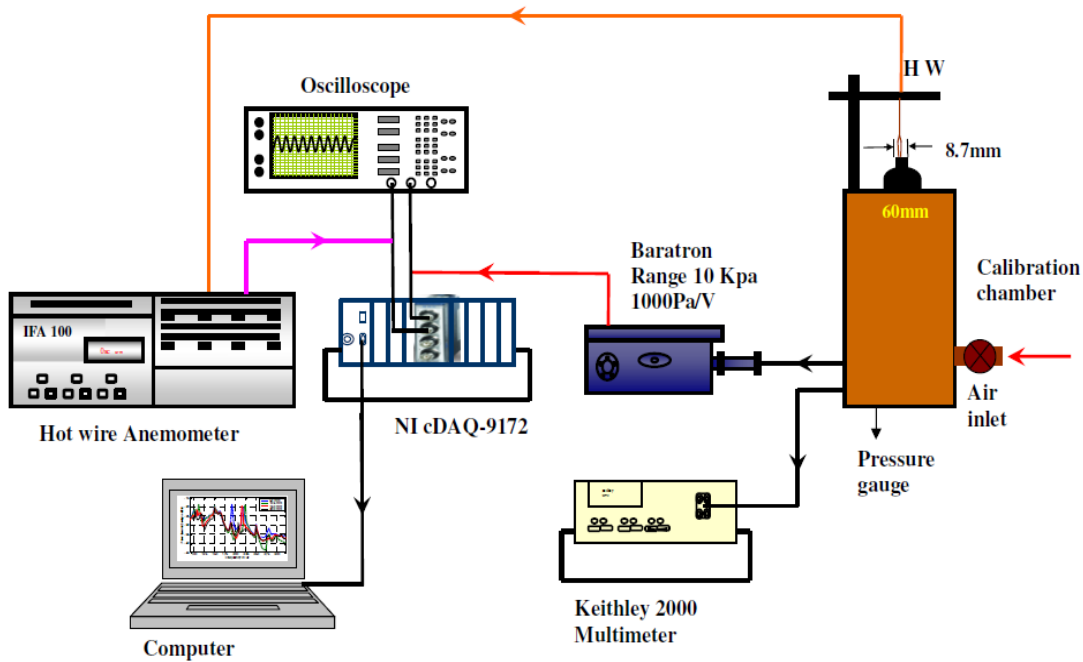


Figure 1.5: Schematic diagram of the Hot Wire calibration system.

Regarding the last equation, the whole parameters are ready to calculate the value of U at different mass flows. Using the hot wire at different mass flows can give directly the voltage range matches the velocity amounts. For safety precautions, the chamber pressure has to be lower than 6 bar. Hot wire signal and baratron signal flow to DAQ- NI cDAQ-9172 and can be shown on the oscilloscope and the computer monitor. During the measurements, the connection of the hot wire is as the next schematic diagram in Fig. 1.6. The hot wire probe is mounted at the vicinity of the fluidic oscillator face and is selected small in width as possible as can for no disturbance to the fluid flow.

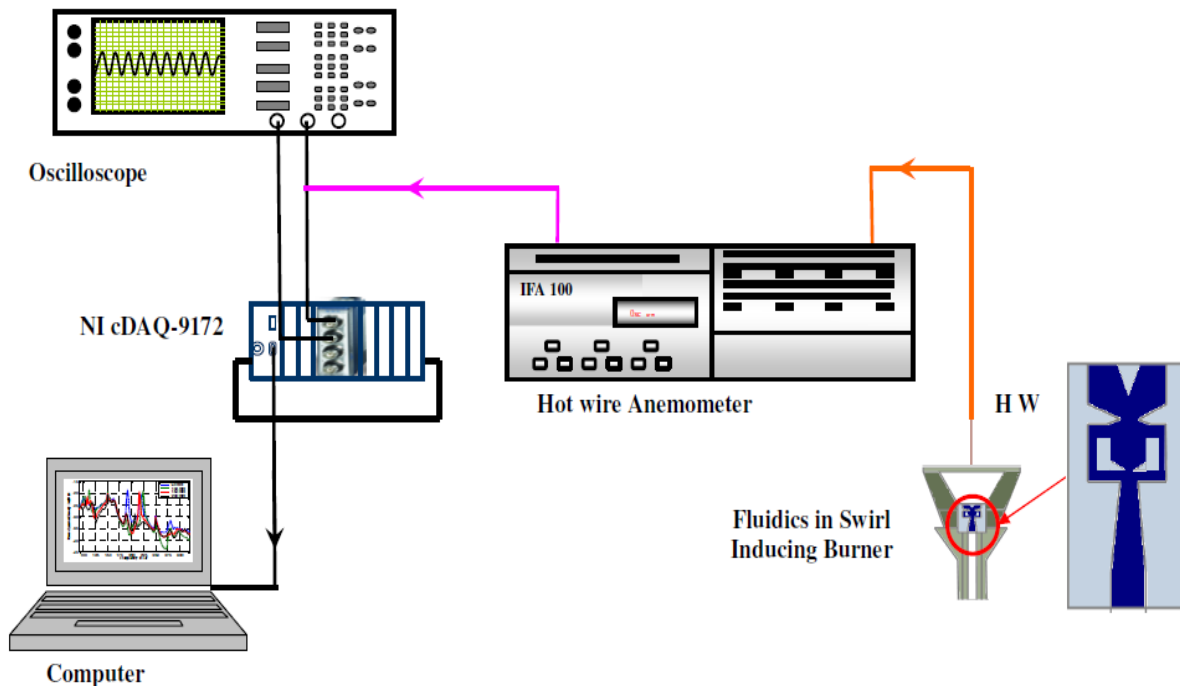


Figure 1.6: Schematic diagram of the Hot Wire measurements technique.

Microphone setup

A condenser microphone is used to measure the sound pressure oscillations of the fluidics' downstream flow. It is mounted at the position which is able to record clearly these oscillations. The used microphone is GRAS- type 26AC- S7. It is a ¼" preamplifier with a 3-m lightweight cable terminating in a 7-pin LEMO series 1B plug and used for high-frequency measurements and high-pressure measurements with wide frequency range, low noise level and very small size. The cable is only 2.5 mm in diameter and withstands temperatures from -40°C to +150°C. The typical capacitance of ¼" microphone capsule is 6.5 pF (Webster 1996). The electrical circuit in

this type of microphones is built on a ceramic substrate using selected low-noise components to gain very low self-noise. The electrical self-noise is very low that system noise is mainly determined by the microphone capsule's thermal noise (GRAS 2009).

The dimensions of the microphone are as follows: 6.35mm diameter and 48mm length while the microphone weight is 4g in addition to 46g for cable and plug. As the size of the microphone is decreased, the useful frequency range of the microphone is increased. The frequency range, which can be obtained, is determined in part by the size of the microphone. The frequency range (± 0.2 dB) is 2Hz- 200 kHz. It has a flat pressure frequency response in its entire frequency range. The frequency response of the microphone is determined by the diaphragm tension, the diaphragm mass, and the acoustical damping in the airgap between the diaphragm and the backplate see Fig. 1.7. When the sound pressure in the sound field fluctuates, the distances between the diaphragm and the backplate will change, and consequently change the capacitance of the diaphragm/backplate capacitor. As the charge on the capacitor is kept constant, the change in capacitance will generate an output voltage on the output terminal of the microphone. The acoustical performance of a microphone is determined by the physical dimensions such as diaphragm area, the distance between the diaphragm and the backplate, the stiffness and mass of the suspended diaphragm, and the internal volume of the microphone casing.



Figure 1.7: Basic elements of a condenser microphone.

It is calibrated by using a Brüel& Kjaer pistonphone type- 4228 at reference frequency 250 Hz and nominal gain of 124dB and the sensitivity was 1.152mV/pa. This type of microphones has proven to be superior with respect to temperature stability, long-term stability, and insensitivity to rough handling. It is designed and produced to ensure well-defined and accurate measurements. The operating temperature is in range of -20°C - $+60^{\circ}\text{C}$ at relative humidity of 0- 90% (Webster 1996), (GRAS 2009).

The diaphragm and the backplate form the parallel plates of an air capacitor. This capacitor is polarized with a charge from an external voltage supply (externally polarized type) or by an electric charge injected directly into an insulating material on the backplate (pre-polarized type). The supply can vary between 28 V_{DC} and 120 V_{DC} single-sided or ± 14 V_{DC} and ± 60 V_{DC} dual-sided.

PIV setup

A Continuum Minilite standard Nd: YAG PIV laser system (wave length 532nm), with pulse energy of up to 25 mJ per pulse was used to form an axial light sheet perpendicular to the plane formed by the slots of the burner. A convex cylindrical lens (f=5mm) and a concave cylindrical lens (f = 500mm) were used to generate a sheet of approximately 2mm thickness, see Fig. 1.8. The time interval between the two laser pulses was set from $t=100- 1150 \mu\text{s}$ with repetition rate of 4 Hz. A total of 500 snapshots were recorded to ensure the convergence of the mean and RMS values for isothermal cases.

Powder tracer ILA silver coated hollow glass spheres with mean particle size 15 μm (10....30 μm), density 1.6 g/ccm, silver content 33% were used to seed the water flow field exit from the fluidics oscillator. This tracer was not enough alone to seed the flow field. Micromete R-redF surface COOH with 25 mg/ml content of solid as suspension in water and mean particle size 6-10-12 μm is used in addition to the silver coated hollow glass spheres to perform the seeding of the flow field correctly. These particles are injected far upstream of the measurement plane to ensure homogenous mixing of the particles in the whole aquarium.

ILA-CCD camera type: SensiCam, 12 bit cooled imaging (1280x1024 pixel resolution) is used to capture the double frames. The camera is equipped with a Sigma optic with a focal lens 105mm during the measurements on the fluidics only while at the measurements on the burner with inserted fluidics, the camera is equipped with a short focal lens 28/1.8 SIGMA to cover the whole flow field for good investigation of the flow field and increasing the spatial resolution. A bandpass interference filter, centered inside Hama C adapter, around 532 nm and is used to reject surrounding light. For post processing of the data, cross correlation and adaptive cross correlation algorithms were used with an interrogation window size of 16x16 pixel and 50% overlap for higher spatial resolution. Local median velocity filters and linear interpolation were used to eliminate spurious vectors.

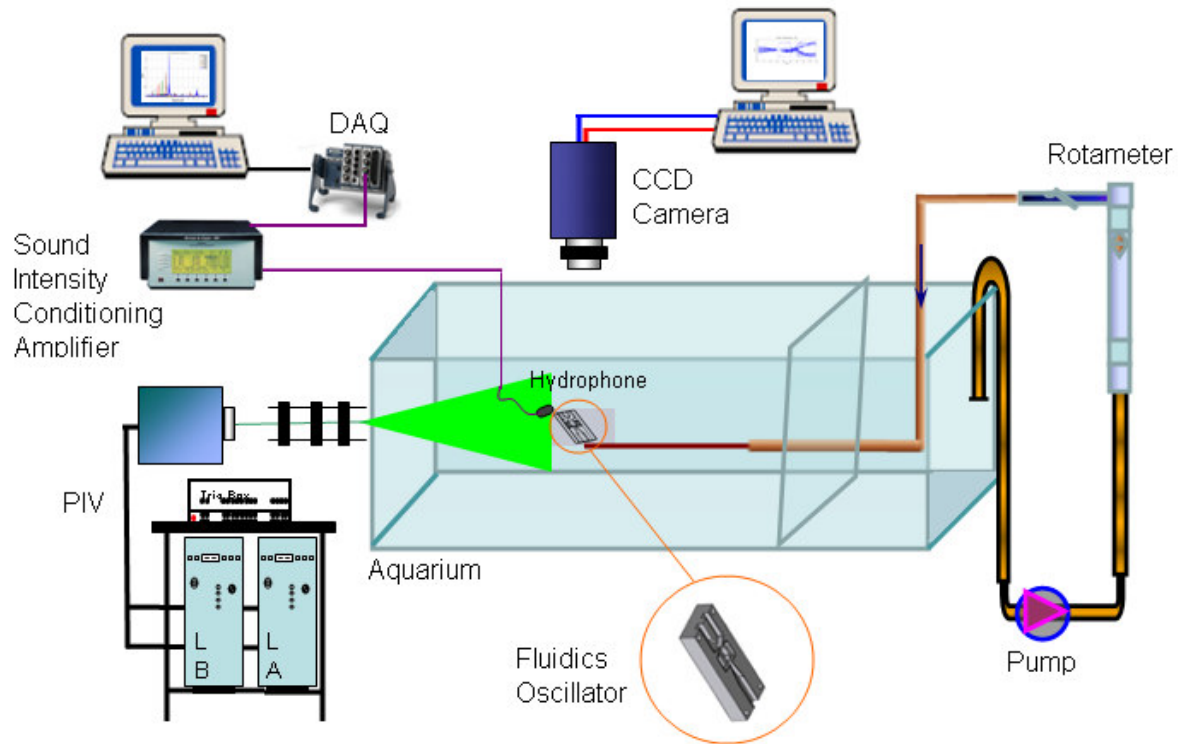


Figure 1.8: Schematic diagram of the fluidics flow field measurements.

As shown in Figure 1.8, this small Plexiglas aquarium is used for the PIV and LIF measurements inside and outside the fluidics oscillator. Maximum mass flow passes inside the fluidics was 252.6 Lit/h. The used pump is a small fish aquarium one. Rotameter 500Lit/h maximum flow rate with fine adjusting flow valve are used to give the required water flow to the oscillator. The measurements when the fluidics is integrated in a lance inside a swirl stabilized burner are performed in a big water tunnel approximately 3000x 440x 440mm. The swirl stabilized burner with fluidics oscillator are mounted inside the big water tunnel and submersed in the water. The main water pump is KSB multi Eco 35.5 ESP S 540 type class F with maximum Head of 45m, power of 800w at 220-240V, capacitance 12 μ F/450V, and 50Hz. Three water connections are required to simulate the gaseous flows in reacting combustion conditions with liquids as follows: one for the main flow, the second for the flow in fuel line, and the third one for fluidics flow (see Fig. 1.9). The Fuel line water flow rate is 224 Lit/h. The transfer of water from the main line inside the fluidic line is in maximum of 632 Lit/h from the total main water of 6.957 m³/hr. The whole water momentum rates are equivalent to those of fuel and air at real reacting conditions.

One difficulty of applying PIV in liquid flow measurements in glass surfaces comes from the total reflection of a small part of the laser light inside the glass. These reflections lead to over-

exposure of the CCD chip and thus to velocity outliers in the PIV processing. If some of the minor reflections could be minimized through background subtraction, a major reflection was visible at the main flow field (Emara et al. 2010). The measurements schedule is performed in axial and azimuthal directions. In the axial measurements, the laser sheet was vertical and the camera was perpendicular to that sheet as shown in figure 1.9- A while in the azimuthal measurements, the camera is mounted over the water tunnel in the direction of water flow and the laser sheet is horizontal (see figure 1.9- B) .

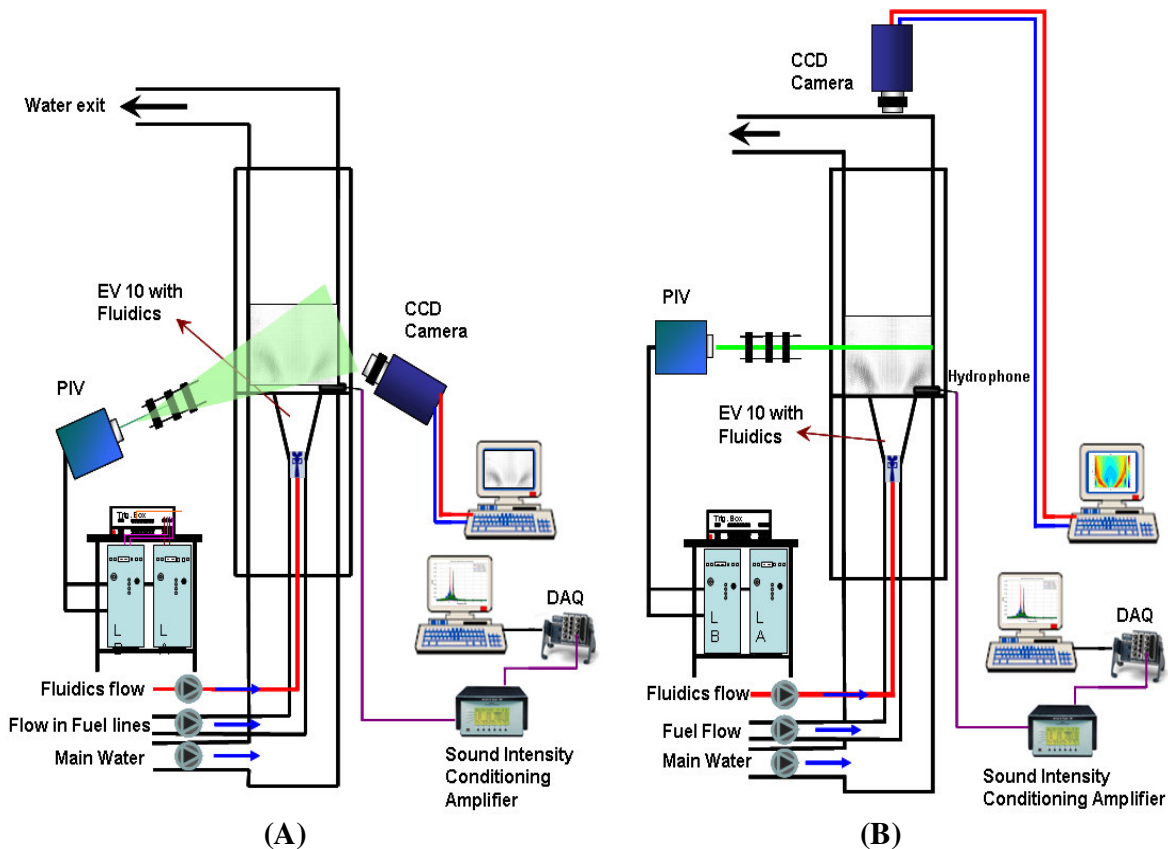


Figure 1.9: Schematic diagram of the water tunnel with fluidics inserted inside a swirl stabilized burner.

Hydrophone setup

A standard hydrophone, type 8104 with integral AC-0034 and 10m standard cable length terminated JP-0108 BNC (M) plug, offers a usable frequency range of 1Hz to 180 kHz and a high sensitivity relative to its size. It further more provides uniform unidirectional sensitivities in both horizontal and vertical planes up to high frequencies. It is an excellent transducer for making absolute sound measurements and calibrations within a broad frequency range. It can also be

applied as a unidirectional reference projector. The overall characteristics make it extremely applicable for laboratory as well as industrial uses. It can also operate underneath water in an operating depth of 700m and 1000m. Operating temperature range from is -2°C to $+80^{\circ}\text{C}$ and the weight in air is 75g.

As shown in Fig. 1.10, encapsulating material is Nitrile Rubber (NBR) which is not only resistant to sea and fresh water but also resistant to oil. It is limited resistant to petrol and most acids and will be destroyed by base, strong acids, halogenated hydrocarbons (carbon tetrachloride and trichloroethylene), nitro hydrocarbons (nitrobenzene and aniline), phosphate ester hydraulic fluids, Ketones (MEK and acetone), Ozone, and automotive brake fluid (RESON 2005).



Figure 1.10: Hydrophone photo in air.

Thermocouple and emissions probe setup

K-type thermocouples with 1.5 mm diameter were used to measure the temperature of the preheated air upstream and the exhaust temperatures at 0.6 m downstream of the burner exit. The water-cooled emissions probe was located 0.6 m downstream of the burner exit and consisted of 0.3 m long tube with 10 mm diameter. A heated tube with a length of 12 m is used to connect the analyzer system. NO and NO₂ were measured wet while CO, CO₂, and O₂ were measured dry. All presented emissions results in this study are normalized to 15 % O₂ Volume.

ICCD setup

The recordings of the OH- Chemiluminescence of the flame were obtained with an ICCD camera equipped with a bandpass filter centered at 312 ± 2 nm (Albrecht 2008). The wavelength range matches OH radical emission spectrum, which has a maximum at 306.7 nm. High emitted light areas or higher in legend counts of the camera pictures represent the maximum intensity of OH radicals and lower emitted light areas are the minimum.

Results and Discussions

Chapter (3)

Fluidics Design Variations

Chapter (3) Fluidics Design Variations

Description of the Fluidics Injector

The challenge of the present work is to provide a fluidic oscillator of relatively small dimensions to meet practical size restrictions of the normal pilot lance in a swirl stabilized burner. Two design variations are performed to reach the final and optimum design.

At the first design variation of the new model, the reduction in size was almost to 53.3% from the original one used by Guyot (Guyot et al. 2007). This model was sustaining the ability of insertion inside the burner but was not suitable for the combustion stability job in the swirl stabilized burner according to higher produced frequencies. The projectile exit areas for the two limbs are altered from round in the original design to rectangular shape at this one. Each limb area is set at 3.3x1.6 mm.

At the second design variation, some changes in design configuration and channels features are done. Four Plexiglas models of the fluidic are investigated freely in cold air depending on changes in some control parameters. These control parameters shown in Fig. 1.11 are as follows:-

- 1) The depth of the whole fluidics channels.
- 2) The width of the exit limbs.
- 3) The throat width and length of fluidics.
- 4) The angel of outlets.
- 5) The thickness and the shape of the fluidics shoulder.
- 6) The width of the feed back channels.
- 7) The throat exit angle.

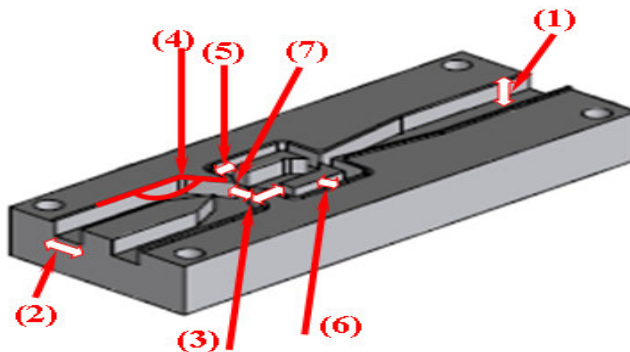


Figure 1.11: Fluidics control parameters.

1st Design Variation- Fx0

As clarified in Fig. 1.12, the first oscillator design failed to produce a flow with fundamental frequencies coincide typically with those matching with combustion stability conditions. The microphone placed upstream of the fluidics recorded the pressure fluctuations induced by a coherent structure. A spectrum analysis displays the relative strengths of different frequencies in the sound signal over time. The power spectra, recorded for different Re-numbers, show a fundamental peak which clearly scales with the Reynolds number. The fundamental peak frequencies are from 9.89- 11.44 kHz which is too noisy in range of 7468-22404 Re number calculated from the equivalent mass flow rates. The first peak value is in range of 0.88- 1.664 kHz but not the fundamental one. Intuitively speaking, the spectral density characterizes the frequency content of the signal. Through observing the signal peaks, the periodicity in the signal is noticed every 9.78 kHz.

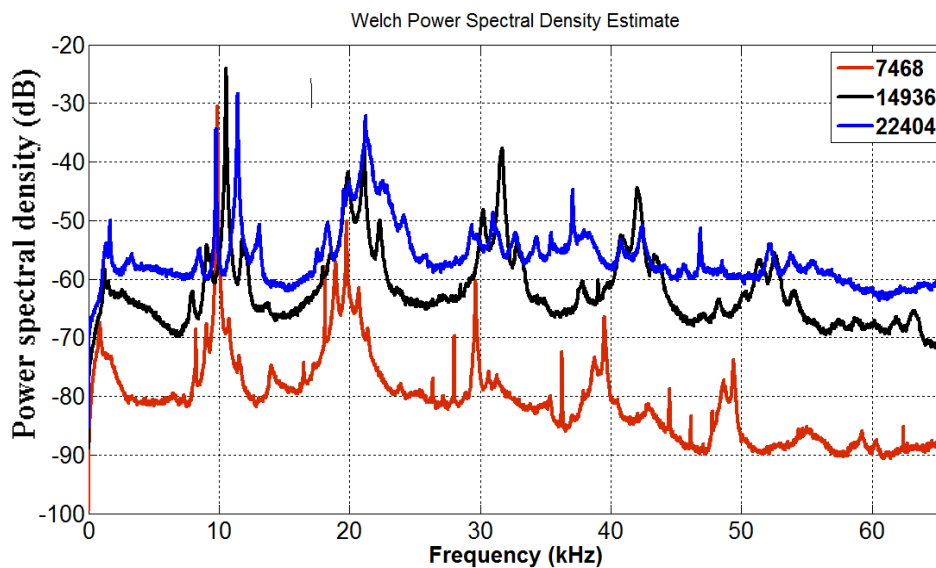


Figure 1.12: Power Spectral Density of the microphone signals for different Re numbers.

The signal has a fundamental frequency of 9.89- 11.44 kHz in the named range of flow which depends slightly on the Reynolds number and shows also strong harmonics and linear relation, specifically for the lower Reynolds number (see Fig. 1.13).

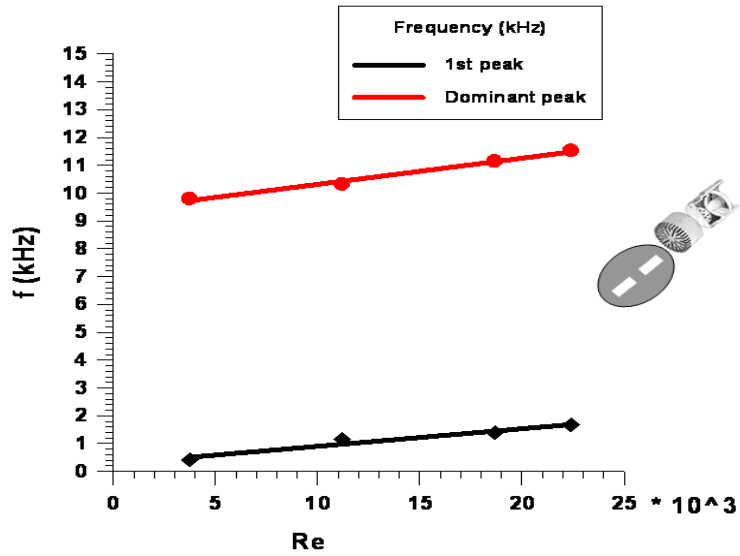


Figure 1.13: Fluidics frequency at different Re numbers.

The Strouhal numbers of the first and dominant peaks are plotted as a function of the calculated Reynolds number (Re) in Fig 1.14. It clearly shows that the Strouhal number remains almost constant around 0.04 with a slight decrease with increasing Reynolds number for the first peak which is relevant to the mass transfer and decreases from 0.58 to around 0.2 for the dominant peak. This shows that the microphone signal peaks presented in Fig. 1.14 are related to flow instability.

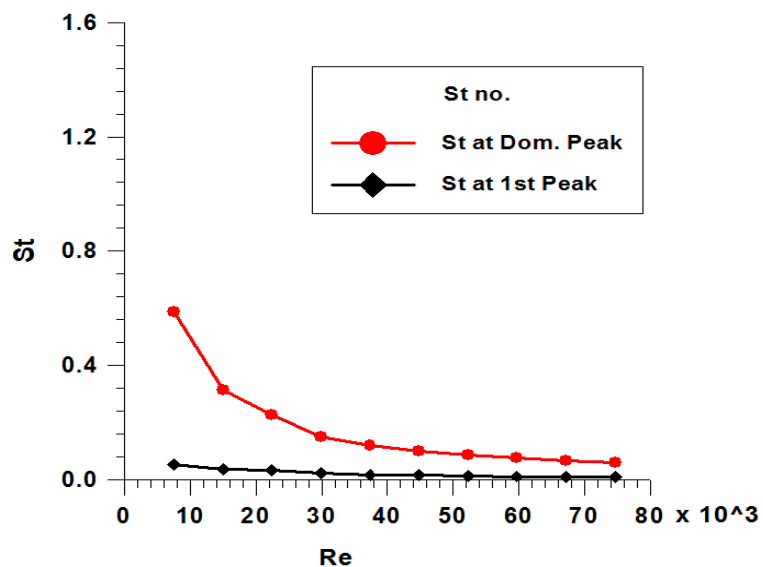


Figure 1.14: Strouhal number of the fundamental and 1st harmonic at different Re numbers for Fluidics.

Upstream of the oscillator, the second harmonics of the helical structure is much stronger in amplitude than the first one. As the strouhal number is considered in-between large Strouhal number (order of 1) and low strouhal number (order of 10^{-4} and below), hence it is classified as an intermediate one. Oscillation at intermediate Strouhal numbers is characterized by the buildup and rapidly subsequent shedding of vortices (Ian 1982).

The RMS values of the pressure oscillations are shown in the next figure in unit of voltage comes out from the field point system and the microphone calibrated by using the piston phone with sensitivity of 867.5616 pa/v. Below the RMS value of 0.8v (694.04928 pa) the combustor was regarded being stable in reacting conditions as depicted by Emara. Values above unity were regarded being unstable and present a clear fundamental peak in the power spectrum density (Emara 2009). Up to Re of 22404 is free of these expected instabilities as shown in Fig. 1.15.

As the flow pattern in the oscillating chamber and particularly the vortex near the control throat provide flow aspiration on one side and surplus of flow on the opposite side of the chamber. This accelerates and respectively decelerates the working fluid in the feed back channels such as to cause a reversal of the vortex after a time delay (Bauer 1981).

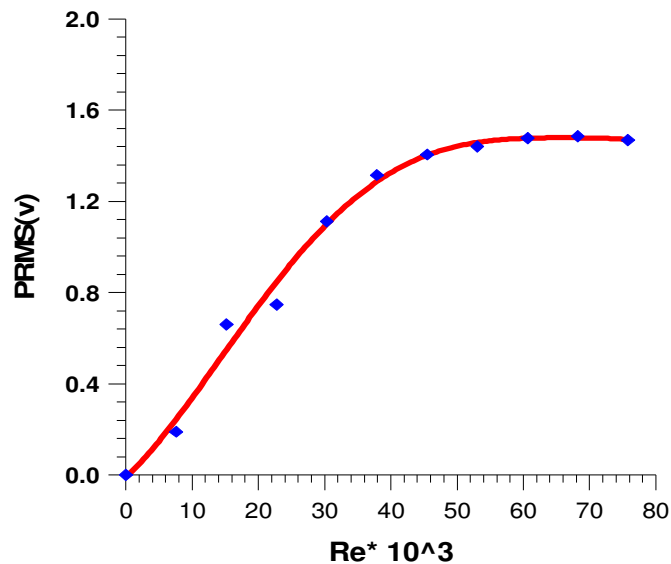


Figure 1.15: P_{RMS} at different Re.

The fluidics device operates at low to high frequencies depending on the length of the feedback channel and thus on its physical size. Some tests are done in atmospheric conditions (20°C and atmospheric pressure) for air using microphone and hot wire techniques. Microphone was used to investigate the sound pressure oscillations and hot wire probes were used to measure the velocity

fluctuations at the fluidics' outlets. Fig. 1.16 exhibits the time history of the velocity oscillations for the fluidics exit limbs at Re of 7468 (1kg/h) air. The mean velocity is around 20 m/s. The peak to peak oscillation period is almost 0.092 ms for each outlet limb corresponding to the dominant 10 kHz peak in spectra as demonstrated in Fig. 1.17.

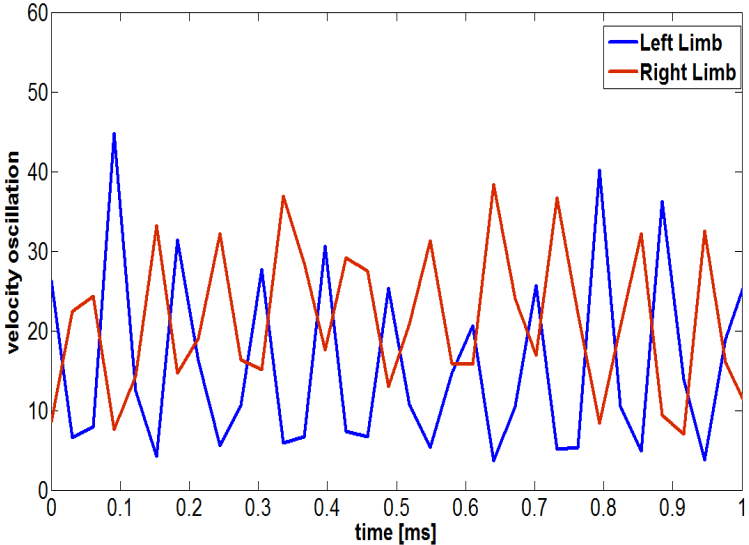


Figure 1.16: Time history of the velocity oscillation for the Fluidics exit limbs at Re of 7468 for air.

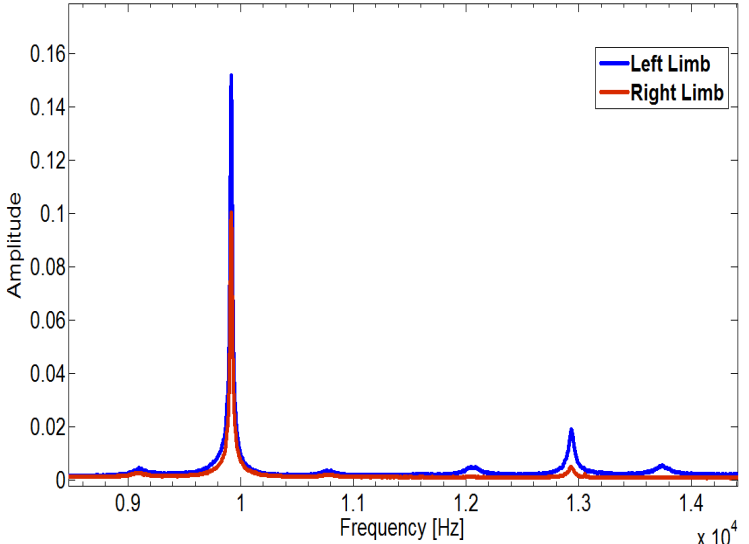


Figure 1.17: Cross power spectrum of hot wire signal for the Fluidics limbs at Re of 7468 air.

2nd Design Variation

The second design variation focused on how to insert a fluidic actuator in a swirl stabilized burner in order to study the flow field interaction at the outlet of the fluidics and the burner and to reduce the emissions at stable conditions. Four design variations were developed trying to reach the optimum one or more for working in the combustion field and achieving the goal. Some parameters are changed in the previous design (Fx0) at the 1st variation and give these four new models.

Design Optimization

1st Fluidic oscillator model- Fx 1

The control parameters applied to this model are the depth of the whole fluidics channels which increased by magnification factor of 3.75, the width of the exit limbs which increased to 1.12 of the old one and the width of the feed back channels which reduced to 0.8 of the old width used in the 1st design variation. Fig. 1.18 shows these parameters location on the schematic of Fx1.

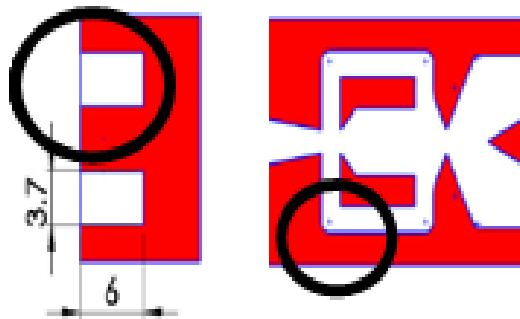


Figure 1.18: 1st Fluidics model Fx1

Power spectra from hotwire data were calculated and are plotted in Fig 1.19. The hot wire anemometry is located in the vicinity of the orifices' exit of the fluidics at around 0.5- 1mm. Spectra of the mass flows between calculated Re numbers of 1820- 18205 (0.5 and 5kg/h) are plotted. As noticed in the figure, the fundamental frequencies of the air flows increase as the mass flow increases. The frequency is directly proportional to the mass flow in linear relation as presented in Fig. 1.20.

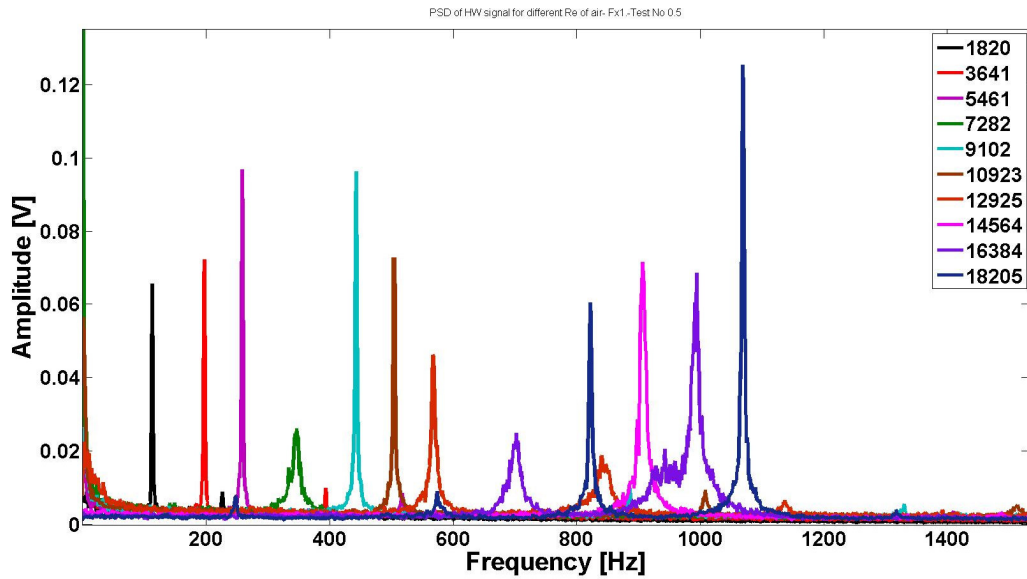


Figure 1.19: Power Spectral Density of HW signal for different Re of air- Fx1.

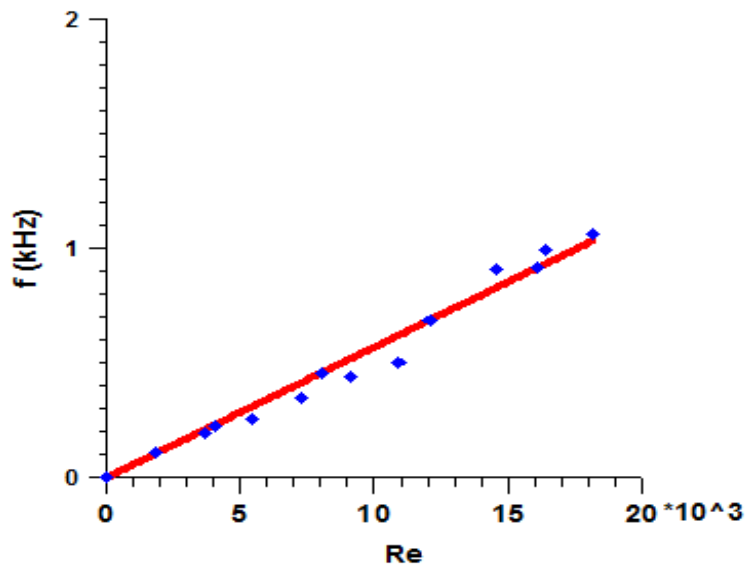


Figure 1.20: Fluidics frequency at different Re of air for Fluidic oscillator Fx1.

Fig. 1.21 demonstrates that the hot wire and Microphone signals offer a consistency of frequency oscillation as the trend of the two signals is identical for the frequency content at certain mass flow rate. The last three figures provide evidence that the fluid flow inside the fluidic oscillator can be modulated by the oscillator itself which is able to generate the oscillated flow without any other means or valves. Corresponding to the fundamental 507 Hz peak in each limb the spectra of both limbs are demonstrated in [Fig. 1.22](#).

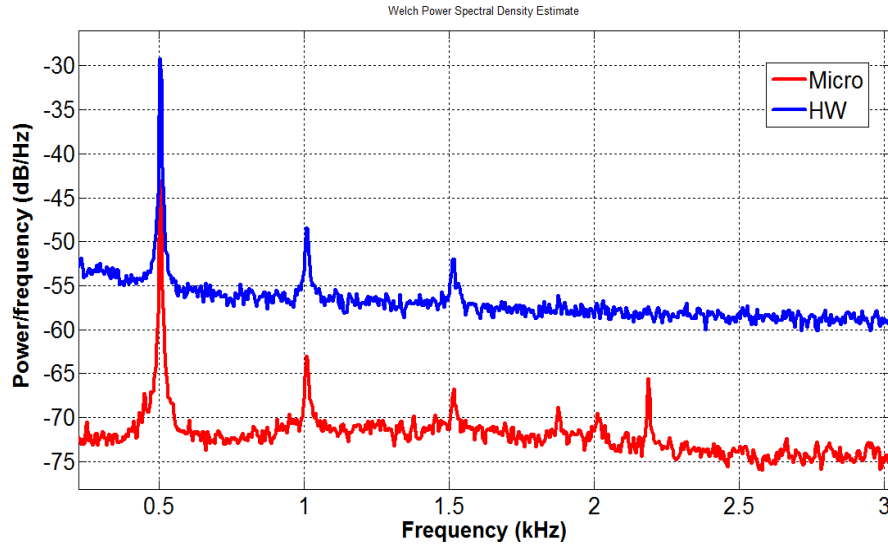


Figure 1.21: PSD comparison between HW signal and Microphone signal at Re 10923 (3kg/hr) of air- Fx1.

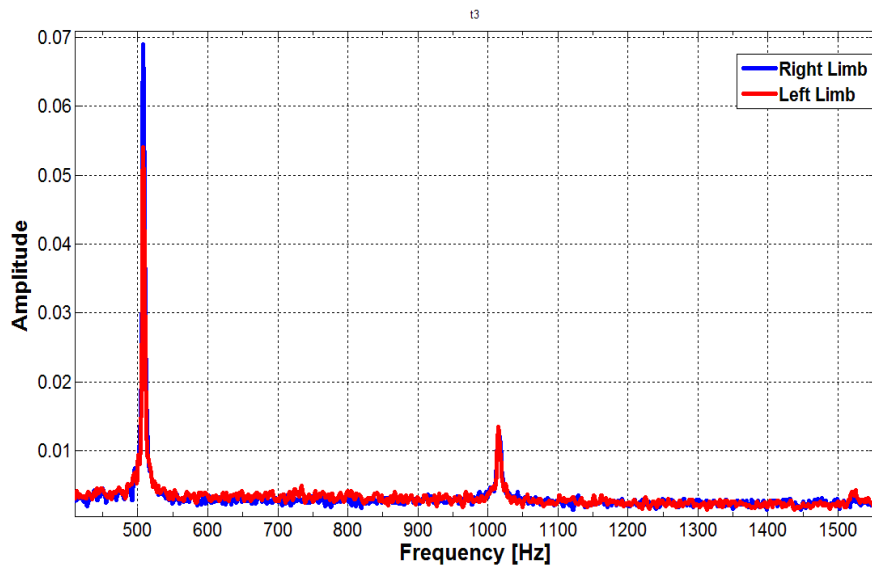


Figure 1.22: Cross power spectrum of the hot wire signal for the Fluidics limbs at Re 10923 (3kg/hr) of air- HW- Fx1.

The time history of the pressure oscillation for the two outlets at Re 18205 (5kg/h) is presented in Fig. 1.23. Two signals, recorded at both outlets using couple of hot wires with 5 μ m diameter and 3mm probe width, are both approximately sinusoidal. The measured two waves, having the same frequency and referenced to the same point in time, are said to be out of phase with each other as presented in the last figure.

The phase difference is 180 degrees (π radians) and the two oscillator limbs signals are antiphase. This difference between the pressure oscillation signals of the two limbs is calculated as 0.49ms.

The oscillation period length is almost 1.099 ms for each outlet limb corresponding to the dominant 1.01 kHz peak in spectra. The modification parameters reduce the frequency by around 10 times and increase the oscillation period to 11.41 times. Oscillation signals are in-between 1.96 as maximum and 1.36 as minimum volt as an indication to pressure oscillations.

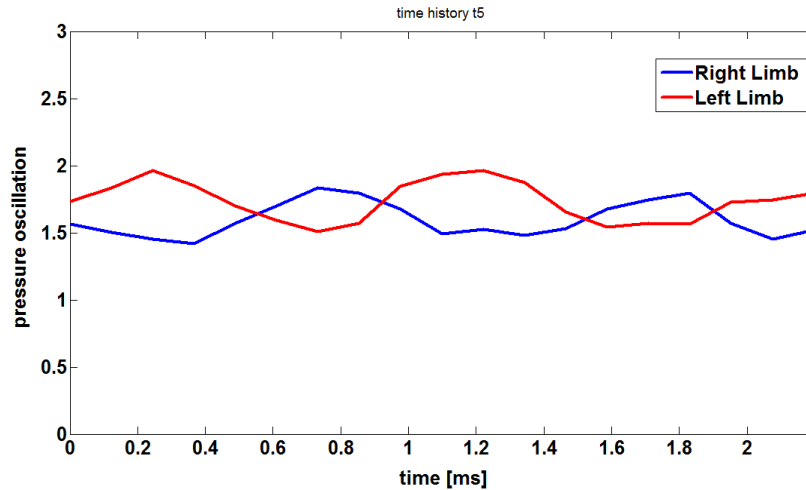


Figure 1.23: Time history of the pressure oscillation for the fluidics limbs at Re 18205 (5kg/h) air for Fluidics- HW- Fx1.

The mean velocity at different oscillator mass flows is shown at Fig. 1.24. The velocity is in linear relation with the mass flow increase as demonstrated in the figure. The hot wire anemometry is used to measure the signal in volt and the calibration is implemented by the calibration chamber to present that in m/s. The mean velocity at this new design is almost 0.1 of that one for the other design in the 1st design variation. Fig. 1.25 exhibits Strouhal number at different Reynolds numbers (Re). Strouhal and Reynolds numbers are in linear relation.

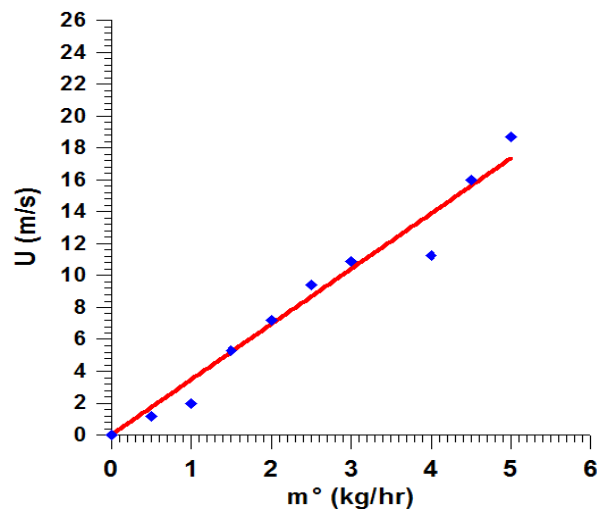


Figure 1.24: Fluidics velocity at different air mass flows for Fluidics Fx1.

The mean strouhal number equals 0.34 which is in intermediate range. Oscillation at intermediate Strouhal numbers is characterized by the buildup and rapidly subsequent shedding of vortices and the oscillation is due to the flow instabilities (Ian 1982 and Emara 2009).

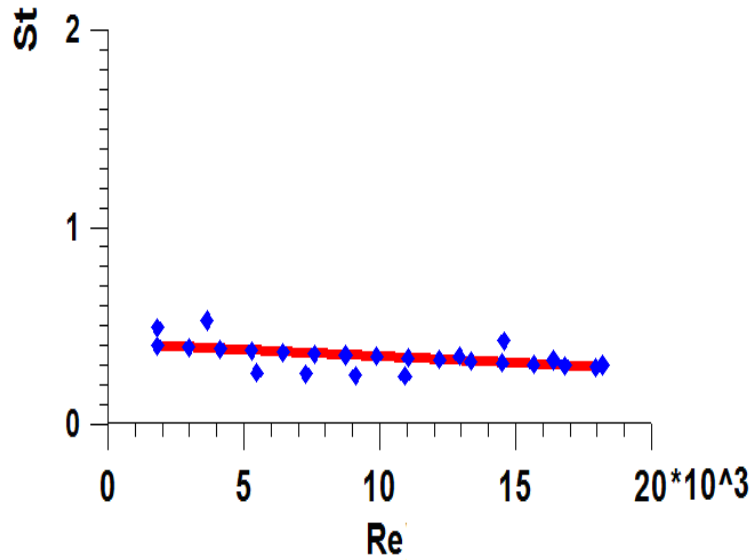


Figure 1.25: Fluidics St at different Re for Fluidic oscillator Fx1.

Pressure oscillations are detected in this fluid. The microphone is used for that and mounted directly near the oscillator exit in right angle with no contact to its surface and for no barring of the fluid flow. The maximum RMS (p) is almost of 0.9v. Pressure oscillations are in the expected stable range of reacting flows at least at the tested band width in maximum of Re 18205 (5kg/h). RMS (p) is presented as a function of calculated Re numbers in Fig. 1.26.

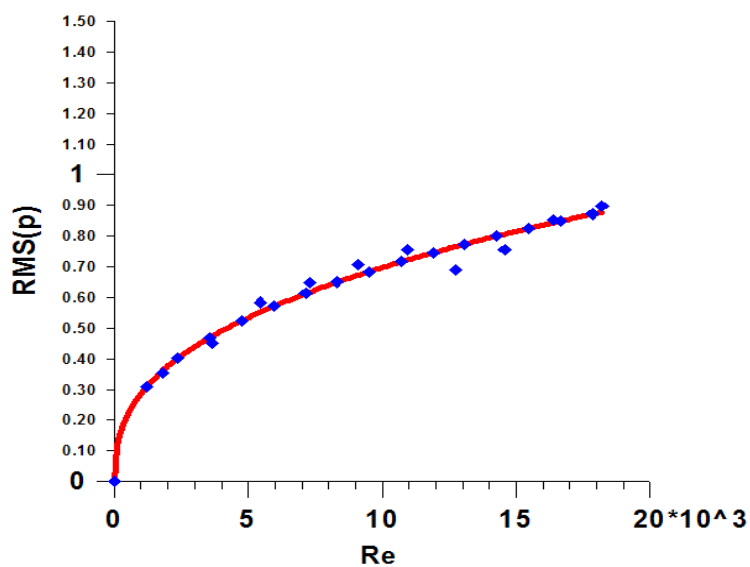


Figure 1.26: Fluidics P_{RMS} (v) at different Re for Fluidic oscillator Fx1.

Comparison of the old design used by Guyot (G- model) at a scale of 1.87% of the tested design offers a good matching in the frequencies even with the change of size and the narrow space allowed for the intrusion of the oscillator inside the burner. Fig. 1.27 shows the power spectral density of the microphone signal for different mass flows- G- model fluidics.

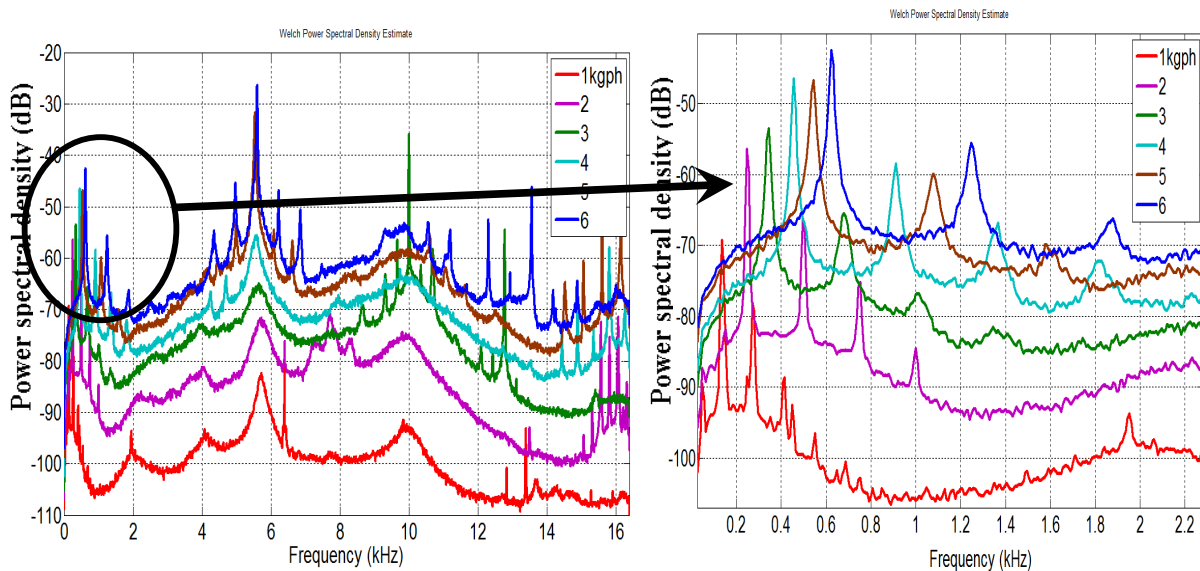


Figure 1.27: Power Spectral Density of the microphone signal for different mass flows- original Fluidics.

The fundamental frequencies are in range of stability but with higher amplitudes in comparison to the first amplitudes resulted in case of analysis of G- model.

Other Fluidic oscillator models

Other control parameters are applied to the design of Fx2 as shown in Fig. 1.28. These parameters, applied to Fx2, are the control throat width which increased to 1.5 times the old width in addition to the whole changed parameters in Fx1- design.



Figure 1.28: 2nd Fluidics model Fx2.

The hot wire is positioned at the exit directly at the same place like Fx1. The spectra of the mass flow in range of Re 1820- 21846 (0.5 and 6kg/h) are represented in Fig. 1.29. The data also show a linear relation between the frequency and Re at the named range of flow.

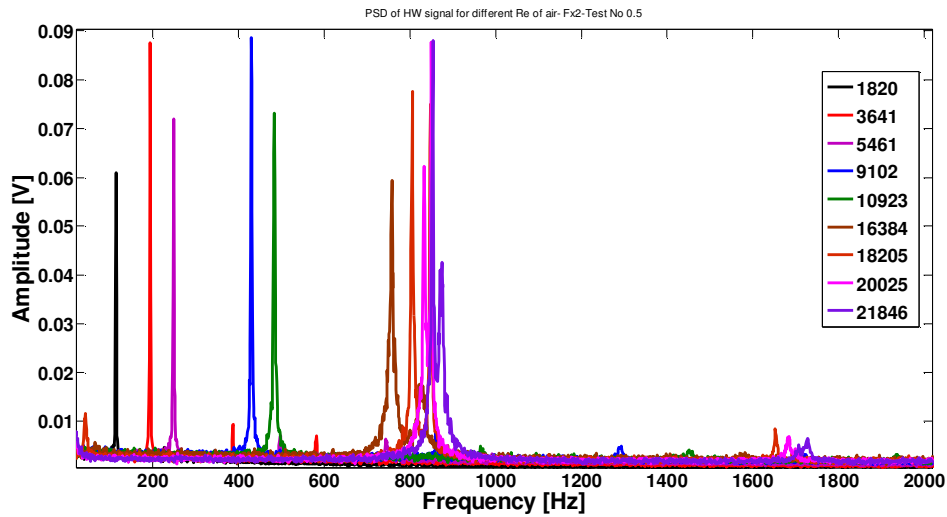


Figure 1.29: Power Spectral Density of HW signal for different mass flows- Fx2.

The control parameters applied to Fx3 are as follows; the control throat angle increased to 1.7 times the old one in the 1st design variation (Fx0) and the throat length increased to 1.67 times Fx0 in addition to the modulations parameters in Fx1 and Fx2. Figure 30 shows Fx3 model with the new modifications, while the spectra are shown in Fig. 1.31. Similar to the previous two models, the frequency is in directional proportion with Re.

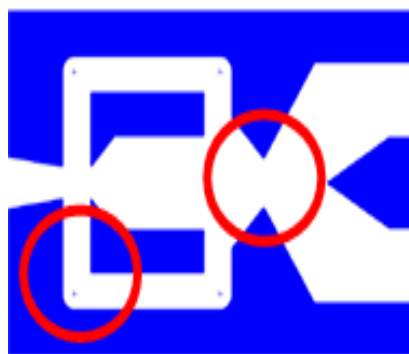


Figure 1.30: 3rd Fluidics model Fx3.

The last design variation ideas in the design are for Fx4 according to some changes performed as demonstrated in Fig 1.32. These changes are: the feed back channels' inlet width from the

chamber side which decreased to 0.3 of the old width, the throat angle in exit direction increased to 2.64 times the old one, in turns the throat length increased to 1.83 times, and the throat exit width increased to 1.33 the old width. These modulations are in addition to the modifications done in Fx1 from the 1st design variation.

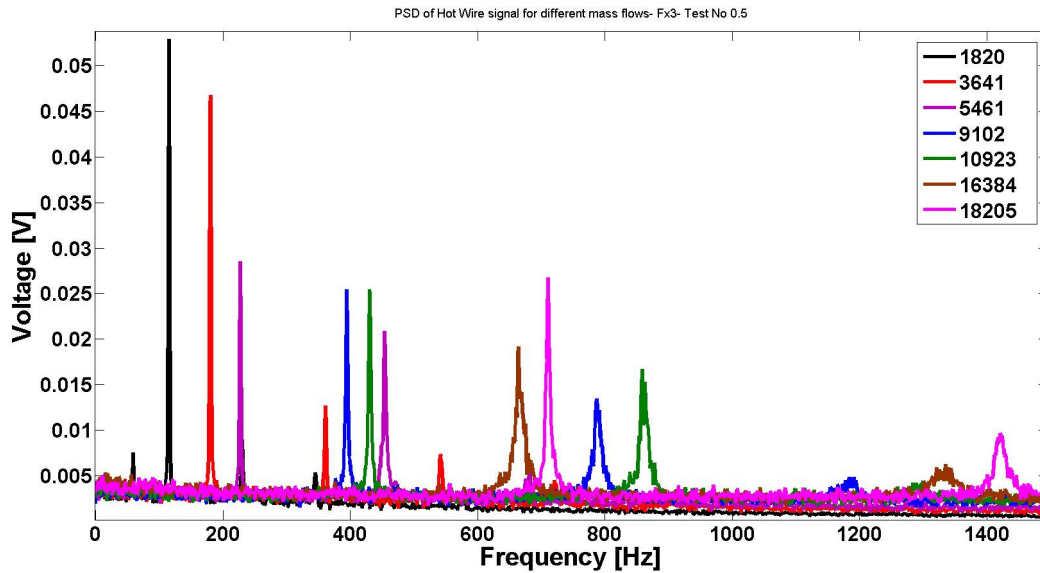


Figure 1.31: Power Spectral Density of Hot Wire signal for different Re numbers- Fx3.

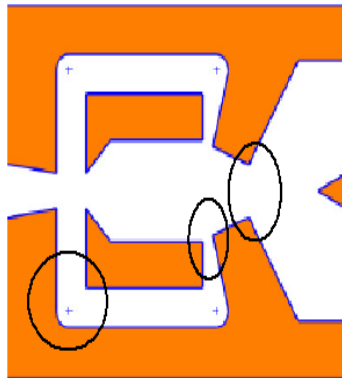


Figure 1.32: 4th Fluidics model Fx4.

The frequency contents of the signals at different mass flows offer a linear representation for the whole oscillator designed models as shown in Fig. 33. Up to Re 18205 (5kg/h) for the first three models, the relation is linear while it is only linear up to Re 10923 (3kg/h) for the last one. The trends for the first and the last models are almost symmetric in the **common range**.

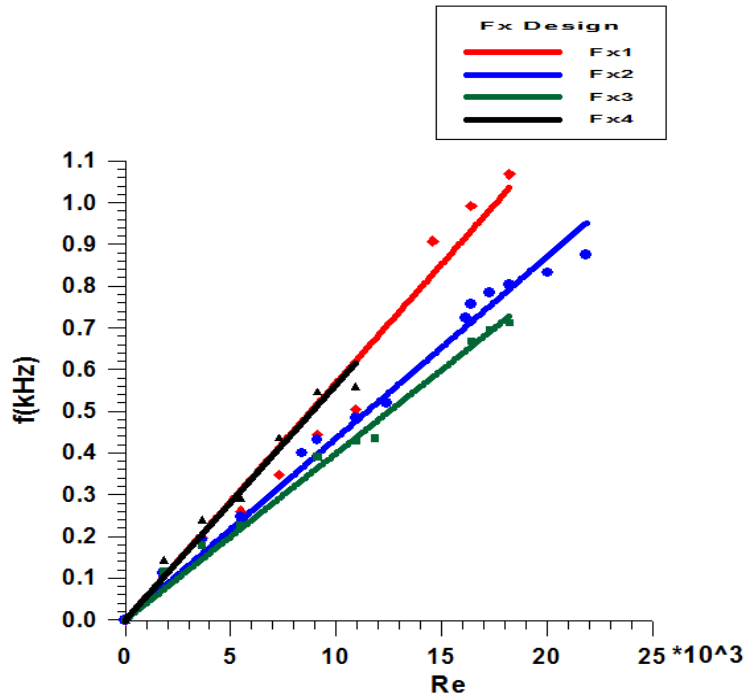


Figure 1.33: Fluidics frequency comparison at different Re numbers of air flows for different fluidic oscillators.

Also the pressure oscillations lie almost in the safe range far from the expected combustion instabilities up to Re 21846 (6kg/h) of air flow (see Fig. 1.34). These four models are giving a pressure oscillations lower than unity.

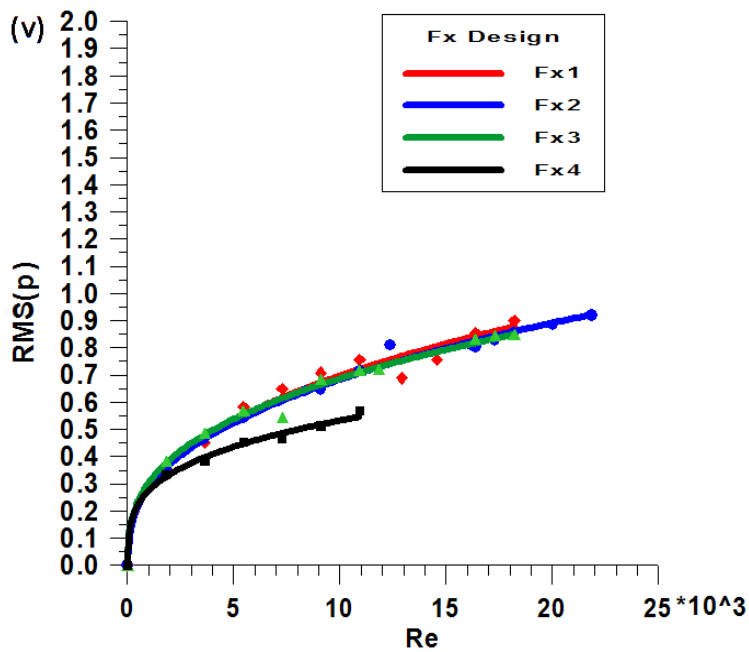


Figure 1.34: P_{RMS} (v) at different Re of flows for different fluidic oscillators.

Fig. 1.35 exhibits the relation between Strouhal and Reynolds numbers for the whole four oscillator models. The Strouhal number reduced to be in between 0.2-0.4 at about Re of $7 \cdot 10^3$. After that it gives almost linear trend for Fx1, Fx2 and F3. For the last model, the strouhal number was almost 0.8. Compared to Fx1, the strouhal number is reduced by 23.5% and 38.2% for Fx2 and Fx3 consecutively, while the number increased 2.35 times at Fx4. Oscillations as for Fx1 are characterized by the buildup and rapidly subsequent shedding of vortices for the whole models behind the flow splitter.

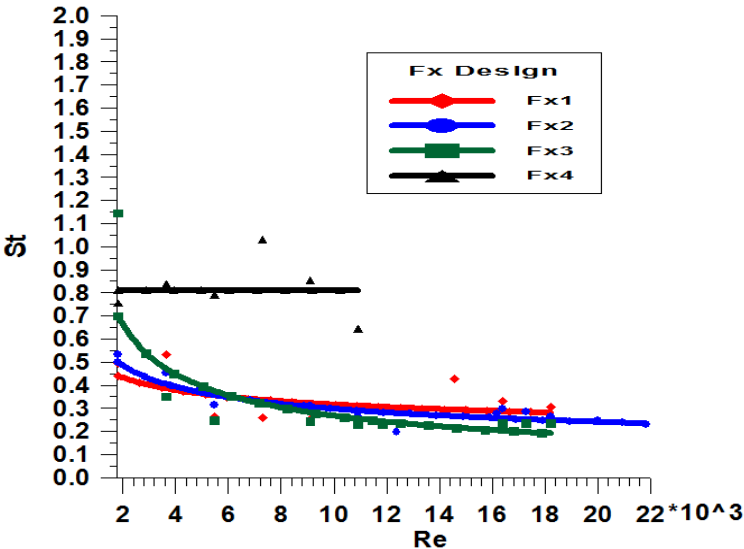


Figure 1.35: St number at different Re numbers- HW mounted directly at exit of different fluidic oscillator models.

Fx1 has almost higher amplitude values than the other three models at certain Re numbers but almost equal to Fx2 model as demonstrated in Fig. 1.36. This may affect in the combustion stability better than the other oscillators even they are also affecting the flame instabilities.

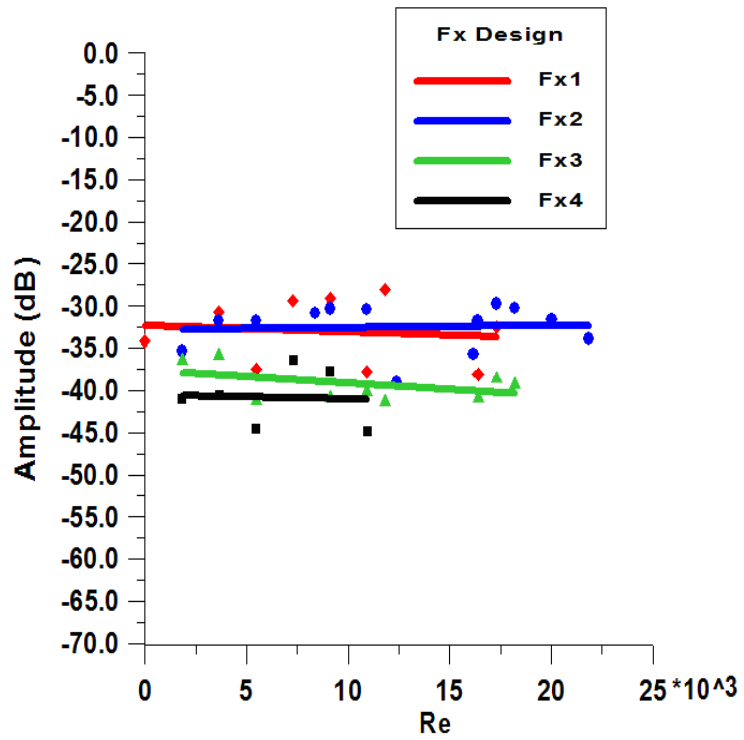


Figure 1.36: Fluidics signal amplitude comparison at different Re numbers for different fluidic oscillators.

Chapter (4)

Fluidics Flow Field (Inside and Outside)

Chapter (4) Fluidics Flow Field (Inside and Outside)

LIF Flow visualization

The study of the flow field, in and out the fluidics models, is performed at water test rig. This water test rig is clarified at Fig. 1.8. This study is performed using a LIF and PIV techniques. The frequencies and the amplitudes can be obtained out of the pressure signal of the hydrophone by means of the subsequent applied Fourier transformation. Figure 1.37 exhibits a linear relation, as in microphone data, between the frequency in Hz and the volume flow rate in l/h. Also the amplitude is in directional proportion with the volume flow rate as shown in the representation of the single sided spectrum in Fig. 1.38. The tested water mass flows are selected as equivalent in momentum as the air mass flows applied in reacting flow conditions as will be explained in next sections .

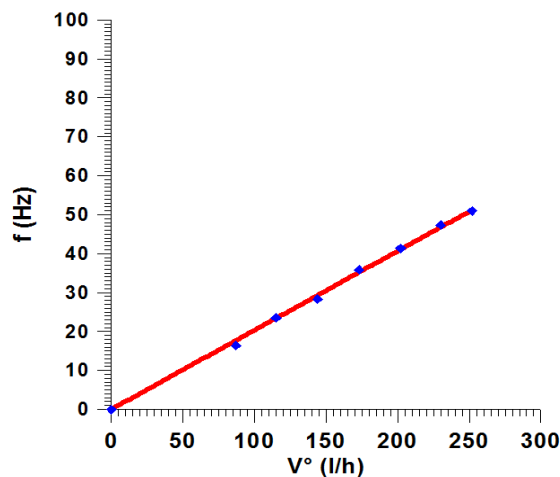


Figure 1.37: Fluidics frequency at different water mass flows for Fluidic oscillator Fx1.

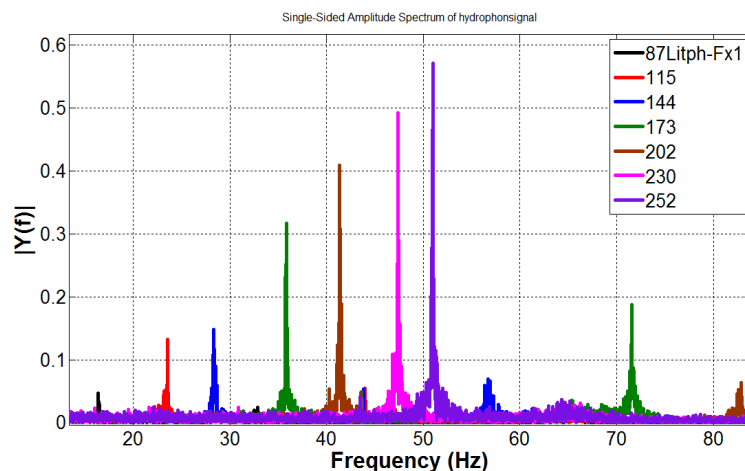


Figure 1.38: Single-sided amplitude spectrum (ν) at different water mass flows for Fluidic oscillator Fx1.

At 87 l/h, the flow field is visualized as demonstrated in Fig. 1.39. The data is recorded at 250 fps. Five pictures are selected to show the fluid oscillations process at the fluidics exit and a part of the fluidics end. The jet stream is deflected towards the oscillating chamber according to the Coanda effect (Nakayama 2005). The lower pressure region, formed at the right wall of the interacting chamber between this deflected stream and the right wall, keeps the jet stream deflected. Because of this deflection, the fluid tends to impinge onto the right feedback (feed back 2) port inlet, upstream of the control throat, transmitting the pressure rise back to the control port by the speed of sound through the right feedback passage. Then, the transmitted pressure rise triggers the jet stream to bend towards the opposite left side. This sequence is repeated with the stream deflection towards the left side exit limb (Outlet 1) so as to form a complete cycle of oscillation. From figure 1.39, the jet stream starts to change its direction at this specified volume flow within 16ms.

Increasing the volume flow rate decreases the time period of the deflection between the two exits. Figure 1.40 verifies this information as the deflection between these two limbs is performed after 8 ms at 184 l/h. The jet length increased according to the volume flow increase as well as the flow velocity.

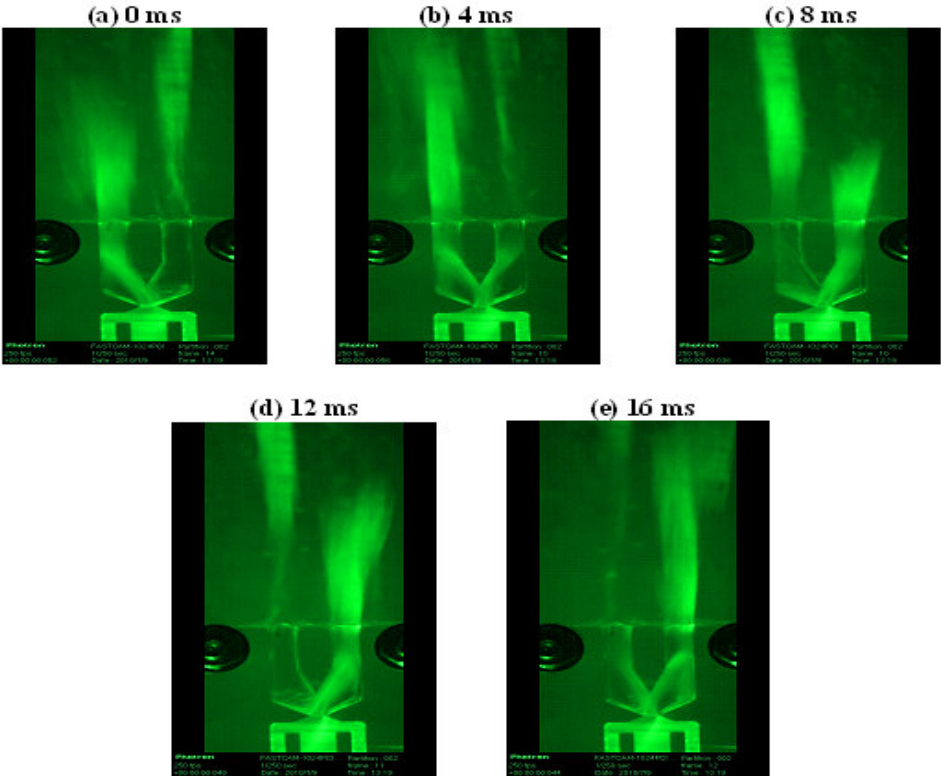


Figure 1.40: Fluidics oscillating water flow field at 184 l/h- Fx1.

Fx1 and Fx2 present a big similarity between the two flow field visualizations and the jet penetration length in the main flow field, while Fx3 proffers a lower jet penetration length at the same volume flow rate. There is also no jet interaction between the two jet limbs at the first two fluidic oscillations. Figure 1.41 shows the flow field visualization at 87 l/h for Fx3. According to the changes of the control throat angle and the throat length, the deflection period is changed to 12 ms and a reduction in penetration length is noticed.

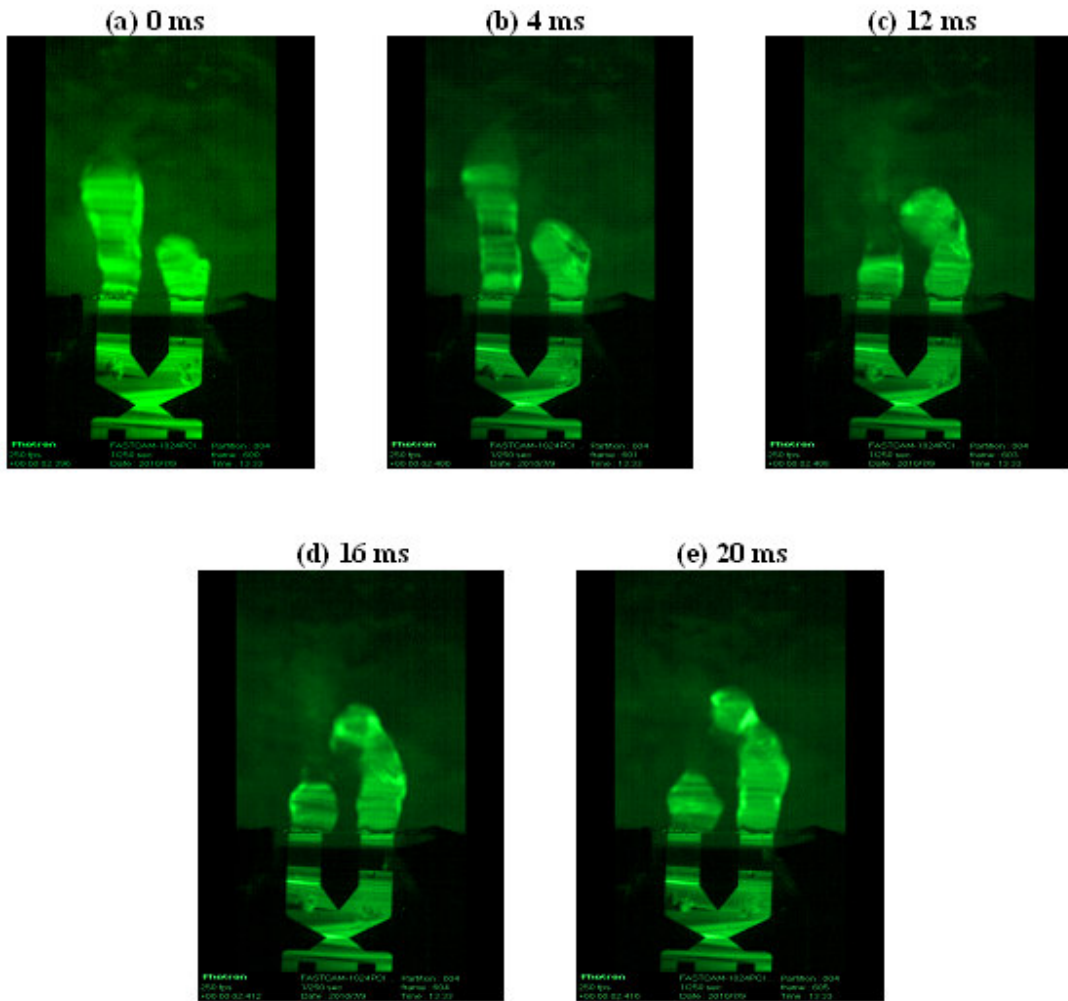


Figure 1.41: Fluidics oscillating water flow field at 87 l/h- Fx3.

The jet interaction is started between the two limbs at 144 l/h in Fx3 while the interaction between jets first is noticed at 202 l/h for the first two fluidic oscillators. Fx3 jet interaction between the right and the left jets started at a distance of about four times the outlet width from the fluidics vicinity and at 144 l/h (see Figure 1.42). The fluid deflection starts after 8ms and the fluid jet is then totally filling the other side.

Fx4 has a different nature as presented from the LIF measurements. Some changes in the fluidics shape, like the smaller feed back channels' inlet width from the chamber side, the increase in throat angle in exit direction, the throat length increase, and the throat exit width increase, are responsible for the flow field visualization change in Fx4. These effects increase the suction in the free limb while the other side is full of fluid as shown in Fig. 1.44.

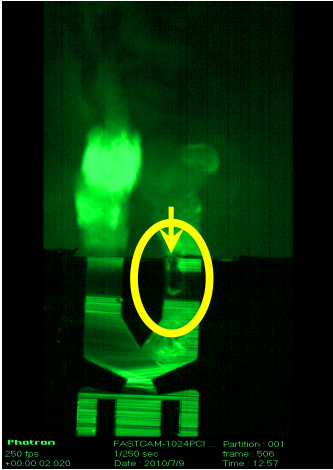


Figure 1.44: Fluidics oscillating water flow field accompanied with the suction resulted from the oscillation process at 144 l/h for- Fx4.

The fourth model demonstrates no jet interaction at any of the volume flows from 87-252 l/h as it gives two separate parallel jets as shown for example in the volume flow of 252 l/h (Fig. 1.45). The deflection period is lengthen and may depend on the changes in design features also as it takes around 8ms for 202 l/h and 4ms for 252 l/h. The jet pulsed at each limb but not fully fill the paths directly. It takes 92ms at 202 and 1060ms at 252 l/h to fill the whole outlets while it gives the oscillation at the named periods. As cleared in Fig. 1.45, which represents four selected pictures to clarify the oscillation process, the higher vortices at the corner are in the passive side and may have an effect on the suction of fluid at its side.

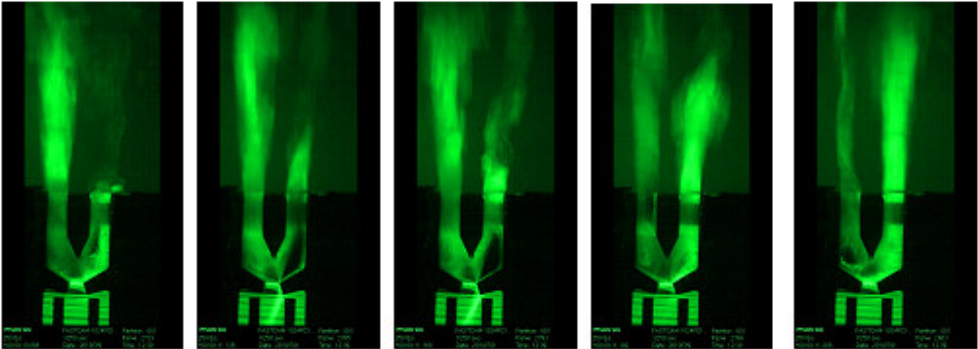


Figure 1.45: Fluidics oscillating water flow field at 252 l/h for- Fx4.

PIV flow field in the fluidic oscillator

The study of the fluidic oscillator is performed in the water test rig as shown in Fig. 8. The PIV technique is used to measure the flowfield inside and outside the fluidics device. The hydrophone is then used to measure pressure fluctuations. PIV data of flow field was phase-averaged on reconstruction using proper orthogonal decomposition (POD) in order to find out the differences between the four designs or the different volume flows in the same fluidics model. The aim of this part is to define the internal jet characteristics through flow visualization by PIV technique. The CCD camera imaged the flowfield and exports that to the PIV processing system then after the image processing to the POD Matlab scripts to find the phase-averaged of the flow pattern. The camera is equipped with a Sigma optic with a focal lens 105mm to cover the whole flow field for good investigation of the flow field and increasing the spatial resolution.

As shown in Fig. 1.46 and 1.47, the velocity field is averaged in six phase angles of oscillation in between. The average is based approximately on 500 recorded images. First, the flow enters the fluidics and crosses the power nozzle at zero phase angle and the jet is starting to exit outside the oscillator. As known, the internal design of the fluidics has a big influence on both jet outlets oscillation asymmetry (Guyot 2008). As the Coanda effect is the tendency of a fluid jet to be attracted to a nearby wall surface, the jet emerges from the power nozzle crosses the narrow inlet of the oscillating chamber into the large space, entrains fluid molecules from both sides, and tends to be attracted to a nearby angled surface on the sides of inlet port of the interacting chamber as at $\alpha = 0^\circ$ (Giles 1977).

Because the nearby wall does not allow the surrounding fluid to be pulled inwards towards the jet (i.e. to be entrained), the jet moves towards the wall instead. The chamber at first contains less fluid for entrainment to the lower side of the jet than to the upper side because of the angle of the nearby surface as at $\alpha = 60^\circ$. Thereby, lower pressure area or a partial vacuum forms to the lower side of the jet and attracts the jet towards the angle surface upper left limb of the exit chamber orifice ($\alpha = 120^\circ$). Because of the outer jet deflection, the fluid tends to impinge onto the lower feedback port (channel 2) inlet, upstream of the control throat, transmitting the pressure rise back to the control port by the speed of sound through the second feedback passage (Nakayama 2005). As the flow impinges onto the upper angled side, and rotates on that side according to the Coanda effect, vortices are formed on that side of the oscillating chamber creating a low pressure zone and the jet implements to the upper limb (1) as noticed at $\alpha = 60^\circ$. These vortices are expanding from the chamber nearby inlet orifice lower side to the end inclined lower shoulder at the vertex

of the chamber in direction of the feedback port 2 ($\alpha= 120^\circ$). The vortices are withdrawn behind the flow with pressure rise until the lower side shoulder. As long as the supply of molecules remains constant, the low pressure area continues to attract the jet and forces it to flow closely to the angled surfaces. A bending is happened according the pressure rise reaching the control port 2 (see Fig. 1.1) and the flow stream opposed the direction of impinging to the upper angled surface of the chamber. At the moment of this inlet stream bending, the vortices vanish in the inlet of the feedback channel 2, tangent to the lower shoulder surface of the chamber as the flow starts to be pulled to the upper angled side inside the chamber, $\alpha= 180^\circ$. The previous sequence is repeated with the stream oscillation towards the lower side (Outlet 1) in order to form a complete cycle of oscillation. The flow transfer from the lower angled side to the upper one starts to create a low pressure vortices zone on the upper side of the oscillating chamber as shown at $\alpha= 180^\circ$. Size of these vortices increases as the fluid flows towards the control throat and the feedback flow goes to the upper channel (1) trying to trigger the continues inlet stream as $\alpha= 240^\circ$. The expansion of the upper side vortices increases by the pressure rise withdrawal in feedback channel (1) and the jet will start to implement again to the lower limb side $\alpha= 300^\circ$.

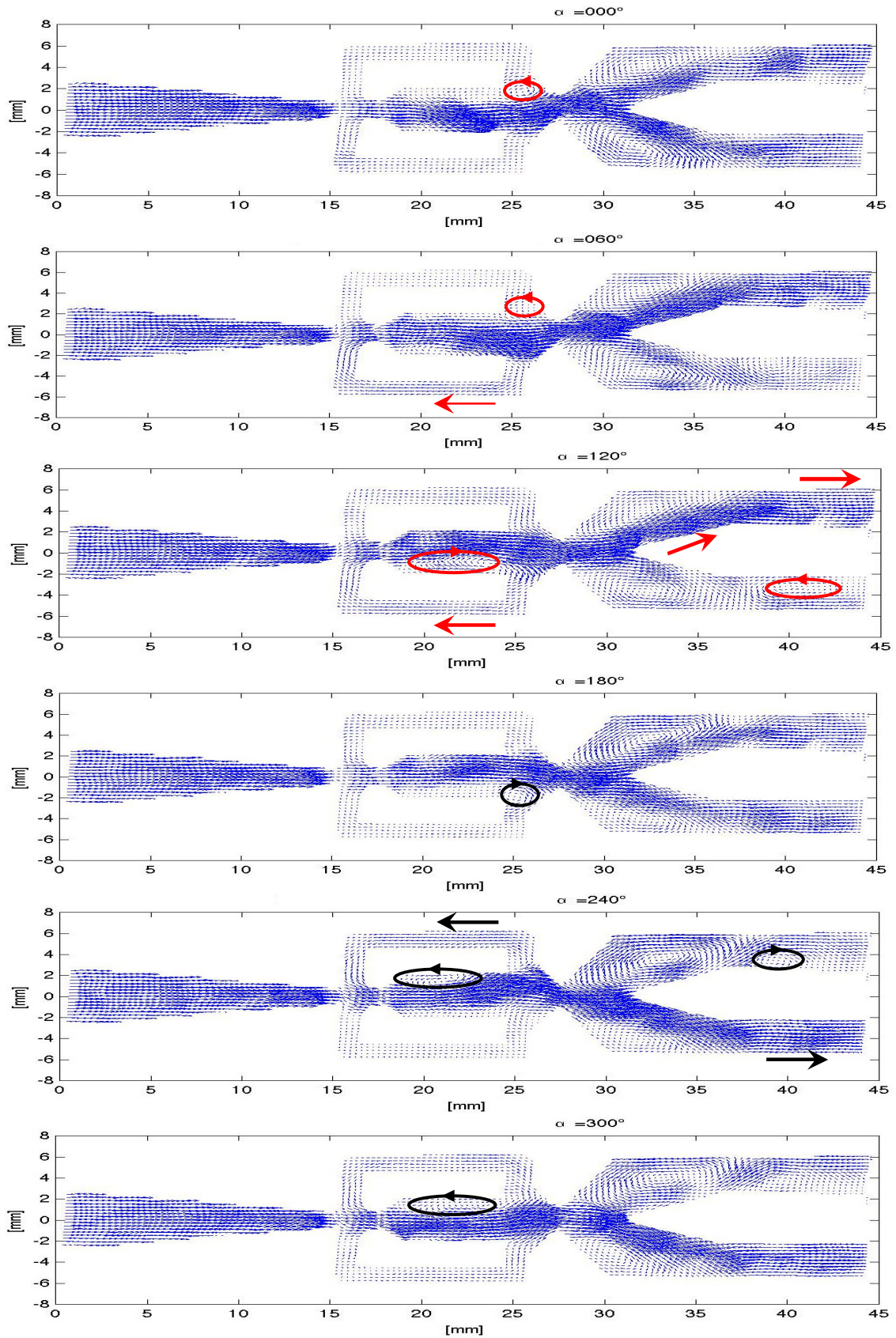


Figure 1.46: Fluidics oscillating velocity vectors field at different phase averaged and at a volume flow of 87 l/h for Fx1.

The vortex in the oscillating chamber exit region will thus cyclically alternate in velocity and direction of rotation to direct outflow through the output orifice such as to produce a cyclically repetitive side-to-side sweeping stream pattern (Bauer 1981). As the jet is directed to one outlet, the other exit expected to be free of fluid flow but this did not happen. Very less back flow (suction flow) is shown as the jet oscillated side-to-side in 16ms (as clarified from LIF measurements). At $\alpha= 120^\circ$ and at $\alpha= 300^\circ$ the suction is noticed at the lower and the upper limbs consecutively. An on-off oscillation like valve is considered at this case (Guyot 2008).

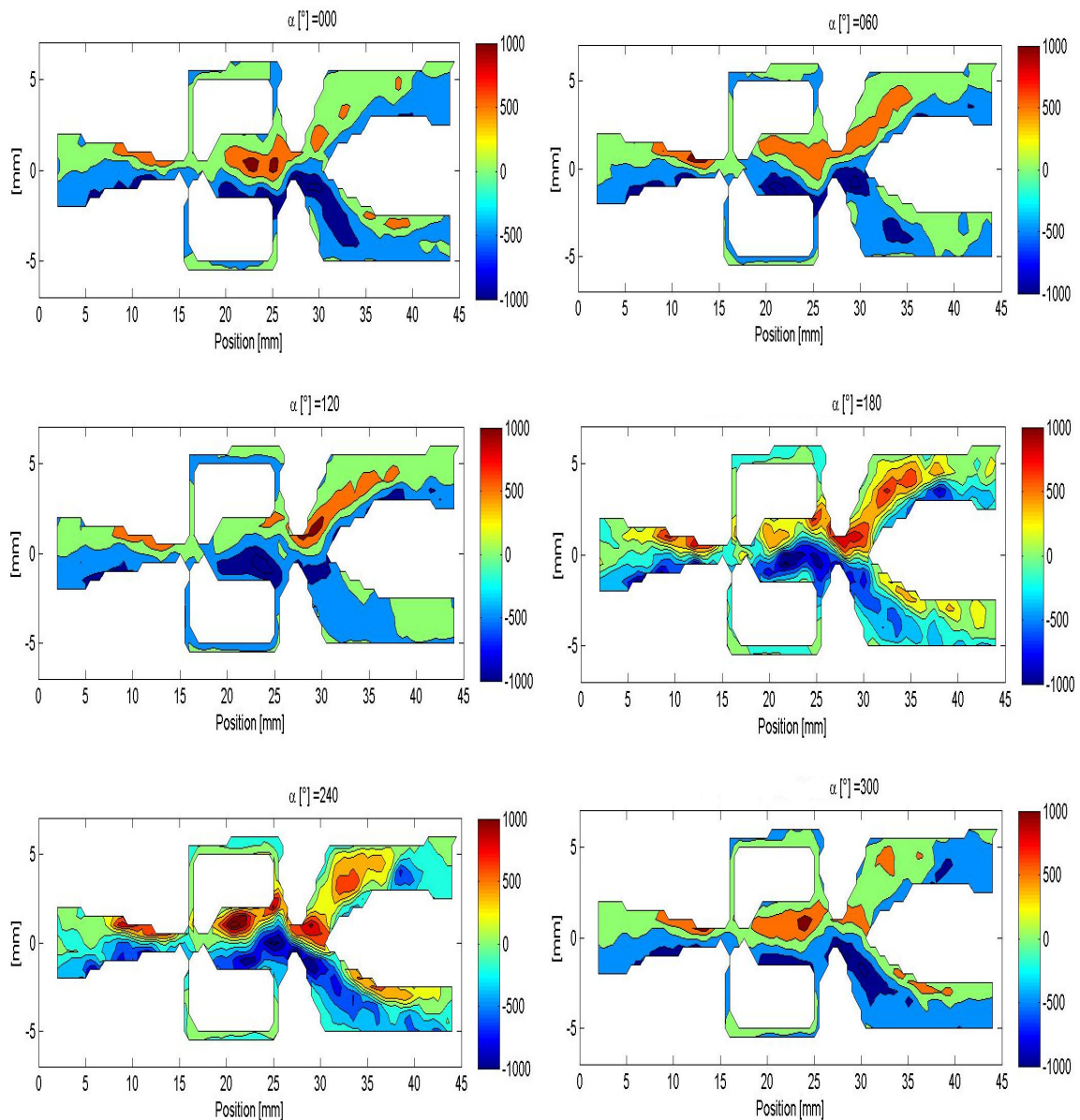


Figure 1.47: Contours of phase averaged vorticity (s^{-1}) at different phase angles and at a volume flow of 87 l/h for Fx1.

As also appears from Fig. 1.48- (left), the streamwise velocity of the flow inside the power nozzle is high and equals around 2.5- 3 times the jet exit velocity. The higher velocity zones are that of the dense vectors shown in Fig. 1.46. The radial velocity contour plots are exhibited in Fig. 1.48- (right). The contour plots have some missed parts during the image processing according to the higher reflection comes from the laser beam as the dimensions are very small (around 10mm between feedback channels) and these pictures are the best in water aquarium that can be captured.

The results offer a big similarity between Fx1 and Fx2 fluidics oscillators in velocity, vorticity, shear strain and normal strain. Comparison between the fluidic oscillators Fx1 and Fx3 is clarified by figures 1.49 to 1.54. PIV visualization data shows the internal fluid dynamics of the oscillator at 202 l/h water flow rate and an oscillation frequency of 41.35Hz. Phase average of 500 PIV images are conducted in step alpha of 60° . The change in the control throat angle and length gives some changes in the flow field in comparison between Fx1 and Fx3. As shown in Fig. 49, six selected images are clarifying the streamwise velocity contour plots and each image represents a successive phase delay of 60° within the oscillation cycle of 16ms. The color scale for the flowfield data inside the oscillator has been adjusted to enhance the contrast. The color scale ranges from -3 to 3m/s. Fx1, inside the channels after the power nozzle, gives a higher streamwise velocity than Fx3. Before the power nozzle, the streamwise velocity is almost similar at the whole averaged phases. At Fx1, the streamwise velocity is almost as equal as 3m/s always nearby each side of the interacting oscillating chamber exit. It is also equal to almost 3m/s at the exit jet working limb. Fx3 is lower in streamwise velocity than in Fx1 as it equals in maximum of 2m/s. The higher negative velocity is at the corners of the two limbs and in the feedback channels. Higher streamwise velocity values are almost at the centerline of the oscillator, at throat exit, and tangent to the angled rightward and leftward facing of the splitter as illustrated from Fig. 1.50. The contour shape inside the interacting chamber is not similar according to the changes in the exit features of the interacting chamber. Two high streamwise velocity regions are appearing in Fx1; one at 23mm and the other at 28mm as it in the normal jet path while one appears at 28mm from the fluidics inlet for Fx3. This may return to the increase in the throat length and the other features of the throat.

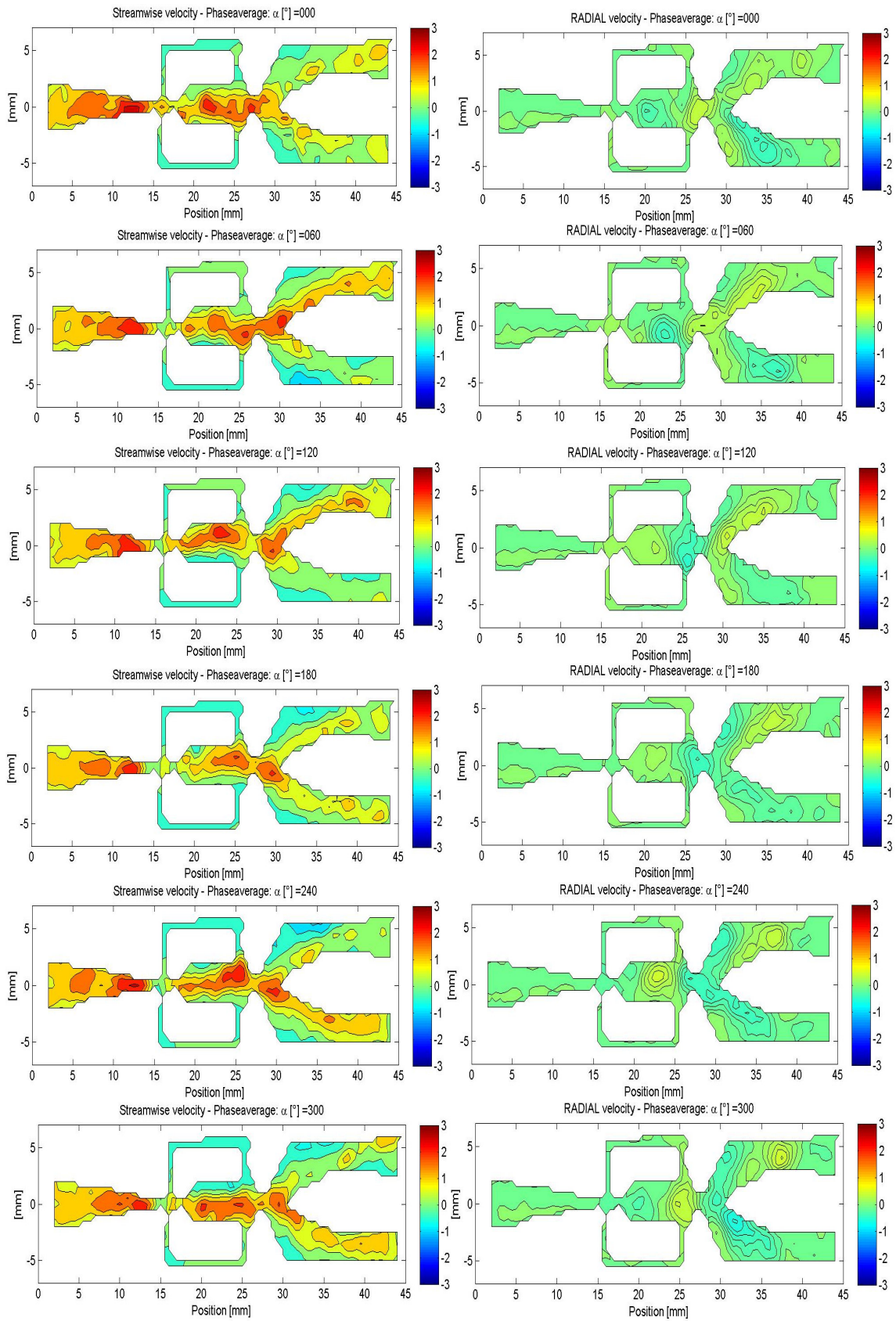


Figure 1.48: Contours of phase averaged streamwise (left) and radial (right) velocity components (m/s) at different phase angles and at a volume flow of 87 l/h for Fx1.

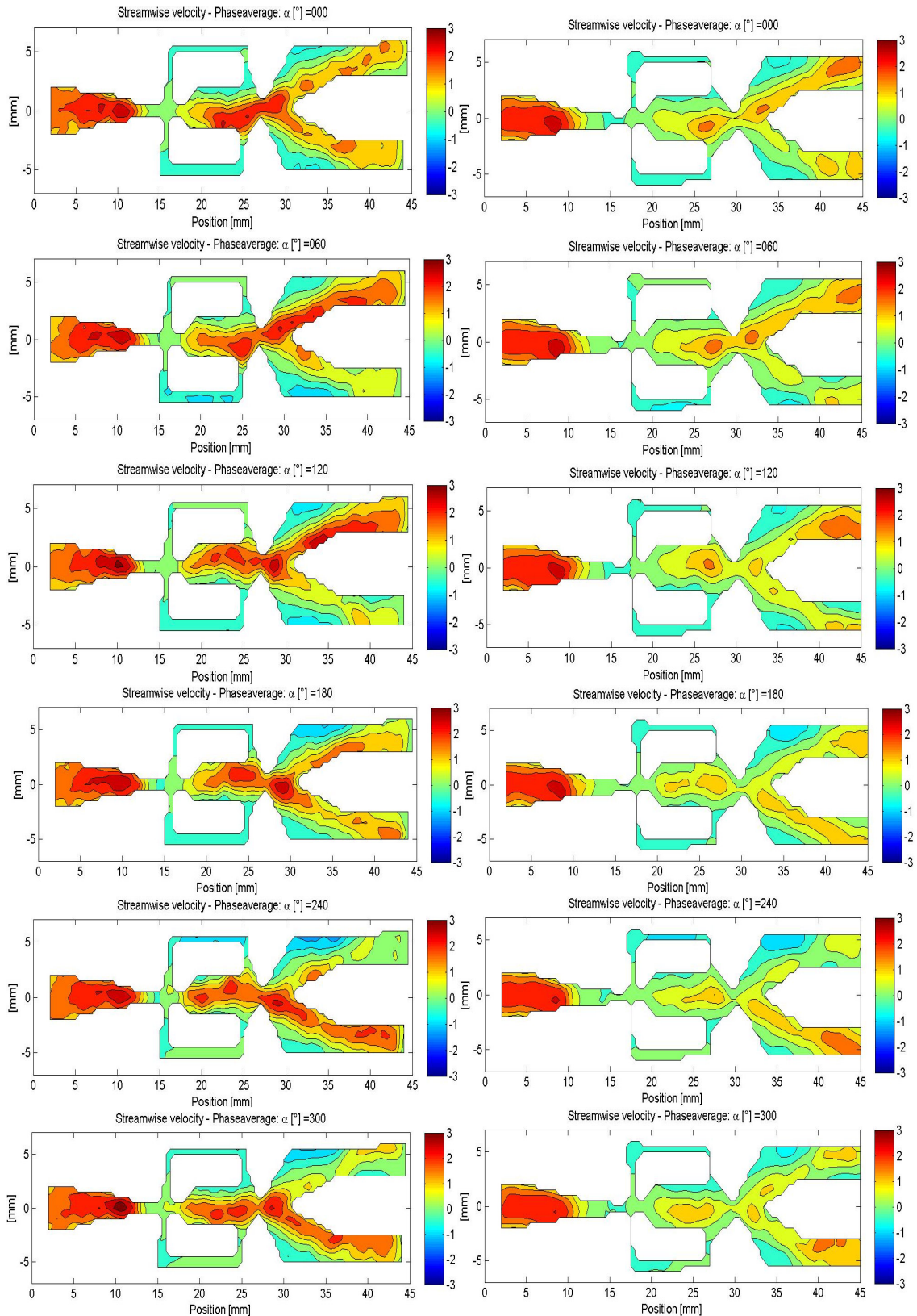


Figure 1.49: Contours of phase averaged streamwise velocity (m/s) components F_{x1} (left) and F_{x3} (right) at different phase angles and at a volume flow of 202 l/h.

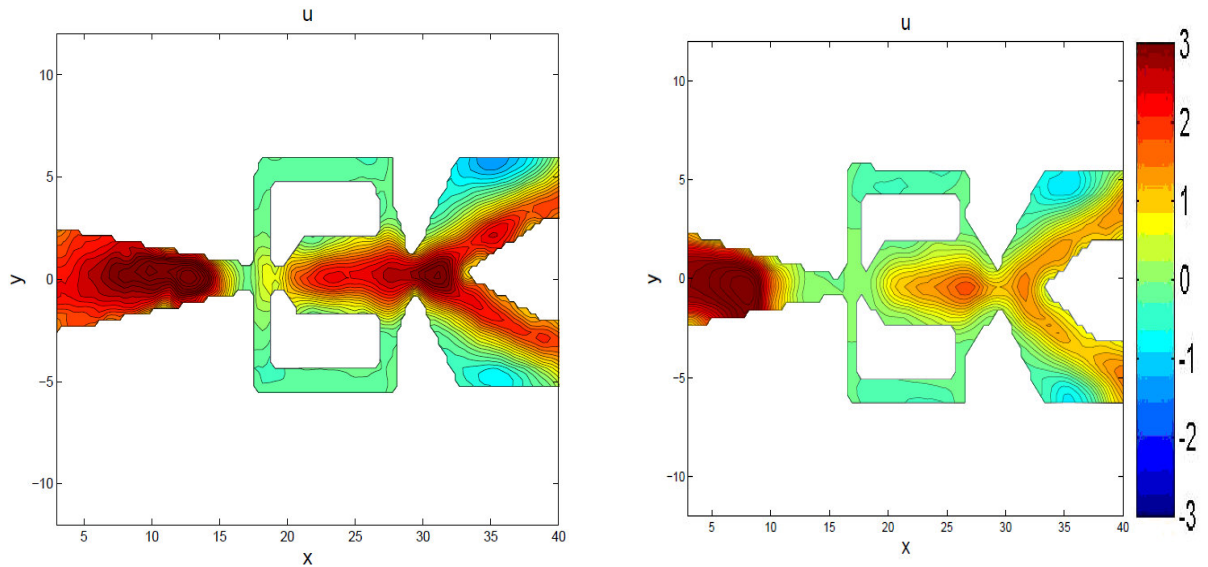


Figure 1.50: Contours of averaged streamwise velocity (m/s) components Fx1 (left) and Fx3 (right) at a volume flow of 202 l/h at average of 500 PIV images.

The average of 500 PIV images of the flow field outside the fluidic oscillator is processed. The streamwise velocity (Fig. 1.51) at exit is higher for Fx1 than Fx3. The maximum streamwise velocity value at Fx1 is almost 1.67 times the third model Fx3.

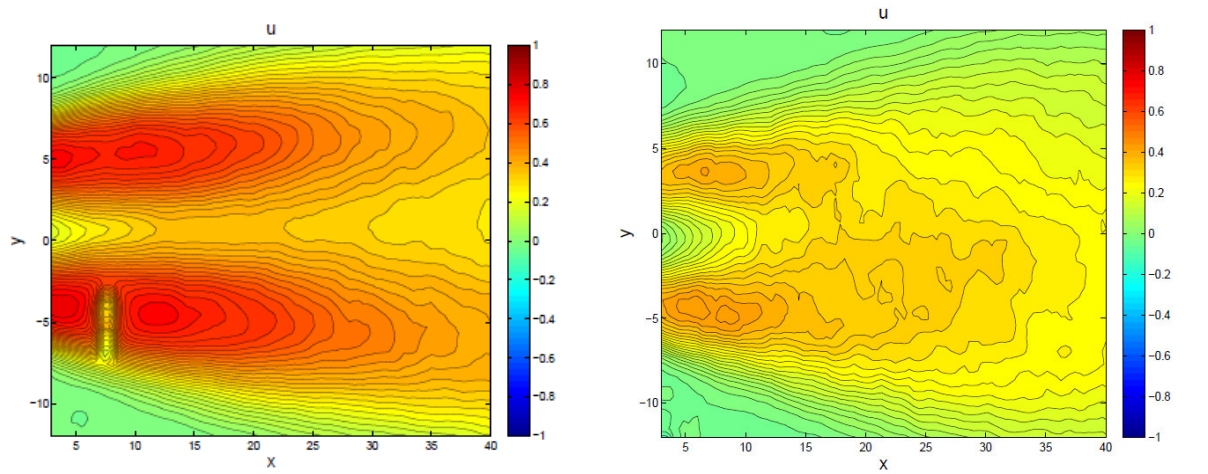


Figure 1.51: Contours of averaged streamwise velocity (m/s) components Fx1 (left) and Fx3 (right) at a volume flow of 202 l/h at average of 500 PIV images directly outside the Fluidics.

The radial velocity contour plots (Fig. 1.52) are the comparison between Fx1 and Fx3. The higher radial velocity values inside the two oscillators are also at the same locations of the maximum streamwise velocity.

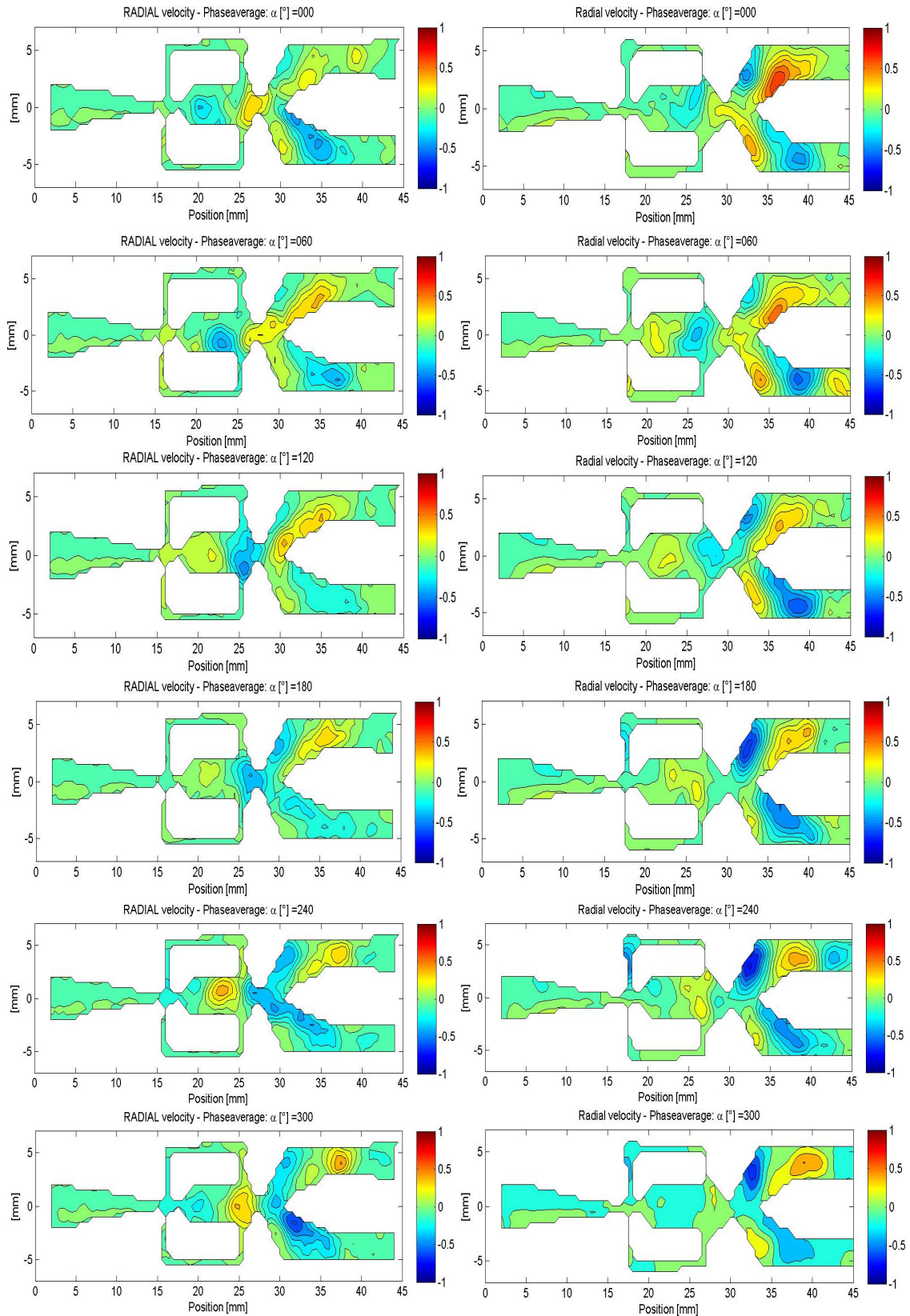


Figure 1.52: Contours of phase averaged radial velocity (m/s) components Fx1 (left) and Fx3 (right) at different phase angles and at a volume flow of 202 l/h.

The increase in the throat length changes the locations of the higher velocity values downstream the oscillator exit in case of Fx3. The maximum radial velocity values at the exit in water are not higher than 0.1m/s water as shown in Fig. 1.53.

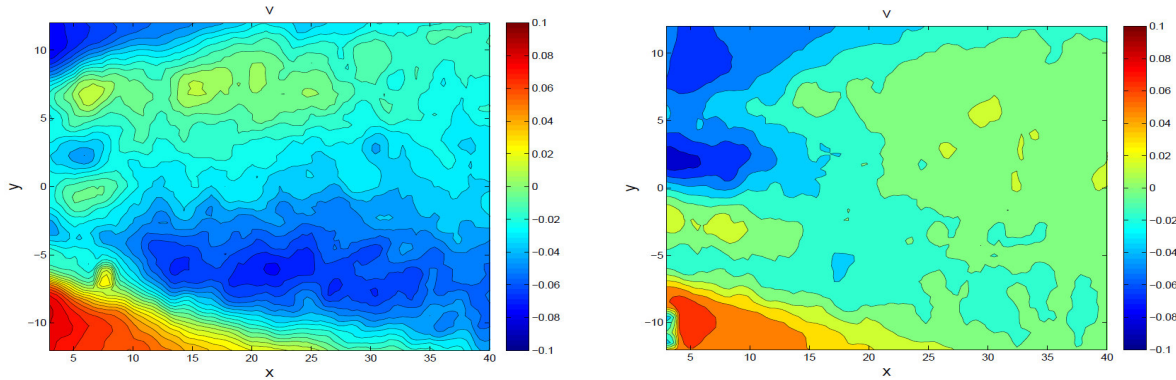


Figure 1.53: Contours of averaged radial velocity (m/s) components Fx1 (left) and Fx3 (right) at a volume flow of 202 l/h at average of 500 PIV images directly outside the Fluidics.

The vorticity results show two counter-rotating vortices within the interacting oscillating chamber as well as the ventilated flow to the two feedback channels drive the oscillations. The shape of the internal oscillating chamber controls the formation and oscillatory growth of counter-rotating vortex pairs, which drive oscillations (Gregory 2005) Fig. 1.55.

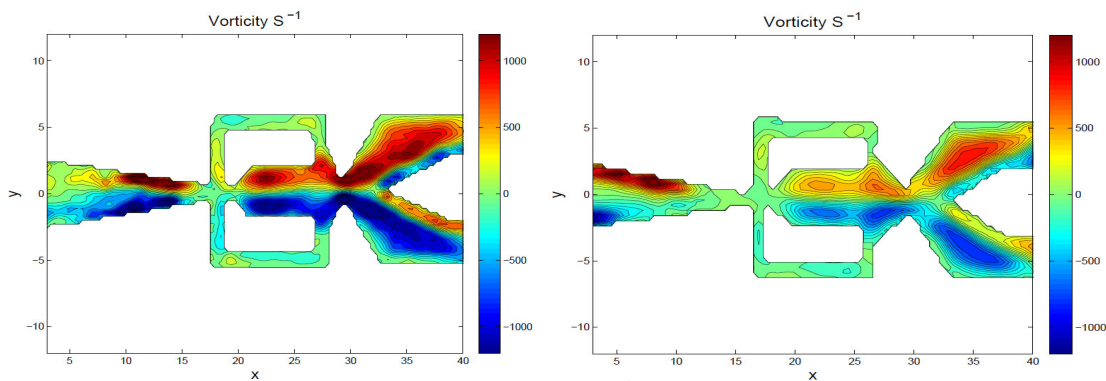


Figure 1.54: Contours of averaged vorticity (s⁻¹) components Fx1 (left) and Fx3 (right) at a volume flow of 202 l/h at average of 500 PIV images.

The higher vorticity values are noticed at Fx1 than Fx3 as shown in Fig. 1.55 which exhibits the six phases in delay of 60° at 202 l/h. Well mixing is performed to the fluid issuing jets from the oscillator because of the interaction and the oscillation inside the chamber. Also the feedback effect contributes to the well mixing in the oscillator. This mixing characteristic highlights the use of the fluidic oscillator for fluid mixing applications as well as the use in the targeting work for NO_x reduction at stable reacting flow conditions.

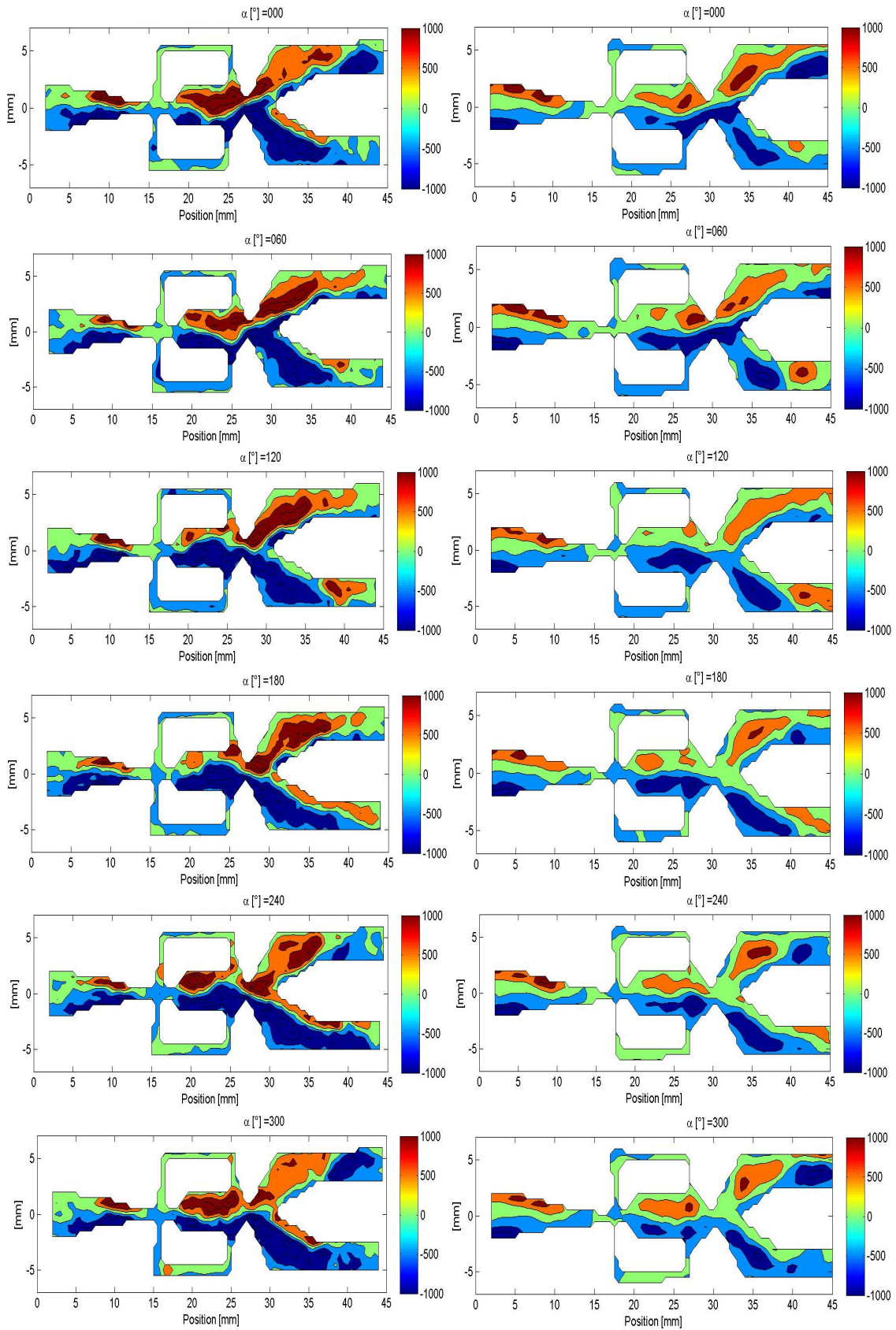


Figure 1.55: Contours of phase averaged vorticity (s^{-1}) Fx1 (left) and Fx3 (right) at different phase angles and at a volume flow of 202 l/h.

The vorticity of the issuing jet flow at the vicinity of the oscillator outlet (Fig. 1.56) gives in maximum of around one third of the vorticity inside the fluidics channels. Fx1 is higher of course in vorticity values than Fx3 outside the oscillator body which may be a good sign to achieve the stability better than Fx3. The maximum values are near the oscillator exit and vanish downstream of the fluidics in direction of the flow. Vorticity zones are in the jet interaction zone and at outside the jets in the interface zone between the pulsated fluid flow from the two jets and between each jet and the stagnant fluid on the shear layer zone. The maximum vorticity values are almost $\pm 300\text{s}^{-1}$.

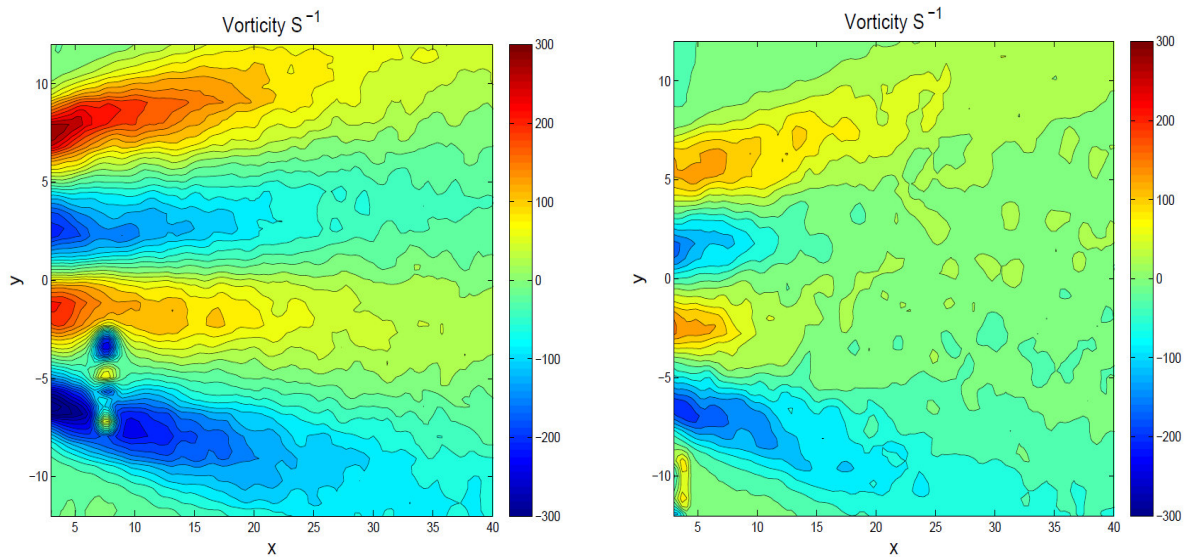


Figure 1.56: Contours of averaged vorticity (s^{-1}) Fx1 (left) and Fx3 (right) at a volume flow of 202 l/h at average of 500 PIV images directly outside the Fluidics.

As demonstrated in Figs. 1.56 and 1.57- left, the location of positive vorticity values is that one of negative shear strain according to the next two equations for the shear strain γ_{xy} and the

vorticity η relations. As the effect of $\frac{\partial u}{\partial x}$ dominates that of $\frac{\partial v}{\partial x}$, then there is opposition in sign of vorticity and shear strain.

$$\gamma_{xy} = \frac{\partial v}{\partial x} + \frac{\partial u}{\partial y}$$

$$\eta = \frac{\partial v}{\partial x} - \frac{\partial u}{\partial y}$$

While: u is the streamwise velocity and v is the radial velocity.

The maximum and minimum shear strain rates are almost $\pm 300\text{s}^{-1}$. The turbulence intensity values are greater than 100%. This can happen when the average exit speed is small and there are large fluctuations present as well as the fluctuations from the feedback channels (Airflow Instruments 2008). The location is at the area tangent to the two jets and in-between jet interaction zone as shown in Fig. 1.57- right.

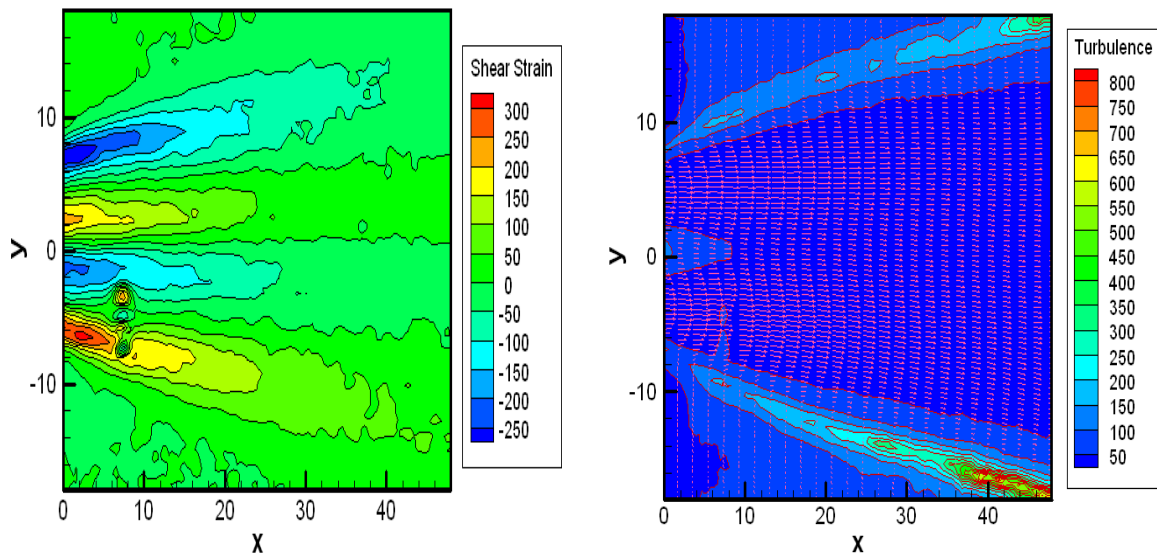


Figure 1.57: Contours of averaged shear strain (s^{-1}) (left) and turbulence intensity with velocity vectors at exit of Fx1 (right) at a volume flow of 202 l/h (average of 500 PIV images) directly outside the Fluidics.

The higher turbulent zones are at some locations inside the fluidics channels as in Fig. 1.58 which represents an average of 500 PIV images. These locations are in the inlet of the power nozzle, the interacting chambers angled inlet corners between the angled surfaces and the straight wall attachment walls, the inlet area to the feedback channels, and both corners at the exit path after control throat orifice. These locations are common for both fluidic oscillators Fx1 and Fx3.

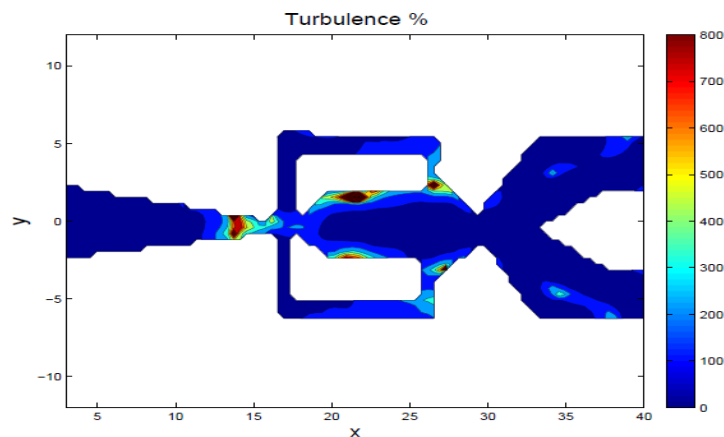


Figure 1.58: Contour plot of averaged turbulence intensity for Fx3 at a volume flow of 202 l/h at average of 500 PIV images.

For the last model Fx4, the fluid issuing jets from the oscillator are pulsated but asymmetric or not fully uniform distributed outside the two outlets as shown in Fig. 1.59.

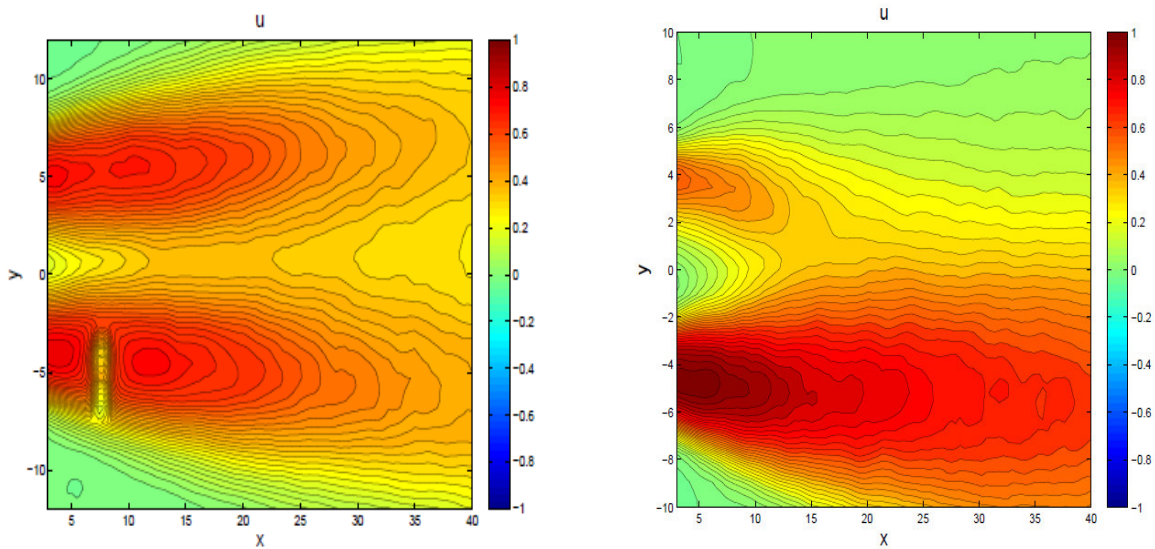


Figure 1.59: Contours of averaged streamwise velocity (m/s) components Fx1 (left) and Fx4 (right) at a volume flow of 202 l/h at average of 500 PIV images directly outside the Fluidics.

The oscillation period between limbs is at almost 8ms while the jet pulsated at each limb but the fluid is not fully fill the jet paths directly as it takes 92ms at volume flow of 202 l/h. As shown in Fig. 1.60, unlike the previous three models, the vorticity is destroyed or almost not found before the inlet of the feedback channels. Suction of fluid is increased in comparison to the last three design models at this model as shown in $\alpha = 240^\circ$ at the upper limb.

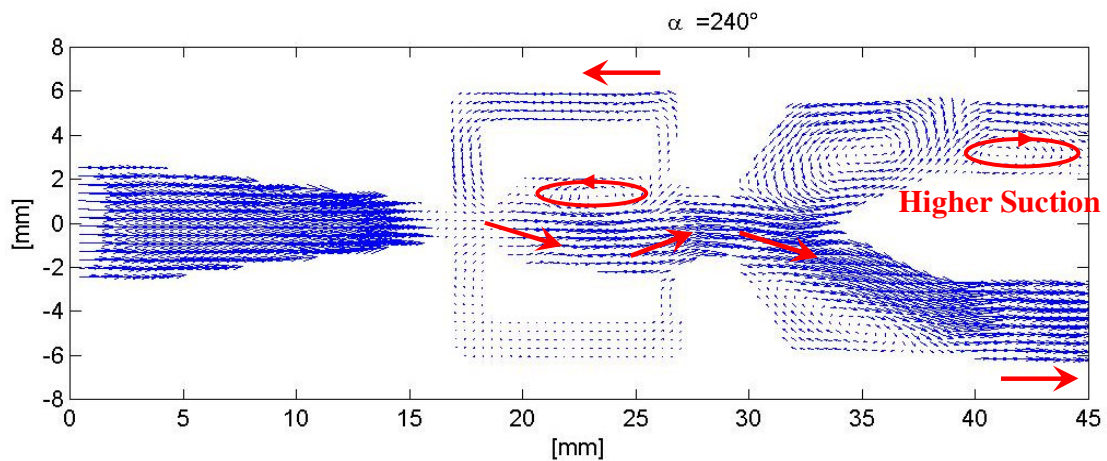


Figure 1.60: Fluidics oscillating velocity vectors field at 240° phase angle and at 202 l/h for Fx4.

The location of the two counter vortices at the inlet of the feedback channels is moved downstream to the control throat inlet. Fig. 1.61 exhibits these locations and demonstrates higher vortices at the first model.

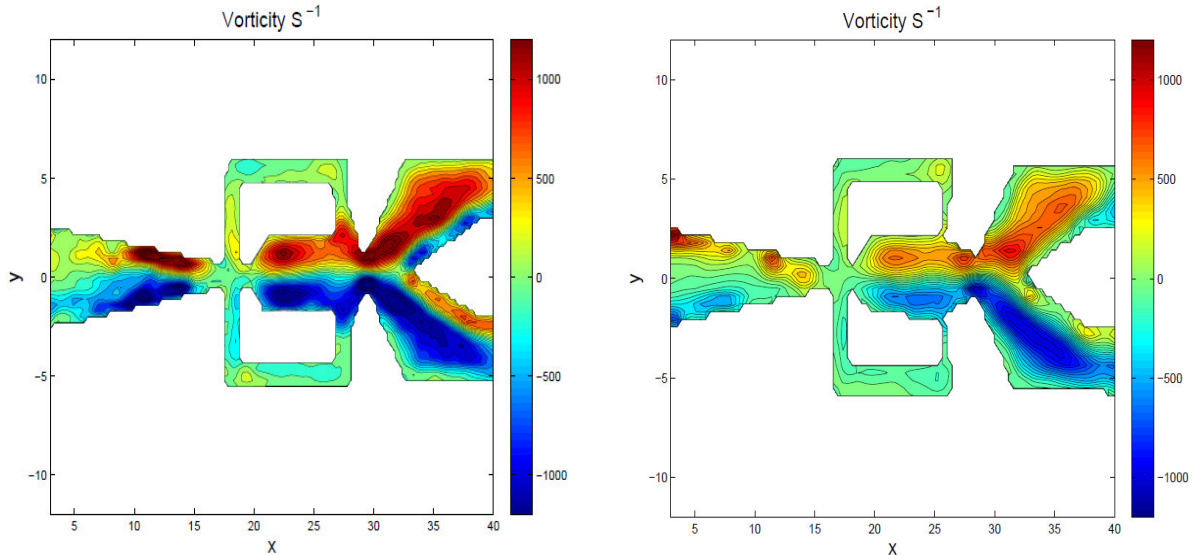


Figure 1.61: Fluidics oscillating averaged vorticity (s^{-1}) Fx1 (left) and Fx4 (right) at 202 l/h and at average of 500 PIV images.

From the last investigations to these four models, Fx1 is considered the best and recommended to be tested. The frequencies are almost in being regarded stability range in the combustion application. Fx2 and Fx3 are also good in use at a certain or a specified operating range. Fx4 needs some tests or changes in the throat area to adjust the operation of oscillation.

Inside a swirl stabilized burner in a water tunnel, Fx1 is investigated to clarify the flow field interaction between the burner and the oscillator. Followed by these investigations, the fluidic oscillator is tested inside the combustion chamber to see how it helps in NO_x and CO reduction at stable conditions by transferring some of the main air or fuel or both inside the fluidic oscillator lance.

Chapter (5)

PIV flow field and influence of a fluidic pilot on combustion in a swirl stabilized burner with the inserted fluidic oscillator inside.

Chapter (5)

PIV flow field and influence of a fluidic pilot on combustion in a swirl stabilized burner with the inserted fluidic oscillator inside.

The water tunnel (3000x 440x 440mm) used for the investigations is exhibited at Fig. 1.9. As explained before, the tunnel is equipped with PIV technique for visualization of flow field and hydrophone system for detection of pressure oscillations inside the water regimes of the flow field to be investigated. Three axial locations inside the swirl stabilized burner are tested; the burner bottom, the middle location and at the burner dump plane. The fluidic oscillator has the ability to move up and down inside the burner from the bottom to the top. The camera is mounted at first to capture the images of the flow field axially downstream of the burner perpendicular to the glass side of the tunnel as in Fig. 1.9- A and then mounted upper the tunnel to capture the images of the flow field azimuthally as in Fig. 1.9- B. The hydrophone is mounted at the burner exit directly tangent to the dump plane while its sensor is adjacent to the flow field outer body for no resistance to the fluid flow.

The momentum ratio is constant between water and air for $Fx1$, so the water flow rates are selected to be equivalent to the values of air flow rates. The total water mass flow is $6.957\text{m}^3/\text{h}$. This is equivalent to the main air value in the combustion test. The mass flow of water transferring inside the fluidic injector is selected in maximum of 474 kg/h. This water transfer keeps the total or the overall amount of water to be constant at the whole work.

1- The fluidics at the burner bottom ($X_f=0$)

The injection of fluid inside the oscillator at this location suppresses the oscillations and destroys the dominant peak by injecting around 2.3 % of the main flow and more (see Fig. 1.62).

This proves that the fluidic oscillator under test ($Fx1$) is able to dominate the oscillations produced from the main flow that exits downstream of the burner. This considers an indicator of stabilizing the flame in combustion tests.

The corresponding frequency of the fluidics for the different pilot fuel ratios is as follows consecutively; at 0% (4.76 Hz), 2.3% (4.55 Hz), and 4.5% (4.57 Hz). The reduction ratio of the amplitude is almost 65% from the higher to the lower value by increasing the transferred fluid from 0% to 4.5%.

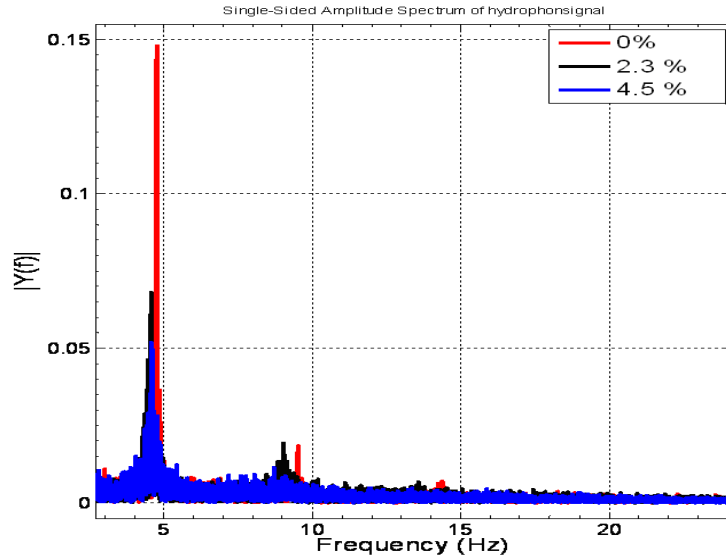
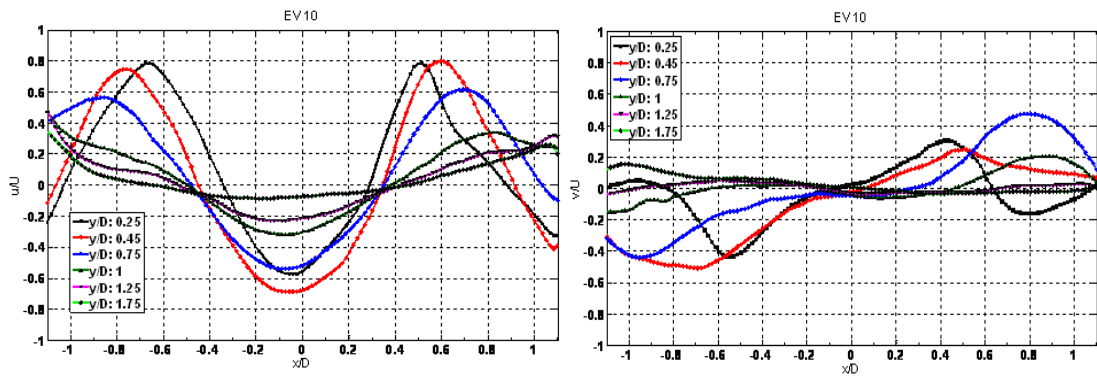


Figure 1.62: Single-sided amplitude spectrum at different fluidics water volume flows % and at burner exit (XF=0).

The changes in the flow field are investigated by the laser PIV technique. The whole velocity components are normalized to the mean bulk velocity at the base case which calculated at the equivalent flow of the main air in reacting flow. Figure 1.63 shows the velocity profiles comparison between the base line and 4.5% of the main fluid flow as a stable case and at different axial locations. The increase in the fluidics fluid flow reduces the maximum streamwise velocity outside the burner at the location of the two lobes and increases the streamwise velocity at the centerline. The reduction ratio is about 9.4% of the maximum streamwise velocity lobes at no injection conditions or the base line at $y/D = 0.25$, 13.6% at $y/D = 0.45$, and 12.6% at $y/D = 0.75$. The increase of the central velocity is about 11% from the base line at $y/D = 0.25$, 15% at $y/D = 0.45$, and 14% at $y/D = 0.75$. The reduction in the maximum radial velocity at y/D of 0.25 is 0%, 13.3% at $y/D = 0.45$, and 20.3% at $y/D = 0.75$ of the maximum one at the base line.

0 %



4.5 %

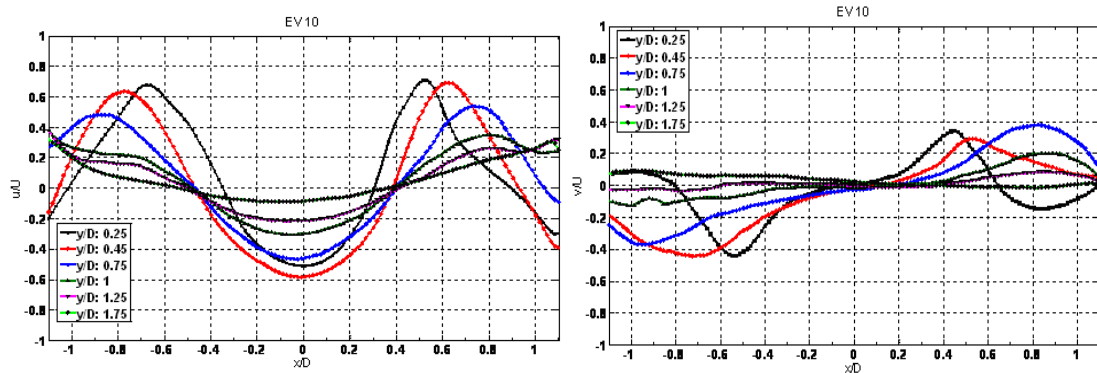
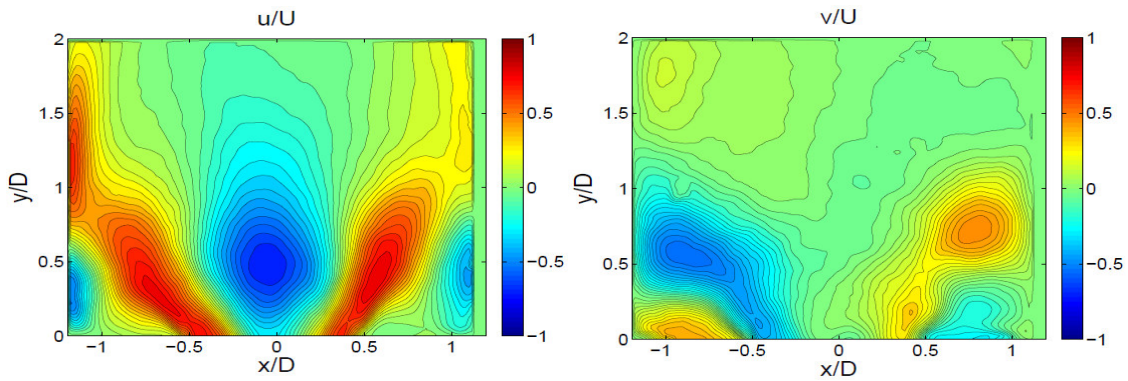


Figure 1.63: velocity profiles comparison between the base line and 4.5% of the main water flow as a stable case at different axial locations (XF=0).

0 %



4.5 %

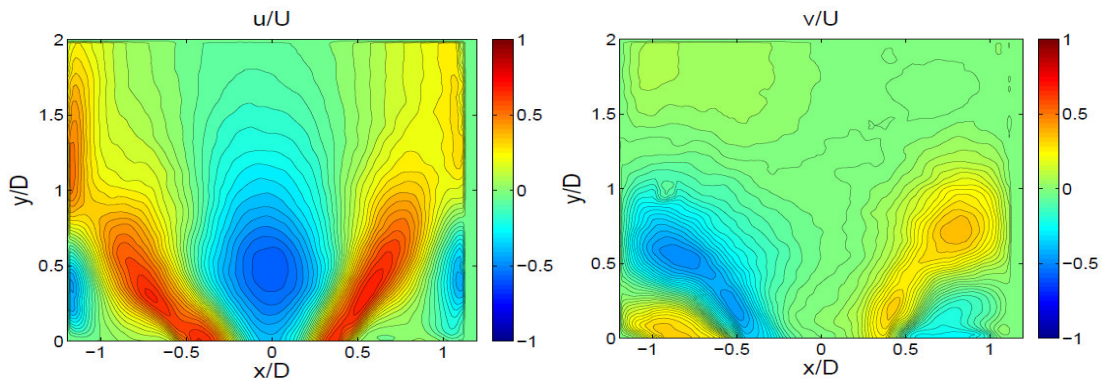
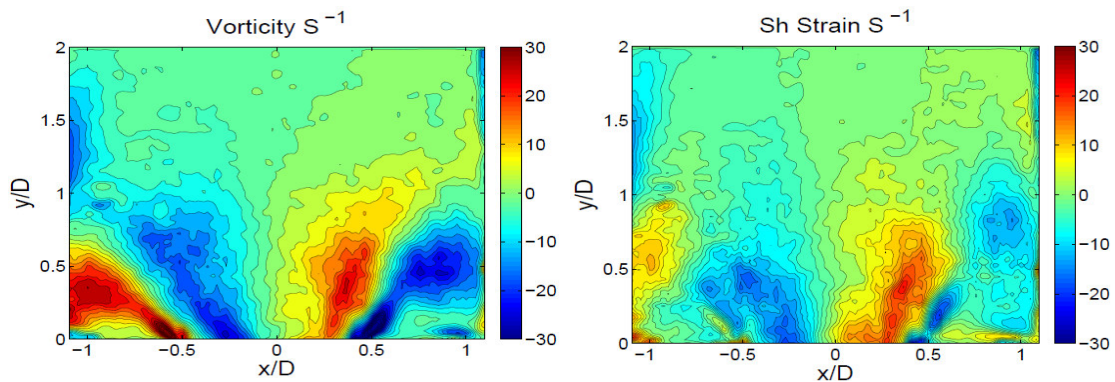


Figure 1.64: Streamwise (left) and radial velocity (right) contour plots at fluidics water mass flows of 0% (up) and 4.5% (down) of the main water mass flow (XF=0).

The interaction between the central jet flow and the main flow is responsible for these changes in the velocities. The changes are also presented in the contour plots of velocity in Fig. 1.64. The figure offers a window of flow field with the height of two times the burner diameter which is enough to cover the whole area of interest. The streamwise velocity reduction at the flow wings is noticed from the color plots while the central velocity increase is also represented by the change of color from dark blue to light blue. The changes in radial velocity are revealed in the right side color plots. Marginal changes are noticed in Fig. 1.65 for the vorticity and the shear strain rate by transfer of water from base case to 4.5% of the main flow.

0 %



4.5 %

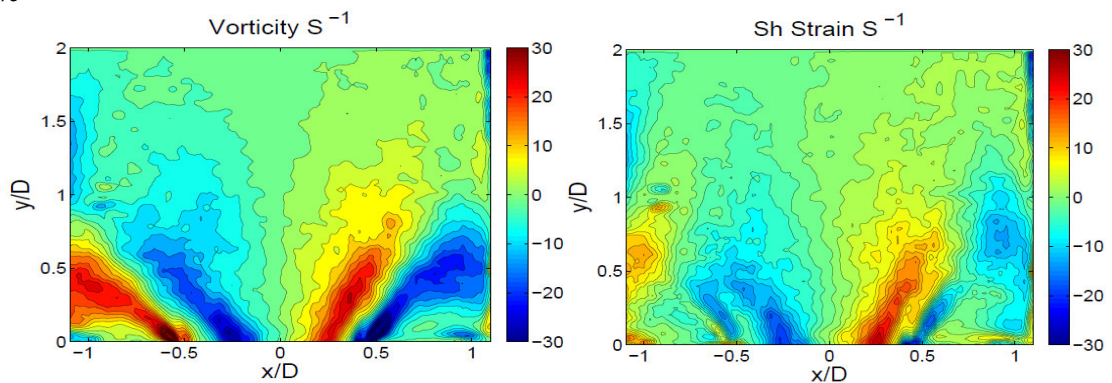


Figure 1.65: Vorticity and shear strain contour plots at fluidics water mass flows of 0% (up) and 4.5% (down) of the main water mass flow (XF=0).

The combustion test is performed at the combustion laboratory in the institute of fluid mechanics and technical acoustics- TU Berlin. The gas analyzer is used to analyze the emissions exhausted from the combustor. The investigation is focused on the nitrogen oxides and carbon oxides. The emission data are based on 15% O₂. Some fluid transferring is done to the flow from the main channels and orifices to the fluidic oscillator trying to enhance the combustion performance at the same equivalence ratio during the study between transfer and no transfer case. According to the measurements plan, the effect of the equivalence ratio is studied at first for the whole movement locations inside the burner from the bottom to its top. Fuel transfer inside the fluidics at constant

main air and at constant equivalence ratio of 0.552 is done to demonstrate the effect of this fuel transfer on the emissions and temperature at stable conditions. Air transfer inside the fluidic oscillator from the main line at constant main fuel and at constant equivalence ratio of 0.552 is also performed to clarify the air transfer only on the performance of the designed oscillator. Mixing of air and fuel transfer is done also to study this effect on the oscillator performance at constant equivalence ratio of 0.552. Air transfer inside the fluidics at constant main premix fuel but at equivalence ratio of 0.575 is done. The last test is by air transfer inside the oscillator at constant equivalence ratio (0.575) in addition to the transfer of some fuel together to see the influence of that on the fluidics performance. OH camera is used to capture around 300 images for each measurement point in order to find the average of these pictures to show the chemiluminescence emitted from the flame in the way to understand the flame physics.

A- Effect equivalence ratio at constant air mass flow rate.

Despite some inevitable fluctuations in equivalence ratio, velocity, pressure and temperature, the flame should neither flash-back nor blow-off in steady state combustion in the tested swirl stabilized burner as the possibility of flash-back downstream of an entry duct arises when there is premixing ahead of the combustion chamber. As shown in Fig. 1.66, the effect of equivalence ratio variation on NO_x emissions is revealed. The range of overall equivalence ratio was from 0.505 to 0.699 between the lean blow off and very noisy point.

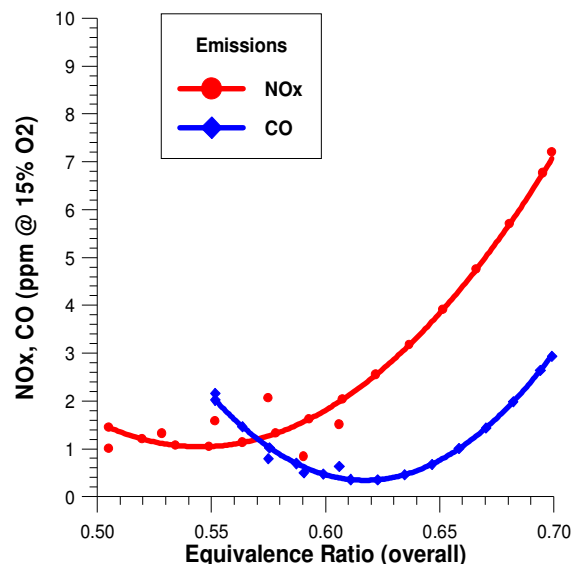


Figure 1.66: Effect of overall equivalence ratio at constant main air mass flow rate and at (XF=0).

According to the literature (Rankin 2007), the nitrogen oxides increase as the equivalence ratio increases near the stoichiometric value ($\phi=1$). The NO_x emissions increased to the maximum value at 0.699 of equivalence ratio. CO trend decreased up to $\phi = 0.62$ and then increased and then inclined. The NO_x emissions involve NO and NO₂. If the values of NO are higher than NO₂, this may return to intermediates produced during the combustion operation which may be an indication to the prompt nitrogen oxides.

The temperature also increased from 1200°C to 1551°C as the overall equivalence ratio increased from 0.505 to 0.699 in a linear relation. The temperature increased around 1.29 times as the equivalence ratio increased to 1.38 times as clarified in Fig. 1.67. Figure 1.66 and 1.67 show the relation between the NO_x emissions and the exhaust temperature. The NO_x emissions lower value is almost at around 1360°C in between 0.552 and 0.575 which will be our area of interest.

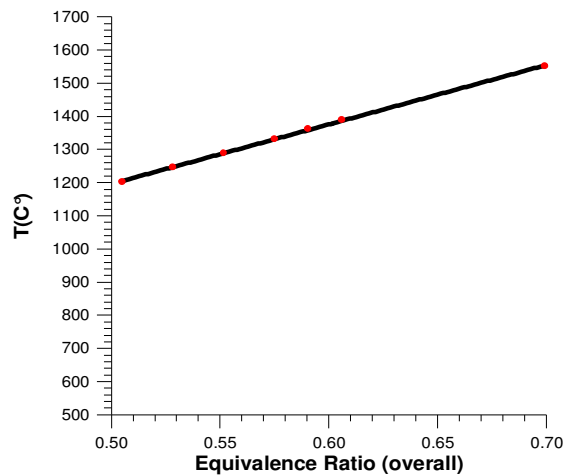


Figure 1.67: Effect of overall equivalence ratio on exhaust temperature ($\chi F=0$).

The selected range of operation is far from the lean blow off and also in the safe range of stability. As shown in Fig. 1.68, no peak value to the pressure oscillation at the range of operation.

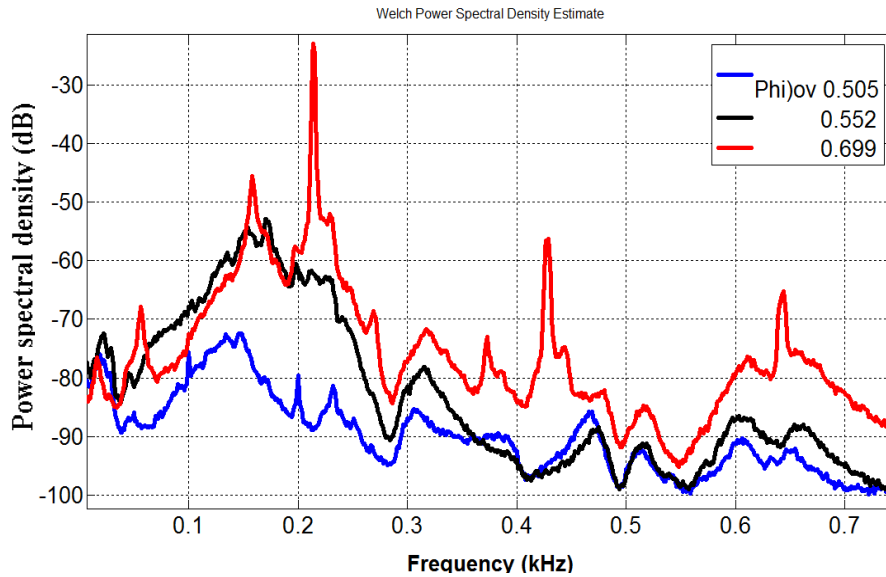
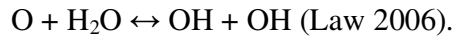
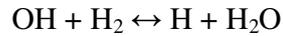
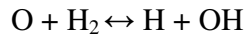


Figure 1.68: Power Spectral Density of microphone signal for different equivalence ratios ($\Phi=0$).

In gaseous fuels, representative components are hydrogen (H_2), carbon monoxide (CO), and the light hydrocarbons (HC). Hydrocarbons form the bulk of the fuel supply and the complete oxidation of a hydrocarbon are usually accompanied by a specified amount of heat release. Hydrocarbon fuel is rarely converted to products in one step as this conversion takes place through many stages of reaction, during which a variety of intermediates are produced. Some of these intermediates are radicals like H, O, and OH. These radicals are extremely reactive due to the presence of unpaired electrons, and in turns are short-lived during combustion. Hence, the reaction pathways are leading to fuel consumption, formation and destruction of intermediate species, and final product formation (Law 2006).

Some oxidation processes show visible chemiluminescences in reacting combustion conditions and the actual luminescence arises through recombination processes between atoms, radicals or ions and electrons inside the reaction phase. The typical prototype of these reactions is represented by the capture of an electron by a positive ion with the emission of a light quantum (Weiss 1938). An elementary reaction could be an important step in the oxidation of hydrogen and hydrocarbons as demonstrated in this equation of $H + HO_2 \rightarrow OH + OH$. Some hydrogen-oxygen chain reactions are also clarified as follows:



As proved by Tilury, electronically excited oxygen species give rise to most of the chemiluminescence (Tilury 1999). The existence of OH expresses the oxidation in the combustion reaction and accompanied by the chemiluminescences. For that the images captured from the OH chemiluminescence, camera system are effective to express, at least qualitatively, the heat release of the combustion reaction depending on the oxidation process.

OH- chemiluminescences images are shown in Fig. 1.69 for different overall equivalence ratios. It demonstrates the effect of ϕ overall on the flame in the form of heat release accompanied with the flame luminosity. The products of a chemical chemiluminescent reaction like combustion are delivered in an excited electronic state. Because the reaction is a chemically exothermic, it is accompanied with heat release and light. As the overall equivalence ratio increases, the heat release increases, and the chemiluminescences are higher especially at the flame shear layer (two balls of light) on the flame boundary.

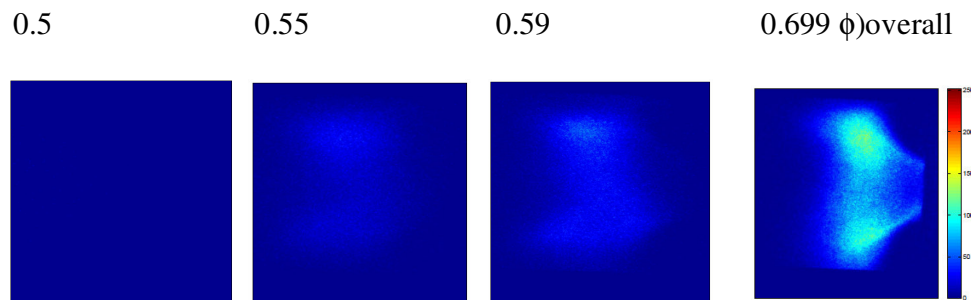


Figure 1.69: OH- chemiluminescence at different overall equivalence ratios ($\text{XF}=0$).

B- Fuel transfer inside the oscillator at constant main air and constant overall equivalence ratio (0.552)

At this part, the fuel is transferred inside the oscillator trying to study the flame performance at this transfer conditions and at a stable range of operation. As the fuel transfer increases from 0 to 42% of the main fuel, the value of normal equivalence ratio decreases from 0.552 to 0.318 at constant $\phi_{\text{overall}}=0.552$ and at constant main air mass flow. The value of NO_x increased up to 7ppm while CO decreased to around 0.36ppm and CO₂ equals almost 3.55% at the whole operating range of transfer. Figure 1.70 exhibits this result. Overall equivalence ratio is calculated depending on the main air and fuel while normal equivalence ratio is calculated from the fuel and air inside the fluidic oscillator.

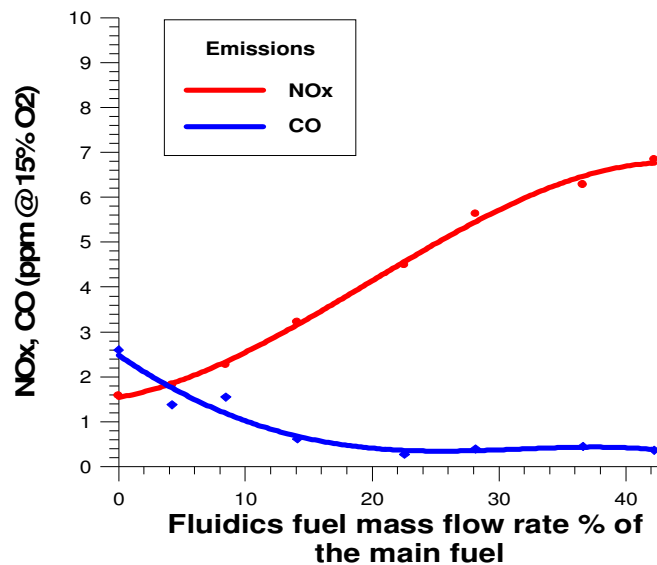


Figure 1.70: Influence of fuel transfer inside the fluidic oscillator on emissions at constant main air mass flow and at overall equivalence ratio = 0.552 (XF=0).

The temperature decreases to around 78% from its value at no transfer which may be an indication to not fully complete combustion case or an indication to prompt or fuel NO_x but not thermal NO_x. The temperature reduction is noticed until fuel transfer of 28% of the main fuel and after that it shows almost a constant value at the minimum temperature of 1000°C.

The higher the fuel percentage transfers, the higher chemiluminescence releases. Also, NO_x emissions increase to 6.84ppm at the maximum percentage of fuel transfer while CO decreases around 7 times of its value at no transfer. The flame shear layer is lighter than the flame centerbody (Fig. 1.71). A linear relationship between concentration of hydrogen oxides and

chemiluminescence intensity is noticed as demonstrated by Arnhold 1991. At these conditions, the fluidics works in stable conditions compared to the pilot injector using this fuel transfer.

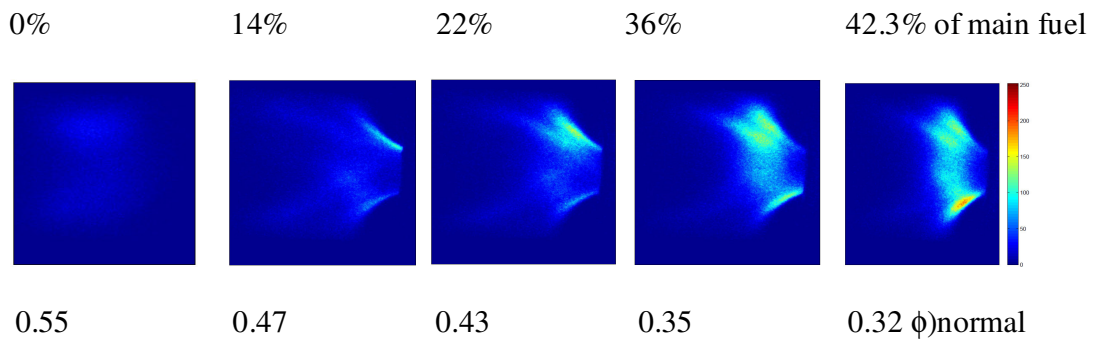


Figure 1.71: OH- chemiluminescence at different fuel transfers inside the oscillator by constancy of the main air mass flow and at overall equivalence ratio= 0.552 (XF=0).

C- Air transfer inside the fluidics at Constant main Fuel and at overall equivalence ratio = 0.552

The air transfer from 0% to 2.73% of the main air at constant main fuel and at constant overall equivalence ratio of 0.552 is performed at this part. The value of normal equivalence ratio increased in turns from 0.552 to 0.567 accordingly. CO reduces until 1.8 % of the main air and then increases after that at normal equivalence ratio of 0.56. The nitrogen oxides decrease by air transfer increase (Fig. 1.72).

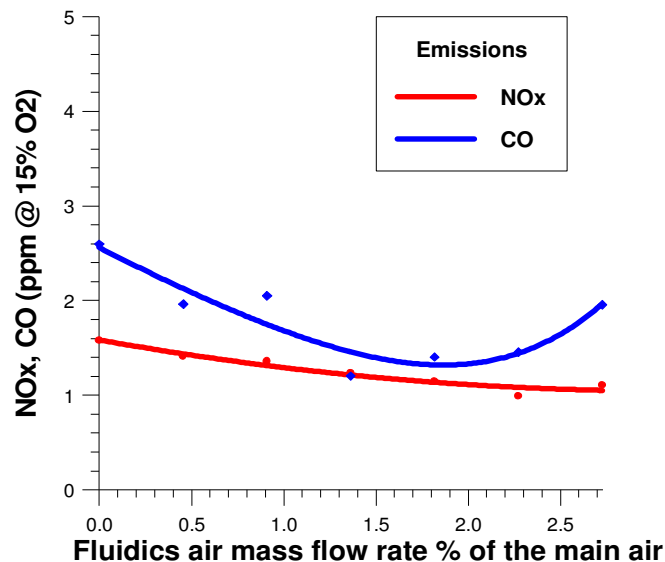


Figure 1.72: Influence of air transfer inside the fluidic oscillator on emissions at constant main fuel mass flow and at overall equivalence ratio = 0.552 (XF=0).

The OH camera records 300 images to see the OH chemiluminescences from no transfer to 2.73% of the main air as in Fig. 1.73. The emission of light in the form of chemiluminescence is dimming as the air transfer increases. The chemical combustion reaction is exothermic and generates the light depending on the excited intermediates which decay to lower energy levels to give luminous flame. The intermediates of NO are small as the ratio of NO₂ is higher at this case of transfer. The flame shape is similar to two fainted balls around the centerbody axis. From these results, this transfer offers a distinguished method for NO_x and CO suppression at stable combustion conditions.

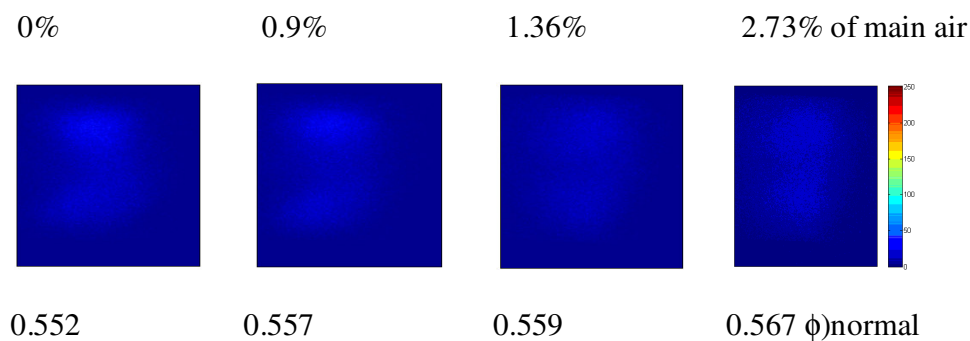


Figure 1.73: OH- chemiluminescence at different air transfers inside the oscillator by constancy of the main fuel mass flow and at overall equivalence ratio= 0.552 (XF=0).

D- Air transfer inside the fluidics at 14% pilot fuel ratio at overall equivalence ratio= 0.552

Creation of reverse flow regions near the jet nozzle (burner exit) has been exploited for swirl-stabilizing the flame. Rapid mixing and faster spreading of the oscillating jet fluid with its surrounding by swirling comes from the swirler in addition to the fluid oscillation generated from the fluidic oscillator enhance the chemical reaction in combustion applications (Liang 2005).

At this case fuel and air are transferred as mix from the main lines to inside the fluidics trying to reach the best conditions of low NO_x and low CO at stable combustion (see Fig. 1.74). The fuel transferred is constant at 14% of the main value besides the transferred air variation. The overall equivalence ratio is kept constant. The air transferred inside the fluidics is between 0% and 2.73% of the main air. Decline in NO_x curve is noticed and very low CO also produced. Unlike the fuel transfer only, the NO_x reduces to almost 30% of its value at the maximum air transfer (2.73%) by injecting 14% of the main fuel together with this air transfer. CO is almost constant at about 0.4ppm which is very low in comparison to the fuel transfer only as it was at 2.6ppm and reduced

by fuel transfer like that case. NO_x emissions reduce also by increase of air transfer similar to the air transfer without fuel and there is a merit in suppression of the higher CO to very small values.

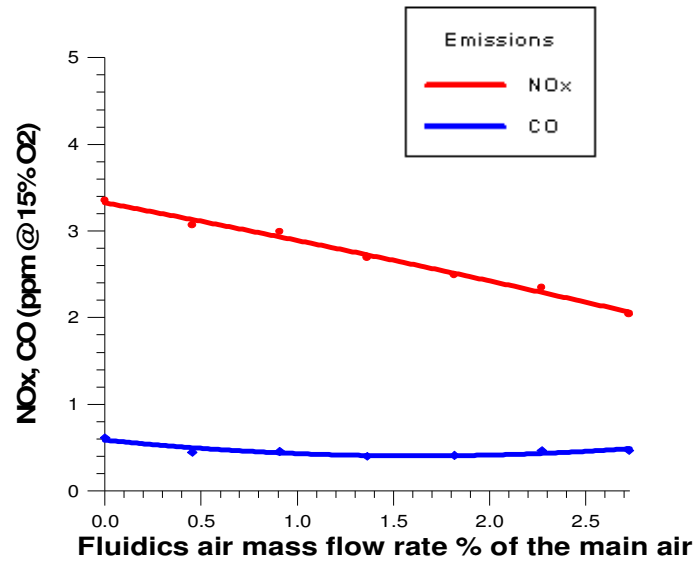


Figure 1.74: Effect of air transfer inside the fluidic oscillator on emissions at 14% pilot fuel ratio and at overall equivalence ratio= 0.552 (XF=0).

As shown in Fig. 1.75, the flame shape has longer cone at transfer of 14% of fuel only. The flame is luminous at the shield between the flame body and the external recirculation zone. Injection of air and fuel together dims the flame luminosity slightly as the air increases from 0% transfer to maximum one according the reduction in heat release.

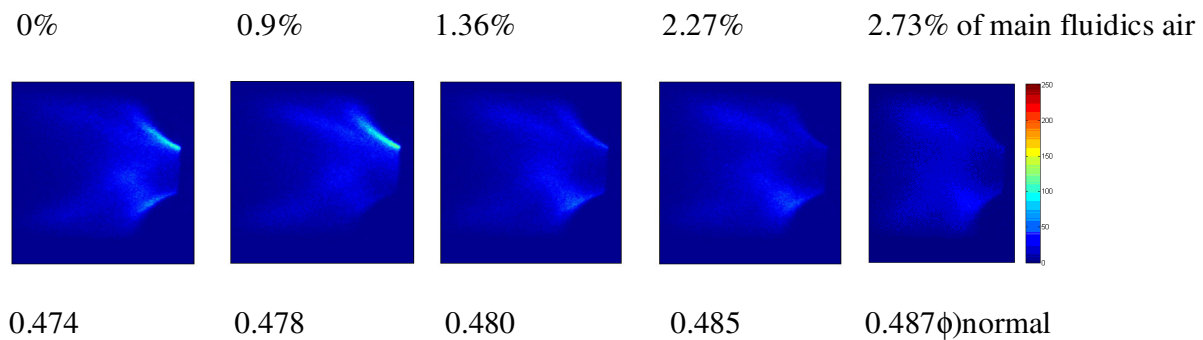


Figure 1.75: OH- chemiluminescence at different air transfer inside the fluidics plus 14% pilot fuel ratio and at overall equivalence ratio= 0.552 (XF=0).

E- Transfer of Air inside the fluidics at 28% and 42% pilot fuel ratio of the main fuel at overall equivalence ratio 0.552

In this case of transfer, the percentage of pilot fuel ratio increased from 14% gradually to double and triple times this value at the increase of the pilot air ratio inside the fluidics. The increase of the pilot fuel ratio to 28% of the main fuel at 0% pilot air ratio increased the NO_x emissions more than 60% of its value at 14% pilot air ratio as demonstrated from Figure 1.76 but still decreases with pilot fuel ratio increase. CO has marginal changes in comparison to the 14% pilot fuel ratio case.

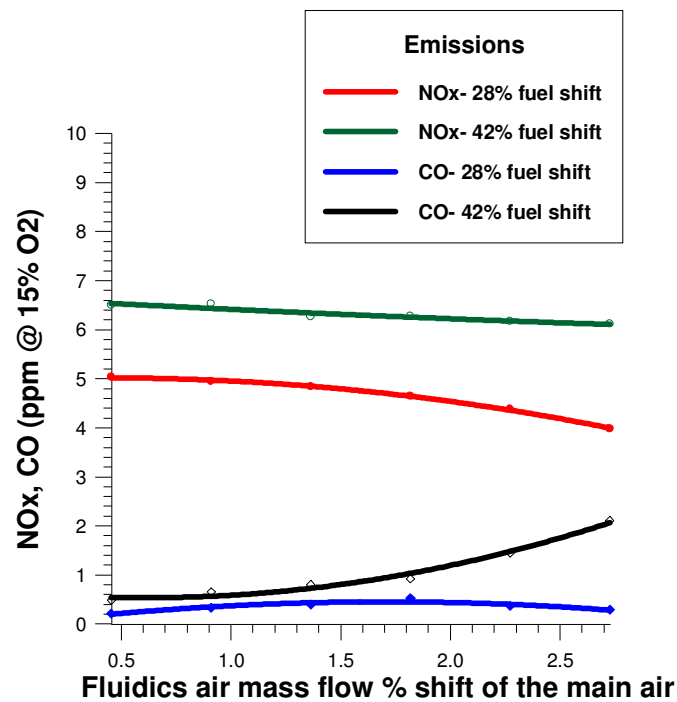


Figure 1.76: Effect of air transfer inside the fluidic oscillator on emissions at 28% and 42% pilot fuel ratio of the main fuel and at overall equivalence ratio= 0.552 (XF=0).

The increase of pilot fuel ratio to 42% of the main fuel raises the NO_x emissions to almost double the value at 14% fuel transfer. CO also rises gradually as the air transfer increases at 42% pilot fuel ratio.

The average of 300 chemiluminescence images is represented in Fig. 1.77 for 28% pilot fuel ratio. The flame represents a tree shape. As the air pilot air ratio increases, the NO_x emissions decrease and the flame luminosity decreases due to the heat release reduction.

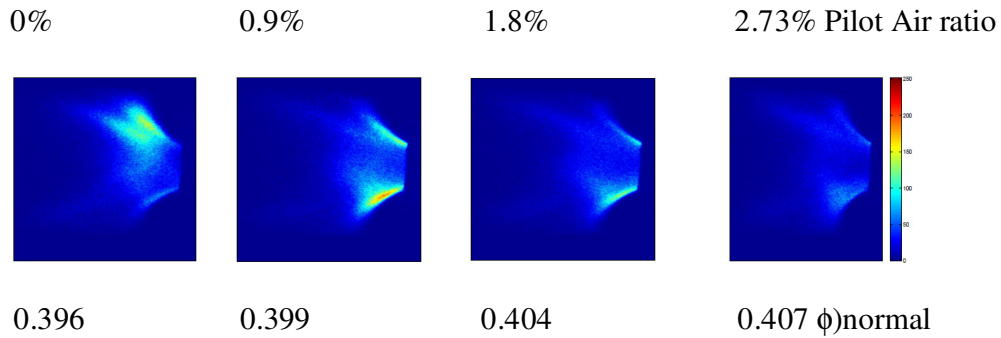


Figure 1.77: OH- chemiluminescence at different pilot air ratios inside the fluidics plus 28% pilot fuel ratio of the main fuel and at overall equivalence ratio= 0.552 (XF=0).

The higher the pilot fuel ratio goes, the lighter the flame is as in images of chemiluminescence which are shown in Fig. 1.78. As before the pilot air ratio up to 2.73% increase dims the light comes from chemiluminescence but not too much like 0% pilot fuel ratio. The raising of pilot air ratio destroys the continuity and the cohesion of chemiluminescences all over the flame and diminishes the chemiluminescences at the flame centerline.

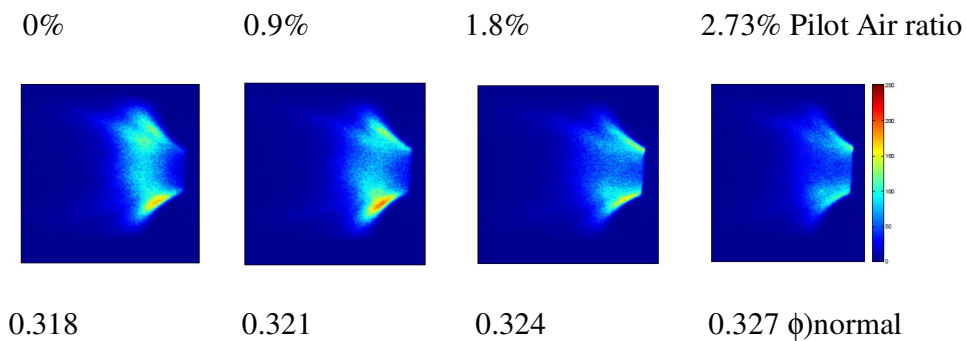


Figure 1.78: OH- chemiluminescence at different air transfers inside the fluidics plus 42% pilot fuel ratio of the main fuel and at overall equivalence ratio= 0.552 (XF=0).

Comparison between the pilot fuel ratio of 14%, 28%, and 42% at different pilot air ratios proves that the NO_x emissions increase by increasing these ratios, CO still almost in marginal changes at 28% but increases at 42%, and the chemiluminescences increased with fuel transfer but decreases with air transfer from the main lines inside the fluidics.

The injection of 14% of the main fuel plus the pilot air ratio up to 2.73% of the main air enhances the combustion better than injection of 28% and 42% of the main fuel as it reduces the nitrogen oxides and carbon monoxide. Cases C and D may be the best operating conditions for a swirl stabilized burner because of low NO_x and Low CO at stable conditions.

F- Air transfer inside the fluidics at constant main fuel and at overall equivalence ratio= 0.575

As mentioned at air transfer inside the fluidics and at overall equivalence ratio = 0.552, the NO_x and CO reduced as the pilot air ratio increases but here at around 1.36% of the main air almost more air transfer inside the fluidics has no effect as shown in Fig. 1.79.

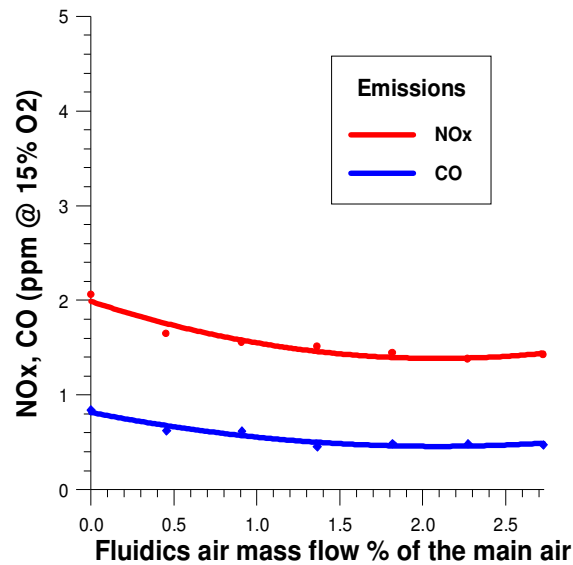


Figure 1.79: Influence of air transfer inside the fluidic oscillator on emissions at constant main fuel mass flow and at overall equivalence ratio= 0.575 (XF=0).

The images of OH chemiluminescence offer a similarity also after pilot air ratio 1.36% in color (Fig. 1.80). The luminosity faints gradually until this value of air transfer related to 0% but still more lighter overall equivalence ratio = 0.552.

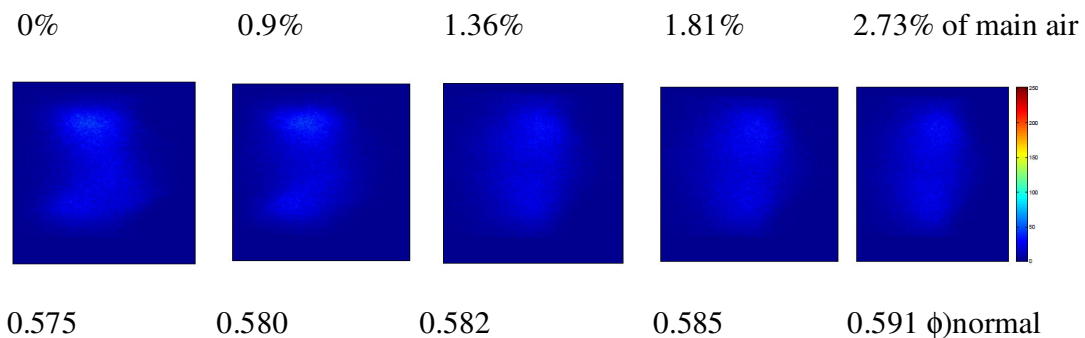


Figure 1.80: OH- chemiluminescence at different air transfers inside the oscillator by constancy of the main fuel mass flow and at overall equivalence ratio = 0.575 (XF=0).

2- The fluidics at the middle of the burner

The fluidic oscillator is mounted at the half of the burner height location inside the burner as it is sliding easily from zero location at the bottom. The PIV measurements technique is used to visualize the flow field at different water mass flows. Five hundred pictures are captured for each measurement's point and processed to find the flow field visualizations. Hydrophone is used to measure the sound pressure oscillations come from the fluid motion and during the fluid flow interaction between the fluidic oscillator and the swirl stabilized burner at different flow conditions. A controller was used to adjust the water amount at the specified value, needed to be tested, with high precision. Single-sided amplitude spectrum at different fluidics water volume flows ($XF=0.5$) is shown in Fig. 1.81.

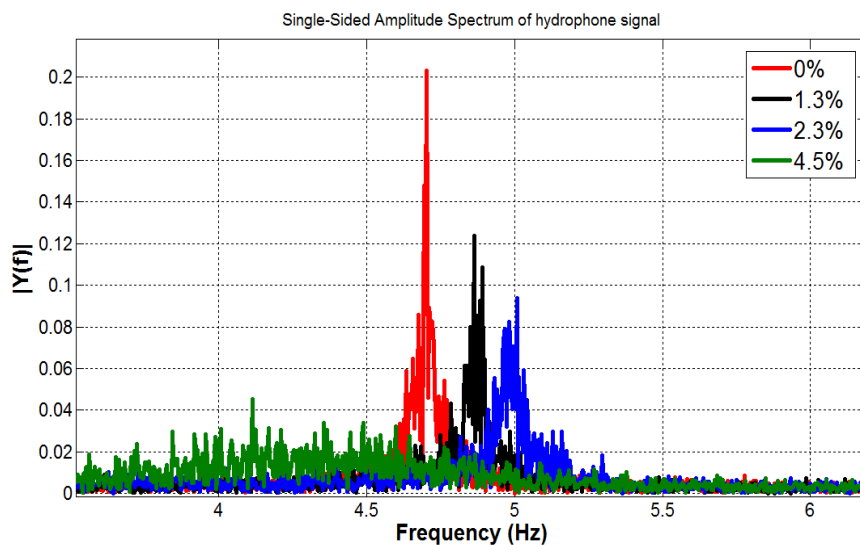


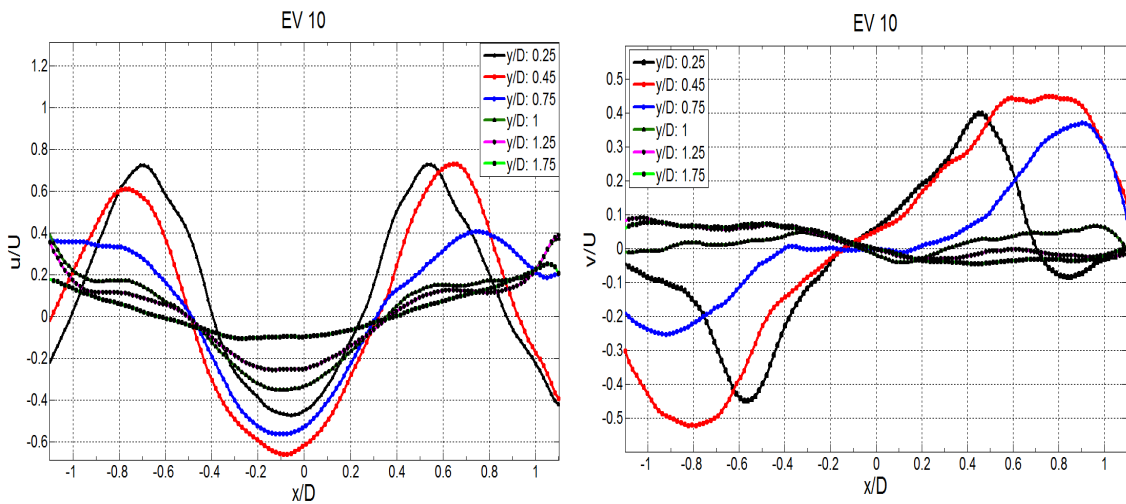
Figure 1.81: Single-sided amplitude spectrum at different fluidics water volume flows ($XF=0.5$).

As mentioned before in the previous sector at the burner bottom, injection of fluid inside the oscillator at this location suppresses the oscillations and destroys the dominant peak. The fluidic oscillator is still able to destroy also the pressure oscillations generated from the jet interaction with the main flow. This proves that the fluidic oscillator under test ($Fx1$) is able to dominate the oscillations produced from the main flow that exits downstream of the burner.

The velocity profiles comparison is done between the base line and 4.5% of the main flow rate as at Fig. 1.82. As the fluidics is now in the middle location of the burner, it is near the flowfield downstream the burner. The increase of the fluidic oscillator mass flow rate to the named value is affecting the total flow field. In the figure the streamwise and the radial velocity profiles at

different y/D are shown. Raising the mass flow makes recession to the two crests of the streamwise velocity higher than that in the previous location. Starting from $y/D= 1$, the streamwise velocity profiles take a bow shape. At this location also the crests and troughs of the radial velocity traces or profiles transferred to almost a linear shape after 4.5% pilot air ratio. The maximum streamwise velocity at the lobes reduced by 19% at y/D equals 0.25 and 28.8% at $y/D= 0.45$. The central streamwise velocity reduced 4.7% at y/D of 0.25, 7.4% at y/D of 0.45, and 26.6% at y/D of 0.75. The radial velocity also reduced from the maximum crest and trough by 15.6% at y/D equals 0.25 and 9% at $y/D= 0.45$. The reduction in the maximum radial velocity at x/D of 0.75 is 33.7% of the maximum one at the base case.

0 %



4.5 %

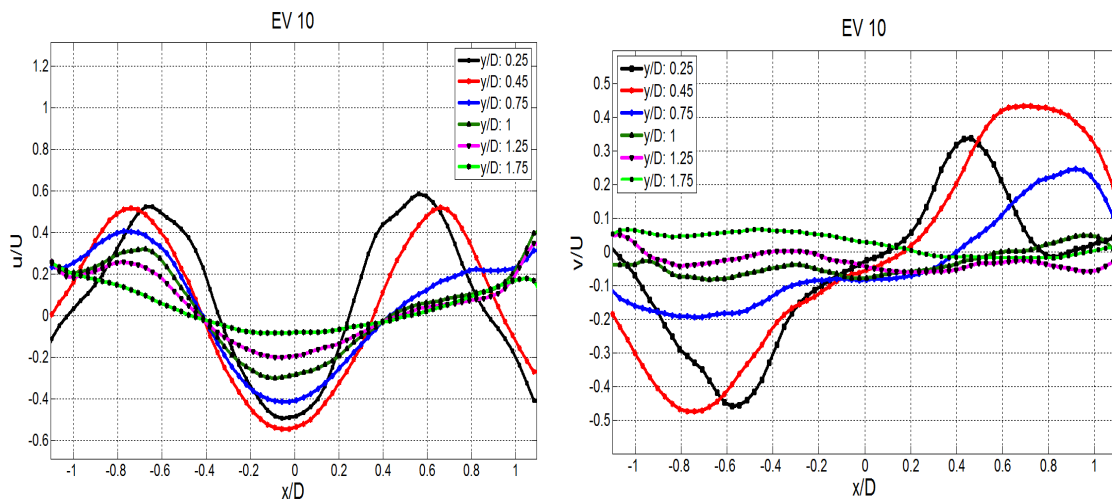
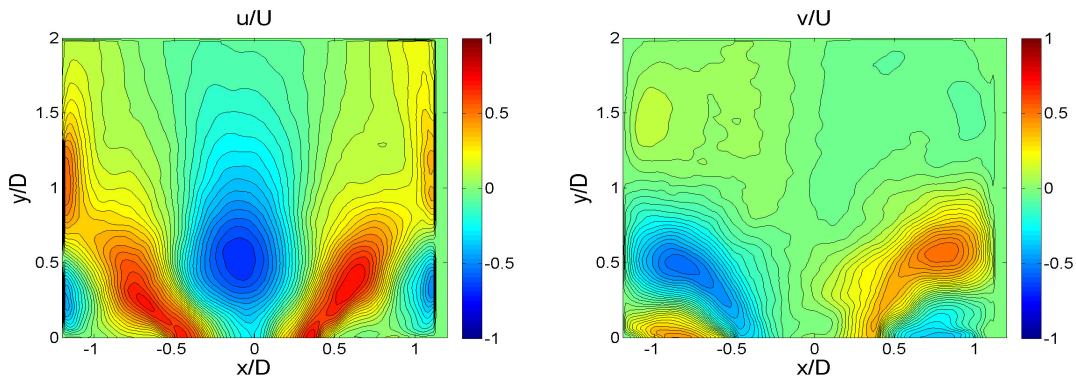


Figure 1.82: Streamwise velocity (left) and radial velocity (right) profiles comparison between the base line and 4.5% of the main water flow as a stable case at different axial locations ($X_F=0.5$).

The contour plots of the streamwise velocity, radial velocity, vorticity, and shear strain are shown at Fig. 1.83 and 1.84. Higher interaction between central jet flow and main flow comes from the swirl stabilized burner as well as the fluidic oscillator which is at the middle location of the burner height. This interaction is responsible for the changes in the flow field. The window of flow field has double the burner diameter in length and width. This is the area of interest. The faded color in the mean axial streamwise velocity reflects the reduction in that velocity at the lobes by increasing the fluidics inner flow. This is according to the pulsations generated from the oscillator. The change in the radial velocity is demonstrated at the right side in Fig. 1.83. The centerline area explains the constancy in the radial velocity profiles after y/D equals 1.

Some changes in the vorticity and the shear strain rate in case of rising the injecting flow inside the oscillator depending on the changes in axial streamwise velocity and radial velocity. The vorticity reduced at the crests and troughs as the flow increased to 4.5% at y/D of 0.25 by 32.3%, at y/D of 0.45 by 14.5%, and at y/D of 0.75 by 31.7%. The shear strain rate reduced by 19% at y/D equals 0.25, 41% at y/D of 0.45, and 46.32% at y/D of 0.75. These changes are represented and derived from Fig. 1.85.

0 %



4.5 %

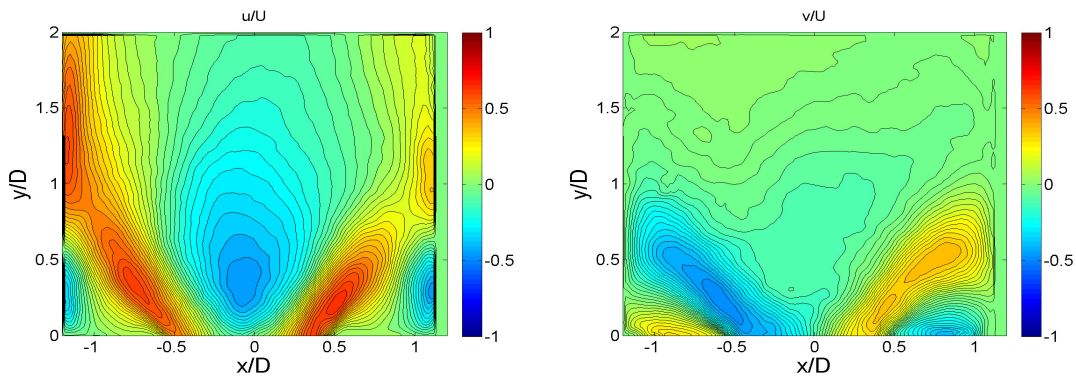
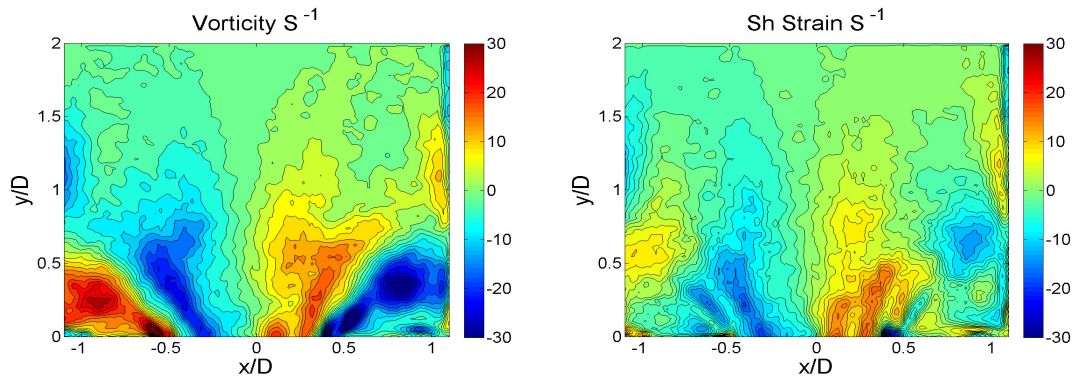


Figure 1.83: Streamwise (left) and radial velocity (right) contour plots at fluidics water mass flows of 0% (up) and 4.5% (down) of the main water mass flow (XF=0.5).

0 %



4.5 %

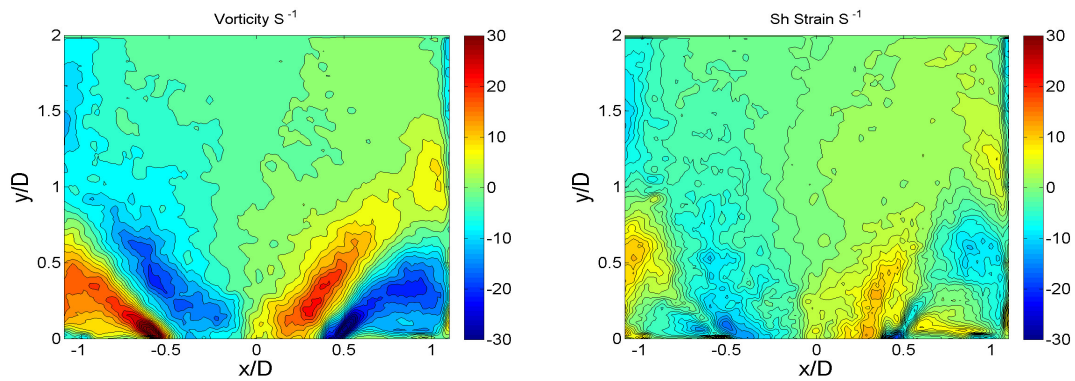
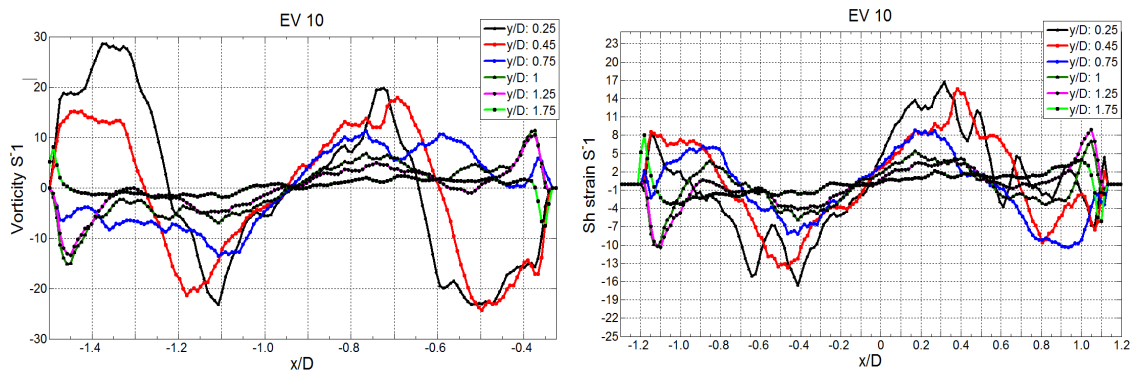


Figure 1.84: Vorticity and shear strain contour plots at fluidics water mass flows of 0% (up) and 4.5% (down) of the main water mass flow (XF=0.5).

0 %



4.5 %

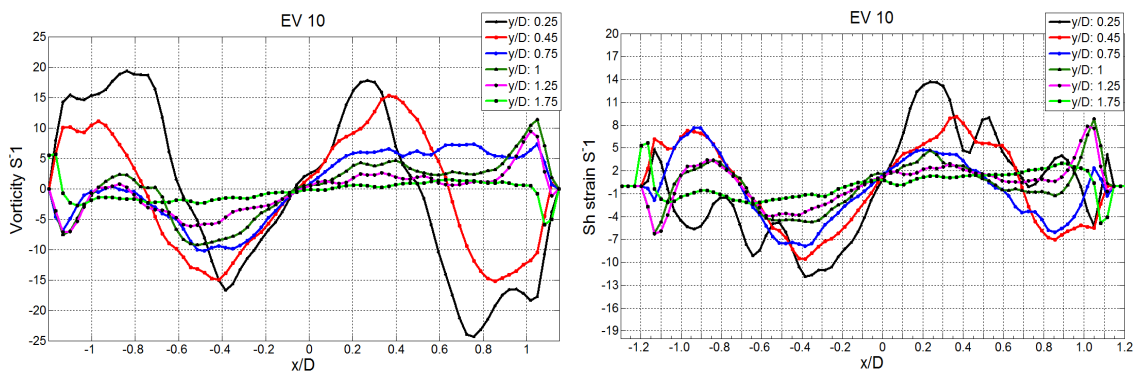


Figure 1.85: Vorticity (left) and shear strain rate (right) profiles comparison between the base case and 4.5% of the main water flow as a stable case at different axial locations (XF=0.5).

A test in a short combustion chamber is done trying to find the best location to mount the fluidics in order to perform the combustion operation with low NO_x and CO emissions and work in stable conditions. The equivalence ratio (ϕ) is kept constant during the whole test at $\phi=0.5$. OH camera is used to capture around 300 images for each measurement point in order to find the average of these pictures to show the chemiluminescence emitted from the flame beside the gas analyzer which used for emissions measurements.

As done before at the burner bottom, the effect of overall equivalence ratio is studied at first at this location. Influence of fuel transfer is studied on the combustion process at constant main air and at constant ϕ overall of 0.552. Effect of air transfer only without fuel is investigated at constant main fuel and at constant ϕ overall of 0.552. Air and fuel are injected inside the fluidics together to see the effect of this mix on the emissions, temperature and chemiluminescence at constant ϕ overall of 0.552. Air transfer inside the fluidics at constant fuel but at ϕ overall 0.575 is done. The last test is the transfer of air inside the oscillator at constant ϕ overall 0.575 and the transfer of some fuel together to see the influence of that on the fluidics performance.

Turbulent flow could consist of the organized nature of coherent structures and the chaotic nature of turbulence. As expected, turbulence increases the burning intensity by enhancing the mixing of reactants and the transport of heat besides the wrinkling of flow. These parameters lead to increase the total flame surface area available for reaction to take place. The combustion efficiency is adversely affected by extremely intense turbulent eddies which can cause local extinction in a turbulent flow. In turn, the NO_x and CO are affected by that in addition to the OH chemiluminescence. The turbulence intensity and structure are affected by the large exothermicity which is one characteristic of combustion reactions while turbulence affects the intensity and extent of reactions in the flow (Law 2006).

This location offers higher turbulent eddies than the last one at burner bottom. The turbulence is increased as the fluidic injector now is near of the main flow filed down stream of the burner exit. The effect of oscillator appears clearly in intensifying the turbulent eddies.

A- Effect of ϕ overall at constant m° air

Figure 1.86 shows the effect of equivalence ratio on the NO_x and CO emissions. The range of ϕ overall was from 0.528 to 0.699 between the lean blow off and a noisy point. According to the literature (Rankin 2007) similar to the previous burner position, the NO_x emissions increased to higher values as ϕ overall reached to 0.699. CO trend declined to around 0.61 and then inclined similar to the previous case at zero location. The NO_x emissions represent NO and NO₂. The values of NO are still higher than NO₂ because of intermediates produced during the combustion operation.

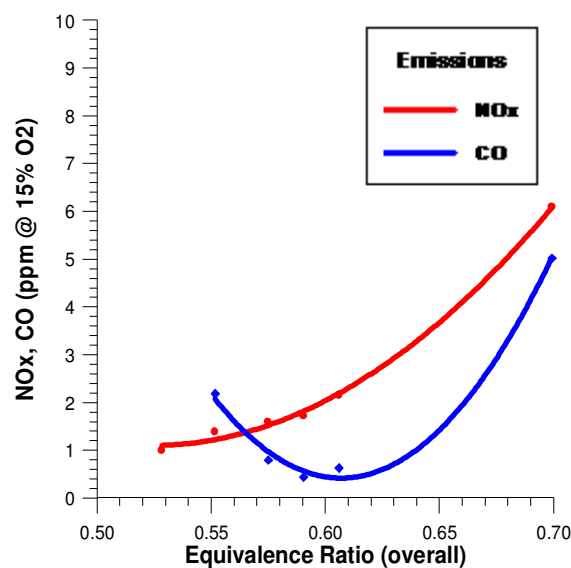


Figure 1.86: Effect of overall equivalence ratio at constant main air mass flow rate and at (XF=0.5).

The images of the OH chemiluminescence camera are shown in Fig. 1.87. Same as the previous location at the bottom of the burner and at the same conditions of equivalence ratios, the oxidation process is in directional proportion with the increase of ϕ overall. The luminous part of flame like the zero location is lighter at the shear layer zone at ϕ overall of 0.699 while at the other parts similar as the burner bottom position and the reaction offers similar chemiluminescence. The mounting of the fluidics, at this position and at these conditions, has marginal effect on the combustion behavior.

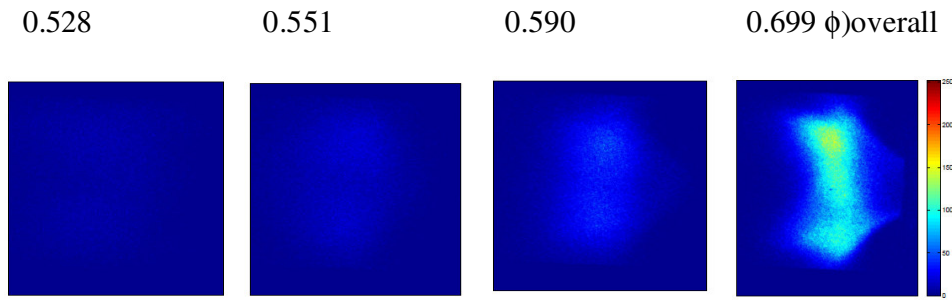


Figure 1.87: OH- chemiluminescence at different overall equivalence ratios ($\bar{X}F=0.5$).

The next parts explain the premix and air transfers as the fluidic oscillator is mounted at this location. The transfer of fuel offers arising in CO and NO_x emissions but the air transfer at the previous part offers better results than the fuel transfer at the whole normal equivalence ratios and at certain ϕ_{overall} . Then the next part focuses on the air transfer and its influence on the emissions and chemiluminescence at different ϕ_{overall} .

B- Air transfer inside the fluidic oscillator at constant main fuel and at constant ϕ_{overall} (0.552)

Figure 1.88 shows the influences of air transfer at certain ϕ_{overall} 0.552 and at a constant amount of main fuel. The air transfer reduces the NO_x emissions but until $\phi_{\text{normal}}=0.557$ and the carbon monoxide takes an increasing trend. This assures that the best location to mount the oscillator is at the bottom of the swirl stabilized burner with air transfer. The previous location gives at this transfer better result in reduction of NO_x and CO together.

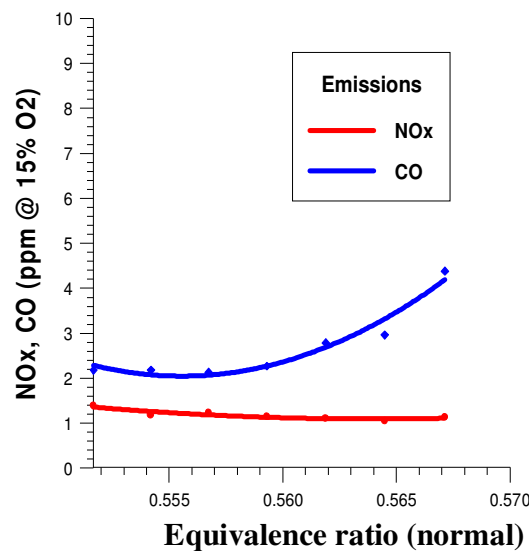


Figure 1.88: Influence of air transfer inside the fluidic oscillator on emissions at constant main fuel mass flow and at $\phi_{\text{overall}}=0.552$ ($\bar{X}F=0.5$).

The temperature is almost constant at 1300°C at the whole transfer percentages and the NOx reduced while CO increases at 0.557. As shown in Fig. 1.89, the chemiluminescence of the flame faint as OH concentration decreases by reaching 2.73% transfer of the main air (Arnhold 1991).

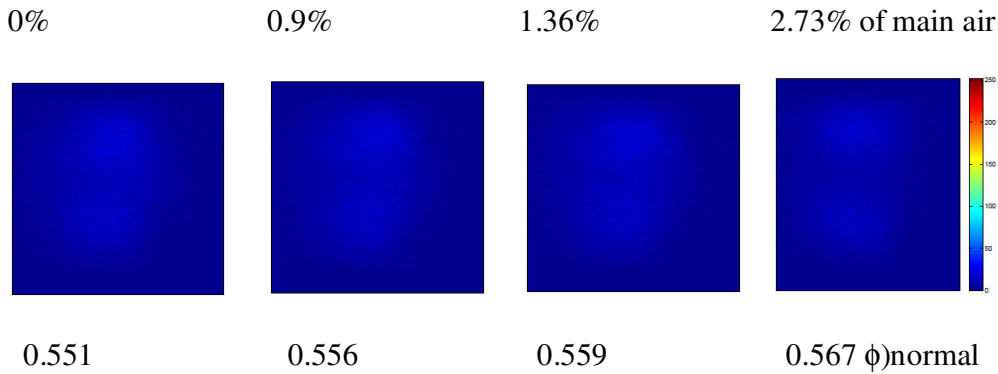


Figure 1.89: OH- chemiluminescence at different air transfers inside the oscillator by constancy of the main fuel mass flow and at $\phi_{\text{overall}}= 0.552$ (XF=0.5).

C- Air transfer inside the fluidic oscillator at constant main fuel and at constant ϕ_{overall} (0.575)

The transfer of air at ϕ_{overall} 0.575 gives good results in NOx reduction at no increase of CO. This still gives the air transfer the best merit between different transfer methods. NOx reduction at ϕ_{normal} of 0.583 is sharp and noticed. The fluidics model at these stable conditions participates in emission reduction which in turn enhances the combustion and complies with the environment laws at the whole world and still has a big influence on emission reduction at this position (Fig. 1.90).

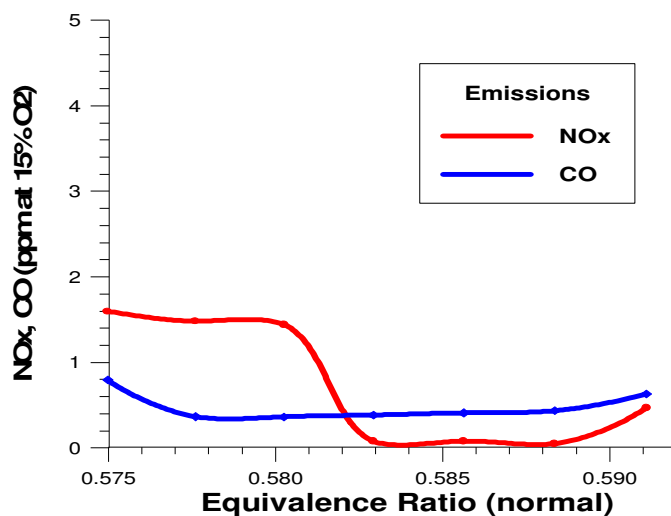


Figure 1.90: Influence of air transfer inside the fluidic oscillator on emissions at constant main fuel mass flow and at $\phi_{\text{overall}}= 0.575$ (XF=0.5).

The OH chemiluminescence gives no bright light as the air transfer increases gradually to 2.73% of the main air which coincides with the previous results at $\phi_{\text{overall}} = 0.552$. The temperature also has slightly increased from 1331°C at zero% air transfer by the air transfer enlargement which may return to the good mixing between the combustibles (Fig. 1.91).

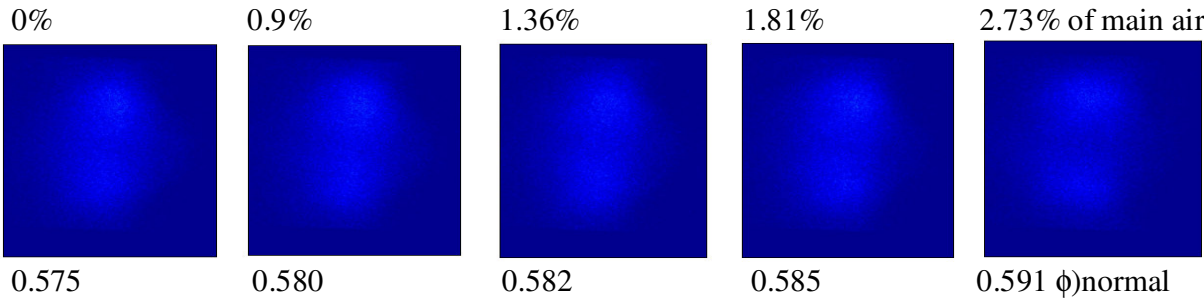


Figure 1.91: OH- chemiluminescence at different air transfers inside the oscillator by constancy of the main fuel mass flow and at $\phi_{\text{overall}} = 0.575$ (XF=0.5).

3- The fluidics at Top of the burner

At this time, the fluidic oscillator is mounted almost at the burner dump plane at a point at the same level of the burner tip and at the starting point of the downstream flow or the combustion chamber. As mentioned before, PIV is used to visualize the flow field at different water mass flows in cold study performed at water tunnel. Also five hundred images are captured for every measurement point to the water flow which equivalent to that applied in combustion conditions. Pressure oscillations are detected by the hydrophone which is mounted directly tangent to the burner tip for no barring of the flow. This hydrophone signals are changing during the fluid injection and at the interaction between the fluidics flow and the swirl stabilized burner main flow. For adjusting the water amount at specified value, a controller was used with high precision. This flow controller is set using a Lab view computer program in water laboratory at institute of Fluid Dynamics and Engineering Acoustics- TU Berlin. Single-sided amplitude spectrum at different fluidics water volume flows ($XF=1$) is shown in Fig. 1.92.

The transfer of flow inside the fluidic oscillator at $XF=1$ suppresses the pressure oscillations and destroys the dominant peak by injecting more than 2.3 % of the main flow. A good proof, like before at the previous two locations, is that the fluidic oscillator under test ($Fx1$) is able to dominate the oscillations produced from the main flow downstream of the burner. This suppression of the oscillations is considered an indication to stabilize the flame at reacting combustion conditions at the whole mounting locations.

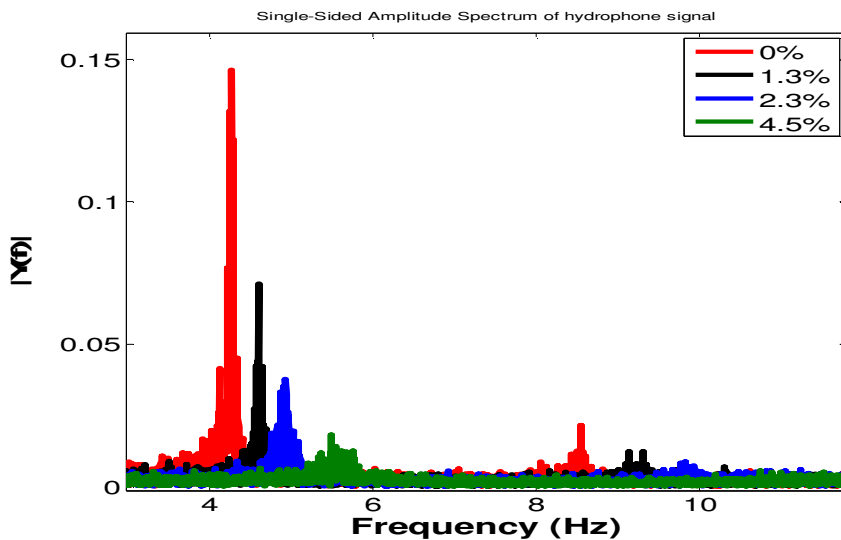


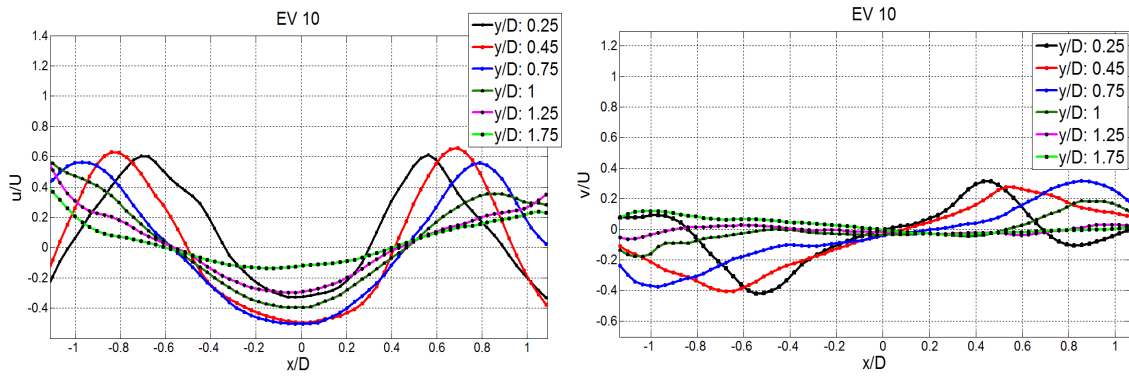
Figure 1.92: Single-sided amplitude spectrum at different fluidics water volume flows ($XF=1$).

The streamwise and the radial velocity profiles comparison is done between the base line and 4.5% of the main flow rate as at Fig. 1.93. The fluidics is located at apex of the burner thereby it is very near of the flowfield downstream. Higher interaction between both fluids that flow from the swirl stabilized burner and the flow generated from the fluidic oscillator. The studied figure demonstrates the higher interaction especially near or around the centerline at the center body flow and at the whole flow field at different y/D from 0.25 to 1.75. The streamwise velocity increases by transferring of 4.5% of the main flow at y/D of 0.25 and 0.45 antithesis the last two fluidics locations. The oscillator flow stretches the whole flow field outside the burner.

The maximum streamwise velocity at lobes increased at y/D of 0.25 by 34% and at y/D of 0.45 by 17.8% while at y/D of 0.75 it decreases by 8.87%. At the centerline, the streamwise velocity is positive at y/D from 0.25 to 1.75. The increase in velocity at y/D of 0.25 is 1.52 times the base line; at y/D of 0.45 is 1.23 times, and 1.12 times at y/D of 0.75. The radial velocity increases also by 74.7% at y/D of 0.25 of base line, 1.17 times the base line at y/D of 0.45, and by 22.3% at y/D of 0.75 of base line.

These changes appear at Fig. 1.94 of the streamwise and radial velocity contour plots. The base line is traditional in the velocity distribution or offers the standard flowfield of this type of swirl flow generated from this swirl stabilized burner while the changes in the transferred inner flow case of 4.5% are shown clearly and their flow zones. At base line as normal case, inner the shear layer zone the low- velocity region and the vortex break down are found and after that the fully turbulent region. Shear layer shed from the burner exit rolls up into discrete and axisymmetric vortex rings at $x \approx 0.47 D$ and $y \approx 1.16 D$. These vortex rings grow in the flow direction. The boost in the maximum streamwise velocity at the two lobes or wings is noticed by fluid transfer at this location while the fluidics streamwise velocity salience at the centerline is shown as the green yellow color at the middle near zero x/D and between the fluid troughs around the centerline. The higher interaction between both flows of the oscillator and the burner leads to this increase in the radial velocity as shown in the contour plots. The oscillator has an effect around the centerline at the exit vicinity represented by the velocity crest (left) and the trough (right) as shown in Fig. 1.94.

0%



4.5%

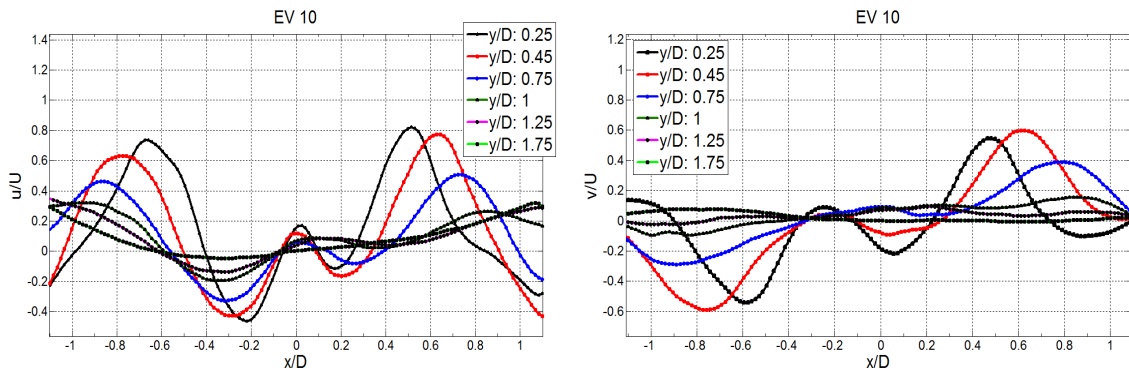
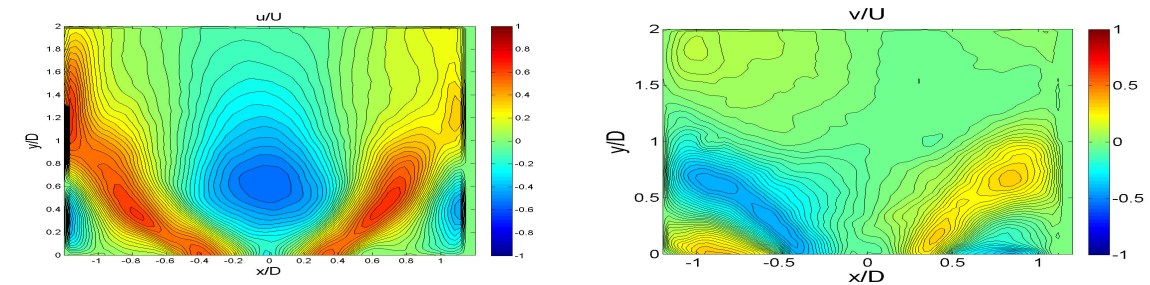


Figure 1.93: Streamwise velocity (left) and radial velocity (right) profiles comparison between the base line and 4.5% of the main water flow as a stable case at different axial locations (XF=1).

0 %



4.5 %

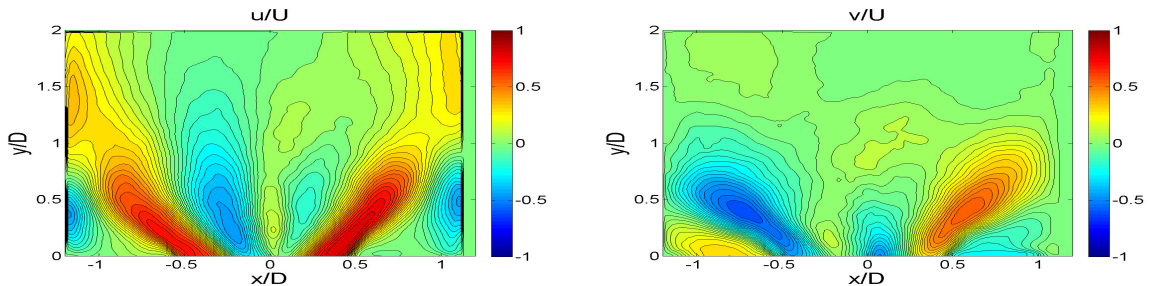


Figure 1.94: Streamwise (left) and radial velocity (right) contour plots at fluidics water mass flows of 0% (up) and 4.5% (down) of the main water mass flow (XF=1).

The Instantaneous velocity vectors six phase averages reconstructed on POD modes at 4.5% fluidics water transfer of the main mass flows are represented at Fig. 1.94. The changes inside the flow field especially at the vicinity of the burner dump, where the fluidics mounted at this location, are clearly explained at the figure. Unlike the base line, transfer of fluid flow inside the fluidics changes totally the inner centerbody structure of the normal swirled flow. As shown in figure 1.95 and 1.96, the instantaneous velocity vectors and vortices change during these six phase averages. At a larger value of fluidics water flow transfer (4.5%), two types of vortices were shed together from the oscillator and the swirl stabilized burner then propagated along the conical shear layer.

At 0° , the effect of the left fluidic oscillating jet appeared with vortices in-between the centerline and the $x/D= 0.25$ (20mm) and $y/D= 0.6$ (50mm). These generated vortices grow downstream inside the known low velocity region in direction near the normal vortex breakdown region and vanish together as shown at 60° . These shed vortices are appearing in the inner (wake) shear layer (between the reverse flow and the conical jet) and affect the normal vortices generated from the swirled flows. This results in asymmetry of the normal vortices around the centerline.

At 120° , the transfer between the two fluidics jets generates high vortices in low velocity region at three main positions; between the right fluidics jet and the inner shear layer, between fluidics two jets, and between the left fluidics jet and the inner shear layer. The two fluidics jets appear at 180° in the way to shift to the other right limb from left one. The phase of 240° offers higher mixing and interaction zones after the end of the fluidics jets. Inner vortices between the oscillating jets are induced and grow in turn in direction downstream of the flow. The jet flow spread much faster and the entrainment rate between jets is high. This highly mixed region moved closer to the burner exit as the mass flow increases further. The normal reverse flow returns back at almost $y \approx 1.2 D$ as shown at 300° . After the vortex breakdown, the flow became regular with fewer small-scale vortices in the shear layer.

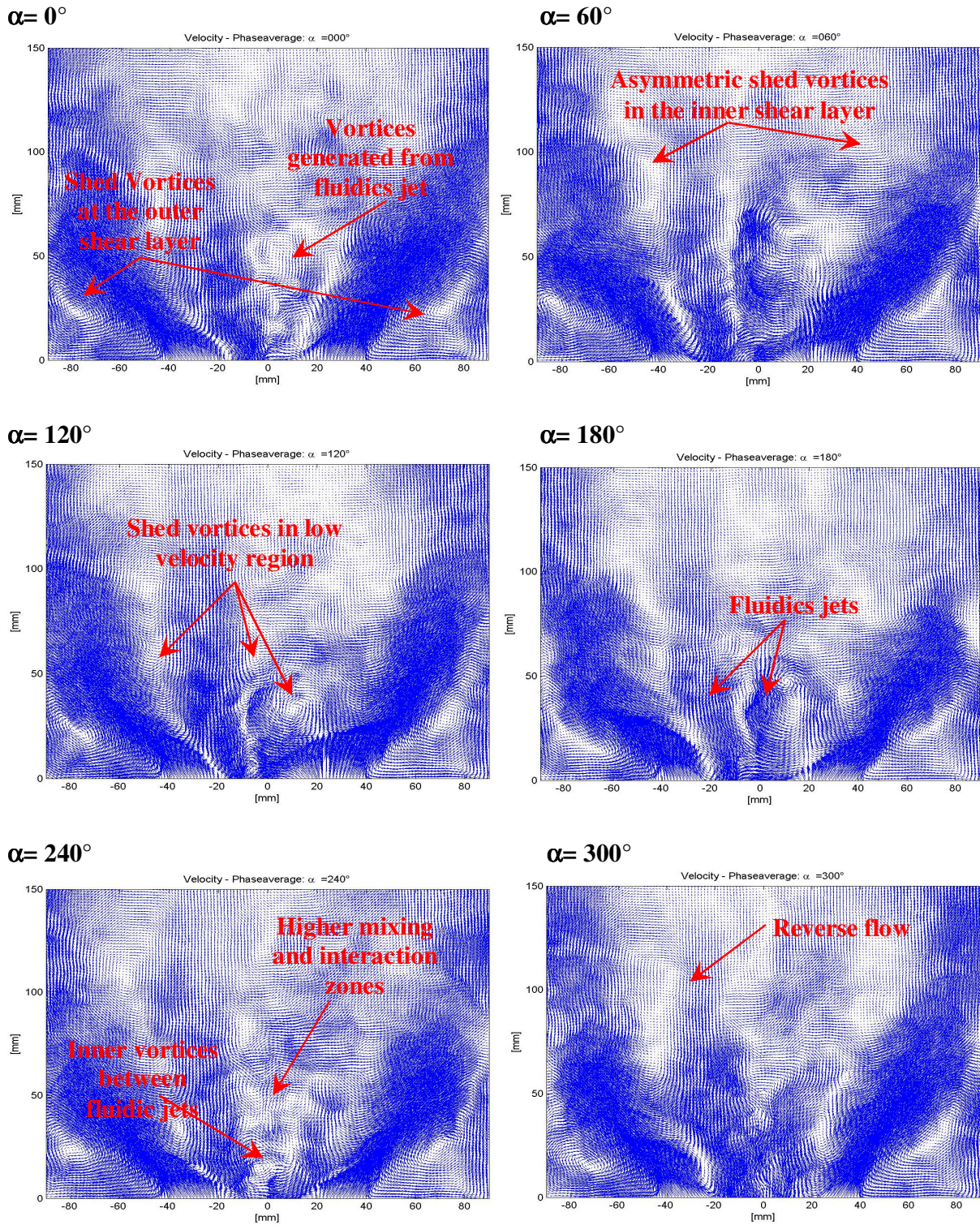


Figure 1.95: Instantaneous velocity vectors six phase averages reconstructed on POD modes at 4.5% fluidics water transfer of the main mass flows (XF=1).

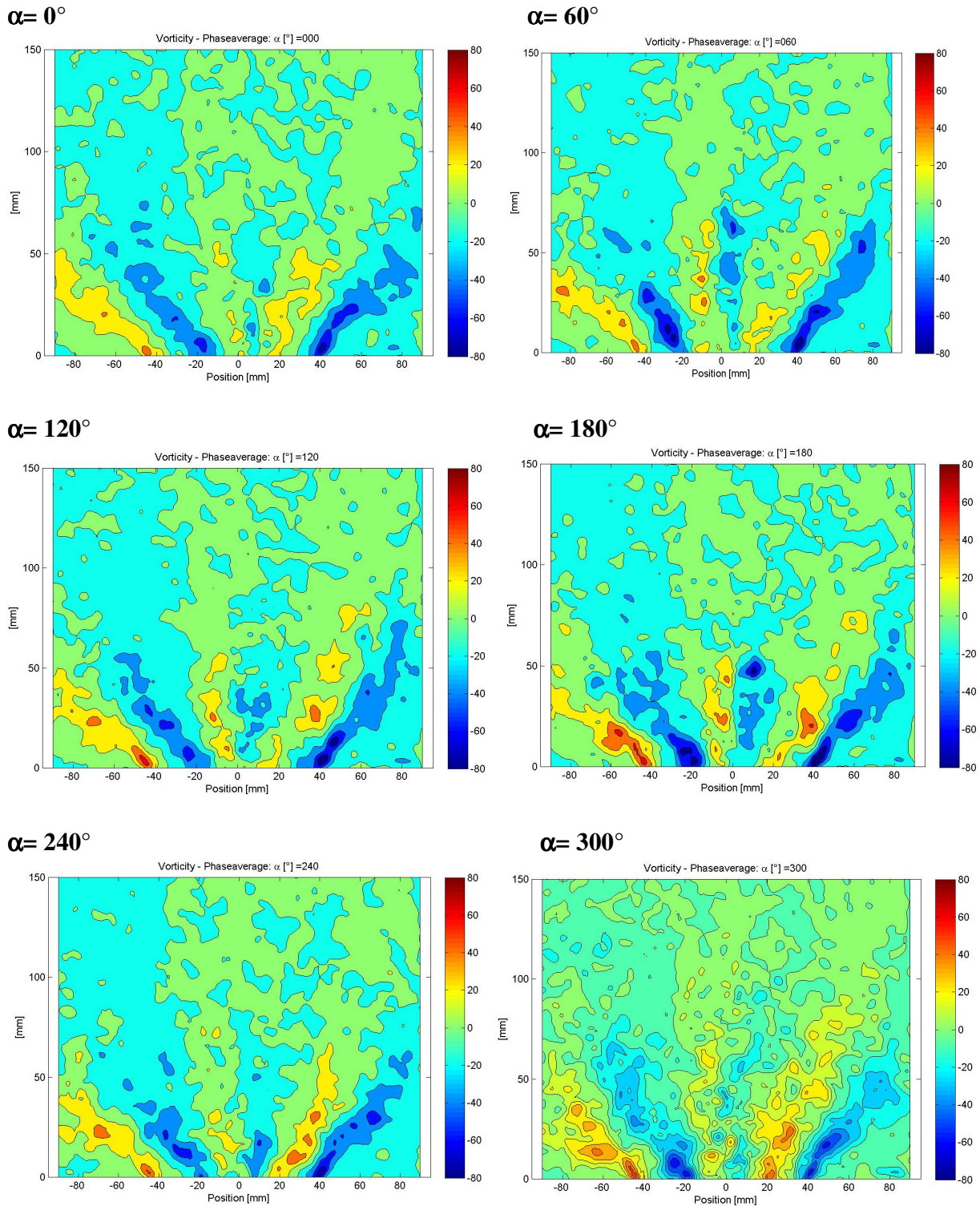


Figure 1.96: Instantaneous vorticity contour plots six phase averages reconstructed on POD modes at 4.5% fluidics water transfer of the main mass flows (XF=1).

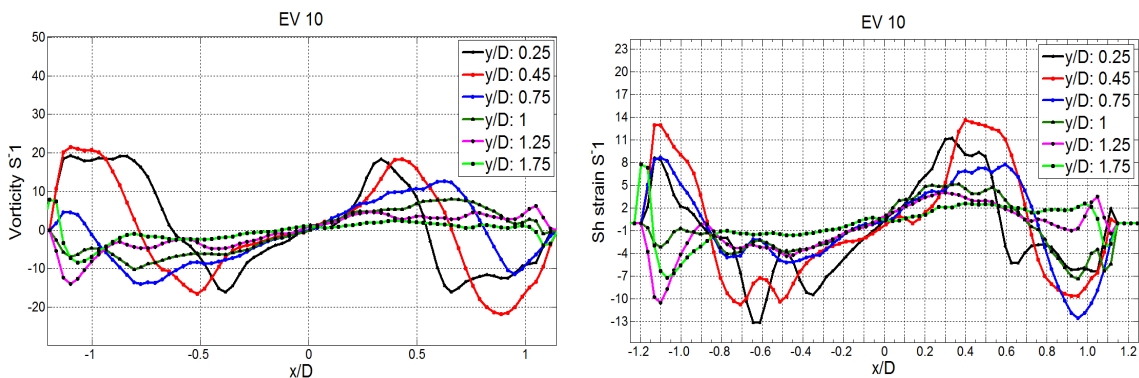
The vorticity and shear strain rate are calculated from average of 500 PIV images and represented in the shape of mean average values. Figure 1.97 represents the Vorticity (left) and shear strain

rate (right) profiles comparison between the base line and 4.5% of the main water flow as a stable case at different axial locations ($XF=1$). In Figure 1.98, vorticity and shear strain contour plots at fluidics water mass flows of 0% (up) and 4.5% (down) of the main water mass flow ($XF=1$).

Increase in the vorticity and the shear strain rate in case of raising the injecting flow inside the oscillator is depending on the changes in axial streamwise velocity and radial velocity. The vorticity changed at the crests and troughs as the flow increased to 4.5%; at y/D of 0.25 increased by 80%, at y/D of 0.45 increased by 16%, and reduced at y/D of 0.75 by 6%. At centerline the vorticity increased by 97% at y/D equals 0.25 from the maximum crest value, 36.4% at y/D of 0.45 from the maximum crest value, and 29% at y/D of 0.75 from the maximum crest value.

The shear strain rate changed at the crests and troughs as the flow increased to 4.5% as follows: increased by 37, 1% at y/D equals 0.25, decreased by 14% at y/D of 0.45, and increased by 51.8% at y/D of 0.75. At the main flow centerline, the shear strain rate increased by 58.6% at y/D equals 0.25 from the maximum crest value, 19.5% at y/D of 0.45 from the maximum crest value, and 32.3% at y/D of 0.75 from the maximum crest value.

0%



4.5%

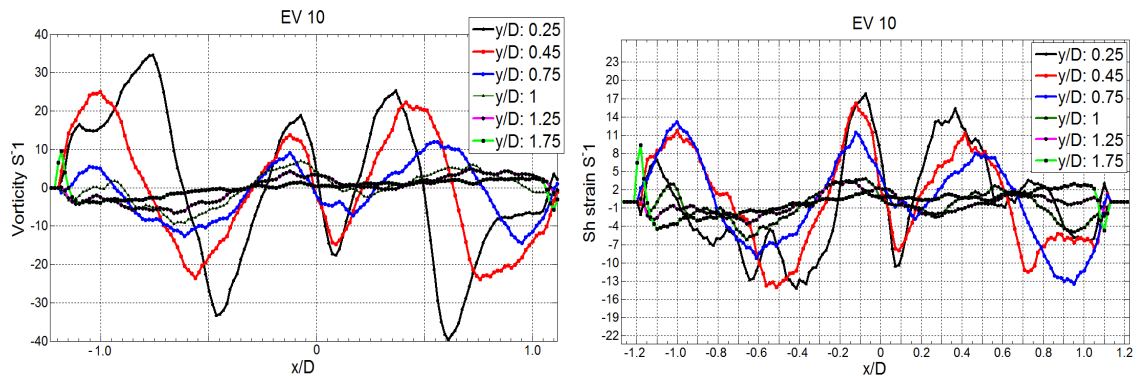


Figure 1.97: Vorticity (left) and shear strain rate (right) profiles comparison between the base case and 4.5% of the main water flow as a stable case at different axial locations ($XF=1$).

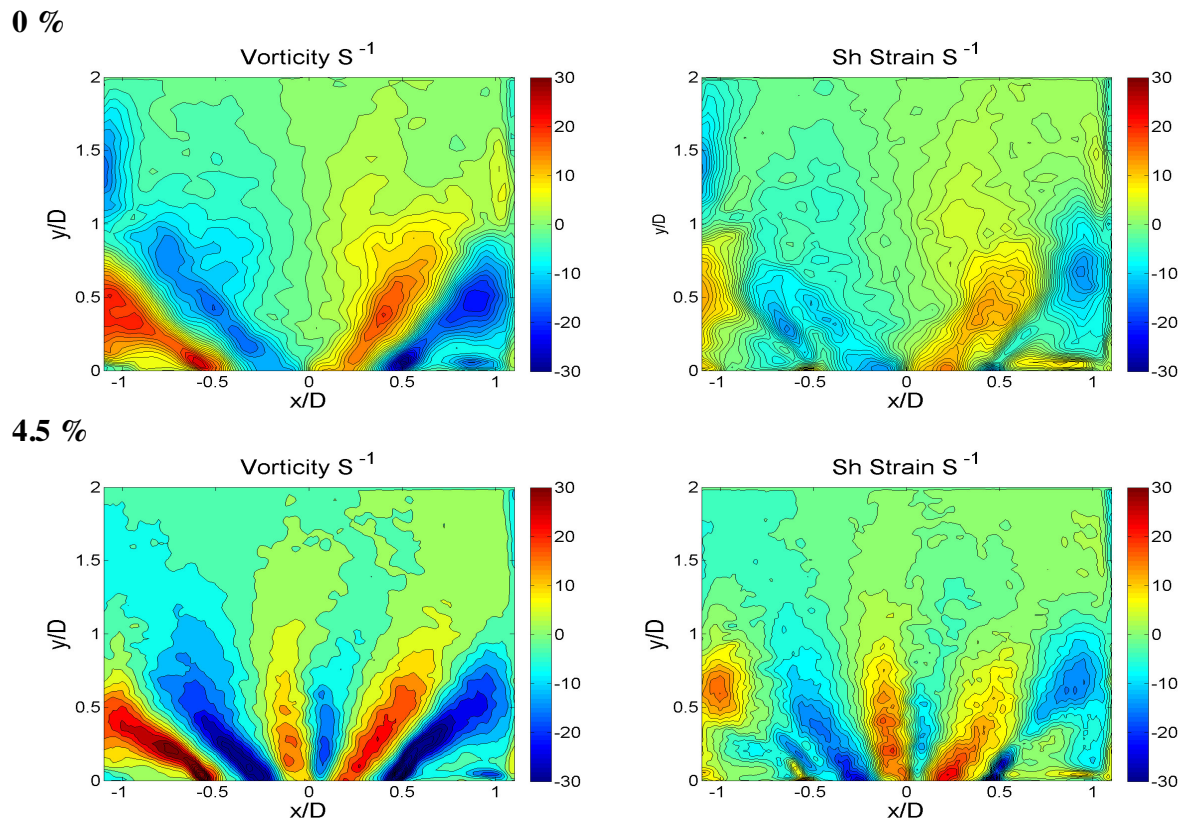


Figure 1.98: Vorticity and shear strain contour plots at fluidics water mass flows of 0% (up) and 4.5% (down) of the main water mass flow (XF=1), average of 500 images.

By increasing the flow transfer inside the fluidic oscillator, the flow became complicated, and vortices, associated with instability of the azimuthal shear layer, grew stronger. Vortices in the azimuthal shear layer, formed by the azimuthal or swirl velocity, grew and became comparable with vortices in the axial shear layer. Azimuthal inner shear layer instability or turbulence is visible in horizontal slices downstream of the flow ($y \approx 0.25 D$), as a vortex ring passed through it (see Fig. 1.99). This instability is evolved between the normal swirl rotating jet and the fluidic oscillating jet. The instability vortices are visible in horizontal cross-sections as well as axial cross-sections and are rapidly convecting away by the mean flow. These vortices grow stronger in advance when a vortex ring passes by from burner mouse, and become weak or even disappear gradually as the vortex ring propagates further downstream of the burner exit.

Due to the solid body rotation of the flow, the vectors and in turns the streamlines in the jet expected to be helical as shown in Fig. 1.100. The rotation direction of the mean flow is clockwise on horizontal slices if viewed from downstream of the burner exit.

Random turbulence grows, as a result of the fluidics flow interaction with the main flow, in the shear layer and makes the flow visibly and measurably more turbulent as noticed from the

comparison in the Figure. From Fig. 1.99, the interaction between the turbulent oscillating fluid and the swirled flow widen the mixing region so that the resulted conical flow jet spread faster than a swirling one alone, and the entrainment of fluid is higher.

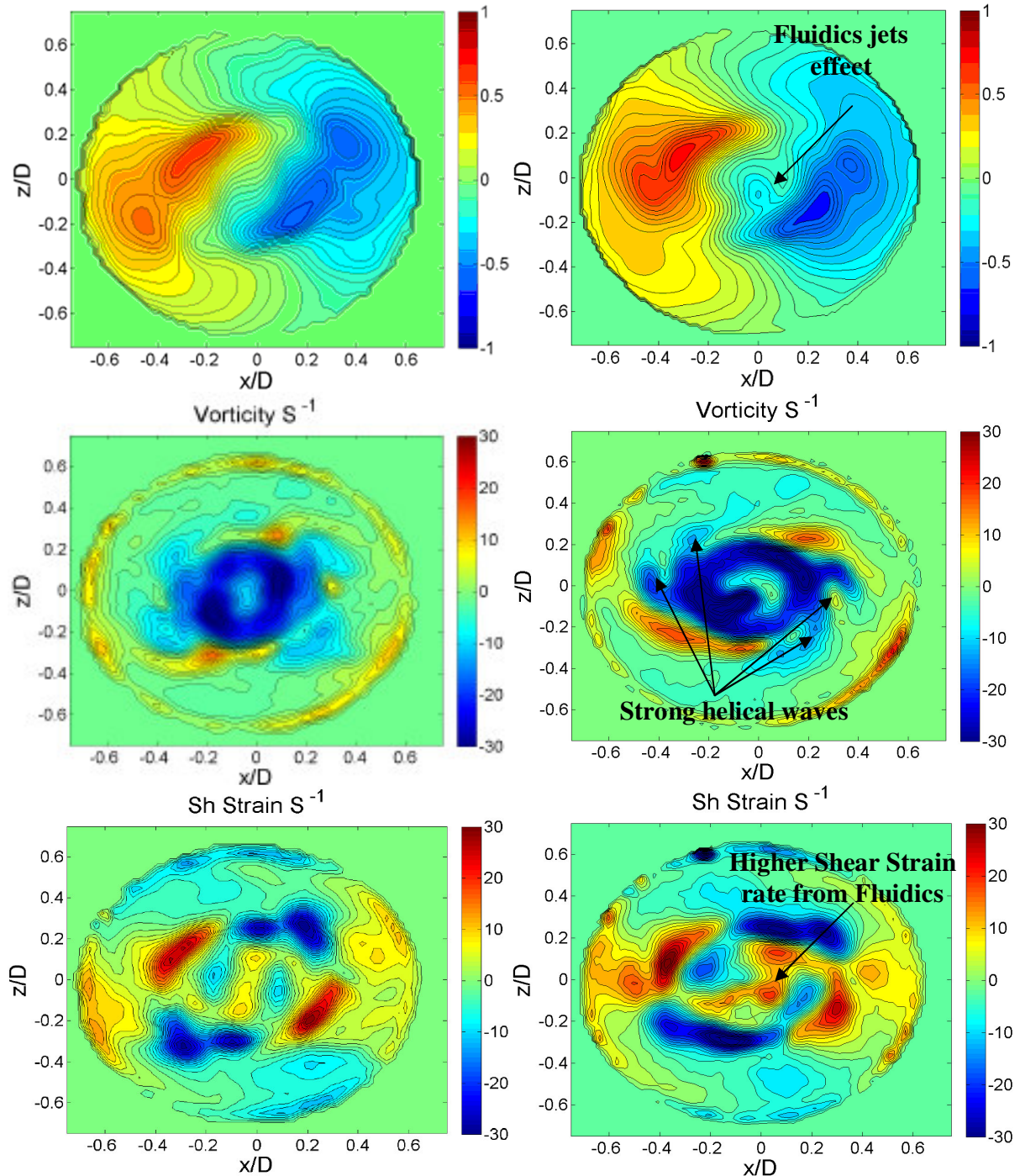
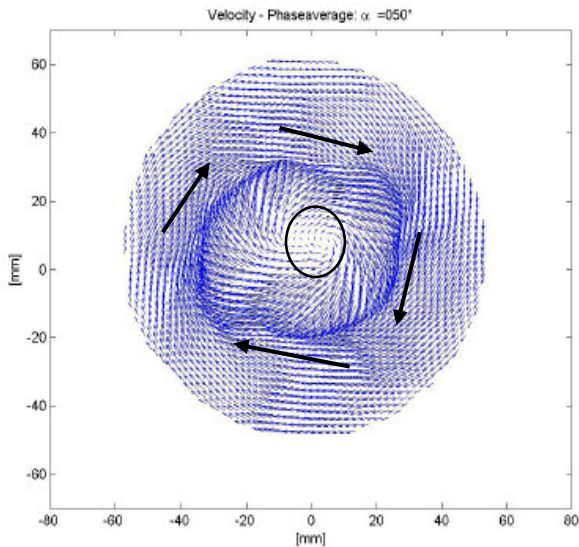


Figure 1.99: velocity, vorticity, and shear strain rate contour plots horizontal slice mean of 500 images of PIV at $y=0.25D$ for 0% fluidics water transfer of the main mass flows (left) and 4.5% fluidics water transfer of the main mass flows (right) ($XF=1$).

0%



4.5%

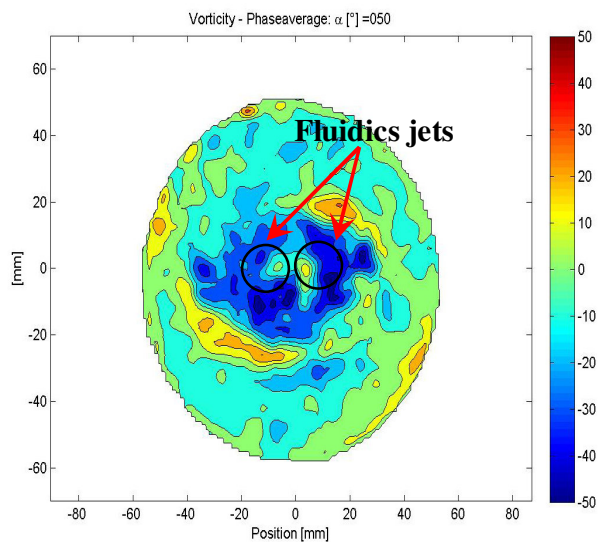
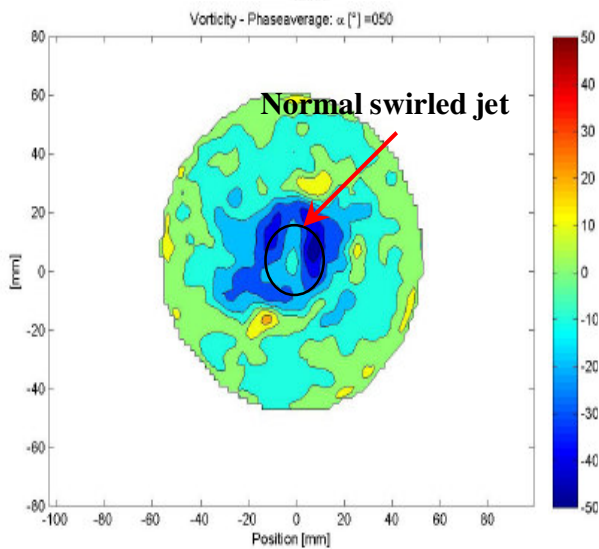
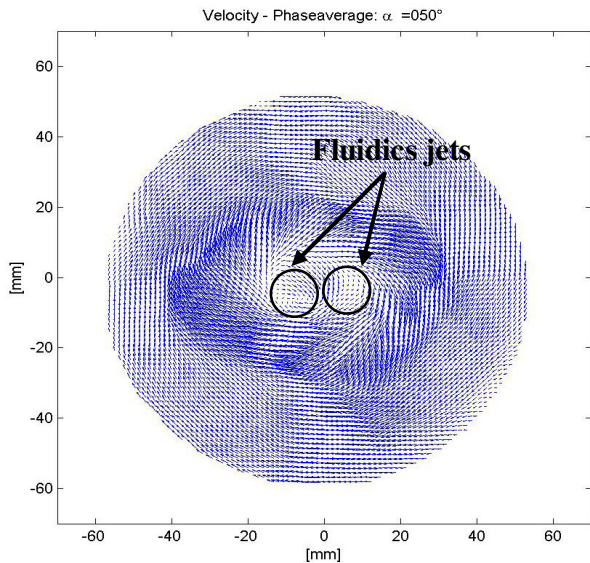


Figure 1.100: Instantaneous velocity vectors at 50° phase average reconstructed on POD at 0% (left) and 4.5% (right) fluidics water transfer of the main mass flow (XF=1).

The vortex core is relatively unstable close to the burner outlet as a result of the oscillator flow together with the swirled flow and the flow rapidly becomes fully turbulent at $y \approx 2D$ while turbulence results from the fluidics increases of the vortices irregularity.

As in Fig. 1.99, the vorticity at 4.5% transfer offers strong helical waves according to the higher turbulence generated from the effect of swirl as well as the oscillating jets. The fluidics jets effect is distinguished or noticed clearly at the centerline of the burner. Higher shear strain rates are noticed also at the shear layers and in the middle centerbody flow. A comparison of Instantaneous velocity vectors and vorticity at selected phase (50°) reconstructed on POD at 0% (left) and 4.5%

(right) fluidics water transfer of the main mass flow ($X_F=1$) is shown at Fig. 1.100. At base line, the influence only of the swirler appears in the middle and its location takes a circular changeable location inner the low velocity region and rotates with the swirled flow clockwise. The transfer of 4.5% exhibits the jet interaction flow between the oscillator and the swirl induced burner.

As mentioned before by Law, turbulent flow could consist of the organized nature of coherent structures and the chaotic nature of turbulence. This turbulence increases the burning intensity by enhancing the mixing of reactants and the transport of heat besides the wrinkling of flow. But intense of the turbulence eddies can cause local extinction in a turbulent flow and the combustion efficiency is adversely affected. Sequentially, the NO_x and CO are influenced by that besides OH chemiluminescence. The turbulence intensity and structure are affected by the large exothermicity which is one characteristic of combustion reactions while turbulence affects the intensity and the extent of reactions in the flow (Law 2006).

This oscillator position gives high turbulent eddies compared to the base location in the burner. The fluidics is almost adjacent to the mean body of the flow field which considers an indication to high vorticity and turbulence. The oscillator participates in rising and intensifying the turbulent eddies. The previous two fluidic lance locations preferred the base line at zero level inside the burner as the optimum mounting place. A test is performed at $X_f=X_{\max}$ and at $8.17D$ combustion chamber length to find the optimum operating conditions at the best location with low NO_x and CO emissions and work in stable conditions. The equivalence ratio (ϕ) is kept constant during the whole test at $X_f/X_{\max}=1$. The heat release rate is calculated by measuring the amount of light radiated from a flame at specific wavelengths of certain radical species such as CH^* and OH^* . At the present investigations, OH camera is used to capture around 300 images for each measurement point in order to find the average of these pictures to show the chemiluminescence emitted from the flame beside the gas analyzer which is used for emissions measurements. Some transfers are done in measurements matrix in order to reach the best combustion conditions and the optimum oscillator mounting position inside the burner.

A- Effect of ϕ overall at constant m° air

As shown in Fig. 1.101, effect of ϕ overall at constant m° air is studied on NO_x and CO emissions. ϕ overall is between 0.505 and 0.699, between the lean blow off and noisy point that can be withstand acoustically. The nitrogen oxides are in directional proportion to the increase of ϕ overall with no drop around 0.6 as the previous two positions but for CO is the same. NO_x

represents the NO and NO₂. The values of NO are still higher than NO₂ because of intermediates produced during the combustion operation as mentioned in the previous two positions.

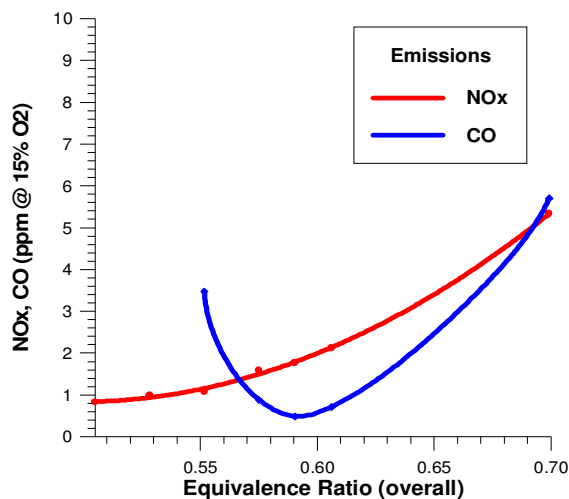


Figure 1.101: Effect of ϕ overall at constant m° air and at (XF=1) on combustion.

Same as the last two positions at the bottom and the middle of the burner and at the same conditions of equivalence ratios, the oxidation process is in directional proportion with the increase of ϕ overall. The luminous part of flame like before is lighter at the shear layer zone at higher ϕ overall of 0.699 and the reaction offers similar OH chemiluminescences.

B- Fuel transfer inside the oscillator at constant main air and constant ϕ overall (0.552)

Unlike at the middle location inside the burner, the oscillator gives a result similar to the base line position. Investigation of the flame behavior at this location with fuel transfer gives good results in CO reduction until 14% of the main fuel while the nitrogen oxides trace shows further increase as base line location (see Fig. 1.102).

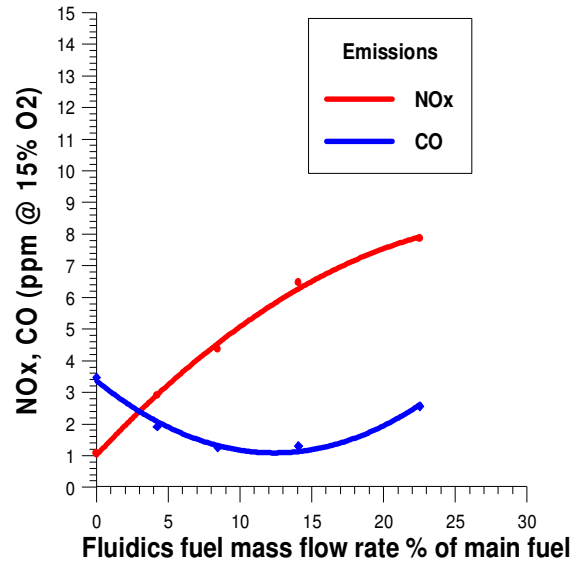


Figure 1.102: Influence of fuel transfer inside the fluidic oscillator on emissions at constant main air mass flow and at $\phi_{\text{overall}} = 0.552$ ($X_F=1$).

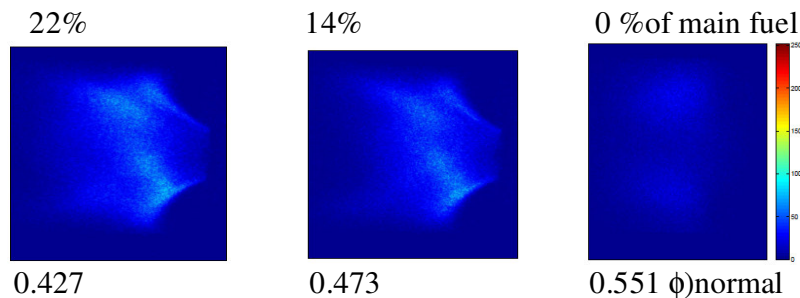


Figure 1.103: OH- chemiluminescence at different fuel transfers inside the oscillator by constancy of the main air mass flow and at $\phi_{\text{overall}} = 0.552$ ($X_F=1$).

The temperature reduced from no transfer by around 16% as the fuel transfer inside the oscillator increases. A linear relationship between concentration of hydrogen oxides and chemiluminescence intensity is noticed as demonstrated by Arnhold 1991. The higher the fuel transfer percentage, the higher chemiluminescences as in Fig. 1.103. NOx emissions also increase to 7.86ppm at the 22% of fuel transfer while CO decreases up to transfer of 15% of the main fuel while ϕ_{normal} decreases .

C- Air transfer inside the fluidics at Constant Fuel and at $\phi_{\text{overall}}= 0.552$

As tested before, the same air transfer was done between 0% and 2.73% of the main air at constant ϕ_{overall} of 0.552. The value of ϕ_{normal} increased in turns from 0.552 to 0.567 accordingly. Reduction in NO_x up to almost zero is reached by injection of transferred air inside the oscillator. CO also reduced and its value at the end transfer point was 2ppm while CO₂ was at 3.5% as exhibited in Fig. 1.104.

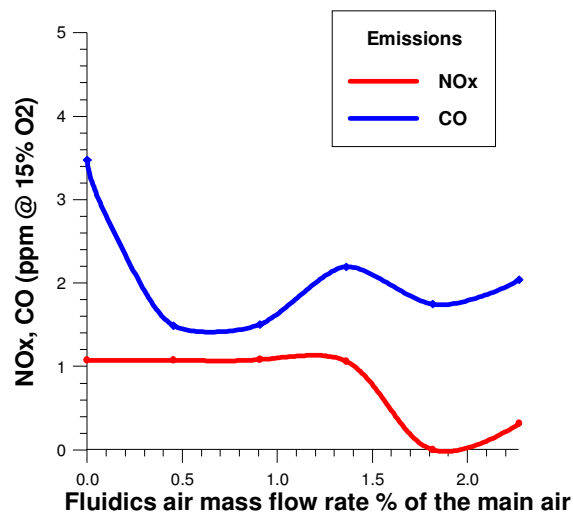


Figure 1.104: Influence of air transfer inside the fluidic oscillator on emissions at constant main fuel mass flow and at $\phi_{\text{overall}}= 0.552$ (XF=1).

The air transfer considers the best and the optimum way to reduce the emissions at the whole mounting locations. This gives merit to the fluidics under test to work better with some new or other burner configurations at different mounting locations inside these burners.

Like before, the increases in air transfer faint the luminosity of the flame as resulted from the average of 300 images captured by OH camera as indication to the chemiluminescence from zero to higher studied air transfer. Generation of light depends on the excited intermediates which decay to lower energy levels that give luminous flame and the intermediates of NO are small as the ratio of NO₂ is higher in this case of transfer which explains the dimming of the flame light.

D- Air transfer inside the fluidics at constant fuel and at $\phi_{\text{overall}}= 0.575$

As mentioned at the previous two fluidics positions, air transfer inside the fluidics at $\phi_{\text{overall}}= 0.552$ results in NO_x and CO reduction. As the air transfer increases to around 1.36% of the main air, no considerable effect on CO appears as shown in Fig. 1.105. Reduction in NO_x emissions is noticed also at this transfer case also.

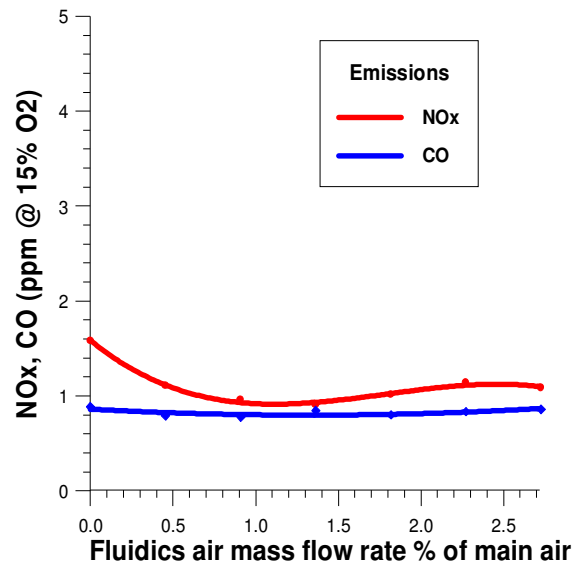


Figure 1.105: Influence of air transfer inside the fluidic oscillator on emissions at constant main fuel mass flow and at $\phi_{\text{overall}}= 0.575$ (XF=1).

The images of OH chemiluminescence offer a similarity also after 1.36% at $\phi_{\text{overall}}= 0.575$ in luminescence color like the previous two cases. The luminosity faints gradually until this value of transfer with respect to the 0% but still lighter than $\phi_{\text{overall}}= 0.552$.

The transfer of fuel only offers arising in NO_x emissions. The Flame rotates from the burner bottom around the oscillator as the fuel increases and looks like Lotus flower. By mixing some fuel with air inside the fluidics, reductions in NO_x and CO are noticed but not lower than at the air transfer only which offers the best conditions for emissions reduction. The flame length increases as the fuel transfer increases as the oscillator is positioned at the same level of the burner dump plane and the flame looks like rod shape out side the fluidics. The higher heat release is at the flame rod centerbody.

Chapter (6)

Conclusion and Recommendations

Chapter (6) Conclusion and Recommendations

1- Conclusion

The present work provides the fluidic oscillator as a mean for emissions reduction at the combustion systems especially in the jet engines and also for reduction of the flow instabilities. The investigated design offers good results at the three mounting positions ($XF=0, 0.5, \text{ and } 1$) inside the swirl stabilized burner which is used in the study. This feedback oscillator is free of maintenance requirements which make it highly appropriate for application in industrial gas turbines and besides it has a long lifetime.

Inserting the oscillator inside the burner as a pilot injector is one of the new ideas which have been clarified at the present study. The challenge was the size restrictions to insert the fluidic oscillator of relatively small dimensions into a swirl stabilized burner. The behavior of the fluid flow (inside and outside the fluidic oscillator) and the performance of the oscillator in active control schemes, which include high frequencies flow modulation, are also studied. The flow field is studied freely outside the oscillator and the interaction of this flow field with the swirl stabilized burner is also inspected. The modulation of dynamic behavior of the fluidic oscillator is performed by the growth of the recirculation flow inside the interaction chamber and the flow structure near step-walls and splitters beside the outlets.

Two design variations are carried out in order to reach the optimum oscillator model design. The first design variation overcomes the size restrictions but was not suitable for working in combustion space because of instability problems according to higher produced frequencies. Design modulations are performed at the 2nd design variation by changing specified factors (depth of fluidics channels, width of exit limbs, throat width and length, throat exit angle, thickness and shape of the fluidics shoulder, width of the feed back channels and angel of outlets) on the produced model from the 1st design variation to find out the optimum models for achieving the required target in combustion field.

At 1st design variation ($Fx0$), the power spectra, recorded for different Re-numbers, demonstrate a dominant peak which clearly scales with the Reynolds number. Frequencies are from 9.89- 11.44 kHz which is too noisy in range of 7468-22404 Re number and does not match the stable combustion requirements. The time history of the velocity oscillations showed very short peak to peak oscillation period for each jet corresponding to the higher fundamental frequency.

At 2nd design variation, four models are modulated from Fx0 and tested to find out the optimum one or more for pilot injector work inside the swirl stabilized burner in reacting flows. The depth of Fx0 rose to 3.75 times as performed in Fx1 while the width of the outlet channels increased to 1.12 times and the feed back channels reduced to 0.8 of the old one at Fx0.

The data evidenced that the fluid flow inside the fluidic oscillator can be modulated by the oscillator itself which is able to generate the oscillated flow without any other means or valves. The time history of the pressure oscillations for both outlets recorded at the vicinity of exit using couple of hot wires which present two sinusoidal signals. These signals, having the same frequency and referenced to the same point in time, are said to be out of phase with each other. The modification parameters reduce the frequency by around 10 times and increase the oscillation period to 11.41 times. Strouhal and Reynolds numbers are in linear relation. Oscillation at this range is characterized by the build-up and rapidly subsequent shedding of vortices and the oscillation is due to the flow instabilities as the Strouhal number is in intermediate range (0.34). Pressure oscillations are in the expected stable range of the reacting flow.

Comparison, between the model used by Guyot (1.87% of Fx1) and Fx1, offers a good matching in the frequencies even with the change of size and the narrow space allowed for the intrusion of the oscillator inside the burner. The fundamental frequencies are in range of stability but with higher amplitudes in comparison to first amplitudes resulted in case of analysis of Guyot model. The frequency contents of the signals at different mass flows offer a linear representation for the whole oscillator designed models. The Strouhal number is in intermediate range and the pressure oscillations lie almost in the safe range far from expected combustion instabilities.

Other control parameters are applied to the design of Fx0 and produce three other models (Fx2, Fx3, and Fx4). The frequency contents of the signals at different mass flows show a linear representation for these oscillator models. Also the pressure oscillations lie almost in safe range of expected combustion instabilities. The Strouhal number is almost linear at a specified range which contains the combustion investigations. The velocity measurements demonstrate that the first fluidics is higher in velocity at the same Re with higher signal amplitudes.

The study of the flow field in the fluidics models using LIF and PIV is performed at a water aquarium. Subsequent applied Fourier transformation produced from the hydrophone signal exhibits a linear relation between the frequency and the volume flow rate. The oscillating period is affected by the volume flow rate as demonstrated from LIF recorded 250 fps data. The

deflection in the jet stream towards the oscillating chamber is according to Coanda effect. The change in the modulation parameters of the different fluidic oscillators has an influence on the oscillating period also. This deflection period may control the industrial applications of the fluidics or may affect the exhaust emissions and instability if used in reacting flows. The first three models offer also a good way of mixing as a result of the interaction between the two jets while the last one is considered a way of that for oscillation with no clear jet interaction at the vicinity of fluidics outlets.

The PIV technique is used to measure the flow field inside and outside the oscillator, and the hydrophone is used to record the sound pressure oscillations resulted from the flow field changes at different mass flows. Defining the internal jet traces, using the flow visualization, is done.

The results from PIV and LIF offer a big similarity between Fx1 and Fx2 oscillators in the flow field but higher vorticity values are noticed at Fx1 (inside and outside). The modulations in the control parameters give the changes in the flow field between Fx1 and Fx3. The vorticity of the issuing jet flow at the vicinity of the oscillator outlet gives in maximum of around one third of the vorticity inside the fluidics channels. The fluid issuing jets from the oscillator Fx4 are pulsed but asymmetric or not fully uniform distributed outside the two outlets. This mixing characteristic highlights the use of the fluidic oscillator Fx1 for fluid mixing applications as well as the use in the targeting work for NO_x reduction at stable reacting flow conditions. From the previous investigations to these four models, Fx1 considers the best design.

First, Fx1 is inserted inside the swirl stabilized burner to study the flow field interaction between the oscillator and the burner. The test of Fx1 is performed in a big water tunnel (3000x 440x 440mm) equipped with PIV technique for measurements of flow field and hydrophone system for detection of pressure oscillations inside the water regimes of the flow field. Three axial locations inside the swirl stabilized burner are investigated; the burner bottom, the middle location and at the burner dump plane. The injection of certain amount of fluid (air or water) inside the oscillator at these three locations suppresses the oscillations and destroys the dominant peak by injecting more than 2.3 % of the main flow for XF= 0, 0.5, and 1. This proves that the fluidic oscillator Fx1 is able to dominate the oscillations produced from the main flow downstream of the burner. Also this considers an indicator of overcoming the instability in reacting flows.

At the burner underside (XF=0), the increase in the fluidics water flow reduces the maximum streamwise velocity outside the burner at the location of the two lobes and increases the

streamwise velocity at the centerline. The interaction between the central jet flow and the main flow is responsible for these changes in the velocities.

At $XF=0.5$, the recession in the streamwise velocity increases higher than in $XF=0$. Starting from $y/D=1$, the streamwise velocity profiles take a bow shape. At this location also the crests and troughs of the radial velocity traces or profiles transferred to almost a linear shape after 4.5% air transfer. The data at the centerline area explains the constancy in the radial velocity profiles after y/D equals 1. The vorticity and shear strain rate reduced at the crests and troughs as the flow increased to 4.5% water transfer. This location has higher turbulent eddies than the previous one at burner bottom. The turbulence increased as the fluidic injector is almost near of the main flow field down stream of the burner exit. The effect of oscillator appears clearly in intensifying the turbulent eddies.

At $XF=1$, higher interaction between the water that flows from the swirl stabilized burner and the water flow generated from the fluidic oscillator as it is very near of the flow field downstream. The streamwise velocity increases by transferring of 4.5% of the main flow at y/D of 0.25 and 0.45 antithesis the last two fluidics locations. The oscillator flow stretches the whole flow field outside the burner. Increase in the vorticity and the shear strain rate in case of raising the injecting flow inside the oscillator depends on the changes in axial streamwise velocity and radial velocity. By increasing the flow transfer inside the fluidic oscillator the flow became complicated and vortices, associated with instability of the azimuthal shear layer, grew stronger. Vortices in the azimuthal shear layer, formed by the azimuthal or swirl velocity, grew and became comparable with vortices in the axial shear layer. The vorticity at 4.5% transfer offers strong helical waves according to the higher turbulence generated from the effect of swirl as well as the fluidics. The fluidics jets effect is noticed clearly at the centerline of the burner. Higher shear strain rates are noticed also at the shear layers and in the middle centerbody flow. This turbulence increases the burning intensity by enhancing the mixing of reactants and the transport of heat besides the wrinkling of flow. But intense of the turbulence eddies can cause local extinction in a turbulent flow and the combustion efficiency is adversely affected. Sequentially, the NO_x and CO are influenced by that besides OH chemiluminescences. The turbulence intensity and structure are affected by the large exothermicity which is one characteristic of combustion reactions while turbulence affects the intensity and extent of reactions in the flow.

A test, by inserting the fluidic injector $Fx1$ inside the swirl stabilized burner, is done trying to find the best position inside the burner to mount the fluidics in order to perform the combustion

operation with low Nox and CO emissions and work in stable conditions. During the combustion test, some transfers are done to the main fuel and air inside the fluidic oscillator trying to enhance the combustion performance at the same equivalence ratio (ϕ) overall during the study between transfer and no transfer cases. The effect of the equivalence ratio is studied at first for the whole mounting locations inside the burner from bottom to top.

At XF=0, the range of ϕ overall was from 0.505 to 0.699 between the lean blow off and very noisy point. The NOx emissions increased to the maximum value at 0.699 of ϕ overall. CO trend declined at around 0.61 and then inclined to higher values. Most of NOx are relating to intermediates produced during the combustion operation which may be an indication to the prompt or fuel nitrogen oxides. The temperature increased around 1.29 times as the equivalence ratio increased to 1.38 times from the lower to the higher selected range. The products of a chemical chemiluminescent reaction like combustion are delivered in an excited electronic state. The reaction is chemically exothermic and accompanied with heat release and light. As the equivalence ratio increases, the heat release increases, and the chemiluminescence is higher especially at the flame two lobes which present two balls of light on the flame boundary.

At XF=0.5, the range of ϕ overall was from 0.528 to 0.699 between the lean blow off and a noisy point. Similar to the previous burner position, the NOx emissions increased to higher values as ϕ overall reached to 0.699. CO trend declined to around 0.61 and then inclined similar to the previous case at zero location. Same as the previous location at the bottom of the burner and at the same conditions of equivalence ratios, the oxidation process is in directional proportion with the increase of ϕ overall. The luminous part of flame, like zero location, is lighter at the shear layer zone at ϕ overall of 0.699 while at the other parts is similar to the burner bottom position and the reaction offers similar chemiluminescence.

At XF=1, the Effect of ϕ overall at constant main air mass flow is investigated. The nitrogen oxides are in directional proportion to the increase of ϕ overall with no drop at around 0.6 as the previous two positions but for CO is the same.

Transfer of Fuel inside the fluidics at constant main air and at constant ϕ overall of 0.552 is done to demonstrate the effect of this fuel transfer on the emissions and temperature. At XF=0, the higher the pilot fuel ratio is, the higher the chemiluminescence is. Also, NOx emissions increase to 6.84ppm at the maximum pilot fuel ratio while CO decreases around 7 times of its value at no

transfer. At $XF=0.5$, the fuel transfer exhibits bad results in emissions reduction. At $XF=1$, unlike at the middle location inside the burner, the oscillator gives results similar to the base line. Investigation of the flame behavior at this location with fuel transfer gives good results in CO reduction until 14% of the main fuel while the nitrogen oxides trace shows further increase as base line.

Transfer of air inside the fluidic oscillator from the main line at constant main fuel and at constant ϕ overall of 0.552 and 0.575 is also performed to clarify the air transfer only on the performance of the designed oscillator in reacting flows. The nitrogen oxides decrease by pilot air ratio increase while CO reduces at $XF=0$ and the emission of light in the form of chemiluminescence is dimming as the air transfer increases. At $XF=0.5$ and ϕ overall of 0.552, the air transfer reduces the NOx emissions but until ϕ normal =0.557 and the carbon monoxide takes an increasing trend. The temperature is almost constant at 1300°C at the whole transfer percentages. The transfer of air at ϕ overall 0.575 gives good results in NOx reduction at no increase of CO. This still give the air transfer the best merit between different transfer methods. NOx reduction at ϕ normal of 0.583 is sharp and noticed. The OH chemiluminescences give no bright light as the air transfer increases gradually to 2.73% of the main air which coincides with the previous results at ϕ overall= 0.552. At $XF=1$, the value of ϕ normal increased from 0.552 to 0.567. Reduction in NOx up to almost zero is reached by injection of transferred air inside the oscillator. CO also reduced and its value at the end transfer point was 2ppm while CO₂ was at 3.5%.

Mix of air and fuel transfer is done also to study this effect on the oscillator performance at constant ϕ overall of 0.552. At $XF=0$, the pilot air ratio inside the fluidics is between 0% and 2.73% of the main air while 14% of the main fuel is transferred and injected together with transferred air. Decline in NOx curve is noticed and very low CO also produced. Unlike the fuel transfer only, the NOx reduces to almost 30% of its value at the maximum air transfer (2.73%) by injecting 14% of the main fuel together with this air transfer. CO is almost constant at about 0.4ppm which is very low in comparison to the fuel transfer only as it was at 2.6ppm and reduced by fuel transfer like that case. NOx emissions reduce also by increase of air transfer similar to the air transfer without fuel and there is a merit in suppression of the higher CO to very low values. Injection of air and fuel together dims the flame luminosity slightly as the air increases from 0% to the maximum one.

The percentage of pilot fuel increased from 14% gradually to double and triple times this value at the increase of the air inside the fluidics. The increase of the pilot fuel ratio to 28% of the main fuel at 0% air transfer increased the NO_x emissions more than 60% of its value at 14% pilot fuel ratio but still decreases with air transfer increase. CO has marginal changes in comparison to the 14% pilot fuel ratio. The transfer of fuel to 42% of the main fuel raises the NO_x emissions to almost double the value at 14% pilot fuel ratio. CO also rises gradually as the air transfer increases. Finally, as the air transfer increases the NO_x emissions decrease and the flame luminosity decreases. The increase in pilot fuel ratio more than 14% induces bad results and is not desired.

At XF=1, the transfer of fuel only offers arising in NO_x emissions. The Flame rotates from the burner bottom around the oscillator as the fuel increases and looks like Lotus flower. By mixing some fuel with air inside the fluidics, reductions in NO_x and CO are noticed but not lower than at the air transfer only which offers the best conditions for emissions reduction. The flame length increases as the fuel transfer increases while the oscillator is positioned at the same level of the burner dump plane and the flame looks like rod shape out side the fluidics. The higher heat release is at the flame rod centerbody.

Finally, the air transfer considers the best and the optimum way to reduce the emissions at the whole mounting locations. Some small amounts of pilot fuel ratio besides air may be also useful in nitrogen oxides reduction at low values of carbon monoxide. This also widens the flammability limit and sustains the flame at some reacting conditions which may have lean blow off or extinction of the flame at the same equivalence ratio without using of the oscillator. From the results, it is expected that the fluidics under test will work better with some new or other burner configurations at different positions inside the burner.

The fluidics model at the mentioned conditions participates in emission reduction which in turns enhances the combustion and complies with the environment laws at the whole world.

2- Recommendations

It is recommended to test the model inside different types of burners (oil or gas burners used in gas turbines, industrial and marine boilers, aircraft and marines) to achieve the stability and emissions reduction in reacting flows.

The present oscillator may be useful if injected liquid fuels which are burnt at reacting flows. It may achieve succession in dispersion of liquid fuels (light and heavy) in the liquid burners. The oscillator outlets are free of the small orifices diameter that may lead to coagulation of fuel inside it, especially at heavy liquid fuels. Some changes have to be done to match the liquid fuels and spray production. Spray formation and liquid atomization have to be investigated in order to unravel the mechanisms involved in the liquid breakup, atomization, mixing and evaporation, and spray drop dynamics especially to face the requirements for combustion. The spray behavior is determined at this case depending on studying the spray characteristics. These characteristics include mean drop size, drop size distribution, drop velocity, patternation, cone angle, dispersion and penetration (see detailed explanation to these characteristics at Emara 2004). The recommended measuring technique is the Phase Doppler particle analyzer which is a drop sizing technique used for this purpose besides the emissions analyzer, the thermocouples and chemiluminescences sensors.

In intermittent combustion, the fluidics may be used for injection inside diesel fuel engines.

The model as a mean of pulsated flow with different frequencies may be used in cooling of the jet engine exhaust and in mixing of gases. The oscillator can be used also in the application of cyclically repetitive momentum or pressure forces to various materials, structures of materials, in liquid dispersion. It is a useful mean also in medical purposes.

It may also be used in production or processing (drying, cooling, spray reactions, and atomized suspension technique). It is also recommended to be used in treatment (evaporation and aeration, cooling (spray ponds, towers, reactors, etc.), humidification and misting, air and gas washing and scrubbing, and industrial washing and cleaning). It may be effective also in coating (surface treatment, painting (pneumatic, airless, and electrostatic), insulation, multicomponent resins (urethanes, epoxies, polyesters. etc.), and particle coating and encapsulation)

In miscellaneous fields it can give a good use as in dispersion of chemical agents, agricultural spraying (insecticides, herbicides, fertilizer solutions, etc.), fumes and fog suppression, printing, and acid etching.

References

- Airflow Instruments, TSI Instruments Ltd., "Turbulence Intensity Measurements", UK, 2008.
- Albrecht, P., Bade, S., Paschereit, C.O., Gutmark, E., "Avoidance strategy for NO_x emissions and flame instabilities in a swirl-stabilized combustor", AIAA20091059 paper, 2008
- Albrecht, P., Bauermeister, F., Bothien, M., Lacarelle, A., Moeck, J., Paschereit, C. O., and Gutmark, E., "Characterization and control of lean blowout using periodically centered flame balls", ASME paper GT2006- 90340, Barcelona, Spain, 2006.
- Arnhold, J., Mueller, S., Arnold, K., and Grimm, E., "Chemiluminescence Intensities and Spectra of Luminol Oxidation by Sodium Hypochlorite in the Presence of Hydrogen Peroxide", John Wiley & Sons, Ltd, 1991.
- Bauer, P, "Fluidic oscillator with resonant inertance and dynamic compliance circuit", United States Patent, USA, 1981.
- Duffin, J., "Fluidics and pneumatics principles and applications in anesthesia" Canada Anaesth. Soc. J., vol. 24, no. 1, January 1977.
- Duwig, C., Fuchs, L., Lacarelle, A., Beutke, M., and Paschereit, C. O., "Study of the vortex breakdown in a conical swirler using LDV, LES and POD", ASME paper GT2007- 27006, Montreal, Canada, 2007.
- Emara, A., "Characteristics of the Conical Fuel Spray in Co-axial Burners", Helwan University, Cairo, Egypt, 2004.
- Emara, A., Lacarelle, A., Paschereit, C. O., "A study of the flow field in reacting and non-reacting conditions in a swirl inducing burner", ICJWSF, Cincinnati, Ohio, USA, 2010.
- Emara, A., Lacarelle, A., Paschereit, C. O., "Pilot Flame Impact on Flow Fields and Combustion Performances in a Swirl inducing Burner", AIAA 2009-5015, August 2009, Denver, Colorado, USA.
- Follows, P., Williams, M., and Murray, P., "Applications of Power Fluidics technology in nuclear waste processing plants", WM'05 conference, Tucson, 2005.

- Guyot, D., Bobusch, B., and Paschereit, C. O., "Active Combustion Control Using a Fluidic Oscillator for Asymmetric Fuel Flow Modulation", AIAA paper 2008-4956, Hartford, CT.
- Griffin, W.A., and Almeida, S.M., "Pulsation nozzle, for self- excited oscillation of drilling fluid jet stream ", US Patent 5495903, 1996.
- Giles, B.D., "Fluidics, the Coanda Effect, and Some Orographic Winds", Springer-Verlag, 1977.
- Gregory, J. W., "Development of fluidic oscillators as flow control actuators", Purdue university, USA, 2005.
- Gregory, J.W., Sakaue, H., and Sullivan, J.P., "Fluidic oscillator as a dynamic calibration tool", AIAA 2002-2701, St. Louis, Missouri, 2002.
- GRAS sound & vibration, "1/4" Preamplifier Type 26AC, General-purpose", GRAS Denmark, 2009.
- Guyot, D., and Paschereit, C. O., "Active control of combustion instability using symmetric and asymmetric premixed fuel modulation", ASME paper GT2007-27342, Montreal, Canada, 2007.
- Guyot, D., Paschereit, C. O., and Raghu, S., "A fluidic actuator for active combustion control", GT50797, Berlin, Germany, 2008.
- Ian J. S., "Oscillatory flows at intermediate Strouhal number in asymmetry channels", Journal of Fluid Mechanics 125, pp. 359-373, 1982.
- Kirshner, J.M., "AGARDograph No. 215 on Fluidics Technology", AGARD, Technical editing and reproduction Ltd, London, 1976.
- Lacarelle, A., Luchtenburg, D. M., Bothien, M. R., Noack, B. R., and Paschereit, C. O., "A combination of image post- processing tool to identify coherent structures of premixed flames", ICJWSF, Berlin, Germany, 2008.
- Lacarelle, A., Faustmann, T., Greenblatt, D., Paschereit, C. O., Lehmann, O., Luchtenburg, D. M., Noack, B. R., "Spatio- Temporal Characterization of a Conical Swirler flow field under strong forcing", ASME paper GT2008- 50970, Berlin, Germany, 2008.

- Law, K.C., "Combustion Physics", Cambridge university press, UK, 2006.
- Liang, H., Maxworthy, T., "An experimental investigation of swirling jets", J. Fluid Mech. (2005), vol. 525, pp. 115–159. c_ 2005 Cambridge University Press.
- Nakayama, A., Kuwahara, F., and Kamiya, Y, "A two-dimensional numerical procedure for a three dimensional internal flow through a complex passage with a small depth (its application to numerical analysis of fluidic oscillators)", International Journal of Numerical Methods for Heat & Fluid Flow, Volume15, pp: 863-871, 2005.
- Rankin, D.D., "Lean Combustion", Elsevier, 2007.
- RESON, "Hydrophone TC4013- Miniature Reference Hydrophone", RESON A/S, Denmark, 2005.
- Tilury, K.C., "Chemiluminescence from the oxidation of model lipid systems", School of Chemical and Physical Sciences Victoria University of Wellington, PO Box 600, Wellington, New Zealand, 1999.
- TSI incorporated, "Operating Manual for TSI IFA-100 Constant-Temperature Anemometer", St. Paul, USA, 1995.
- Webster, J.G., "Measurement, Instrumentation, and Sensors Handbook", CRCnetBase, UK, 1999.
- Weiss, J., "Oxidation and Chemiluminescence", University of Durham, Department of Chemistry, King's College, Newcastle-upon-Tyne, 2, UK, 1938.
- Yang, J., Chen, C., Tasi, K., Lin, W., and Sheen, H., "A novel fluidic oscillator incorporating step-shaped attachment walls", Elsevier, 2006.
- Yang, J., Lin, W., Tsai, K., and Huang, K., "Fluidic Oscillator", US 6,860,157 B1, 2005.

Part (2)

Pilot injector influence on Flow Field Interaction and Combustion characteristics in a Swirl stabilized Burner

Chapter (1)

Introduction

Chapter (1): Introduction

Gas turbine manufacturers have developed and continued to enhance lean premixed combustion systems to comply with emissions regulations for NO_x, carbon monoxides, and unburned hydrocarbons. Most of gas turbine injectors make swirl configurations that produce a central toroidal recirculation zones to provide the dominant flame stabilization mechanism (Yang 2005). Swirl increases fuel-air mixing, improves flame stabilization, and has a strong influence on flame characteristics and pollutant emissions (Emara 2009). The use of swirl to stabilize the reaction is taken of design practice from combustors designed to operate stoichiometrically. As such, the central recirculation zone provides a low velocity region that allows the reaction to anchor. Such strong swirl also causes high strain on the reaction.

The demand for gas turbine engines with reduced emission levels, stable combustion conditions and low specific fuel consumption is the goal at the past two decades (Rankin 2007). Combination of prior requirements is the way to an efficient combustion (Seyfried 2007). Strategies for reducing NO_x emissions from engines have been developed over these decades to comply with environmental concerns and government regulations. For power generation, premixed gas turbine combustors need to be operated as lean as possible to secure sub-10 ppm concentrations of NO_x emission. In a combustor under fuel-lean conditions, achieving stable combustion requires overcoming several inter-related problems such as flame stabilization, flame stability and extinction, and combustion oscillations or thermoacoustic instabilities which depend on the boundary conditions of the engine.

Thermocoustic instabilities can arise if pressure amplitude oscillations $p'(t)$ are in phase with heat release fluctuations $Q'(t)$ and if the acoustic energy E exceeds the dissipation losses. This can be summarized by the

$$Q' \propto p' \Rightarrow E = \int \int_{V_t} p' Q' dt dV > 0 \quad \text{may be unstable (Bellucci 2008)} \quad (1)$$

Some significant stability and noise control breakthroughs have been developed by the gas turbine designers but it still in instability ranges and produces significant noise levels that must be mitigated or reduced to make these engines compatible with either environmental or occupational regulatory noise requirements (Giampaolo 2003). To suppress combustion oscillations some modifications are taken in consideration. These modifications are constriction of duct, use of

resonators, use of sound absorbent material, modified sudden expansion, modified disk-type flame holder and modified fuelling arrangement.

It is common to rely on a pilot injector to operate lean premixed gas turbines. The pilot fuel allows the reaction to continue even if the reaction produced by the main fuel/air mixture starts to suffer some degree of instability. The pilot is generally directed into a strategic location in the combustor to enrich a region that will help sustain the reaction. A common location is along the centerline into a recirculation zone (Rankin 2007). Numerous experimental works have been performed to control or characterize combustion instabilities on the swirl stabilized burner (Albrecht 2008, Lacarelle 2008, and Paschereit 1999). Different pilot fuel injection types and locations have been tested and showed for several configurations positive results regarding NO_x and stability. An axisymmetric mode matching the $\frac{1}{4}$ wave of the resonance tube was typically occurring and dominated the instability mechanism. Phase averaged flame visualization showed that the flame is oscillating between two positions; one located inside the burner and the other located at the outlet of the burner. The oscillation of the flame position leads to an oscillation of the flame surface at the fuel injection location, generating fuel air ratio oscillations. Fuel air ratio fluctuations lead to oscillation of the heat release, which feeds the thermoacoustic cycle and may sustain combustion instabilities.

Albrecht is stabilizing the flame by a pilot fuel injection only. When switching on the pilot fuel, the flame stabilizes in numerous cases inside the burner, leading the diffusion like flame. This flame, when it is stable, has the disadvantage to generate high NO_x emissions. To circumvent this problem, Albrecht proposed to use premixed pilot fuel injection as well as pulsated pilot fuel injection and decreased successfully the NO_x penalties compared to a standard pilot injection (Albrecht 2008). Lean burn combustors comprising round sudden expansions use a pilot stream at the core to stabilize an otherwise lean flow (Rankin 2007).

The present part of thesis work investigates the changes induced by pilot injections in the main flow field at reacting and non-reacting conditions in a swirl stabilized burner. The behavior of these injections, regarding stability and NO_x and CO emissions in that burner, is studied also at several acoustic boundary conditions represented in the combustion chamber length (short and long). These changes are affecting the flame stability especially in the lean premixed combustion due to large structures resulting from the vortex breakdown and the swirling shear-layers.

The pilot injector is mounted on the centerline inner the burner, upstream of the internal recirculation zone. The arts of injection (fuel only, air and fuel premixed, and air only) as well as the shape and axial location of the injector are exhaustively investigated at different overall equivalence ratios.

Two different pilot injectors are used: a single injection pilot and a multi injection pilot. The single injection pilot contains a single hole with diameter of 5mm. The multi injection pilot has 5 holes of 1 mm orifice diameter one at the center and 4 holes of 45° around it. Three pilot locations inside the burner are tested (X_p/X_{max} = 0, 0.5, and 0.68).

Forcing the flame to stabilize outside the burner should be regarding NO_x emission positive, as it ensures a long enough mixing path of gas and air, and would also prevent the oscillating movement of the flame which could lead to strong instabilities. To achieve this, a new pilot injector is designed where a high amount of air is injected through a reduced number of holes. The strong jet momentum thus achieved, has a strong impact on the flow field and should make possible to force the flame to stabilize outside of the burner, preventing instabilities and ensuring low NO_x emissions. Different pilot injectors are tested and the multi injection pilot showed good results in stability without NO_x penalties (Emara 2009).

A detailed PIV measurements are performed downstream of the burner and reveal the pilot impact on the mean flow field at the stabilized locations. A microphone is mounted 411 mm upstream of the burner and allows for identification of the acoustic pressure oscillations corresponding to the flow downstream of the combustion chamber.

Chapter (2)

Experimental Techniques and Facilities

Chapter (2): Experimental techniques and facilities

2.1. The Burner

A full size conical swirl burner, designed by ABB with a cross-sectional area expansion ratio of 4 for flame stabilization, is the burner under investigation (Fig. 2.1-left). It consists of two half cones shifted with respect to each other in radial direction (Guyot 2007). Each cone-half diameter at the outlet is $D = 82$ mm. The airflow enters the cone circumferentially through two lateral inlet slots of constant width. This generates a strong azimuthal velocity component resulting in a high degree of swirl (Swirl no. = 0.7). Together with the area dump at the burner outlet, this leads to a vortex breakdown near the burner mouth followed by a recirculation zone where the flame may be stabilized aerodynamically (Duwig 2007). Through the reacting flow, mixing of swirling air and main fuel, results in nearly premixed combustion (Albrecht 2006).

A natural helical flow structure corresponding to a helical instability could be observed at the burner outlet in isothermal and reacting cases (Lacarelle 2008). The recirculation of hot combustion gases at reacting conditions leads to a second oxidation and in turns a reduction of carbon monoxide. Flow instabilities are the disadvantages of this type of flame stabilization and accompanied by complex three-dimensional coherent structures (Lacarelle 2008).

Typically, gas or liquid fuel is injected through the pilot to influence the combustion. The work performed by Albrecht shows that the premixing of fuel and air may have a positive impact on the stability and NO_x emissions of a premixed swirl inducing burner (Albrecht 2008). The typical fuel staging, presented by Alstom, deals only with the injection of fuel through the pilot lance in order to increase the control authority on pulsations and emissions. The fuel injection in this case has a marginal impact on the flow field. In this work, a specially designed pilot injector is tested and shows that a strong jet momentum with a lean pilot injection can help to stabilize the flame.

Two different pilot injectors are used: a single injection pilot and a multi injection pilot. The single injection pilot is a single hole with diameter of 5mm. The multi injection pilot injector has 5 holes of 1 mm diameter one at the centerline and 4 holes of 45° distributed circumferentially around it (see Fig. 2.1- right). The single injection pilot remains unchoked in the whole range of air mass flows considered (<20 kg/h at 20°C) while the multi injection pilot is choked for air mass flows superior to 5.5 kg/h (20°C). The pilot lance is prepared to move easily from the burner underside to the burner dump plane.

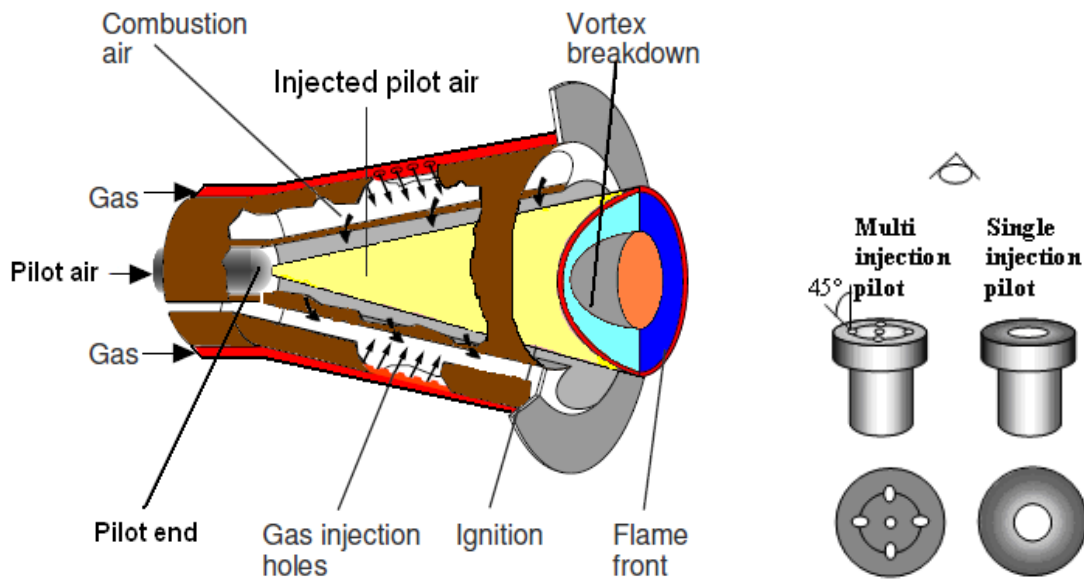


Figure 2.1: Sketch of the Swirl Stabilized Burner (left) and the pilot injectors (right).

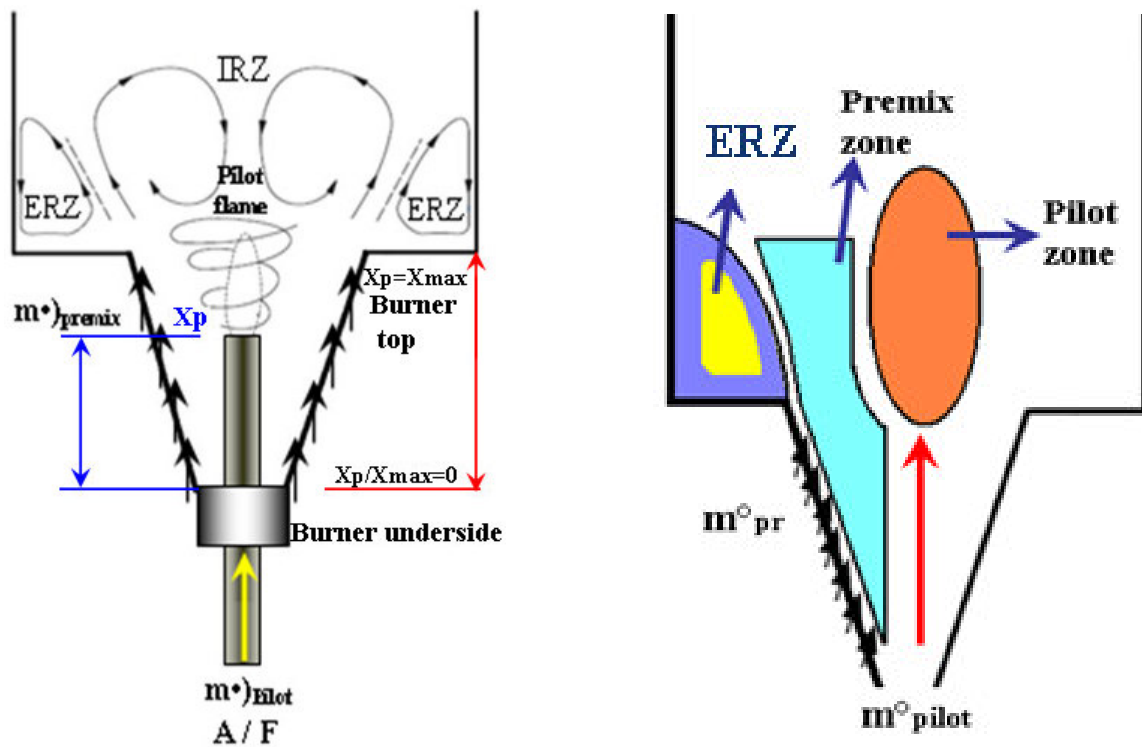


Figure 2.2: Sketch of the Swirl Stabilized Burner flow (left) and flame zones (right).

Figure 2.2 exhibits two sketches for flow zones and flame zones. As shown in the figure, the pilot can move from up to down in length of $X_p=X_{max}$. Pilot injection at the burner centerline serves to force the flame to stabilize outside the burner. Three flow zones are noticed in the left figure. First one is the internal recirculation zone which resulted from the swirl configurations. The flow inside this region is associated with high shear rates and strong turbulence intensities resulting from vortex breakdown. The second zone is the corner recirculation zone and constructed between the burner dump plane and the silica glass lower combustor surface. The third is the pilot flow zone which is on the burner centerline. In reacting flow, three flame zones are shown in the right figure: the premix zone, the mixing zone, and the pilot zone.

2.2. The test facilities

All measurements were performed in the combustion laboratory in HFI- TU Berlin. The test facility is illustrated in Fig. 2.3.

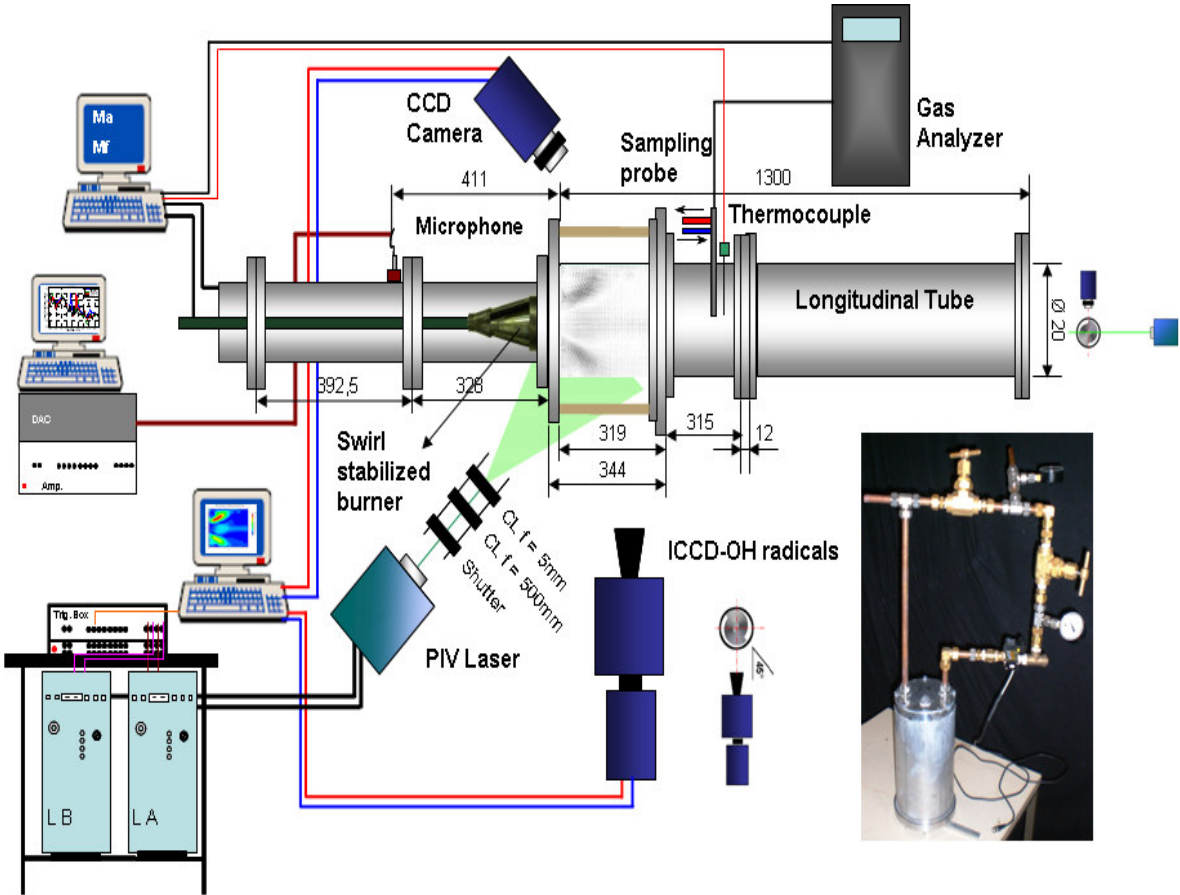


Figure 2.3: Schematic of the test facility accompanied with Photo of the powder disperser.

The burner is mounted just upstream of the combustion chamber. The first part of the combustion chamber is a silica tube of 3.66 D height and 2.44 D diameter followed by a steel tube giving a length of 8.17D from the burner dump to the combustion chamber outlet. A second longitudinal tube can be placed on the top of the steel one to increase the length to 15.85D to simulate other practical conditions. An electrical pre-heater can be used to provide certain air inlet temperatures and in turns resulting in a highly stable reaction with high heat release. Coriolis mass meters are used for the mass flow measurements of the pilot fuel and air and the main fuel, while the air mass flow was measured by a laminar flow element. All mass flows were set by metering valves and a constant mass flow could be achieved within a tolerance of 5 %.

2.3. Thermocouple and emissions probe setup

K-type thermocouples with 1.5 mm diameter were used to measure the temperature of the preheated air upstream and the exhaust temperatures at 0.6 m downstream of the burner exit. The water-cooled emissions probe was located 0.6 m downstream of the burner exit and consisted of 0.3 m long tube with 10 mm diameter. A heated tube with a length of 12 m is used to connect the analyzer system. NO and NO₂ were measured wet while CO, CO₂, and O₂ were measured dry. All presented emissions results in this study are normalized on 15 % O₂ Volume dry.

2.4. Microphone setup

The used microphone is GRAS- type 26AC- S7. It is a general purpose ¼" preamplifier with 5m cable terminated in a 7 pin LEMO 1 B plug. The frequency range (± 0.2 dB) is 2Hz- 200 kHz. It has a flat pressure frequency response in its entire frequency range. It is calibrated by using a Brüel& Kjaer Pistonphone type- 4228 at reference frequency 250 Hz and nominal gain of 124dB and the sensitivity was 1.152mV/pa (GRAS 2009). The microphone is mounted 411 mm upstream of the burner and allows for identification of the acoustic pressure corresponding to the flow downstream of the combustion chamber. At this position, it is still possible to record pressure oscillations induced by the flow field in the combustion chamber.

2.5. ICCD setup

Recordings of the OH- Chemiluminescence of the flame were obtained with an ICCD camera equipped with a bandpass filter centered at 312 ± 2 nm (Albrecht 2008). The wavelength range matches OH radical emission spectrum, which has a maximum at 306.7 nm. High emitted light

areas or higher in legend counts of the camera pictures represents the maximum intensity of OH radicals and lower emitted light areas are the minimum as explained in the fluidic oscillator part.

2.6. PIV Setup

A Continuum Minilite standard Nd: YAG PIV laser system (wave length 532nm), with pulse energy of up to 25 mJ per pulse was used to form an axial light sheet perpendicular to the plane formed by the slots of the burner. Beam thickness up to 2 mm, was used to form two 532 nm laser beams separated by an optimum time interval selected depending on the pictures quality. The system offers excellent beam quality, long term stability and increased overall reliability. The dual pulses have the same spatial overlap, energy, beam uniformity, polarization and symmetry. The time interval was regulated by an Optical flow systems TC 412 triggering box which directly controls the ash lamp and Q switch of the laser. A convex cylindrical lens ($f=5\text{mm}$) and a concave cylindrical lens ($f = 500\text{mm}$) were used to generate a sheet of approximately 2mm thickness in the combustion chamber for visualizing the flow. The time interval between the two laser pulses was set to $\tau = 10 \mu\text{s}$ with repetition rate of 4 Hz for 220 kg/h as main air. A total of 500-750 snapshots were recorded to ensure the convergence of the mean and RMS values for isothermal cases but at maximum of 300 at thermal conditions for the difficulties of the measurements in combustion atmosphere and the powder seeding generator problems. A beam shutter is mounted at an arbitrary distance in a position close to the Laser beam exit before the cylindrical lenses and has an aperture thereon which when the shutter pin is rotated to the proper position, permits passage of the light there through (ILA 2005).

Liquid tracer particles (SiO_2 , $0.8 \mu\text{m}$ \varnothing , Merck) were used to seed the flow field at cold cases. Powder tracer is designed and manufactured in the institute of Fluid Dynamics and Engineering Acoustics, University of technology Berlin by the author. The volume capacity is 0.53 m^3 and the nominal maximum pressure is 6bar. TiO_2 particles (Merck) were used to seed the flow field in reacting flows. These particles are injected far upstream of the measurement plane to ensure homogenous mixing of the particles at gage pressure in between 0.6 to 1.2 bar. ILA-CCD camera type: SensiCam, 12 bit cooled imaging (1280x1024 pixel resolution) is used to capture the double frame. The camera is equipped with a short focal lens Sigma 28mm -1:1.8D to cover the whole flow field and another one of 55 mm to investigate one half of the flow field and increase the spatial resolution. A bandpass interference filter centered around 532 nm and is used to reject surrounding light. The light sheet illuminates the small tracer particles that seed the observed

flow region in a homogeneously distributed way and are also sufficiently small to follow the fluid motion with no altering the fluid properties or flow characteristics (Tropea et al. 2007).

For post processing of the data, cross correlation and adaptive cross correlation algorithms were used with an interrogation window size of 16×16 pixel and 50% overlap for higher spatial resolution. To improve the spatial resolution, decreasing the size of the interrogation spot is known to be a common procedure as it is clearly related to the minimum size of the correlation window that can be used in the image interrogation. To eliminate spurious vectors, local median velocity filters and linear interpolations were used (Lacarelle 2008) and (Scarano 2002).

The accuracy of correlation depends on a number of factors like: random, acceleration, gradient, bias, and tracking errors. Random error is due to noise in the recording and subsequent interrogation of PIV images. The cause of the acceleration error is the approximation of the local Eulerian velocity from the Lagrangian motion of tracer particles. The rotation and deformation of the flow within interrogation spot result in the gradient error which also has random and bias components. Bias errors due to the choice of the correlation peak detection scheme. The inability of the particle to follow the flow without slip results in the tracking error (Boillot 1996). A frame grabber card was used in conjunction with VidPIV software to digitize the images.

One difficulty of applying PIV in non-reacting and reacting flow conditions with round glass surfaces comes from the total reflection of a certain part of the laser light inside the glass. This reflection leads to over-exposure of the CCD chip and thus to velocity outliers in the PIV processing. If some of the minor reflections could be minimized through background subtraction, a major reflection was visible at the main flow field which may lose some data but can be treated by making some mathematical interpolations.

Chapter (3)

Results and Discussion

Chapter (3): Results and Discussion

3. 1. Control Authority and Combustion Characteristics

A. Injection of pilot fuel and premixed pilot fuel

A.1 Stability by Pilot fuel at short combustion chamber

Some investigations are performed to the burner in short combustion chamber ($L=8.17 D$) during the injection of pilot fuel and proved at lean mixtures ($\Phi_{\text{overall}}=0.552$) that the baseline combustor with no pilot injection and at $X_p/X_{\text{max}}=0$ is remaining stable. The test is performed at different axial locations from burner bottom to burner dump plane. The RMS values of the pressure oscillations are used as an indicator to the combustion instability. For RMS values smaller than 0.8, the combustor is stable, see Fig. 2.4.

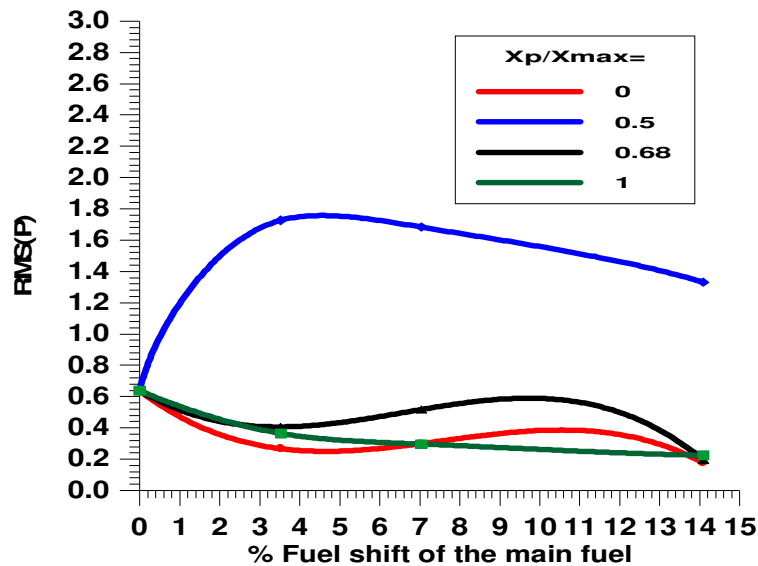


Figure 2.4: P_{RMS} (v) at different pilot locations for the short combustion chamber.

Values above unity are considered unstable and present a clear dominant peak in the power spectrum density as shown in Fig. 2.5. The figure shows the consistency of the pressure spectra and OH^* spectra (measured by photo multiplier of OH) at the unstable location ($X_p/X_{\text{max}}=0.5$) and stable locations ($X_p/X_{\text{max}}=0, 0.68, \text{ and } 1.0$) (Emara 2010).

From these four injection locations at 7% pilot fuel ratio, only $X_p/X_{max}=0.5$ injection location shows an unstable behavior, generating higher NO_x emissions (see Fig. 2.6). A dominant peak at 159 Hz at pressure spectrum and OH* spectrum is noticed as a result of the instability. For the other injection locations, the increase of pilot fuel injection leads to a typical decrease of pressure oscillations or combustion noise.

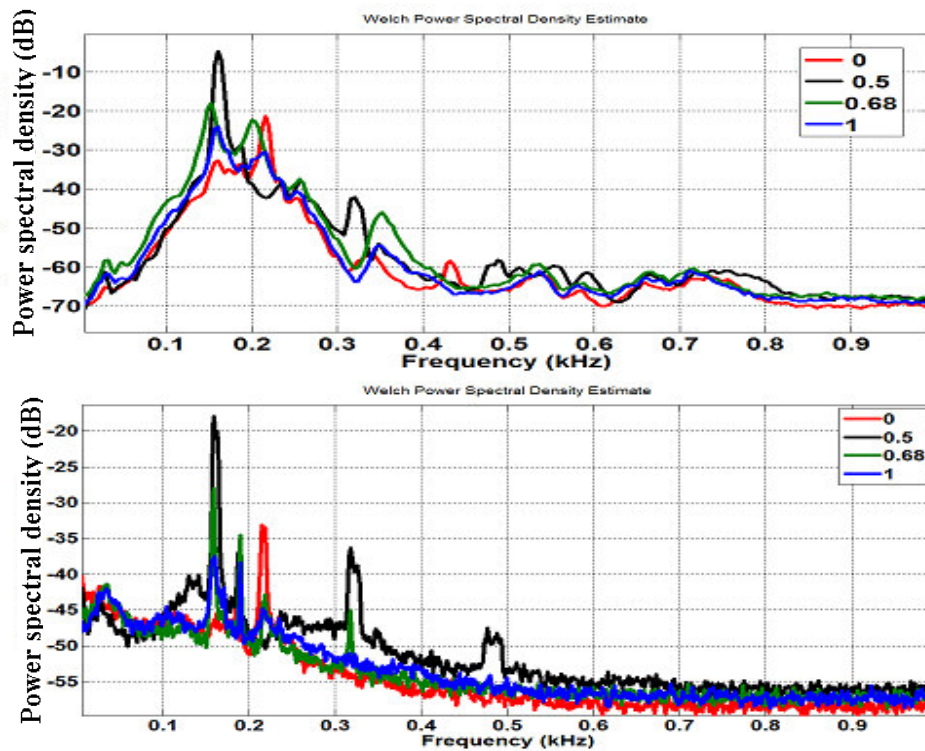


Figure 2.5: Pressure spectra (top) and OH* spectra (bottom) for different X_p/X_{max} at 7% pilot fuel ratio for the short combustion chamber.

At the same time, NO_x emissions increase as the pilot fuel injection increases which leads to a decrease in the mixture quality. The best injection location regarding low noise, low NO_x, and low CO emission is the baseline one at $X_p/X_{max}=0$ (Fig. 4, 6 and 7).

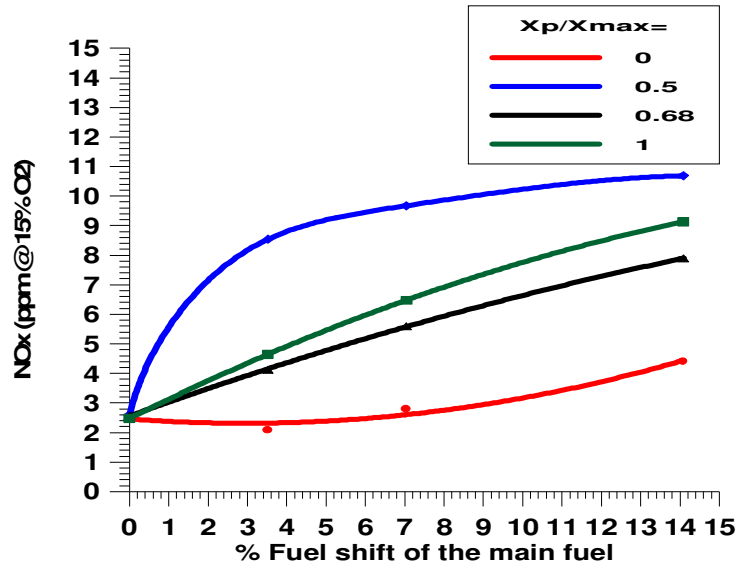


Figure 2.6: NOx (ppm) ref. to 15% O₂ at different pilot locations for the short combustion chamber.

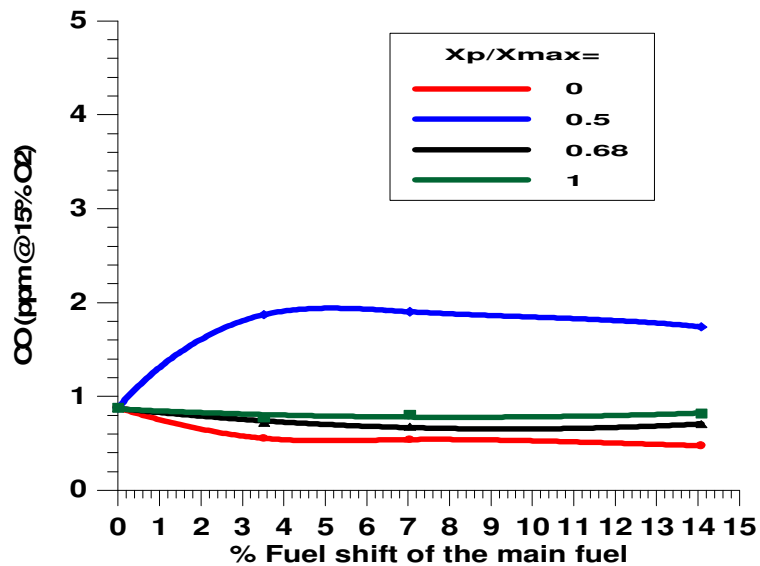


Figure 2.7: CO (ppm) normalized to 15% O₂ at different pilot locations.

Electronically excited oxygen species give rise to most of the chemiluminescence (Tilury 1999). The existence of OH expresses the oxidation in the combustion reaction and accompanied by the chemiluminescence. For that, the images captured from the OH chemiluminescence camera system are effective to express the heat release of the combustion reaction depending on the oxidation process. OH* chemiluminescence images are shown at Fig. 2.8 for different pilot fuel injection ratios. It demonstrates the effect of pilot fuel injection on the flame in the shape of heat release accompanied with the flame luminosity. The products of a chemical chemiluminescent

reaction like combustion are delivered in an excited electronic state. Because the reaction is a chemically exothermic, it is accompanied with heat release and light. As the pilot fuel injection increases, the heat release increases and the OH* chemiluminescence is higher especially at the flame lobes, which offer a higher light on the flame boundary, and leads to an anchoring of the flame at the pilot lance end (Fig. 2.8).

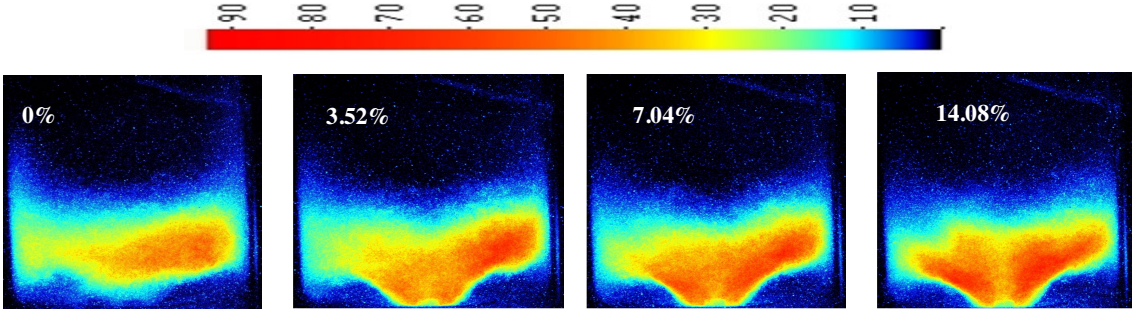


Figure 2.8: OH- chemiluminescence at different pilot fuel mass flows and at the burner apex.

A.2. premixed pilot fuel injection at short combustion chamber

To reduce the instability and enhance the combustion performance for $X_p/X_{max}=0.5$, a small percentage of the main air (0.45% of the main air), just for tuning, was transferred through the pilot injector and mixed together with the fuel in pilot injector. The stable cases remained as before, and a slight decrease of the instability level at the location of $X_p/X_{max}=0.5$ is obtained compared to the pure injection of fuel (Fig. 2.9 and 2.10). It is better for the whole locations in the stability compared to the last case.

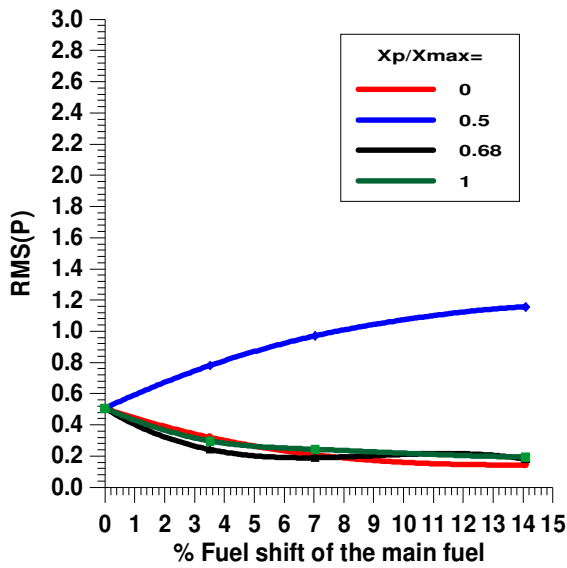


Figure 2.9: RMS P at different pilot locations and at 0.45% pilot air ratio.

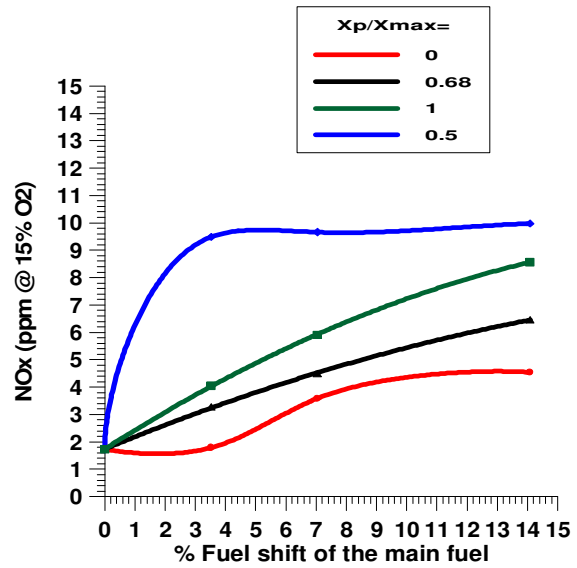


Figure 2.10: NO_x ref. to 15% O₂ at different pilot locations and at 0.45% pilot air ratio.

See also Fig. 11, it proofs that the transfer of pilot air accelerates to stability faster than the case with pilot fuel only at 8.17 D short combustion chamber and at using of multi injection pilot end.

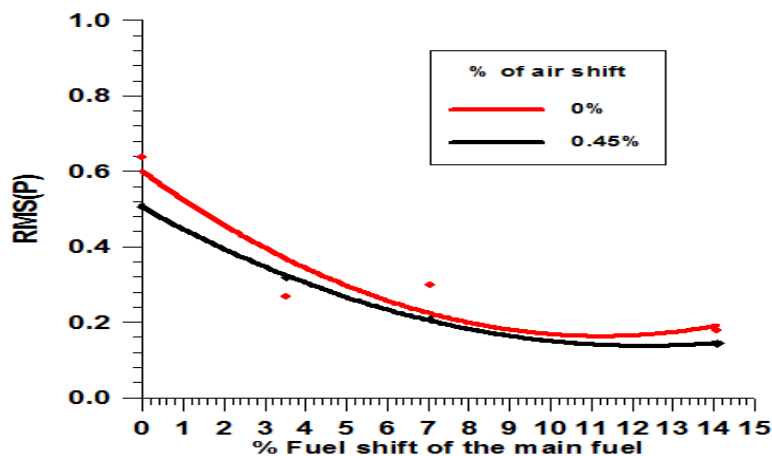


Figure 2.11: P_{RMS} (v) at different pilot air mass flows at $X_p/X_{max}=0$.

The pressure and OH* spectra presented at Fig. 2.12 show that the unstable case for position $X_p/X_{max}=0.5$ can be stabilized by injecting more air through the pilot lance transferred from the total air mass flow.

Two strong peaks are present around 160Hz and 220Hz. The peak around 320Hz corresponds to the helical structure of the flow field evidenced in previous investigations. An increase of air injected through the pilot for the unstable case decreases the main peak by 20dB. It also suppresses completely the peak of the helical structure, suggesting that the multi injection pilot strongly affects the coherent structure. These results show that the unstable case at $X_p/X_{max}=0.5$ could be stabilized by increasing the pilot air ratio ($\Phi_{overall} = \Phi_{inj}$), and the methodology was further applied to the other equivalence ratios and boundary conditions. $\Phi_{overall}$ is calculated from the total fuel and the main air while Φ_{inj} is calculated from the pilot fuel and injected pilot air.

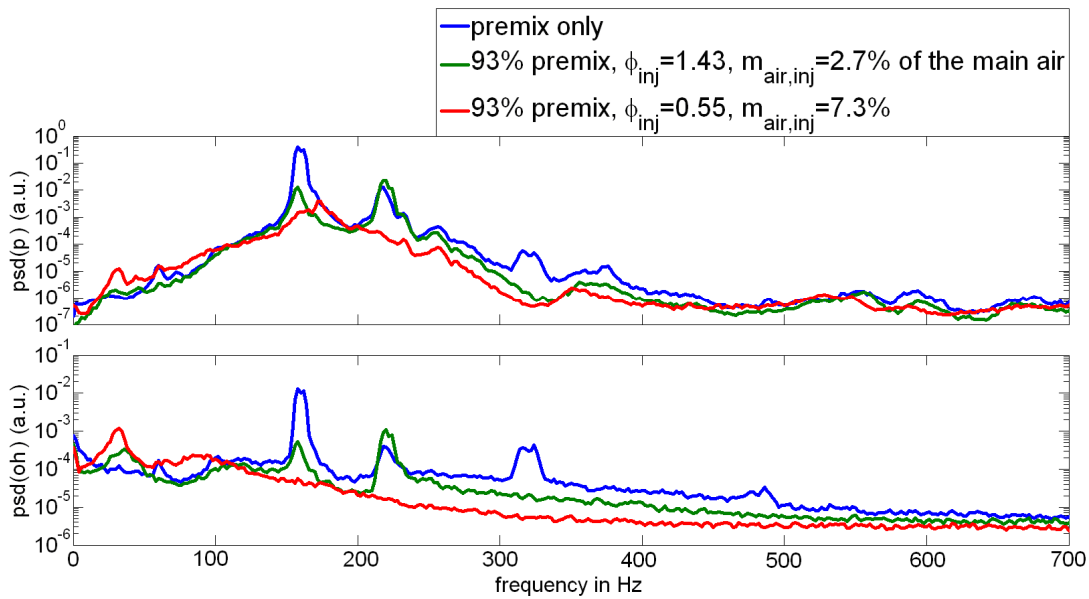


Figure 2.12: Pressure (top) and OH* spectra (bottom) for the multi injection pilot, position $X_p/X_{max}=0.5$ showing the stabilizing effect of increasing air injection (green, 2.7% of the main air and red, 7.3% of the main air) at constant fuel mass flow compared to the case without pilot injection (blue).

A.3. Stability of long combustion chamber with pilot fuel only

The control authority of the multi injection pilot (fuel injection) was tested in the long combustion chamber. As shown in Fig. 2.13, for an equivalence ratio of $\Phi_{\text{overall}}=0.552$ and at the burner bottom location ($X_p/X_{\text{max}}=0$), the combustor is unstable at the long combustion chamber when pilot fuel only is injected. This means also that stabilization with a transfer of fuel to the pilot injection is not possible. The pilot fuel injection is not able to stabilize the combustor and NO_x are thus high. At other operating points, the pilot injection may be able to stabilize the combustor, but leads at the same time to increase NO_x emissions. Using pilot air was expected to solve the problem of instability without NO_x penalties.

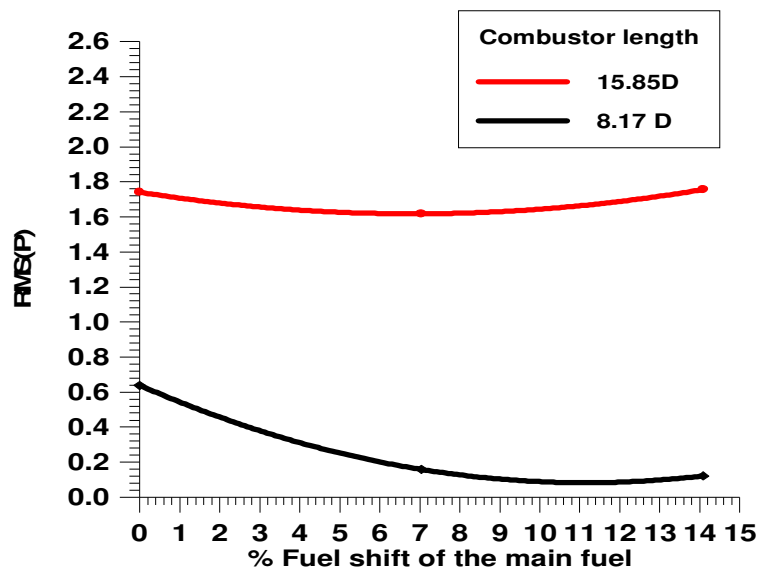


Figure 2.13: P_{RMS} (v) at burner bottom for long and short combustion chambers and at different fuel transfer.

B Transfer of part of main air flow through the pilot injector

B.1. Pilot air transfer at short combustion chamber

The tests with pilot air injection only were performed first in the short combustion chamber. For these tests, the power as well as the total equivalence ratio are maintained constant, the control occurs only with a transfer of the main air flow through the pilot injection.

For different pilot end locations of the multi injection pilot and at $\Phi_{\text{overall}} = 0.552$, the effect of air injection on the combustion performance is inspected. The preheating temperature is set at 150°C. It is evident that the best injection location is again at the bottom of the burner, as high amount of air reduces pressure pulsations at the whole locations. At two third of the burner height location, the P_{RMS} is higher but it is still in stable range (Fig. 2.14) and NOx emissions also are higher at this position (Fig. 2.15). Air transfer also offers a reduction in CO for all locations as shown in Fig. 2.16.

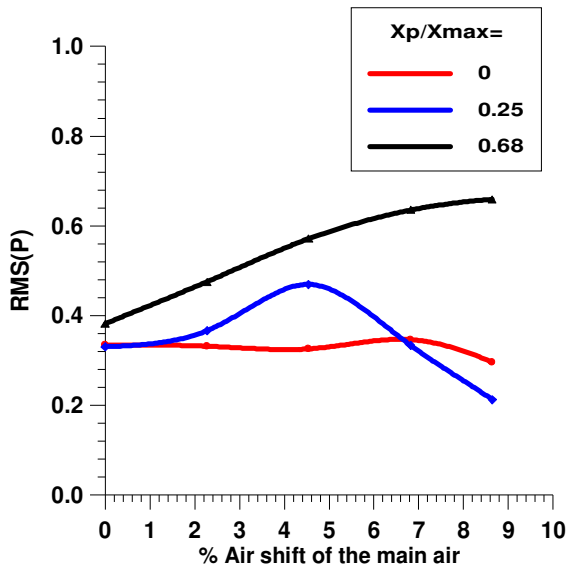


Figure 2.14: P_{RMS} at different axial locations.

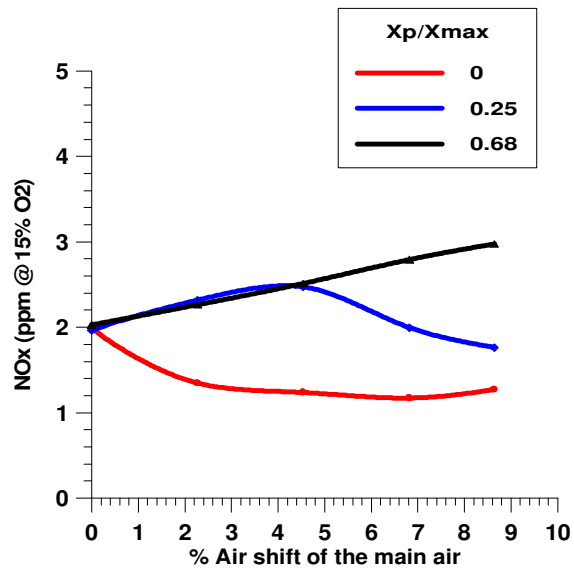


Figure 2.15: NOx (ppm) ref. to 15% O₂ at different axial locations.

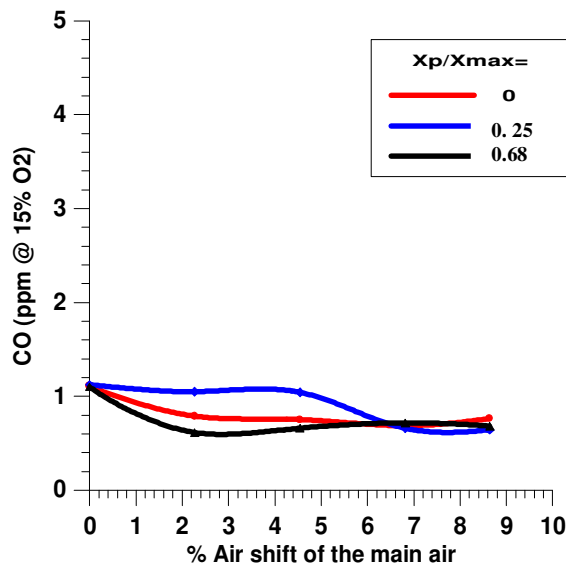


Figure 2.16: CO (ppm) ref. to 15% O₂ at different axial locations.

Flame visualization, performed with OH-Chemiluminescence, shows the impact of the multi-injection pilot located at quarter the burner height ($X_p/X_{max}=0.25$) and at $\Phi_{overall} = 0.552$ on the flame location. Figure 2.17 reveals that the injection of 6.8% of the total air flow through the pilot changes completely the flame shape. While the standard injection presents a homogeneous reaction zone at the burner outlet, the pilot air injection transfers the flame location on 2 sides of the combustion chamber.

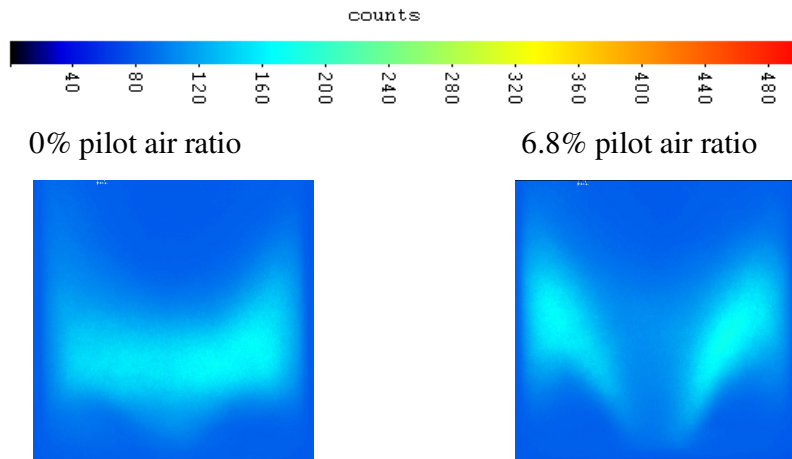


Figure 2.17: Influence of pilot air injection on OH-chemiluminescence at short combustion chamber (8.17 D). Multi- injection pilot located at burner quarter ($X_p/X_{max}=0.25$) axial location, left: no air injection, right: air injection is 6.8% of total air mass flow.

B.2 Control authority for long combustion chamber

The long combustion chamber (15.85 D) of the test rig was known to exhibit a strong $\frac{1}{4}$ instability, and the capacity of air injection to stabilize the combustor was investigated. It reveals high combustion instability levels without air injections inside the pilot lance. By transferring the air inside the pilot injector, the stability is performed at combustion with low NO_x and CO emissions. The best results for emissions are presented in Fig. 2.18 and 2.19.

At different pilot injector locations with pilot air and at $\Phi_{overall} = 0.552$, effect on the combustion performance is also inspected. The multi-injection pilot end is investigated at preheating temperature of 150°C. As expected from the long tube, high combustion instability levels are noticed (see Fig. 2.18). Pilot air mass flow superior to 15kg/hr (6.8% of the main air) achieves the stability of combustion for the whole axial locations of the pilot lance. The best location is at

$X_p/X_{max}=0$ as it is stable for pilot air mass flow superior to 10 kg/hr (4.5%). Stabilizing the combustor leads also to a decrease of NO_x emissions.

The location of $X_p/X_{max}=0.5$ that was unstable by pilot fuel only is stabilized by injecting the pilot air after around 17kg/hr (7.73%). Figure 2.19 shows that NO_x emissions are still down 10ppm for the whole cases and declined to low values lower than 2ppm at 19kg/hr (8.64%) pilot air. Figures 2.18 and 2.19 show further that the axial location of the pilot lance for moderate air mass flows has a stabilizing effect as pressure oscillation decreases with increasing lance location for 5kg/hr (2.27%) pilot air.

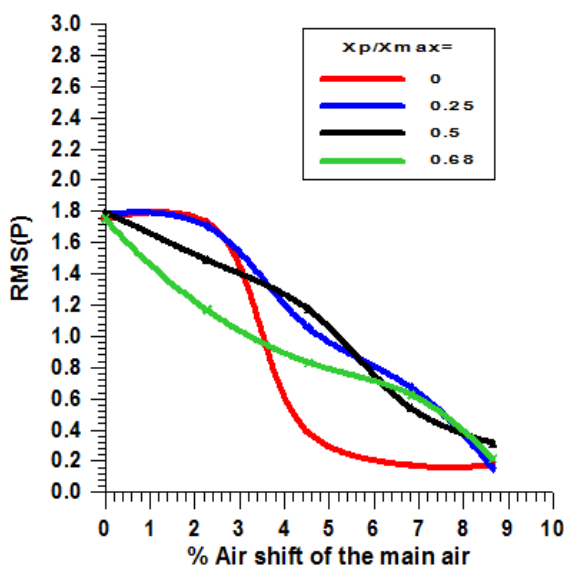


Figure 2.18: P_{RMS} (v) at different pilot locations, long combustion chamber (15.85 D), and $\Phi_{overall}$.

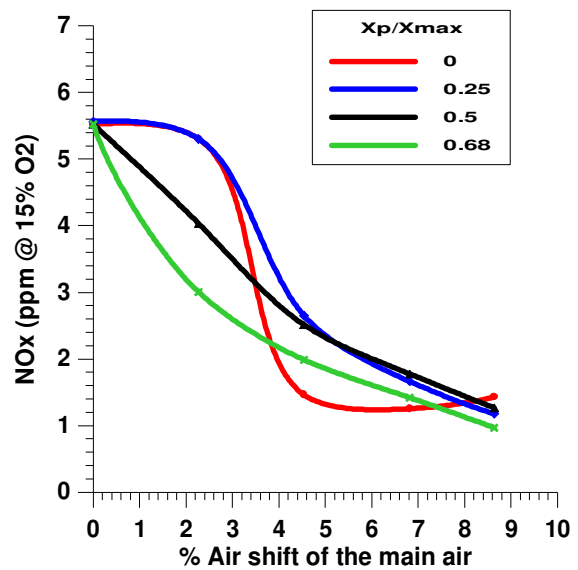


Figure 2.19: NO_x ref. to 15% O₂ at different pilot locations, long combustion chamber (15.85 D), and $\Phi_{overall}$.

As shown in Figure 2.20, a complete stabilization of the combustor is achieved for pilot location at the burner bottom and with an air mass flow superior to 4.5% of the main air flow. For an air mass flow slightly lower than this percentage, the combustor is still unstable but the amplitude of the dominant peak significantly decreases (18 dB). Stabilizing the combustor leads also to a decrease of NO_x emissions as shown by Emara 2009.

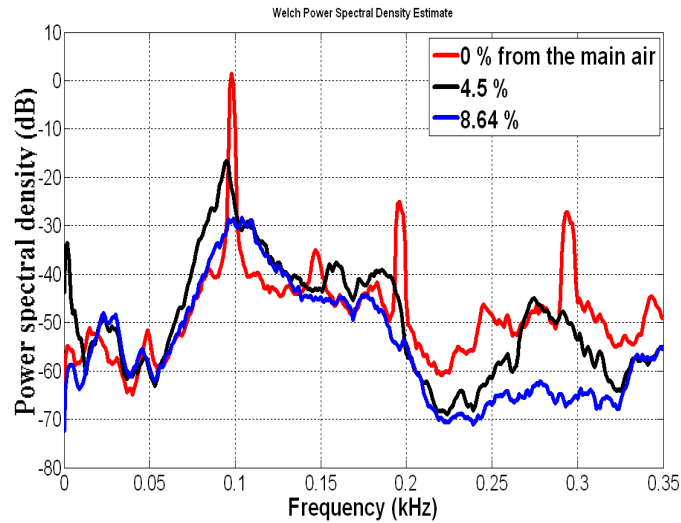


Figure 2.20: Pressure oscillations for $X_p/X_{max}=0$ at different pilot air mass flows for the long chamber.

Transfers of 8.64% of the main air at $X_p/X_{max}= 0.25$ reduces the dominant peak by around 27dB and still performs the stability of combustion at this axial location Fig. 2.21.

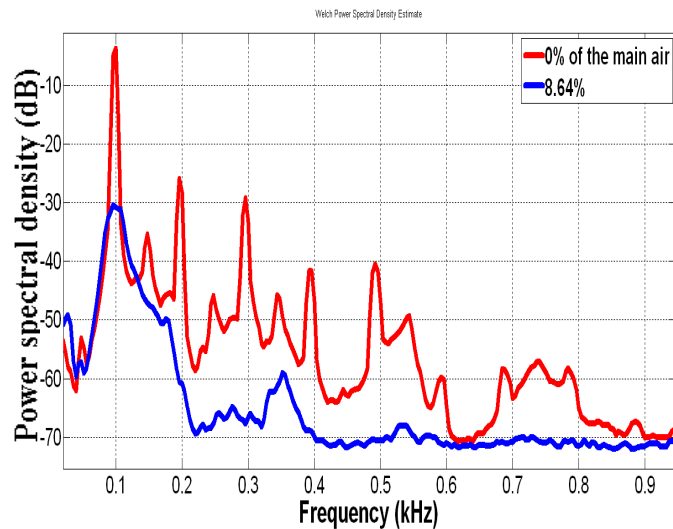


Figure 2.21: Pressure oscillations for $X_p/X_{max}=0.25$ at different pilot air mass flows for the long chamber.

Pilot air mass flow superior to 8% of the main air reduces the instability of combustion for most of axial positions of the pilot lance. The dominant peaks are at 98Hz and 196Hz at 0% of main air and at $X_p/X_{max}=0.5$. By transferring 4.5 % of the main air, the dominant peak reduced by 7dB. An increase of pilot air ratio to 8.64% decreases the first dominant peak by 18dB and suppresses also the peak of the helical structure (Fig. 2.22).

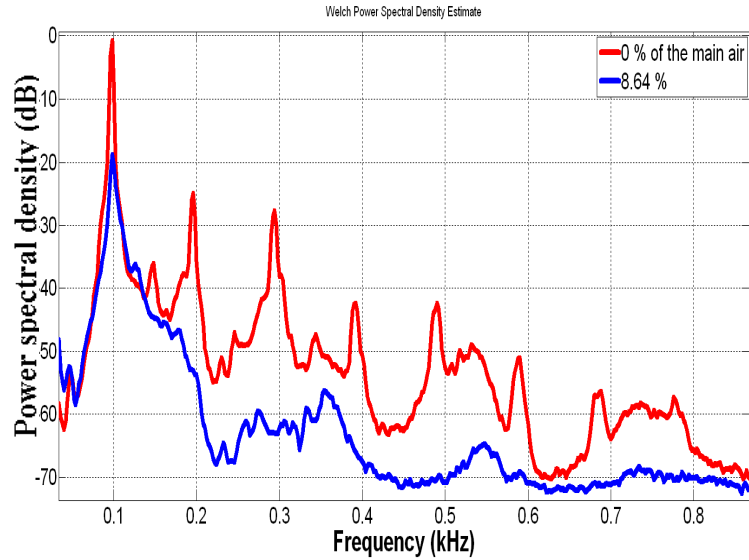


Figure 2.22: Pressure oscillations for $X_p/X_{max}=0.5$ at different pilot air mass flows for the long combustion chamber.

Sliding of the pilot injector to position $X_p/X_{max}=0.68$ changes the dominant peaks to 96Hz and 192Hz at 0% of the main air. Transferring 8.64% of the main air leads to a reduction in the dominant peak amplitude by 21dB and contributes to an instability damping at this position (Fig. 2.23).

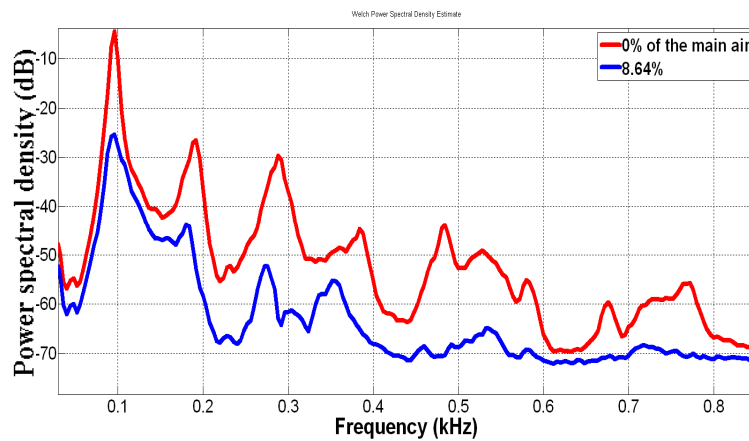


Figure 2.23: Pressure oscillations for $X_p/X_{max}=0.68$ at different pilot air mass flows for the long combustion chamber.

Figure 2.24 shows the impact of pilot air injection on the OH chemiluminescence. While low pilot air mass flow leads to high and concentrated OH emissions in and out of the burner, adding around 4.5% of air through the pilot dramatically decreases the light intensity.

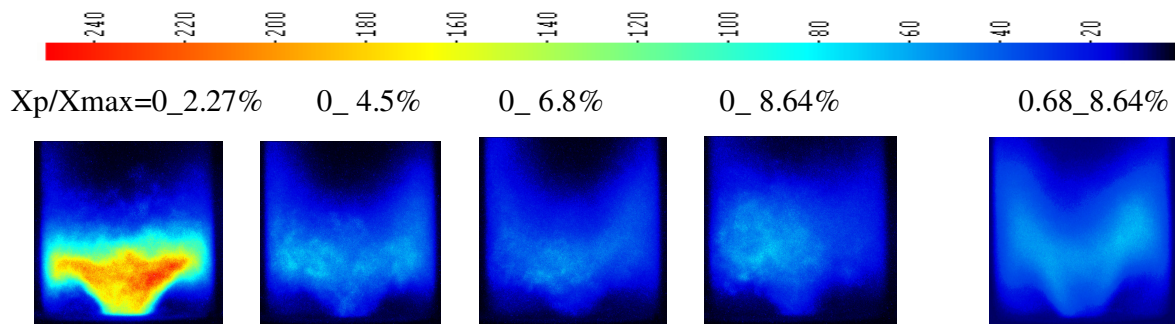


Figure 2.24: Influence of pilot air injection on OH-chemiluminescence at multi injection pilot, $\Phi= 0.552$ and $15.85 D$. The left four figures at $X_p/X_{max}=0$ and the last right one at $X_p/X_{max}=0.68$ pilot position.

The flame appears less compact and lifted from the burner outlet in direction downstream the flow. This is particularly true for the highest pilot air ratio of 8.6%. Increasing the pilot air flow decreases the flame compactness. The strong decrease in OH chemiluminescence intensity between an unstable (pilot air ratio = 2.27%) and a stable (pilot air ratio = 8.64%) flame is due to the combination of fuel air ratio oscillations with the non linear response of OH* chemiluminescence by changing of fuel/air ratio. For a defined heat release, the mean intensity emitted by an unstable flame facing fuel/air ratio oscillations would be much higher than the intensity emitted by the same but stable flame.

The previous results show that the high jet momentum has a strong impact on the structure of the flame, helps to stabilize this flame at the burner outlet, and prevents the flame oscillations when using the multi pilot injector. The best control authority is still achieved with lower pilot lance location using this injector. The multi pilot injector is succeeding in emission reduction and flame stability especially when compared to the single hole injector.

The effect of pilot injector shape on stability at different total (overall) equivalence ratios ($\Phi_{overall}$) is studied first in the long combustion chamber which offered higher instabilities without air injection. The pilot injector is located at the bottom of the burner ($X_p/X_{max}=0$) which represents the best stable position. The preheating temperature was set at $150^\circ C$ and two equivalence ratios $\Phi_{overall} = 0.552$ and $\Phi_{overall} = 0.583$ were tested. The results presented in Fig. 2.25 and 2.26 show that both injections are able to give a stable flame but the multi hole injector is still more efficient than the single one in reducing the pressure oscillations.

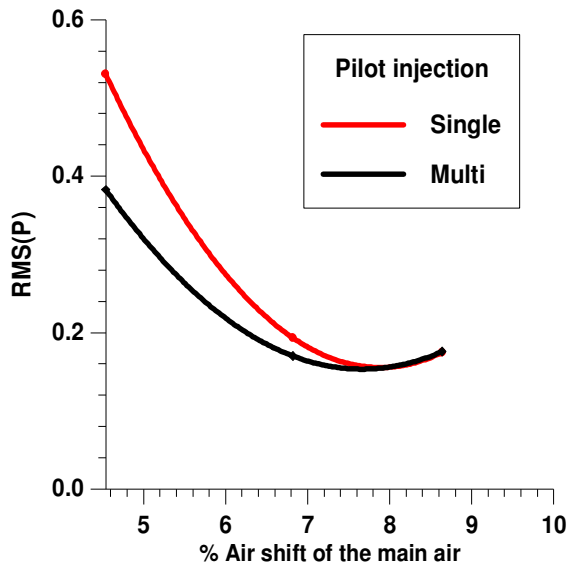


Figure 2.25: RMS P at different pilot shapes and at $\Phi_{\text{overall}}= 0.552$.

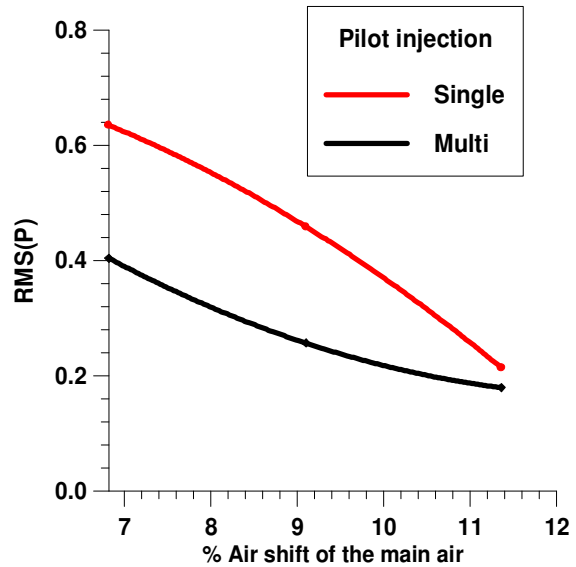


Figure 2.26: RMS P at different pilot shapes and at $\Phi_{\text{overall}}=$

Shortly, the transfer of a certain percentage of air mass flow has a positive effect on the stability and emissions. To help to understand this effect of the injected air on the flow field and clarify the jet interaction with the main flow field, PIV details the flow field at different reacting and non-reacting flow conditions for the short combustion chamber and the results are discussed at the next part.

3.2. Flow field Characteristics

A. Isothermal flow

At $X_p = 0.5 X_{max}$

An investigation of the flow field while the pilot injector is at the middle position of the burner in isothermal conditions is more interesting. Figure 2.27 demonstrates the axial velocity profiles at different pilot air ratios. The reduction of the instability is achieved for the short and long combustion chambers at 8.64% of the main air. Figure 27 shows that the impact on the flow field of a moderate air injection (4.5%) is marginal, as the resulting velocity profiles are similar to those profiles without air transfer. However, if the air flow through the pilot is increased up to 8.64%, a much stronger change in the flow field is observed; the central recirculation zone becomes narrower over the whole axial locations. As the pilot air ratio increased, the total width between the two peak velocity values decreased.

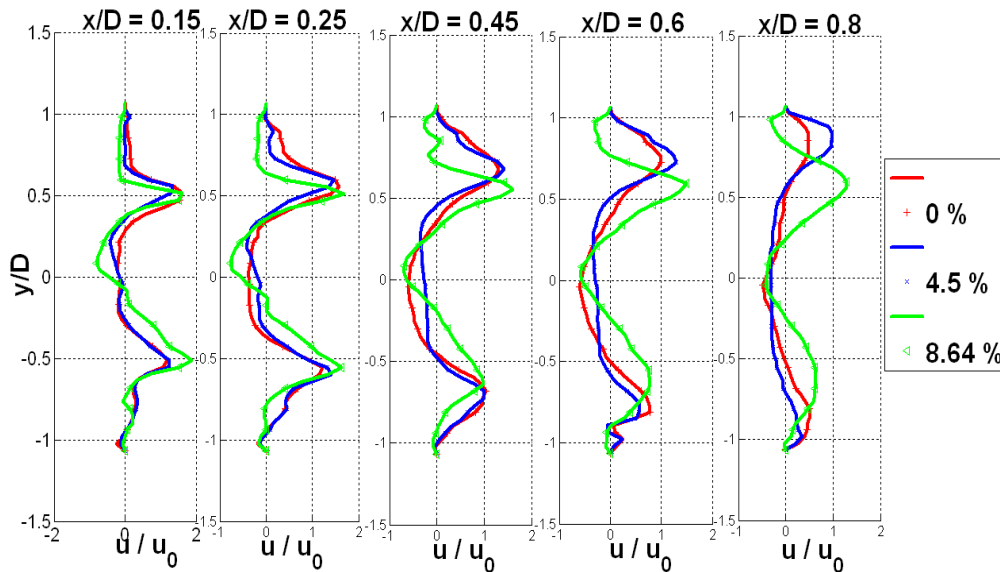


Figure 2.27: Radial profiles of the streamwise velocity at different pilot air injections while the injector is at burner middle position.

Increasing the air transfer is the key for stability of the flame by the pilot air injection to force the flame downstream of the burner and preclude it from returning back. The flow inside the toroidal internal recirculation zone is associated with high shear rates and strong turbulence intensities resulting from vortex breakdown to provide the dominant flame- stabilization mechanism.

As shown in Fig. 2.28, two panels are clarifying the effect of pilot injection on the flow field. The internal recirculation zone is elongated on expense of its width as the pilot momentum increases.

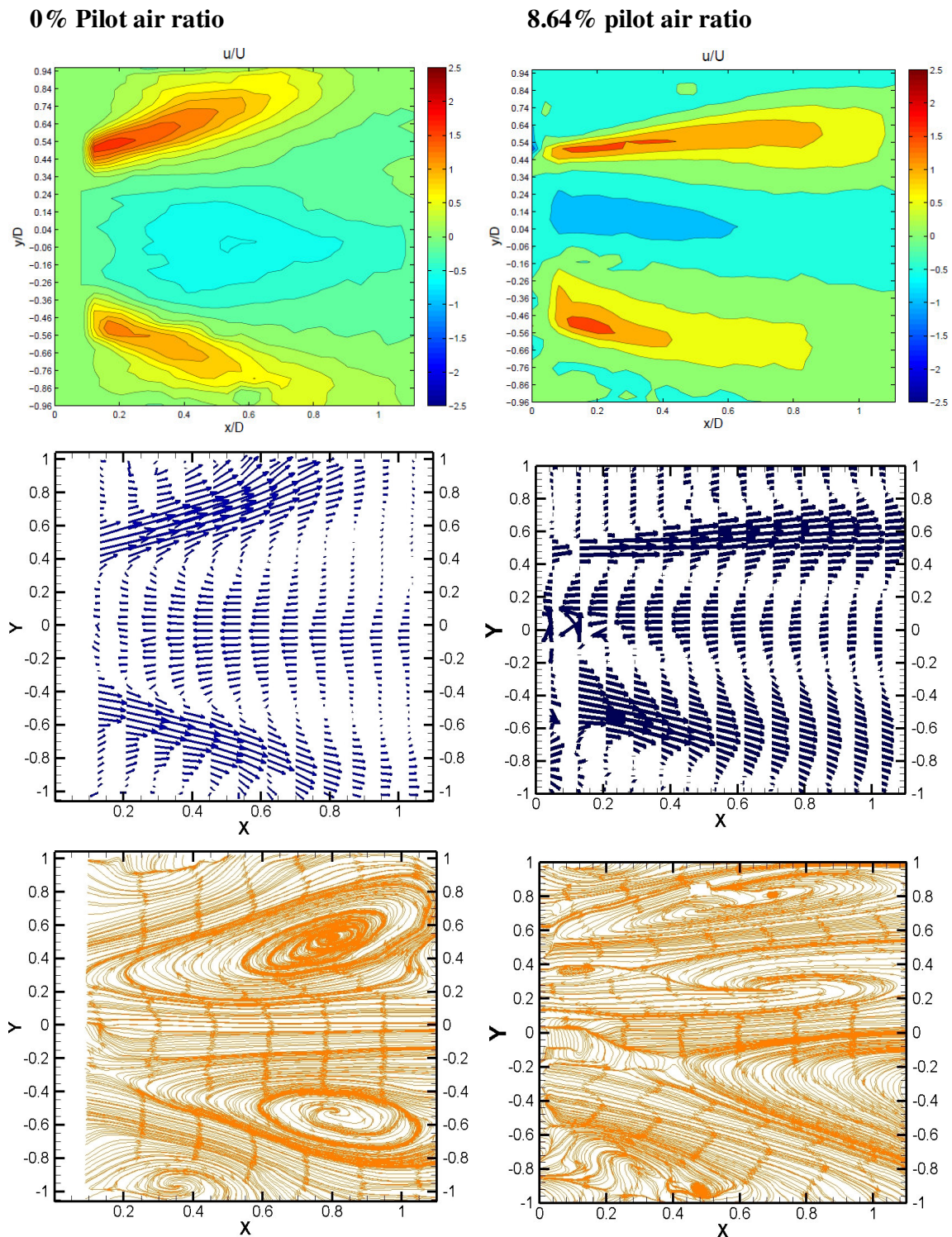


Figure 2.28: Streamwise velocity contours, velocity vectors, and streamtraces at pilot air mass flows 0% (right) and 8.64% pilot air (left).

The length of the corner recirculation zone is longer also by transferring of the 8.64% of the main air inside the pilot lance. This air transfer forces the flow inside the combustion chamber downstream of the burner and reduces the tangential expansion of the main flow resulting from the centrifugal force inside the flow. The information in this figure reveals typical features of a swirling jet breakdown zone with a central reverse flow (Shtork 2007).

At $X_p = 0.68.X_{max}$

As shown in the next figure for streamwise velocity and radial velocity components, there is a clear change in the shape of the central recirculation zone after injection of the pilot transferred air. This change is noticed at 4.5% pilot air ratio.

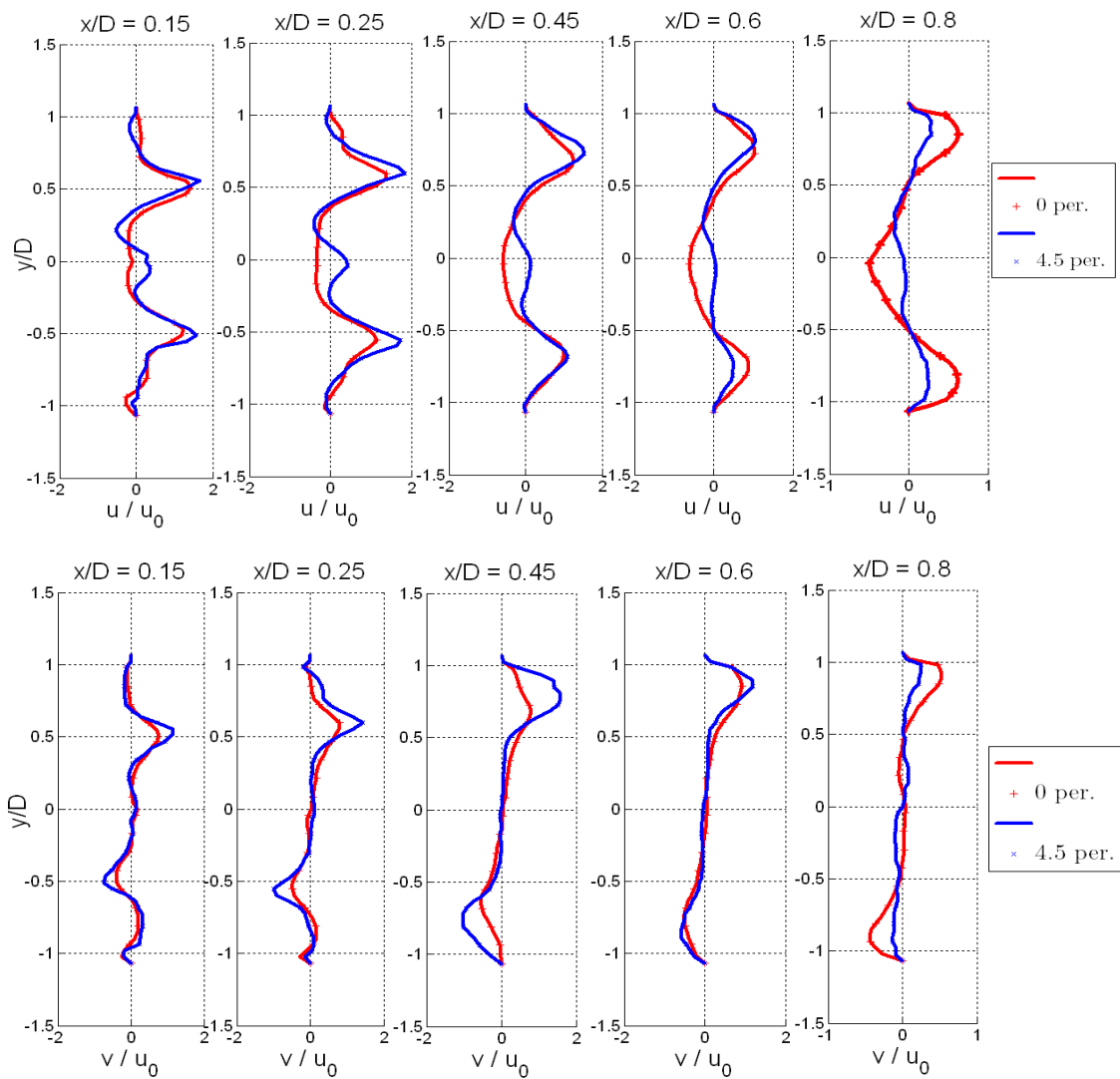


Figure 2.29: Radial profiles of the streamwise velocity (up) and radial velocity (down) at different pilot air injections and at different axial locations.

The great streamwise and radial velocity components exist around the centerline and represented by the two lobes of the conical swirled flow. The air transfer inside the pilot increases the centerline velocity. A new thumb shape of the central recirculation zone appeared as a result of the pilot injection (Fig. 2.29). This shape expresses a change in the nature and characteristics of the central toroidal zone. Positive velocity components are noticed correspond to the pilot air transfer. An inversion in the central velocity component from positive to negative is noticed almost after $x/D=0.6$. The streamwise velocity is always higher at most of axial locations from the burner exit. After $x/D=0.6$, a shift in the streamwise velocity happened as the maximum velocity value decreased in comparison to 0% pilot air ratio. At x/D of 0.8, the ratio of the maximum streamwise velocities reduced by 45.4% and the radial velocity reduced by 51.6% from the higher one. By comparing the streamwise velocity components at these cases, the flow structure of the pilot injection case diminished earlier by transferring to 4.5% of the main air flow. The scale structures are dissipated by turbulent diffusion and viscous damping when the flow convects downstream.

Figure 30 shows two panels of pilot mass flow injections. The left side one represents a zero pilot air ratio case, while the other one represents a transfer of 4.5% of the main air. The streamwise velocity contours demonstrates the main structure of the flow field. The maximum velocity values are on the two sides of the centerline. The green central zone shown in the right contour plot represents the positive central velocity components and ended almost at $x/D= 0.6$.

The velocity vectors show that the flow field at both cases has a steep mean velocity gradient but higher with pilot air transfer. Injection of the transferred air shows the positive zone directly near the injector exit at the centerline.

Forcing of the flow by pilot injection inside the combustion chamber near the burner top together with the centrifugal force resulting from the swirl inside the flow are affecting also the internal recirculation zone length and width at the burner exit. The resulted tangential expansion leads to a short corner recirculation zone. The corner and internal vortices squeeze together the swirled flow result in a small shear layer thickness.

The streamtraces at the transferred flow case show clearly the changes inside the flow field which lead to the destruction of the helical structure as shown from the microphone data after injection of this amount of mass flow. High turbulence is shown at the entire flow field in the streamtraces of the right panel resulting from the central injection.

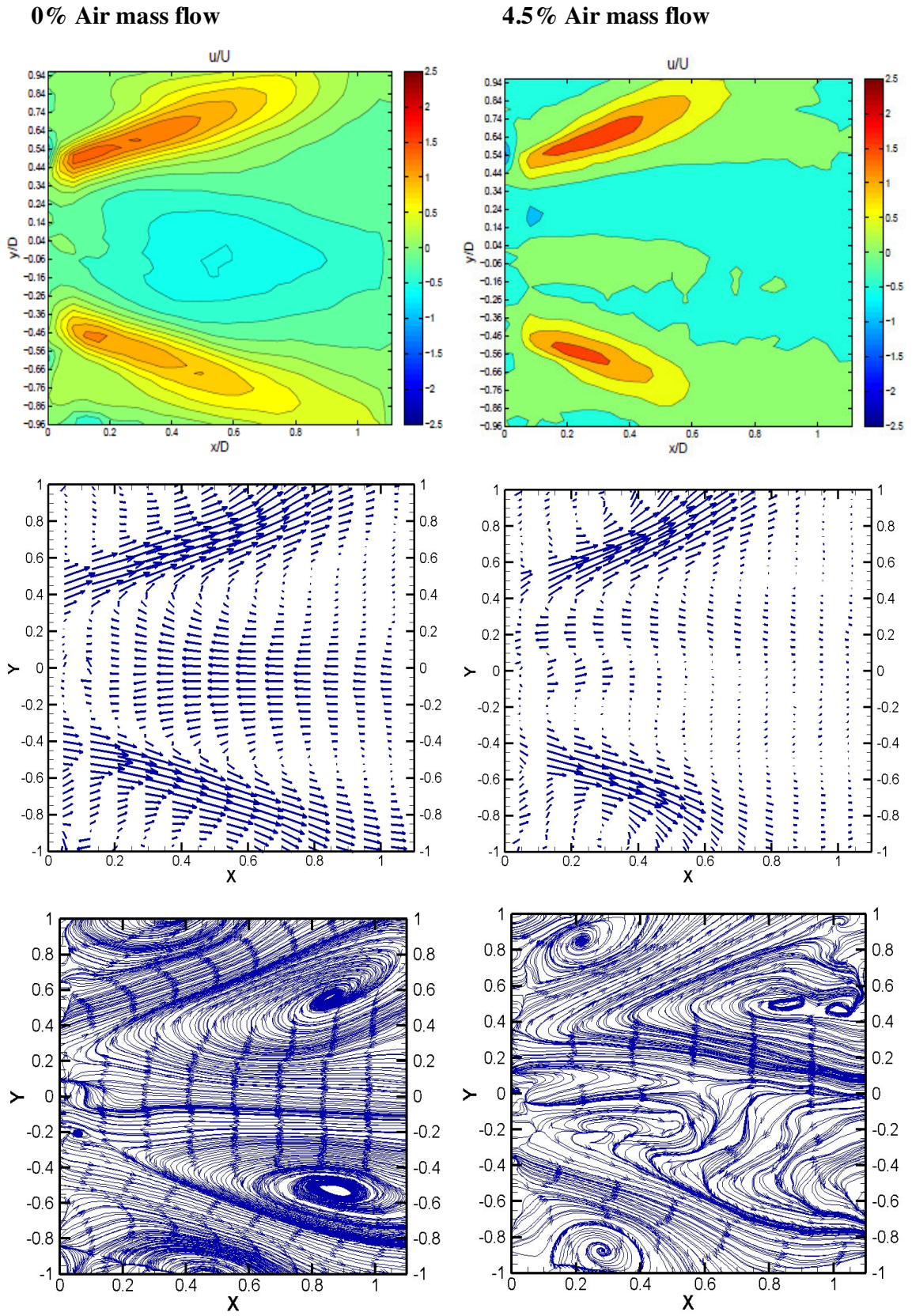


Figure 2.30: Streamwise velocity contours, velocity vectors, and streamtraces at pilot air mass flows 0% (left) and 4.5% of the main air (right) at $X_p/X_{max}=0.68$.

A clear flow structure map summarizes the whole fluid flow zones and is shown in Fig. 2.31.

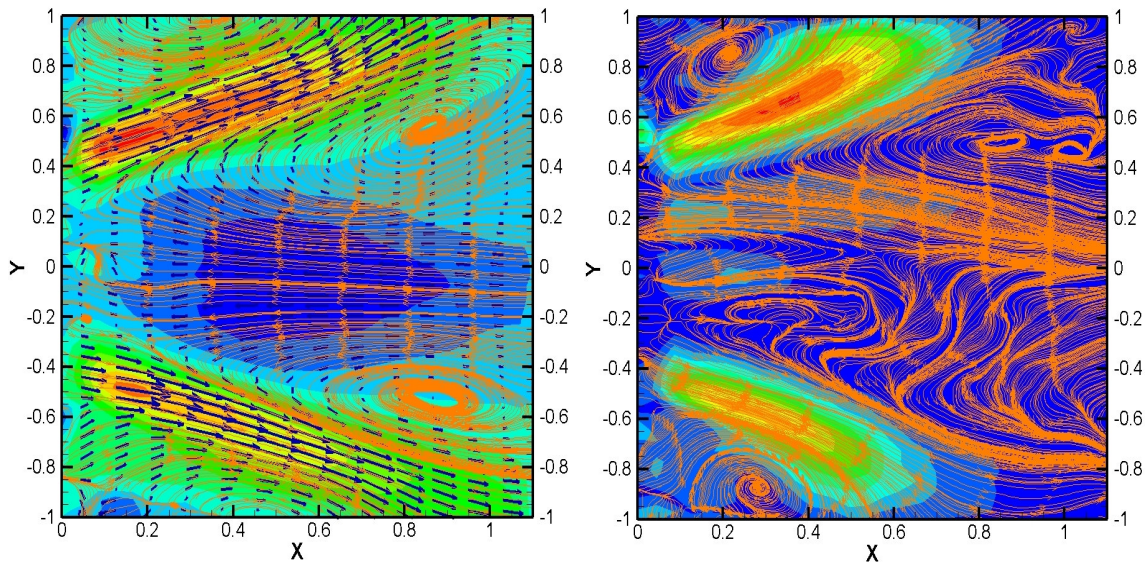


Figure 2.31: Flow map of absolute velocity contours, velocity vectors, and streamtraces at pilot air mass flows 0% (left) and 4.5% of the main air (right) at $X_p/X_{max}=0.68$.

As known, shear layers are produced at the trailing edges of the centerbody and the backward-facing step because of the Kelvin-Helmholtz instabilities in both axial and azimuthal directions (Yang 2005). The shear layer, originating from the backward facing step, remains almost symmetric directly downstream of the burner dump plane. By transferring the central air flow, it forms large asymmetric structures appear especially at $x/D=0.6$ on the centerbody side as the shear force increases in the axial direction. The location of every flow zone and the vortices positions for the two focused mass flows are also offered by Fig. 2.32.

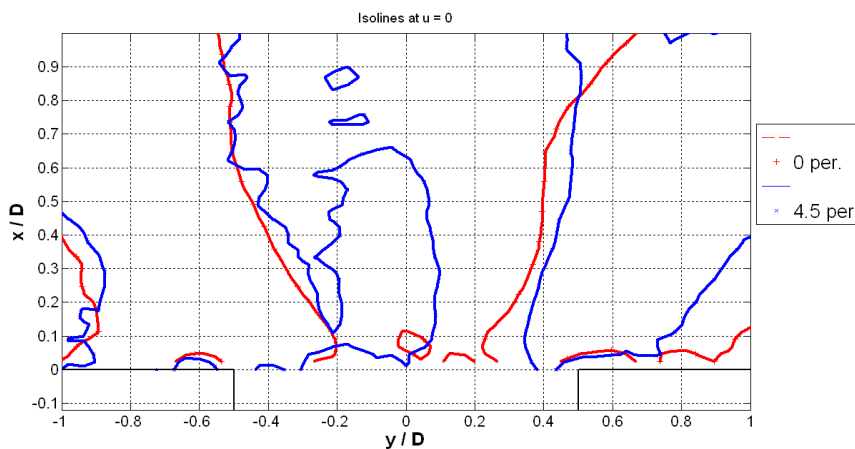


Figure 2.32: Isolines of $u=0$ for different pilot air mass flows; 0% and 4.5% pilot air ratios at $X_p/X_{max}=0.68$.

As shown in Fig. 2.33, the recirculation area is characterized by the lack of vortical flow between the lobes of the swirled flow cone. The flow in the swirl cone area represents a turbulent shear layer which periodically space the vortical structures (0%). Directly, at the nozzle exit the flow exhibits a strong shear and some reverse flow at 4.5% pilot air ratio. Further downstream of the flow up to $x/D = 0.6$, the flow broadens in radial direction. The figure exhibits a localized area of high vorticity. A strong positive peak can also be noticed at $x/D = 0.04$ (i. e. at the burner exit) and moves radially around the centerline at different axial locations. The positive vorticity may be produced by the azimuthal shear flow while the negative is according to the flow swirling sense.

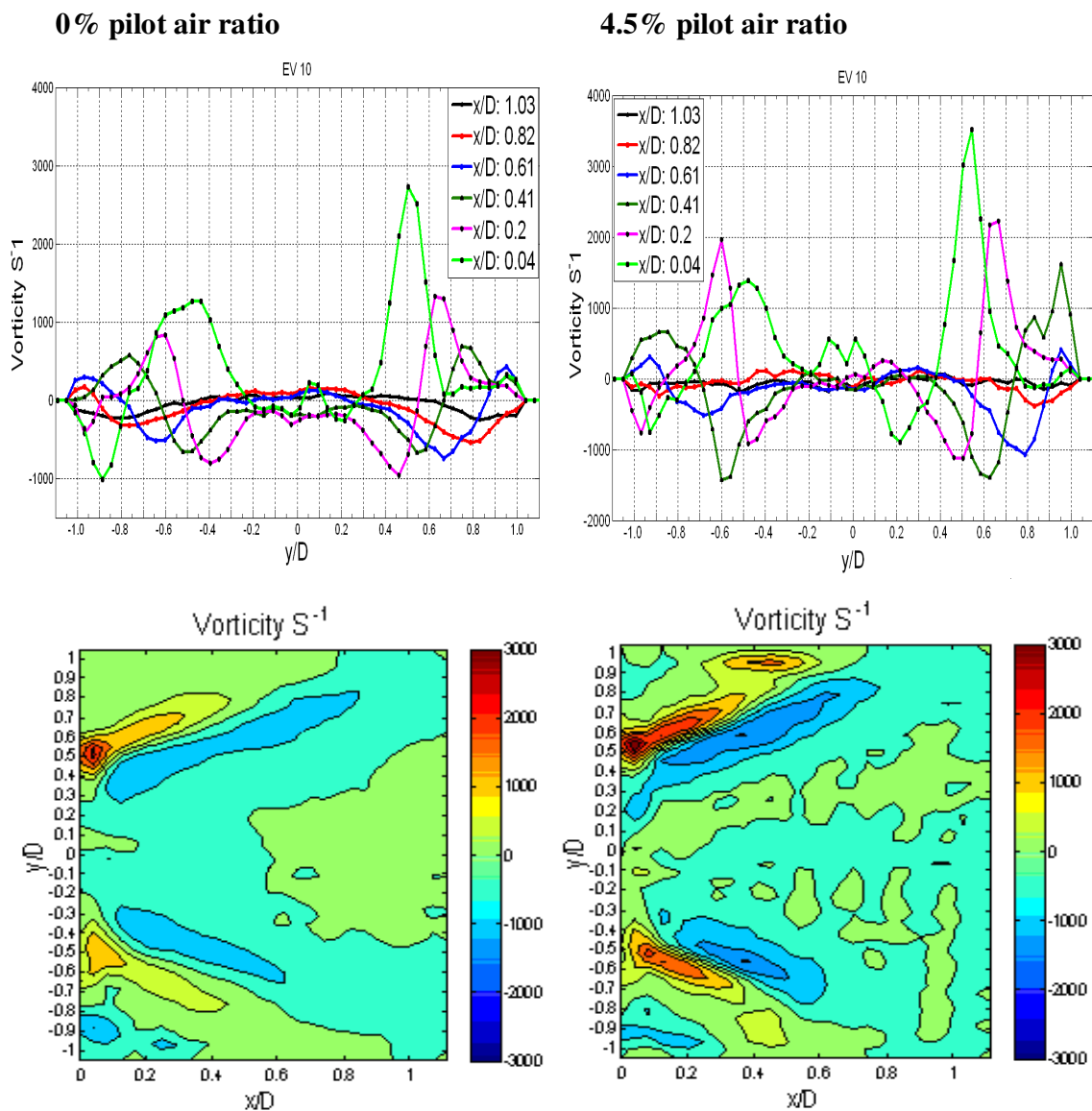


Figure 2.33: vorticity axial profiles and vorticity contour plots at pilot air ratios of 0% (left) and 4.5% (right) and at $X_p/X_{max}=0.68$.

Some differences are noticed also at the contours of the normal strain rates as the pilot air ratio increases to 4.5 %. The internal recirculation zone is completely changed and the positive normal strain is increased at expense of the negative part as shown in Fig. 2.34.

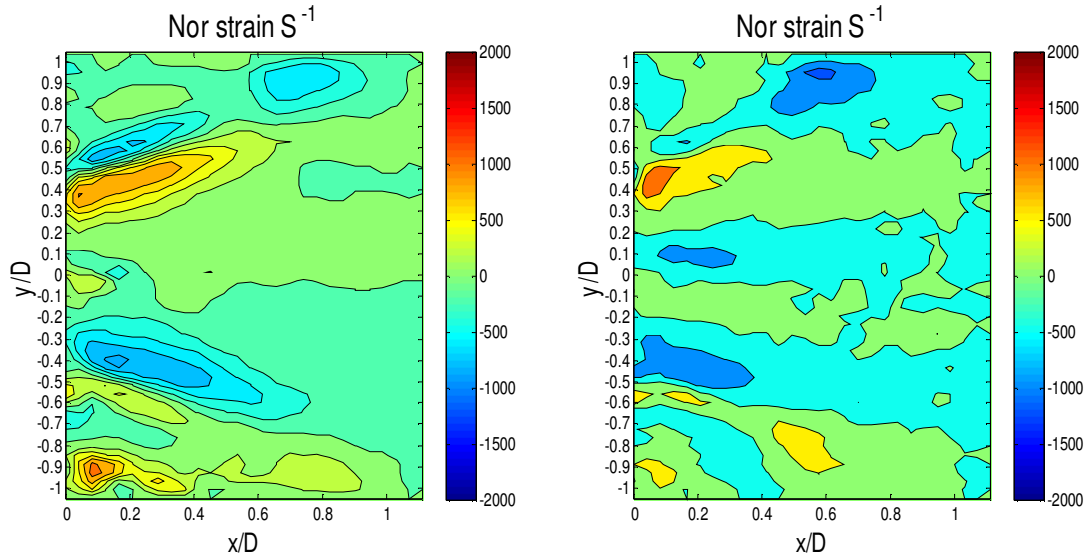


Figure 2.34: Normal strain rate contour plots at pilot air ratios of 0% (left) and 4.5% (right) and at $X_p/X_{max}=0.68$.

B. Isothermal and reacting flow field comparison

Figure 2.35 shows a comparison between reacting and non reacting flow field at 8.64% pilot air ratio and at the burner underside location which is the most stable location in the pilot cases as proved by Emara (Emara 2009). Isothermal flow was at $Re=52220$ while the reacting flow was at $\Phi_{overall} = 0.552$. Some increase in the flow velocity starts especially at $x/D= 0.45$ as hot spots move faster than the flow in isothermal case.

Directly at the burner exit, no more differences between the reacting and none reacting flows. Velocity magnitudes in the conical jet as well as in the recirculation zone increase as a consequence of the heat released by the flame at after $x/D= 0.45$. The velocity ratio between the maximum streamwise velocity components for the two cases increased from 8.35% at $x/D= 0.45$ to 77.43% at $x/D= 0.6$ and to almost double the streamwise velocity (2.177) at $x/D= 0.8$.

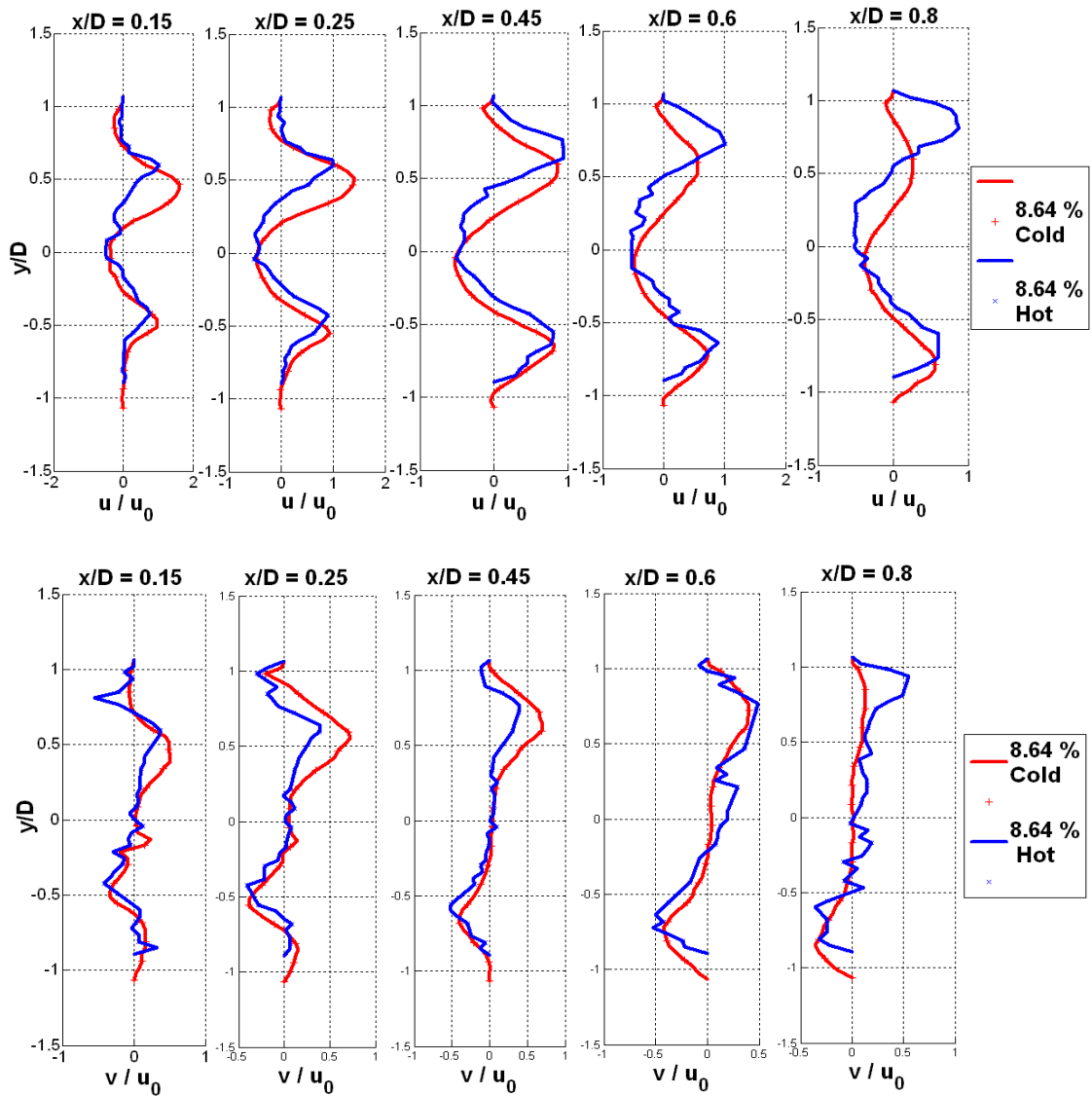


Figure 2.35: Radial profiles of the streamwise velocity and radial velocity at 8.64 % of the main air and at $X_p/X_{max}=0$ for reacting flow (blue) and isothermal conditions (red).

The flame is stabilized by a central recirculation area as well as the central injection in the present study (Willert 2002). The cone angle in the reacting flow increases because of effect of buoyancy plus the centrifugal force in comparison to isothermal flow as shown in Fig. 2.36. Some changes are shown of the main body of the flame, the thickness of the shear layer, and the thickness and width of the whole IRZ and ERZ. Higher velocities exist only directly at the exit of the burner.

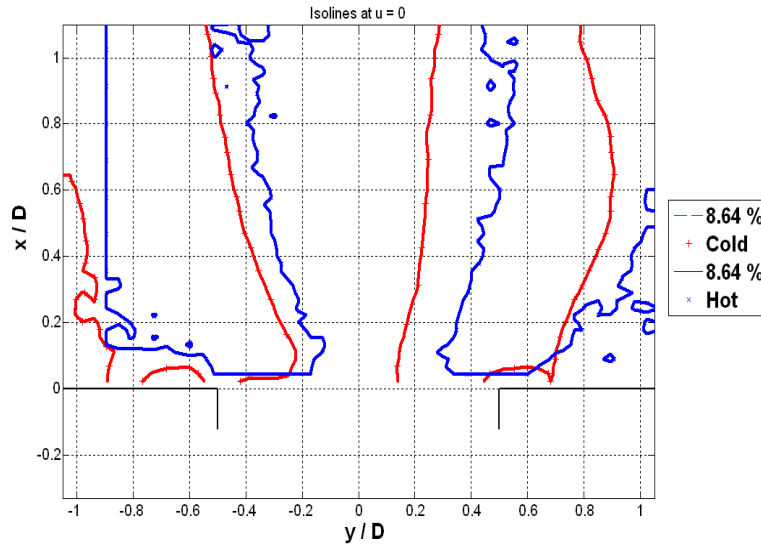


Figure 2.36: Isolines at $u=0$ for 8.64 % transfer of the main air and at $X_p/X_{max}=0$ for reacting flow and isothermal conditions.

As noticed at the burner underside plane, the increase in the streamwise velocity is performed far from the burner dump plane. At the burner middle and $x/D=0.8$ for 7.3% of the main air, the increase ratio is not high as the last case. The ratio is 12.2% at the highest streamwise velocity value (Fig. 2.37).

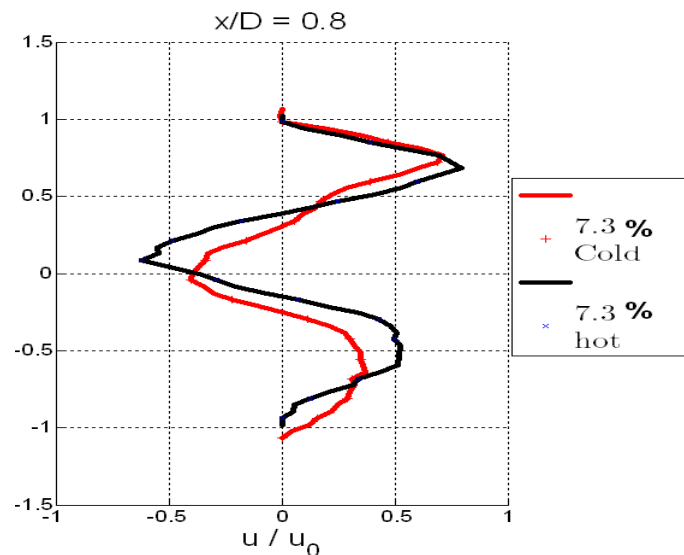


Figure 2.37: Radial profiles of the streamwise velocity at 7.3 % of the main air and at $X_p/X_{max}=0.5$ for isothermal and reacting flow.

C. Reacting flow field

At $X_p = 0.5 X_{max}$

Figure 2.38 shows the effect of increasing the central pilot air ratio from 0% to 8.64% at the burner middle location in reacting flow conditions at $\Phi_{overall} = 0.552$.

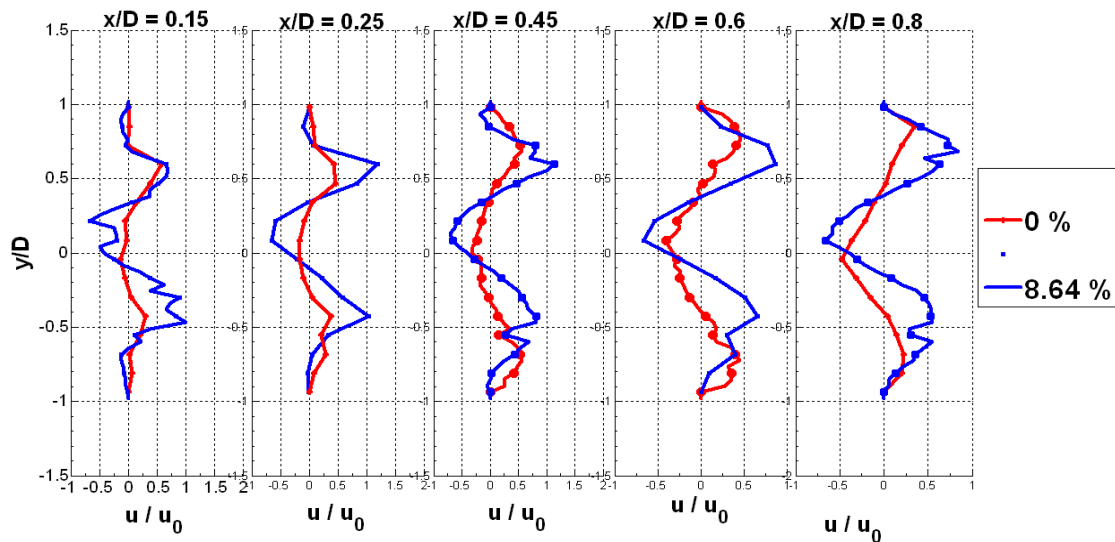


Figure 2.38: Radial profiles of the streamwise velocity at different pilot air mass flows (0 %, and 8.64 %) and at $X_p/X_{max}=0.5$ for reacting flow at $\Phi_{overall}= 0.552$.

More pilot air ratios result in higher pressure gradients and turbulence intensities. The resulted internal recirculation zone is similar to a rod shape as exhibited in Fig. 2.39.

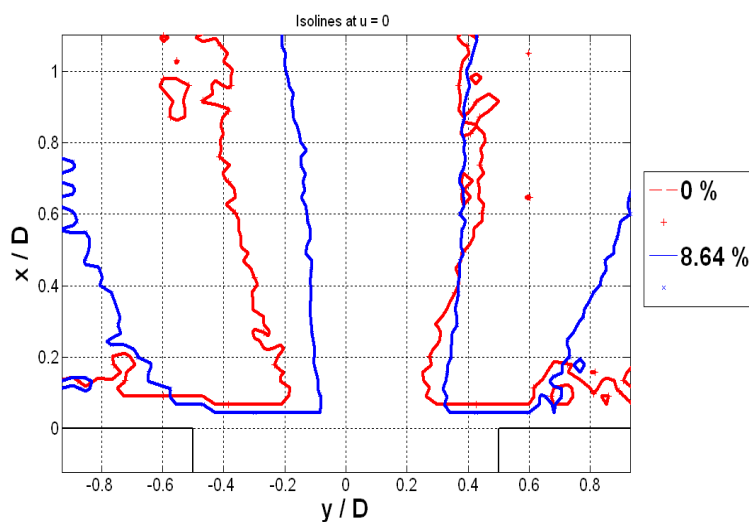


Figure 2.39: Isolines of $u=0$ at different pilot air mass flows (0 %, and 8.64 %) and at $X_p/X_{max}=0.5$ for reacting flow at $\Phi_{overall}= 0.552$.

Its width is thinner than that one at no pilot air injection. The cone angle is smaller than that one with zero central flow injection. High increase in the maximum streamwise velocity components resulted from an increase of the pilot air ratio (8.64%). Axially at $x/D= 0.15, 0.25, 0.45, 0.6,$ and $0.8,$ the streamwise velocity increased by 0.17, 1.63, 1.1, and 1.4 of the zero pilot air velocity consecutively. The radial velocity components also increased at maximum of up to double the radial one at 0% and at $x/D=0.8$ from the burner exit.

At $X_p/X_{max}=0.68$

Increasing the pilot air ratio, especially near the burner exit, forces the flame outside the burner as shown in Fig. 2.40.

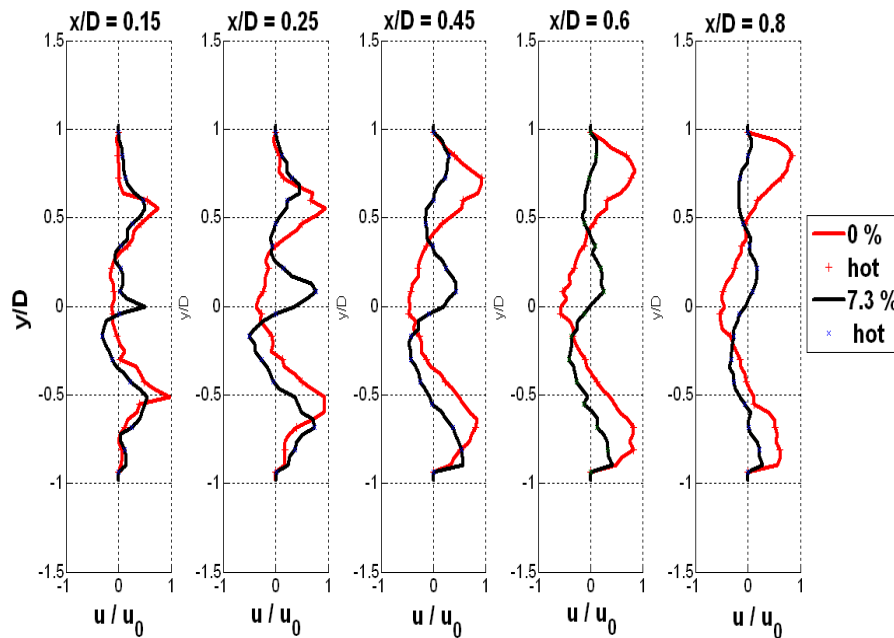


Figure 2.40: Radial profiles of the streamwise velocity at different pilot air mass flows (0 %, and 7.3 %) and at $X_p/X_{max}=0.68$ for reacting flow at $\Phi_{overall}= 0.552$.

At the normal flow without any pilot injection, the swirling effect generates a centrifugal force which produces a radial pressure gradient as indicated by the simplified momentum equation.

$$\frac{\partial p}{\partial r} = \frac{\rho U^2}{r} \quad (2)$$

In the regions that the strong swirling motions occur, the pressure tends to minimize. The flow expands and the streamwise velocity decays axially far from the burner exit as shown in Fig.

2.40. Then the pressure is recovered downstream of the flow. A positive pressure gradient is consequently generated along the axial centerline (Yang 2005).

After injection of 8.64% of pilot air, the positive pressure gradient increased much more than the normal case. The streamwise velocity profiles draw a hump shape at the centerline as it increases at the expense of the velocity at lobes or wings of the swirl cone. Unlike the normal recirculation zone, a third positive zone appeared at the centerline due to the injection.

The corner recirculation zone is also shorter due to the expansion of the flow in radial direction as clarified by Fig. 2.41 and Fig. 2.42.

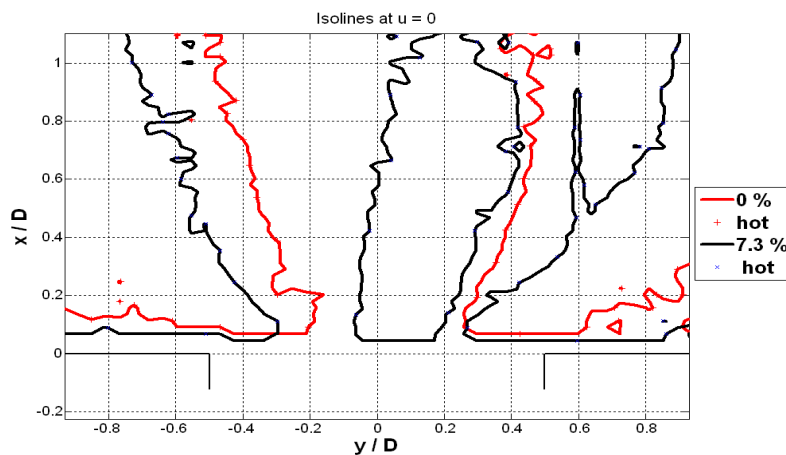


Figure 2.41: Isolines of $u=0$ at different pilot air ratios (0 %, and 7.3 %) and at $X_p/X_{max}=0.68$.

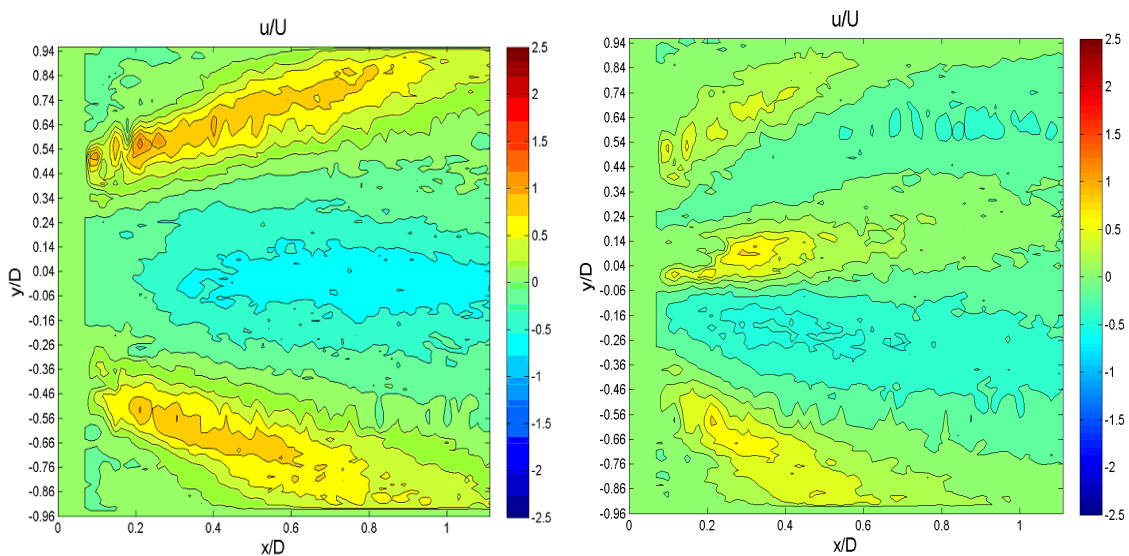


Figure 2.42: Streamwise velocity contour plots at pilot air injections of 0 % (left) and 7.3 % (right) and at $x/D= 0.68$ for reacting flow at $\Phi_{overall}= 0.552$.

Chapter (4)

Conclusions and Recommendations

Chapter (4) Conclusions and Recommendations

1- Conclusions

The control authority of the flame instability and emissions is performed at this part of work by repartition of the fuel and air inside the burner at constant overall equivalence ratio and power. Two pilot injectors are used for these investigations. A single-hole pilot injector and a multi-holes pilot injector give the same momentum flow. Different secondary injection combinations (pilot fuel, premixing of pilot fuel with air, air injection only) were fed inside the swirl stabilized burner at different locations of the pilot injector as well as at different total equivalence ratios.

It is quite difficult to define simple rules which should be always valid for a good design of secondary pilot injectors. For example, depending on the acoustic boundary conditions, the position of the lance has a strong influence on the flame stability. Nevertheless, a multi pilot injector fed only with air and located upstream of the recirculation zone showed good results in stabilizing the combustor.

The best results were achieved when the injector was positioned at the bottom of the burner ($X_p/X_{max}=0$). It is a position for which the flame stability was achieved with less secondary air injection than the other pilot end locations. At this location, decrease of NO_x emissions through mixing enhancement was also achieved.

The strong air momentum induced by the multi-injection pilot, performs the flame stability, enhances the mixing upstream of the flame, and prevents the flame from traveling upstream into the burner.

An oscillation of the flame stabilization location is a source of thermoacoustic instabilities. Precluding the flapping of the flame can thus prevent the thermoacoustic instabilities and is achieved by the injection of air upstream of the flame.

PIV details the flow field in isothermal and reacting flow conditions. At the burner mid, pilot air transfer, (8.64%) in non- reacting conditions case, forces the flow downstream, precludes back flow, and extends IRZ and CRZ due to lack of tangential expansion of the main flow resulted from the centrifugal force.

A new thumb shape of IRZ is noticed at $X_p/X_{max}=0.68$ by pilot air injection of 4.5% which leads to a steep mean velocity gradient at the lobes of the swirl cones.

The velocity components in the conical jet as well as in IRZ increase as a consequence of the heat released by the flame and the cone angle in the reacting flows increases because of effect of buoyancy plus the centrifugal force in comparison to isothermal flow.

For reacting flows at $X_p = 0.5.X_{max}$, more pilot air ratio increase results in higher pressure gradients and turbulence intensities, and IRZ is similar to a rod shape with thinner width than that one at 0%.

Pilot air ratio of 8.64% at $X_p/X_{max}=0.68$ leads to a high positive pressure gradient and the streamwise velocity profiles represent a central hump shape positive zone accompanied with a shorter CRZ resulted from tangential expansion.

2- Recommendations

It is recommended to test the multi-pilot injector by repartition of different types of fuel as it may be valuable. Liquid fuel is required also to be tested inside the swirl stabilized burner. The transfer of this liquid fuel inside the pilot injector may be good for combustion characteristics enhancing at that type of burners or others. The injector provides a good chance for evaporation of fuel at this test and gives a good dispersion to the fuel inside the main air space. Penetration also will be higher inside the flow field by liquid injector. The amount of transferred liquid fuel also may be valuable for determining the type of produced flame if it is long flame or short one. The application of the flame at that time will depend on its length. The design also helps to use combined fuels of gas and liquid burned together with air.

The design features also may be changed and studied. A change of the pilot injector holes diameter may be achieved to sustain a good mixing, dispersion, and penetration inside the flow field. The number of holes may be increased to give higher mixing between fluids to be burned. The exit angle of the holes of that new injector may also act as an important factor in improvement of the combustion characteristics and the flow field interactions.

The injection of these amounts of air that achieve the stability may be reduced by altering the normal pilot design by the jet excitation method called resonator which may perform the stability at low emissions. Jet excitation at a certain frequency forms the fluid jet into discrete pulses of

fluid upon discharge. The pulses may have an intermittent percussive effect on the main flow field that it blends with upon impact. As well as the fluidic oscillator, the oscillation comes without any external excitation and as such is described as "self-exciting". Thus, no moving parts or valve arrangements are required to bring a pulsed flow. It can be used for gas turbines in liquid or gaseous burners for flame stability.

References

Albrecht, P., Bade, S., Paschereit, C.O., Gutmark, E., "Avoidance strategy for NO_x emissions and flame instabilities in a swirl-stabilized combustor", AIAA20091059 paper, 2008.

Albrecht, P., Bauermeister, F., Bothien, M., Lacarelle, A., Moeck, J., Paschereit, C. O., and Gutmark, E., "Characterization and control of lean blowout using periodically centered flame balls", ASME paper GT2006-90340, Barcelona, Spain, 2006.

Boillot, A., and Prasad, A. K., "Optimization procedure for pulse separation in cross-correlation PIV", Experiments in Fluids 21 (P996) 87-93 _9 Springer-Verlag 1996.

Duwig, C., Fuchs, L., Lacarelle, A., Beutke, M., and Paschereit, C. O., "Study of the vortex breakdown in a conical swirler using LDV, LES and POD", ASME paper GT2007- 27006, Montreal, Canada, 2007.

Emara, A., Lacarelle, A., Paschereit, C. O., "Pilot Flame Impact on Flow Fields and Combustion Performances in a Swirl inducing Burner", AIAA 2009-5015, August 2009, Denver, Colorado, USA.

Guyot, D., and Paschereit, C. O., "Active control of combustion instability using symmetric and asymmetric premixed fuel modulation", ASME paper GT2007-27342, Montreal, Canada, 2007.

Giampaolo, T., "The Gas Turbine Handbook: Principles and Practices", 2nd Edition, the Fairmont Press, 2003.

GRAS sound & vibration, "1/4" Preamplifier Type 26AC, General-purpose", GRAS Denmark, 2009.

ILA, Intelligent LASER Applications GmbH, "Particle Image Velocimetry Software Brochure ", VidPIV 4.6, 2005.

Lacarelle, A.; Luchtenburg, D. M.; Bothien, M. R.; Noack, B. R. & Paschereit, C. O. "Coherent Structure Characterization of Premixed Flames under Varying Forcing Conditions" Int. Conf. on Jets, Wakes and Separated Flows, September 16 – 19, 2008, Berlin, Germany, 2008.

Lacarelle, A., Luchtenburg, D. M., Bothien, M. R., Noack, B. R., and Paschereit, C. O., "A combination of image post-processing tool to identify coherent structures of premixed flames", ICJWSF, Berlin, Germany, 2008.

Lacarelle, A., Faustmann, T., Greenblatt, D., Paschereit, C. O., Lehmann, O., Luchtenburg, D. M., Noack, B. R., "Spatio- Temporal Characterization of a Conical Swirler flow field under strong forcing", ASME paper GT2008-50970, Berlin, Germany, 2008.

Paschereit, C. O., Gutmark, E. J., Weisenstein, W., 1999, "Coherent structures in swirling flows and their role in acoustic combustion control", *Physics of Fluids*, vol. 11, pp. 2667-2678.

Rankin, D.D., "Lean Combustion", Elsevier Inc., 2007.

Seyfried, H., Brackmann, C., Lindholm, A., Linne, M., Aldén, M., Barreras, F., and Bank, R., "Optical Investigations of the Combustion Characteristics of a Gas Turbine Pilot Burner", 45th AIAA Aerospace Sciences Meeting and Exhibit 8 - 11 January 2007, Reno, Nevada.

Scarano, F., "A super-resolution particle image velocimetry interrogation approach by means of velocity second derivatives correlation", *Meas. Sci. Technol.* 15 (2004) 475–486.

Shtork, S.I., *Experimental Thermal and Fluid Science* 31 pp.779–788 (2007).

Tilury, K.C., "Chemiluminescence from the oxidation of model lipid systems", School of Chemical and Physical Sciences Victoria University of Wellington, PO Box 600, Wellington, New Zealand, 1999.

V. Bellucci "TUB TA Course - Noise & instability", TU Berlin, Apr. 2008.

Willert, C., Jarius, M., "Planar flow field measurements in atmospheric and pressurized combustion chambers", *Experiments in Fluids* 33, pp 931–939, 2002.

Yang, V., and Lieuwen, T. C., "Combustion Instabilities in gas turbine engines: Operational experience, fundamental Mechanisms, and Modeling", Vol.210 *Progress in Astronautics and Aeronautics*, Arlington, Texas, 2005.

Part (3)

Planar Investigation of outlet boundary conditions effect on isothermal flow fields of a swirl- stabilized burner.

Chapter (1)

Introduction

Chapter (1) Introduction

Turbulent swirling flows are state of the art for fast mixing and stabilization in industrial combustion systems like gas turbines, boilers and furnaces. Swirl increases fuel-air mixing, improves flame stabilization and has a strong influence on flame characteristics, and pollutant emissions. It may also extend the lean blowout limit (LBO) (Li 2003). A common feature of flow at high swirl intensity (swirl number, $S > 0.6$) is the generation of a central recirculation zone which allows for a flame stabilization in the surrounding shear layer at the burner outlet (Escudier and Keller 1985). The recirculation zone increases also the mixing between exhaust gases and reactants, leading to a rapid homogenization of the combustible mixture and a shortening of the combustion chamber (Solero 2002).

The understanding of swirling flow phenomena remains very challenging, when looking at their mean, coherent and turbulent flow fields, and is still the subject of intensive research. Regarding the mean flow field, Escudier and Keller showed that the nature of the swirling flow (supercritical or subcritical) downstream of the swirler explains the impact of outlet boundary conditions on the flow field (Escudier and Keller 1985). A flow field which remains subcritical after the recirculation zone is strongly changed if the contraction ratio (ratio of outlet area to combustion chamber area) at the outlet of the chamber decreased, while a supercritical flow will only be marginally influenced.

Coherent flow structures are common for swirling flows. These structures take different shapes like precessing vortex core (PVC) which shows mostly a helical structure, or axisymmetric Kelvin Helmholtz vortices generated at the dump plane expansion. These structures may have a positive effect regarding the macro mixing of fuel with air, but may also become critical regarding the stability of the reacting flow in the combustor (Paschereit 1999). How the coherent structures are influenced with changes of the outlet conditions (combustor length and diameter of outlet) still needs to be investigated and is one of the aims of this work.

The swirling flow velocity profiles can be strongly influenced by the outlet conditions of the combustion chamber especially at subcritical flow conditions. The effect of such changes on the mean flow or coherent structures is still unclear. It is investigated in the present work in an industrial swirl stabilizing burner in cold flow conditions with help of PIV. Proper orthogonal decomposition (POD) as well as acoustic measurements were used to characterize the coherent structures shed from the burner mouth.

The combustor length (8.17 D, and 24.63 D) and the outlet area contraction ratio (1, 0.56, 0.27, and 0.09) are varied. Major changes in the flow field are achieved when using a short combustor and the smallest contraction ratio. For this case, a central jet with streamwise velocity is added to the typical central recirculation zone. The POD analysis of the contraction ratios 1 and 0.09 for the long combustor shows that the first helical mode as well as Kelvin Helmholtz vortices is present with minor changes for both cases. At a contraction ratio of 0.09, some new structures at the jet location and near the combustor wall appear.

The presented work characterizes first the flow field of the burner which is as expected independent on the Reynolds number. Mean field as well as RMS velocities and coherent structures are shown. The third part deals with the influence of outlet geometry on the same characteristic flow field properties. The last part evidences with Proper Orthogonal Decomposition the impact of the outlet conditions on the coherent structures.

Chapter (2)

Experimental Techniques and Facilities

Chapter (2) Experimental Techniques and Facilities

The Burner

The same swirl stabilized burner under test, used in this investigation, is a full size conical swirl burner designed by ABB with a cross-sectional area expansion ratio of 4 for flame stabilization (Fig. 1). It consists of two half cones shifted with respect to each other in radial direction (Guyot 2007). The diameter of each cone-half at the outlet is $D = 82$ mm. This diameter is used as a reference length for all characteristic numbers. The airflow enters the cone circumferentially through two lateral inlet slots of constant width. This generates a strong azimuthal velocity component resulting in a high degree of swirl (Swirl no. = 0.7). Together with the area jump at the burner outlet, this leads to a vortex breakdown near the burner mouth followed by a recirculation zone where the flame is stabilized aerodynamically (Duwig 2007). During the combustion conditions, mixing of swirling air and main fuel, results in nearly premixed combustion (Albrecht 2006).

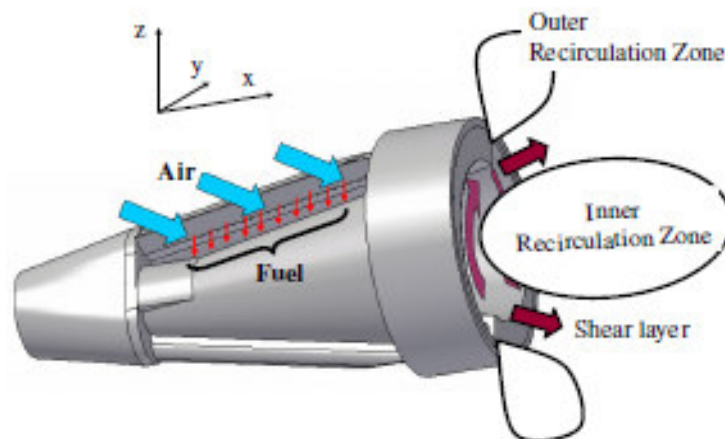


Figure 3.1: Sketch of the Swirl Stabilized Burner

A natural helical flow structure corresponding to a helical instability could be observed at the burner outlet in the cold and reacting cases (Lacarelle 2008). During combustion, the recirculation of hot combustion gases, inside the flame, leads to a second oxidation and a reduction of carbon monoxide. The disadvantages of this type of flame stabilization are flow instabilities accompanied by complex three-dimensional coherent structures (Lacarelle 2008).

The test facilities

All measurements presented in this work were carried out in the combustion test facility illustrated in Fig. 3.2, and the setting is similar to the one used by Bothien (Bothien 2007). The burner is mounted just upstream of the combustion chamber (2.44 D in diameter). The first part of the chamber is a silica tube of 3.66 D in height followed by a steel tube, giving a length of 8.17 D from the burner outlet to the combustion chamber outlet. A second longitudinal tube can be placed on the top of it to increase the length to 26.63 D.

The same condenser microphone which is GRAS- type 26AC- S7 is used to measure the pressure oscillations of the flow downstream of the burner. The microphone is mounted around 5 times the burner diameter in distance upstream of the burner and is used to record the sound pressure oscillations of the flow downstream of the combustion chamber. At this position, it is still possible to record pressure oscillations induced by the flow field in the combustion chamber.

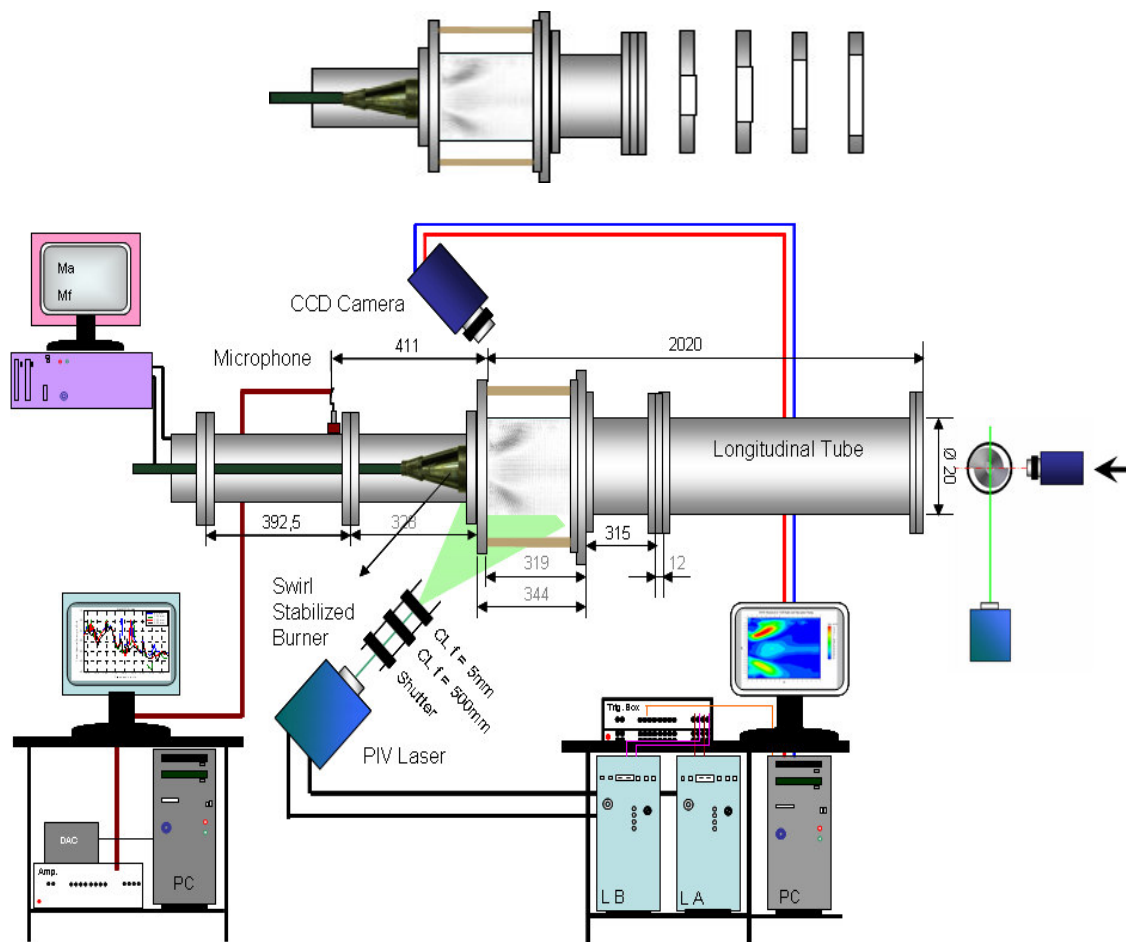


Figure 3.2: Schematic of the test facility with outlets display.

The parameters of the test cases investigated are shown in Table 1

Table (1): Measurement cases

Mass flow	Re	Comb. Chamber length	Contraction	Outlet Diameter
Kg/h		in mm	Ratio, Cr	in mm
160	37917	670 (8.17 D)	1	200
220	52136	670	1, 0.56, 0.27, 0.09	200, 150, 105, 60
220	52136	2020 (26.63 D)	1, 0.56, 0.27, 0.09	200, 150, 105, 60
260	61616	670	1	200

PIV Setup

A Continuum Minilite standard Nd: YAG PIV laser system (wave length 532nm), with pulse energy of up to 25 mJ per pulse, was used to form an axial light sheet perpendicular to the plane formed by the slots of the burner. A convex cylindrical lens ($f= 5 \text{ mm}$) and a concave cylindrical lens ($f = 500\text{mm}$) were used to generate a sheet of approximately 2mm thickness in the combustion chamber. The time interval between the two laser pulses was set to $\tau = 13 \mu\text{s}$ for 220 kg/h and was slightly varied for other mass flows. A total of 800 snapshots were recorded to ensure the convergence of the mean and RMS values.

Liquid tracer particles (SiO_2 , $0.8 \mu\text{m } \varnothing$, Merck) were used to seed the flow field. These particles are injected far upstream of the measurement plane to ensure homogenous mixing of the particles (Tropea 2007). A CCD camera (PCO Sencicam, 1280x1024 pixel resolution) is used to capture the double frame. The camera is equipped with a short focal lens ($f 28/1.8 \text{ SIGMA}$) and a bandpass interference filter centered around 532 nm and is used to reject surrounding light.

For post processing of the data, cross correlation and adaptive cross correlation algorithms were used with an interrogation window size of 16×16 pixel and 50% overlap for higher spatial resolution. Local median velocity filters and linear interpolation were used to eliminate spurious vectors (Lacarelle 2008).

One difficulty of applying PIV in gaseous conditions with round glass surfaces comes from the total reflection of a small part of the laser light inside the glass. This reflection leads to over-exposure of the CCD chip and thus to velocity outliers in the PIV processing. If some of the minor reflections could be minimized through background subtraction, a major reflection was visible at radial coordinate $y/D = 0.5$.

Chapter (3)

Results and Discussion

Chapter (3) Results and Discussion

Independency of the flow field with varying Reynolds Number

The following section details the flow fields of the burner as well as the velocity profiles for three Reynolds numbers (37917, 52136, and 61616) typical for reacting conditions. The short combustion chamber with no contraction ($Cr=1$) is used for these measurements. The results are normalized by the mean bulk velocity based on the burner diameter (D).

A vector flow field contour plot at Re 52136 and $2.44 D$ combustion chamber exit diameter is shown in Fig. 3.3. It illustrates a back flow internal recirculation zone (IRZ), and an external recirculation zone (ERZ) surrounding the shear layer zone. This flow shape is typical for swirling flows with a sudden expansion (Olivani 2007). The IRZ is between $y/D = \pm 0.35$ at the burner outlet and the jet angle surrounding the IRZ widens with increasing distance from the burner exit. Note that the wall of the combustion chamber is located at $y/D = \pm 1.2$ and the short region near the wall could not be properly resolved.

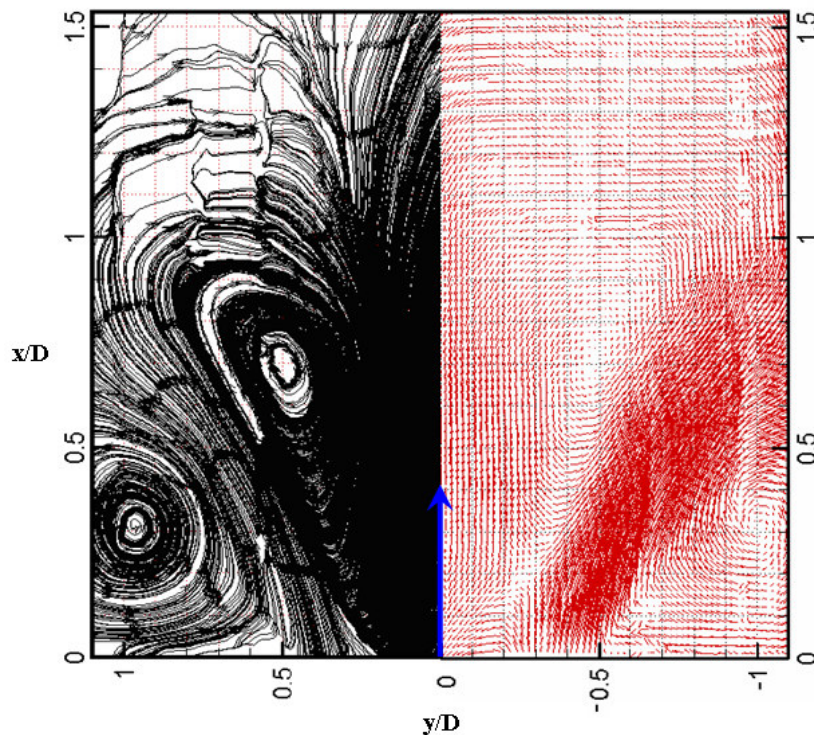


Figure 3.3: Flow streamlines (left half) and vector flow field (right half) plot at $Re=52136$, $Cr=1$ and short combustion chamber ($8.17 D$).

A corner recirculation zone which is created as a result of the confinement enlarges outside the main flow streams and ends approximately downstream of the flow at $x/D \cong 0.6$.

The flow structure zones are also illustrated in Fig. 3.4, where isolines at $u=0$ for the three Reynolds numbers are shown. The position of the isolines is clearly Reynolds independent, as one could expect for high turbulent Reynolds numbers.

This is also confirmed by the profiles shown in Fig. 3.5, 3.6, and 3.7. At different axial locations downstream of the burner outlet, the radial non dimensional profiles for the mean axial velocity, the radial velocity, and the turbulence intensity show no changes. The peak of turbulence is roughly located at the maximum of the radial gradient of the axial velocity, i.e. in the inner shear layer between the conical jet and the IRZ. The flow streams are diffused from the burner outlet with fixed swirl angle. This angle relocates the peak values positions at each radial profile. The reduction in the velocity components is generally according to the momentum dissipation far axially from the burner outlet (Emara 2004).

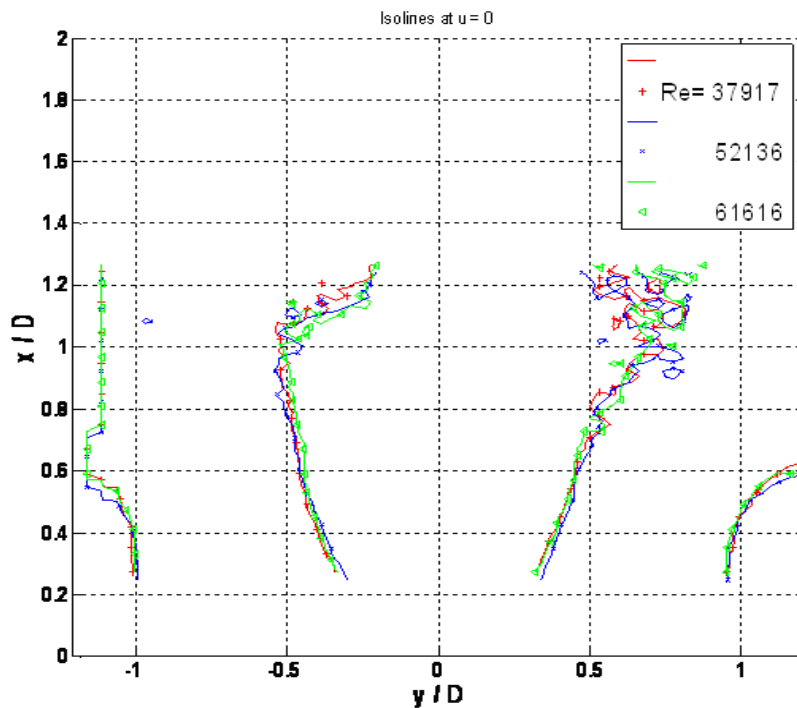


Figure 3.4: Isolines of $u=0$ for different air mass flows (Reynolds numbers 37917, 52136, and 61616).

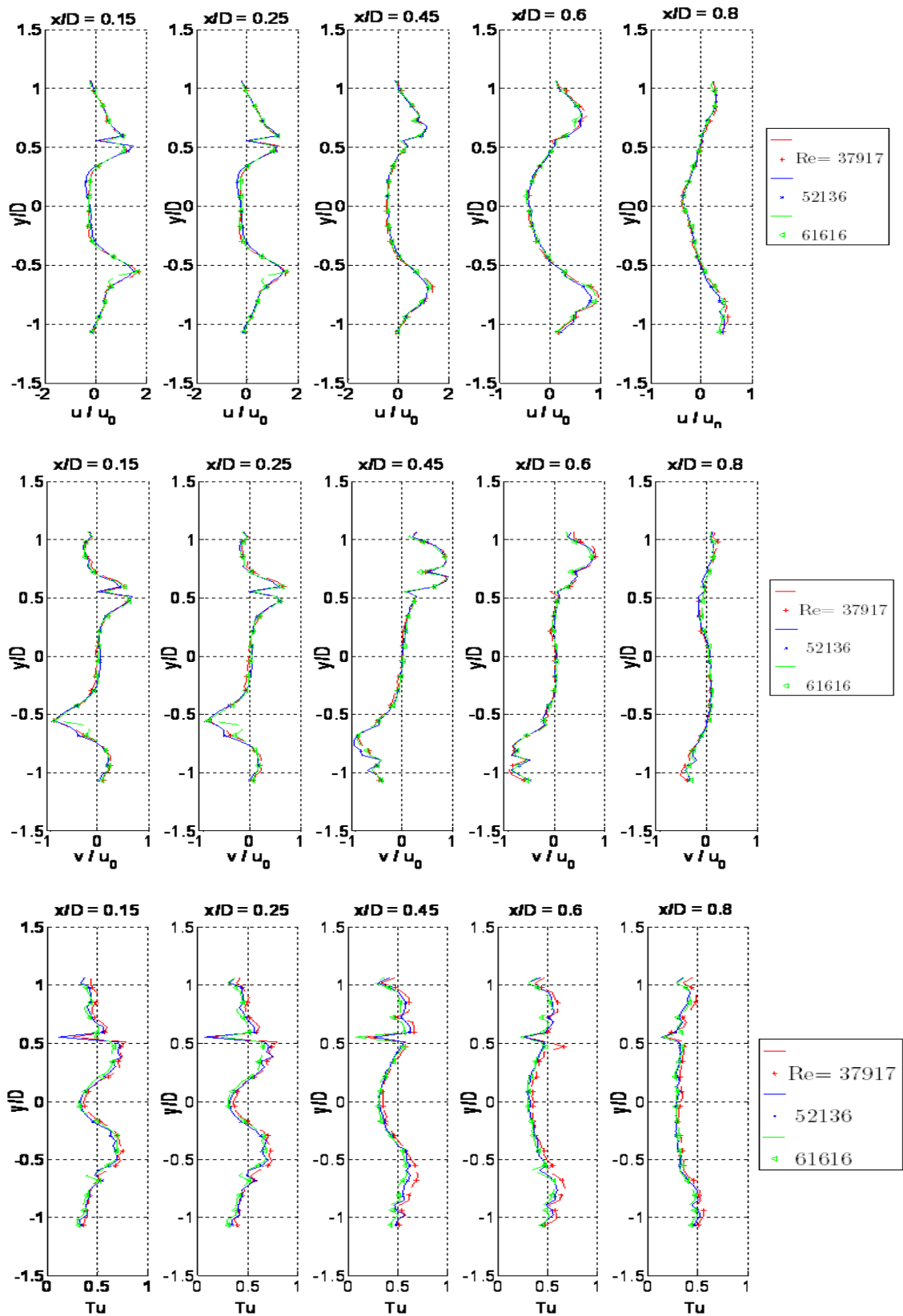


Figure 3.5: Radial profiles of the streamwise velocity u , radial velocity v , and turbulence intensity Tu at different air mass flows and at different axial locations.

High turbulence levels are found near the burner outlet. They decrease with increasing the distance downstream of the flow. The ratio between maximum components of streamwise velocity and mean radial velocity is approximately three times near the burner vicinity (almost to limit of $x/D=0.25$). This ratio is not the same for the flow field far from the burner lips and this is similar to results of Barbosa (Barbosa 2008).

Coherent structure

The microphone placed upstream of the burner recorded the sound pressure fluctuations induced by a coherent structure. The power spectra, recorded for different Re-numbers and presented in Fig. 3.6, show a dominant peak which clearly scales with the Reynolds number.

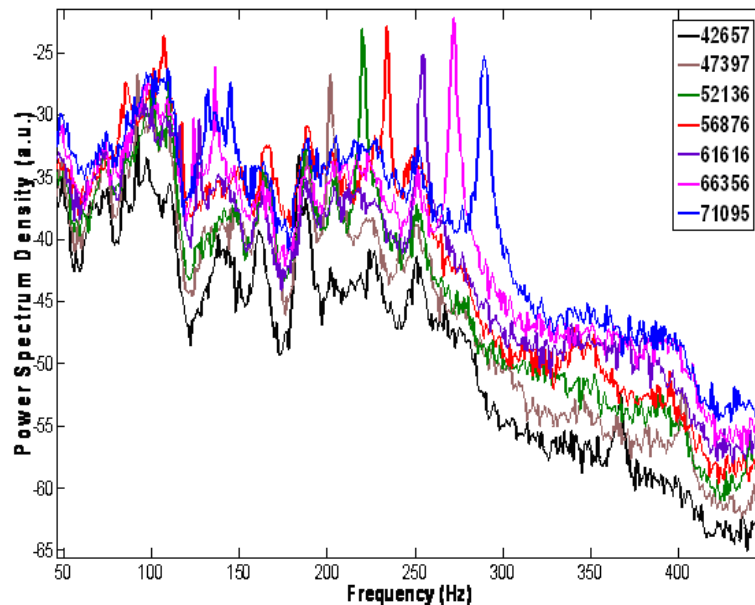


Figure 3.6: Power Spectral Density of the microphone signal for different Reynolds numbers at short combustion chamber length (8.17 D) and $Cr=1$.

The Strouhal numbers of the dominant peak are plotted as a function of the Reynolds number in Fig 3.7. It clearly shows that the Strouhal number remains almost constant around 1.8 with a slight decrease with increasing Reynolds number. This shows that the peaks of Fig. 3.6 are related to flow instability. Their frequencies correspond to the second harmonics of the helical structure for which a Strouhal number of $St=0.92$ was already measured (Tropea 2007). Hence, upstream of the burner and for the short combustion chamber, the second harmonics of the helical structure is much stronger in amplitude than the first harmonics.

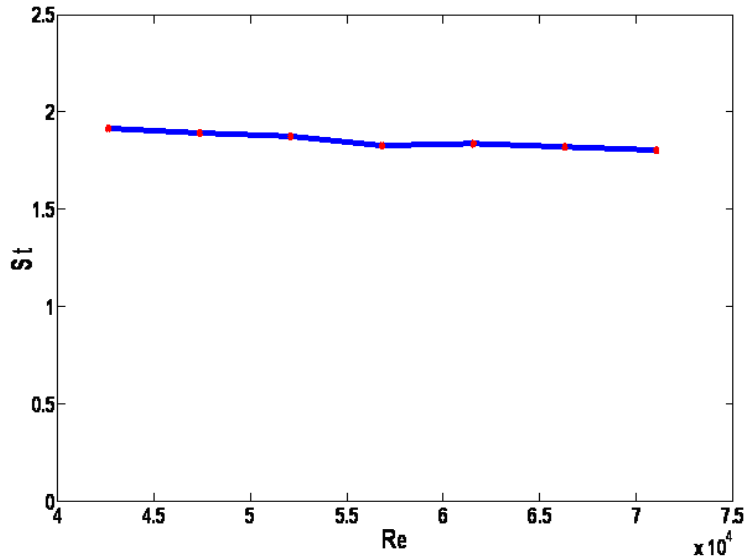


Figure 3.7: Strouhal number of the dominant frequency peaks depending on the Reynolds number.

Outlet boundary conditions effect at short combustion chamber.

If the downstream flow inside the combustion chamber is subcritical, then a great care must be taken over the specifications and the effect of the downstream outlet boundary conditions. Thus, the contraction ratio was varied and the results for the outlet diameters 60, 105, 150, and 200 mm ($Cr=0.09, 0.27, 0.56, 1$), for the short combustion chamber length and a Re of 52220 (220kg/hr) is shown in this section (see Fig. 3.8).

For a contraction ratio of 0.56, the velocity profiles coincide with the profiles of the standard exit ($Cr=1$). Decreasing the exit contraction ratio to 0.27 results in a change in the flow fields which is visible at the axial position $x/D=0.45$. There, a decrease in magnitude of the axial velocity is visible in the IRZ as well as in the shear layer. The vortex core seems to be a lump shape, as the streamwise velocity on the flow axis is positive when $x/D= 0.6$. Hence, a reduction of the contraction ratio to 0.27 affects the standard shape of the recirculation zone and influences strongly the flow field.

Comparing to the other outlets, a contraction ratio of 0.09 has a strong influence on the entire flow field. The internal back flow zone shape is completely changed comparing to the standard outlet condition (see Fig. 3.9, and 3.10). Moreover the vortex core, along the entire centerline becomes jet like and the axial velocity increases with increasing axial position. This behavior is not typical for jet or wake profiles, for which the absolute velocity on the centerline decreases

with increasing axial position. The vortex core resulting from the exit contraction may have been created due to the convection of the flow streams from the endwall boundary layer or the internal diffusion of the vorticity (Escudier 1985).

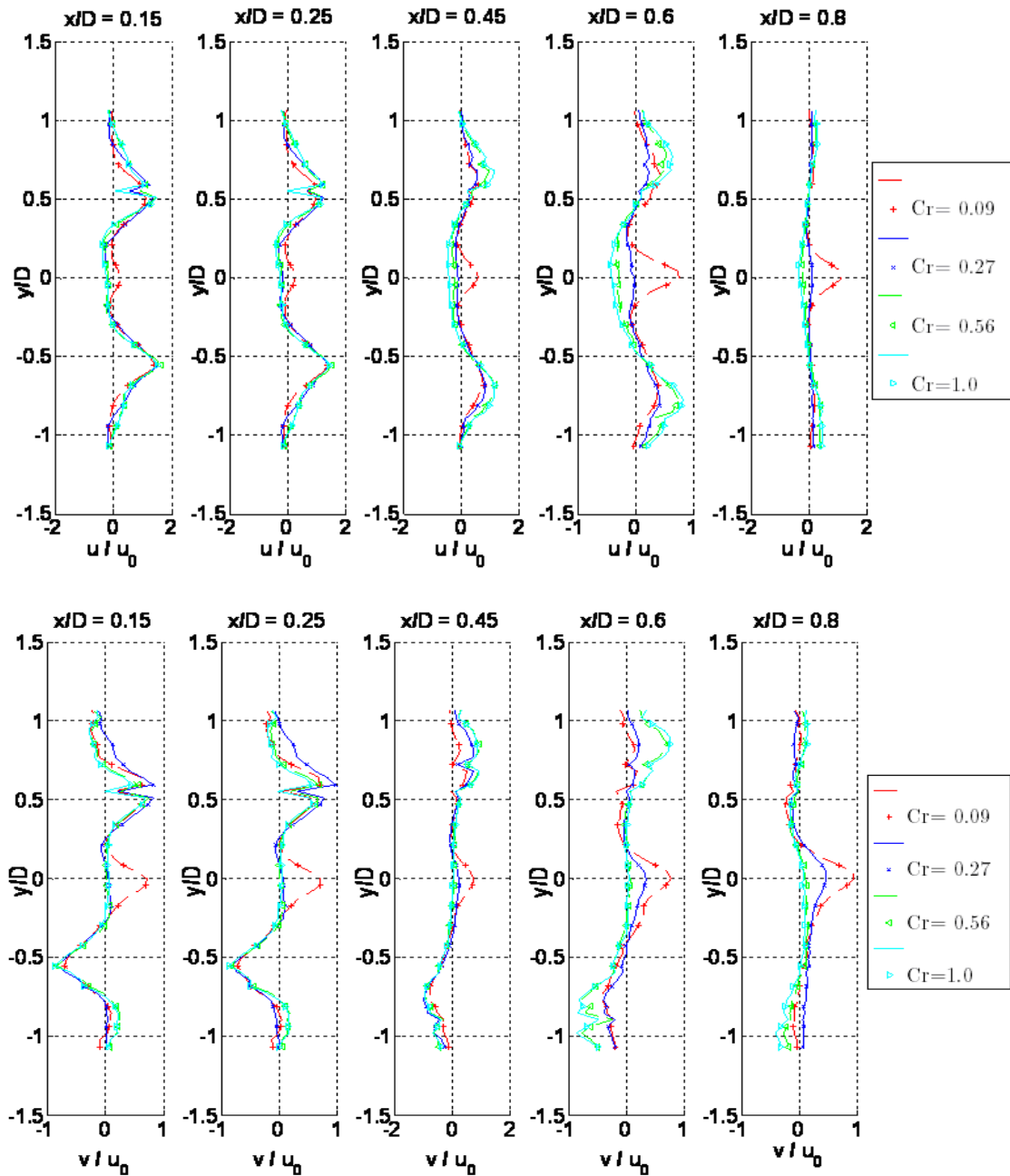


Figure 3.8: Radial profiles of the streamwise velocity u and radial velocity v at different exit contraction ratios ($Cr= 0.09, 0.27, 0.56,$ and 1.0), and at $8.17 D$ height from burner exit for air mass flow of $Re= 52136$.

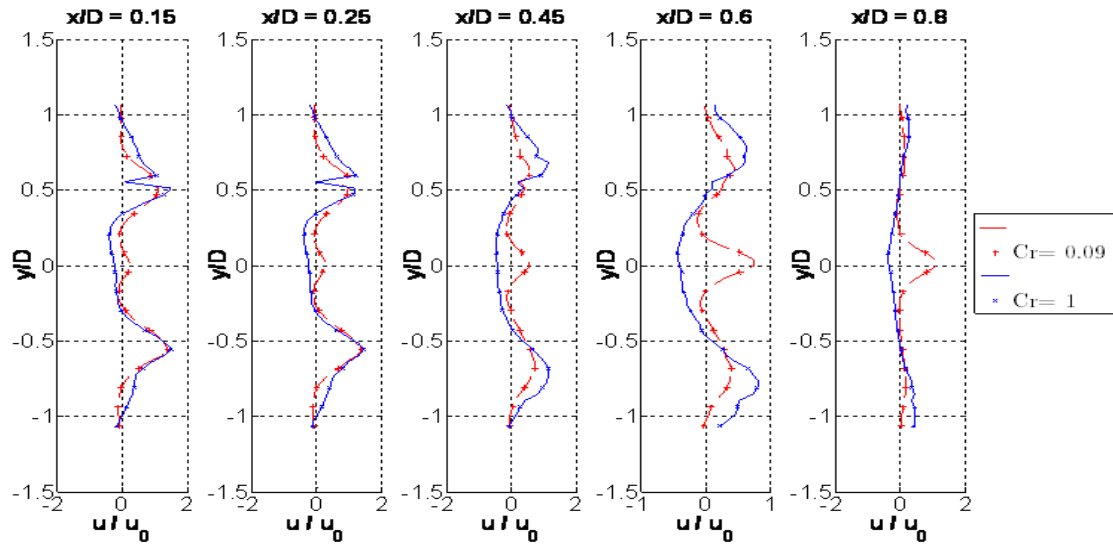


Figure 3.9: Radial profiles of the streamwise velocity u at different exit contraction ratios ($Cr=0.09$ and 1.0), and at $8.17 D$ height from burner exit for air mass flow of $Re= 52136$.

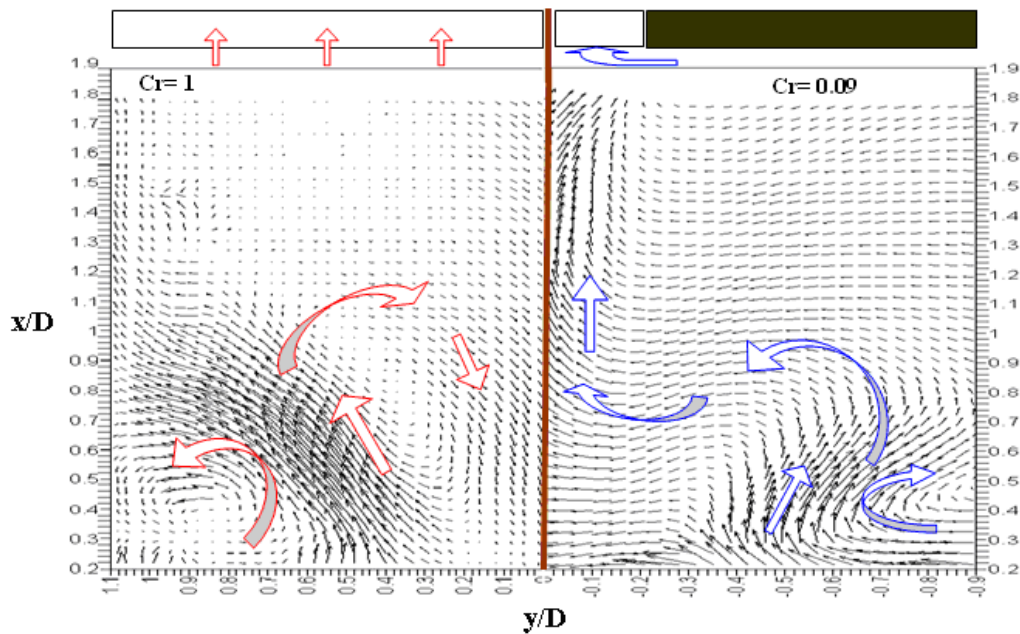


Figure 3.10: Vector flow field contour plots- Comparison between minimum (right $Cr= 0.09$) and maximum (left $Cr= 1$) exit contraction ratios at $Re= 52136$ of air mass flow and at height $8.17 D$ from burner mouth.

As shown in Fig. 3.9, the ratio between the vortex core velocity to the peak mean axial velocity at each radial profile increased from around 0.2 at $x/D = 0.15$ to around 5.0 at $x/D= 0.8$ according to the effect of burner exit geometry. The central mean axial velocity increased around 4 times at the last range ($x/D= 0.8$) for the maximum contraction case while the central radial one is increased

1.3 times at the same range of x/D , see Fig. 3.8, and 3.9. Figure 3.11 gives a picture of the vortex core width which is in direct proportion with the contraction ratio and broadens axially downstream of the flow.

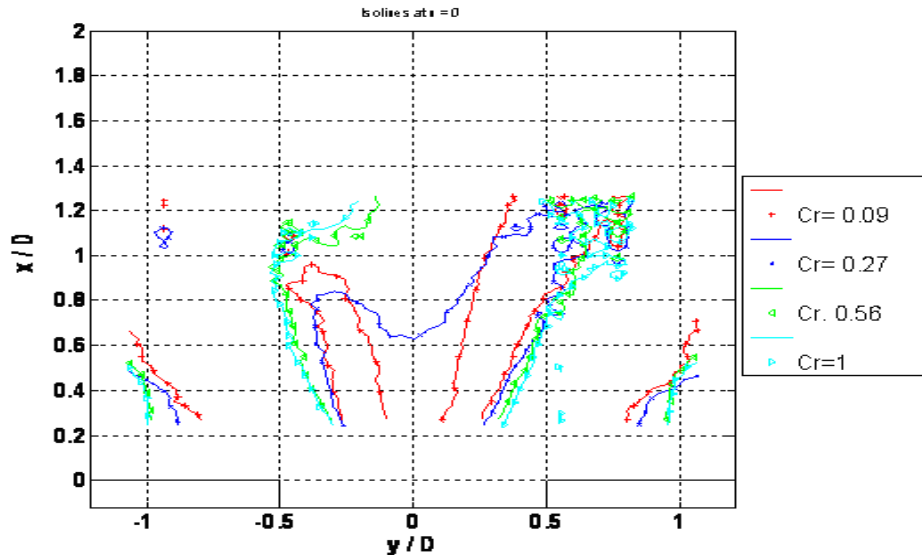


Figure 3.11: Isolines of $u=0$ for different exit contraction ratios ($Cr= 0.09, 0.27, 0.56, \text{ and } 1$) and at $8.17 D$ height from burner exit for $Re= 52136$.

Outlet boundary conditions effect at different combustion chambers

Increasing the combustion chamber length to $24.63 D$ decreases the effect of the smallest contraction ratio on the velocity profiles downstream of the burner outlet. As shown in Fig. 3.12, there is similarity in the velocity field, but at the higher length case the axial velocity on the centerline becomes positive for axial values larger than $x/D = 0.6$.

The central jet which appears clearly at $x/D=0.45$ for the short combustion chamber, moves further downstream when the combustion chamber length is increased to $24.63 D$. At $x/D= 0.8$, where the velocity on the centerline is positive for both combustor lengths, the central mean axial velocity for the longest one is equal to 16% of the central mean axial velocity to the shortest combustion chamber. This means that the flow at the vicinity of the burner mouth propagates in direction of the chamber end and does not sense, at the centerbody location, a big effect of the contraction at this length.

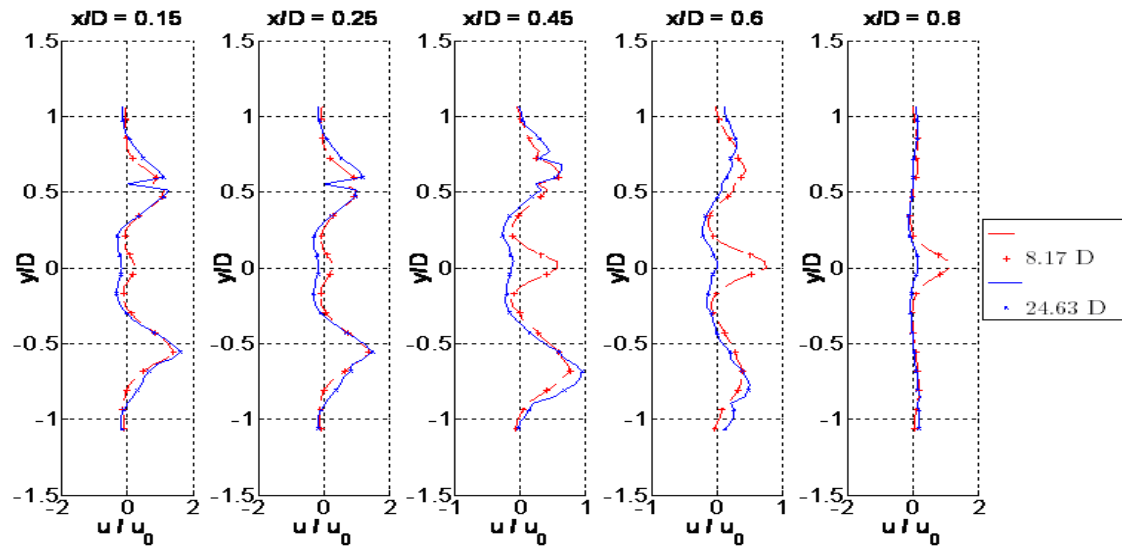


Figure 3.12: Radial profiles of the streamwise velocity u at exit contraction ratio $Cr= 0.09$, and at different heights from burner exit (8.17 D and 24.63 D) for air mass flow rate at $Re= 52136$.

Impact of outlet conditions on coherent structure

The different outlet conditions did not only an impact on the mean flow field but also on the coherent structure which are induced by the swirling flow. Figure 3.13 shows how a reduction of the outlet diameter enhances the dominant peak of the power spectral density (PSD) by around 10 dB and shifts its frequency from 207 Hz to 216Hz ($Cr= 1$ and $Cr= 0.56$). A further reduction to $Cr= 0.27$ makes the peak move further to higher frequencies. A further reduction of the diameter to 60mm ($Cr = 0.09$) generates a second peak around 191 Hz.

To obtain more information about the effect of the outlet diameter on the turbulent flow field, proper orthogonal decomposition (POD) of the radial velocity component v was performed on a series of 600 snapshots for each case ($Cr= 1$ and $Cr= 0.09$ outlet diameter, and at 24.63 D combustor length). The method of the snapshots of Sirovich was used, and more details on the methodology can be found in Holmes (Holmes 1998). The POD allows for filtering the PIV data by extracting the dominant coherent structures relative to their energy content. The resulting modes are sorted from the most energetic to the last energetic. In flows with strong coherent structures, the first 10 to 15 modes have generally a physical meaning, higher modes being too noisy to allow for a reliable interpretation.

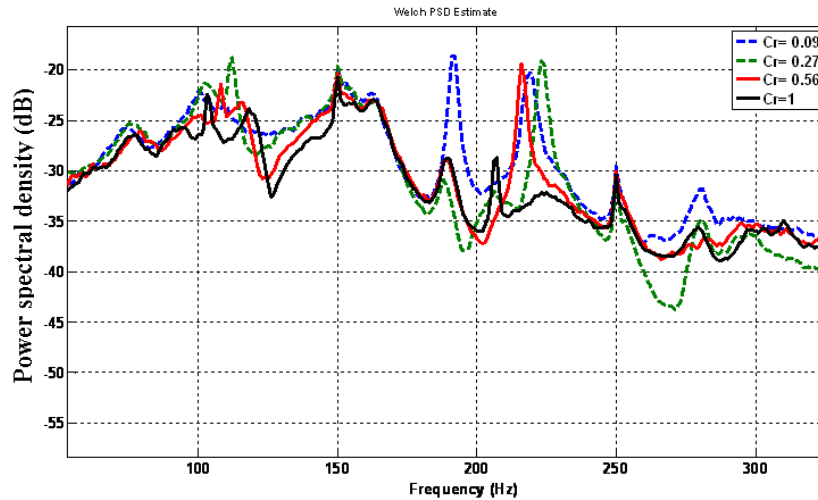


Figure 3.13: Influence of the outlet diameter on the dominant frequency recorded by the microphone mounted upstream of the burner (Combustor length =24.63 D).

For the two cases chosen, the 6 first dominant modes were sorted out and are shown in Fig. 3.14. The modes are normalized and the sign of the velocity gives information on the nature of the structure, which can be whether axisymmetric or antisymmetric. The definition of our radial velocity, which is defined for a Cartesian coordinate system centered in the middle of the burner outlet, leads to an opposite interpretation color / structure. An antisymmetric structure (like the helical structure) will have a symmetric color plot of the radial velocity and vice versa.

Following this, the modes 1 and 2 of contraction ratio $Cr=1$ case are typical for a helical instability (axisymmetric color plot = antisymmetric structure). They are slightly shifted with each other in the main flow direction (orthogonality condition of POD) and their energy contents are almost identical, as shown by the total turbulent kinetic energy repartition of Fig. 3.15. They represent thus the helical motion, which dominates the coherent flow field. Modes 3 and 4 represent an axisymmetric structure (antisymmetric color plot) which moves from the center of the burner outlet to the wall of the combustor. They correspond to axial vortices shedded from the dump plane at the burner outlet. Such structures were already observed on a similar burner by Paschereit (Paschereit et al. 1996). Further mode shapes remain noisier and do not show clear patterns. $Cr= 0.09$ shows also the helical structure in modes 1 and 3 mainly, but also in mode 2 which appears to be a combination of the jet downstream of the vortex breakdown and the helical structure. The mode shape of modes 1 and 3 is very similar to the shape of the modes 1 and 2 of $Cr= 1$, confirming that the helical structure remains present for both outlet conditions. The mode 2 suggests that the jet core ($x/D > 0.5$) rotates around the centerline.

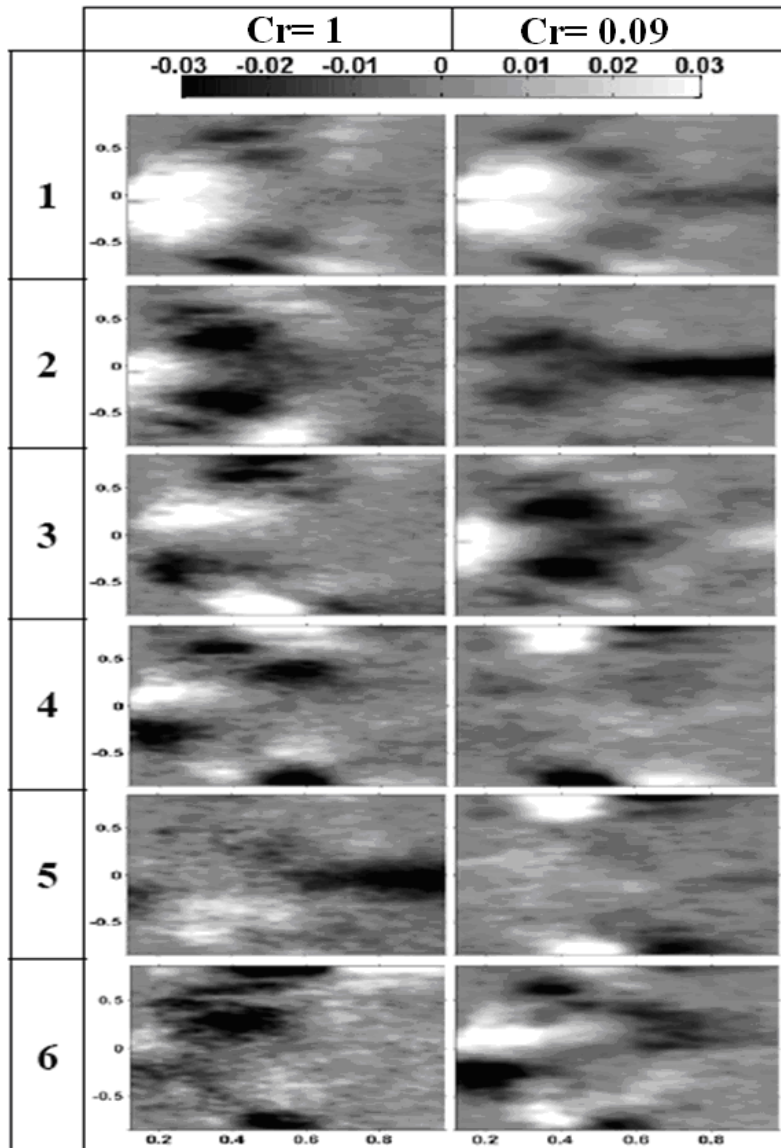


Figure 3.14: First six POD modes of the radial velocity v for $Cr= 1$ and $Cr= 0.09$ outlet conditions. The analysis was done with 600 snapshots for each case.

The mode 6, which represents an axisymmetric structure, is very similar to the mode 3 of $Cr= 1$. Hence, these coherent structures are practically uninfluenced by the contraction ratio. Finally, 3 new modes appear when the $Cr= 0.09$ is used: the mode 2, which is a consequence of the jet like velocity profile, and modes 4 and 5, which show, near the wall, axisymmetric and antisymmetric structures respectively.

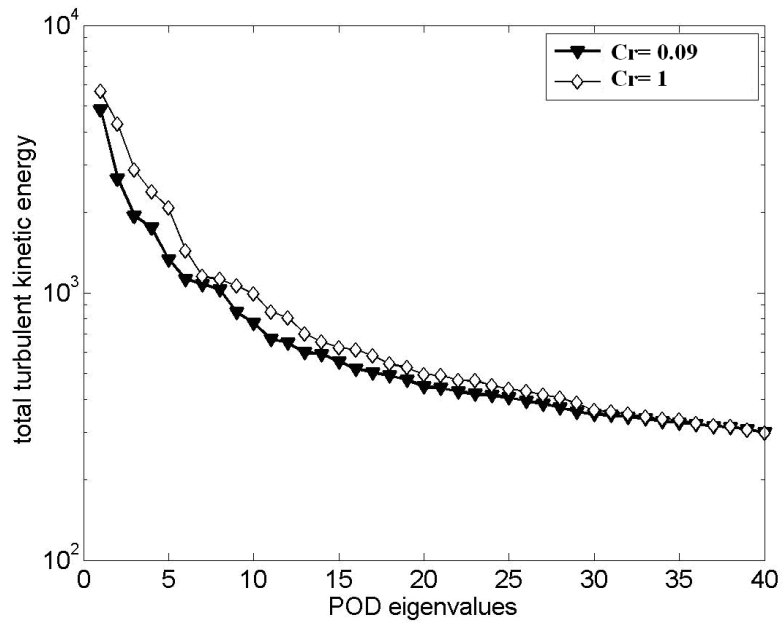


Figure 3.15: Total Turbulent Kinetic Energy of the POD eigenvalues for $Cr = 1$ and $Cr = 0.09$.

Chapter (4)

Summary and conclusion

Chapter (4): summary and conclusion

The turbulent isothermal flow in a conical swirl stabilized burner was studied for different combustion chamber lengths downstream of the burner and at different contraction ratios.

Measurements performed at different Reynolds numbers, but remaining in the turbulent range, show that the normalized mean velocity and turbulence intensity profiles are identical. The normalized flow field is thus not depending on the Reynolds number.

The contraction effect, at contraction ratio smaller than 0.56, influences the character and the common shape of the back flow zone and the flow field. The vortex core appears as a lump shape, as there is a positive velocity vectors noticed along the chamber axis. A contraction ratio of 0.09 exhibits a strong influence on the entire flow field and the vortex core (along the burner flow centerline) becomes jet like. This vortex core elongates axially downstream of the flow despite of momentum dissipation to the rest of the flow field.

The jet like vortex starts further upstream of the burner when the contraction ratio decreases. When using small area ratios, an increase of the combustion chamber length decreases its influence on the recirculation zone.

The POD showed that a reduction of the outlet exit diameter has a little impact on the helical structure which dominates the coherent motion of the flow. Some differences in the mode shapes still appear (modes 2, 4, 5 for $Cr= 0.09$) and may explain the occurrence of the secondary peak observed close to the frequency of the helical structure for $Cr= 0.09$.

Finally, outlet contraction influences the character and the common shape of the back flow zone and the entire flow field. Higher contraction exhibits a strong influence on the entire flow field and the vortex core becomes a jet like. An increase of the combustion chamber length decreases influence of the contraction on internal recirculation zone. Contraction has an impact on the helical structure and dominates the coherent motion of the flow.

References

Albrecht, P., Bauermeister, F., Bothien, M., Lacarelle, A., Moeck, J., Paschereit, C. O., and Gutmark, E., "Characterization and control of lean blowout using periodically centered flame balls", ASME paper GT2006-90340, Barcelona, Spain, 2006.

Barbosa, S., Scouflaire, P., and Ducruix, S., "Time resolved flowfield, flame structure and acoustic characterization of a staged multi-injection burner", Proceedings of the Combustion Institute (2009), Elsevier Inc., 2008.

Bothien, M. R., Moeck, J. P., Paschereit, C. O., "Impedance tuning of a premixed combustor using active control", ASME paper GT2007- 27796, Montreal, Canada, 2007.

Duwig, C., Fuchs, L., Lacarelle, A., Beutke, M., and Paschereit, C. O., "Study of the vortex breakdown in a conical swirler using LDV, LES and POD", ASME paper GT2007- 27006, Montreal, Canada, 2007.

Emara, A., "Characteristics of the Conical Fuel Spray in Co-axial Burners", M.Sc. Thesis, Helwan University, Cairo, 2004.

Escudier, M.P., and Keller, J.J., "Recirculation in Swirling Flow: a Manifestation of Vortex Breakdown", AIAA, Vol. 23, No. 1, January 1985.

Guyot, D., and Paschereit, C. O., "Active control of combustion instability using symmetric and asymmetric premixed fuel modulation", ASME paper GT2007-27342, Montreal, Canada, 2007.

Holmes P., Lumley J., and Berkooz G., "Turbulence, Coherent Structures, Dynamical Systems and Symmetry", Cambridge University Press, Cambridge, 1998.

Lacarelle, A., Luchtenburg, D. M., Bothien, M. R., Noack, B. R., and Paschereit, C. O., "A combination of image post- processing tool to identify coherent structures of premixed flames", ICJWSF, Berlin, Germany, 2008.

Lacarelle, A., Faustmann, T., Greenblatt, D., Paschereit, C. O., Lehmann, O., Luchtenburg, D. M., Noack, B. R., "Spatio- Temporal Characterization of a Conical Swirler flow field under strong forcing", ASME paper GT2008-50970, Berlin, Germany, 2008.

Li, G., and Gutmark, "Geometry effects on the flow field and the spectral characteristics of a triple annular swirler ", ASME paper 2003-GT-38799, Atlanta, Georgia, USA, 2003.

Olivani, A., Solero, G., Cozzi, F., Aldo and Coghe, A., "Near field flow structure of isothermal swirling flows and reacting non-premixed swirling flames" *Experimental Thermal and Fluid Science* 31, 427–436, 2007.

Paschereit, C. O., Gutmark, E. J., Weisenstein, W., 1999, "Coherent structures in swirling flows and their role in acoustic combustion control", *Physics of Fluids*, vol. 11, pp. 2667-2678.

Paschereit, C. O., Gutmark, E. J., and Weisenstein, W., "Excitation of Thermoacoustic Instabilities by Interaction of Acoustics and Unstable Swirling Flow", *AIAA Journal*, vol. 38, Nr. 6, pp. 1025-1034, 1999.

Solero, G., and Coghe, C., "Experimental analysis on turbulent mixing in a swirl burner", *Open Meeting on Combustion*, Dipartimento di Energetica - Politecnico di Milano, Italy, Ischia, May 22-25, 2000.

Tropea, C., Yarin, A.L., and Foss, J.F., (Eds.), "Springer Handbook of Experimental Fluid Mechanics", Springer-Verlag, Berlin Heidelberg, 2007.

Final Conclusion

Final Conclusion

The present work is divided into three main parts. The first one provides a fluidic oscillator as a mean for emissions reduction at the combustion systems, especially in the jet engines, and also for reduction of the thermoacoustic instabilities. The fluidics is modified to overcome the size restrictions inside the swirl stabilized burner at the first design variation. Design modulations are performed at the second design variation by changing several specified factors on the produced model from the first design variation to find out the optimum models that achieve the required stable combustion. The fluidic oscillator is tested freely in air and water aquarium. It is tested also after insertion inside the swirl stabilized burner in the water tunnel and the combustor. The fluidics can stabilize the flame at different positions inside the burner and also reduces the products emissions. The air repartition considers the best and the optimum way to reduce the emissions at the whole mounting locations. Some small amounts of pilot fuel besides air may be useful in nitrogen oxides reduction at low values of carbon monoxide. This also widens the flammability limit and sustains the flame at some reacting conditions which may have lean blow off or extinction of the flame at the same equivalence ratio applied without using of the oscillator. The fluidics enhances the combustion to comply with the environmental laws at the whole world.

The control of the flame instability and emissions is performed at the second part of work by repartition of the fuel, air, or premix, from the main flows of the same swirl stabilized burner, inside the multi- pilot injector at constant overall equivalence ratio and power like the fluidic oscillator. Two pilot injectors are tested. Nevertheless, the multi- injector pilot showed good results in stabilizing the combustor. The best results for stability and emissions reduction were performed when the injector was positioned at the burner underside. The strong air momentum, induced by this injector, performs the flame stability, enhances the mixing upstream of the flame and in turn reduce the emissions, and prevents the flame from traveling upstream into the burner inside the whole burner positions.

The turbulent isothermal flow field was studied for different combustors at different outlet geometries. Outlet contraction influences the character and the common shape of the back flow zone and the entire flow field. Higher contraction exhibits a strong influence on the entire flow field and the vortex core becomes a jet like. An increase of the combustion chamber length decreases influence of the contraction on internal recirculation zone. Contraction has an impact on the helical structure and dominates the coherent motion of the flow.

